

Programa de Doctorado en:

Métodos Matemáticos y Simulación Numérica en
Ingeniería y Ciencias Aplicadas

**DEVELOPMENT OF A MULTIDISCIPLINARY AND OPTIMIZED
DESIGN METHODOLOGY FOR SURFACE PERMANENT
MAGNETS SYNCHRONOUS MACHINES**

Doctorando

Alejandro L. Rodríguez González

Directores

Alfredo Bermúdez de Castro López-Varela

Irma Villar Iturbe



Facultad de Matemáticas

23/12/2015



Acknowledgements

Some time has passed since the idea of start a thesis was conceived by first time. It is not true that those years are only full of great things, encouraging challenges and generous companions in that interesting journey, although they were always present. During this time I have learned that a work as exhaustive as a thesis has both, peaks and valleys, moments of personal improvement and days of tedious and despair where nothing seems to fix.

However, spite of the bad moments and some unforeseen abrupt changes I have realized that the shadows are no more than the necessary contrast in order to see the bright, and there was so much bright in the recent pass; especially because, through the thesis, I meet people, listen to many points of view and learned useful approaches to face different problems, both technical and professional, and this is invaluable.

I do not know if the past years were the best, but I am sure that they were pretty intense. And that is because many people make it possible, my sincere gratitude to all of them.

First of all, especial thanks to my thesis directors, prof. Alfredo Bermúdez de Castro for accepting me as a PhD student at the Applied Mathematics Department of the University of Santiago, and for the confidence and continuous support he provides me and to Dr. Irma Villar for they advise, supervision and encouragement which impelled me to improve day by day.

I am also grateful to IK4-Ikerlan for its essential financial support and, especially, to its Mechatronics Unit director, Ion Etxeberria-Otadui, for encourage me to start this long journey, without him the very first step was no possible.

I am greatly indebted to prof. Emilio Carrizosa of Sevilla and prof. Custódio of Coimbra because of their decisive help in the selection and adaptation of the DMS optimization algorithm; and with the IK4-Ikerlan Mechanical Engineering companions Markos, Ekhi, Félix, Iker and Aitor whose help and advice was indispensable in order to carried out the mechanical tests and correctly interpret the obtained results. I also would thanks my comrade Andoni for translate the thesis abstract to Euskara.

I would like to thanks to LANCOR who manufactured the machine prototype (IkerMAQ) and who provided me a case of study with thermal sensors included.

My warm and sincere gratitude goes to Damian, partner and friend in the journey, because the valuable discussions, the interesting questions and the sharp answers.

I am also grateful to all the people in IK4-Ikerlan Control and Power Electronic Area, for the excellent atmosphere they always create all around. Especial thanks to my “car-mates”, Jean Francoise, Josu, Alex, Andoni and Karlos for the fellowship and the jokes.

Thanks to all the USC Applied Mathematics department staff who makes me feel at home. Especially I want to thank Elisa, Elena, Dolores, Pilar, Marta, Chuco and Saray for being there in every moment helping me with any difficulty.

And last but not least I would thank many people in my personal life, because without them the trip were darker and the lights trembling.

Thanks my closest friends Fer, Raúl and Ainara for their comfortable presence and their continuous encouragements. Thanks to my overseas phoenix, Teresa, who touched my soul with her words and let me recover my own missing voice.

Thanks to my friends in Vitoria, Marcos, Alex, Heri and Aitor for the “*pintxo-pote*”, the runs and for accepting me as one more in their “*cuadrilla*”. It is for them that I feel Vitoria like a second home city.

Thanks to my family, my aunt Inma, my grandmother Carmen “*tita*”, for being there warming my hearth, believing in me in any time and circumstance. Thanks to my parents, for all these years of abnegation, for the sweet memories.

My last and most heartfelt gratitude to my beloved Lara, for being music in the wind, dawn in the night and hope every single day.

During these acknowledgements I have compared a thesis with a long journey, so I would finish them with the best definition of voyage I have ever read, perhaps it will bring to your minds the exact meaning that this thesis has had for me.

*“As you set out for Ithaka
hope the voyage is a long one,
full of adventure, full of discovery.
[...]
Keep Ithaka always in your mind.
Arriving there is what you are destined for.
But do not hurry the journey at all.
Better if it lasts for years,
so you are old by the time you reach the island,
wealthy with all you have gained on the way,
not expecting Ithaka to make you rich.*

*Ithaka gave you the marvellous journey.
Without her you would not have set out.
She has nothing left to give you now.*

*And if you find her poor, Ithaka won't have fooled you.
Wise as you will have become, so full of experience,
you will have understood by then what these Ithakas mean.”-C.P. Cavafy*

Abstract

Electric energy is one of the supports of modern civilization. In the actual context, the electrical machines are of capital importance since most of power plants, from nuclear plants to wind turbines, need an electrical machine working as a generator. Moreover, it is estimated that nowadays the 65% of the total energy supplied by the grid is consumed by electric motors working in an industrial environment.

Electrical machines are complex systems where a great amount of physical phenomena are produced simultaneously; that is why a proper design requires detailed multidisciplinary models. However, most of the design methodologies and tools are only focused on machine electromagnetic performance in order to achieve power, efficiency and mass to volume ratio goals, performing an adequate more than an optimized design. In the best cases, the features related with other physical domains are taken into account through figures or merit or rules of the thumb based on designer particular experience (e.g. thermal sizing); or even they are treated as an afterthought if needed (typical case of the machine vibro-acoustic performance).

These approaches are only suitable for very well-known applications where machine features are perfectly known and characterized. However, these methodologies are unsystematic by nature so they have serious difficulties in order to extrapolate the obtained results to a new set of specifications or to more challenging applications where not only electromagnetic criteria but other physical domains, such as vibro-acoustic, should be taken into account.

More precisely, since the advent of neodymium iron boron (NdFeB) magnets, permanent magnets synchronous machines (PMSM) has become a suitable option both in industrial and domestic applications such as aircraft industry, elevation, electric vehicle or power generation. Due to their attractive features (e.g. high efficiency, compactness and power density) PMSMs are an emerging technology and an attractive field of study, as it is highlighted by the great amount of publications devoted to that topic in the last years.

Therefore, the thesis main goal is the development of a pioneering PMSM design methodology based on a holistic, multidisciplinary and optimized approach. Moreover, this proposed methodology takes into account not only the electromagnetic and thermal conventional aspects but also the machine vibro-acoustic behaviour.

In order to fulfil this aim, a complete multiphysical analytical model has been carried out, including a detailed study of the electromagnetic, thermal and vibro-acoustics PMSM features, paying a special attention to these physical domains interactions.

The developed models have been used in order to implement a PMSM design optimized methodology based on an innovative heuristic algorithm labelled Direct Multisearch (DMS).

In order to validate the physical models, a 75 kW PMSM prototype (IkerMAQ) has been designed and built. A huge amount of tests were carried out and the analytical models have been exhaustively validated, including electromagnetic, thermal and vibro-acoustic domains.

Keywords: Permanent magnets synchronous machines, Analytical multiphysical modelling, Vibro-acoustic modal study, PMSM experimental characterization, PMSM design methodology.



Resumen

La energía eléctrica es uno de los soportes de la civilización moderna. En el contexto actual, las máquinas eléctricas son de capital importancia dado que la mayoría de las centrales generadoras de energía, desde las plantas nucleares a los molinos eléctricos, necesitan una máquina eléctrica trabajando como generador. Por otro lado, se estima que el 65% de la energía eléctrica producida es consumida por motores eléctricos en un entorno industrial.

Las máquinas eléctricas constituyen sistemas complejos en los que se producen numerosos fenómenos físicos, por ello su proceso de diseño requiere de detallados modelos multidisciplinarios. No obstante, las metodologías y herramientas que habitualmente se emplean se centran en consideraciones electromagnéticas y eléctricas con el objeto de alcanzar las prestaciones de potencia, de eficiencia y de relación volumen/masa definidas y realizando diseños más bien adecuados que óptimos. Los aspectos referentes a otras disciplinas bien se tienen en cuenta mediante reglas empíricas y figuras de mérito basadas en la experiencia previa del diseñador (caso del dimensionado térmico), bien se relegan a un segundo plano, dándoles una importancia menor durante el proceso de diseño (por ejemplo, el estudio vibro-acústico de la máquina).

Dicho enfoque resulta efectivo para la realización de máquinas muy similares a las que ya existen y cuyo comportamiento está muy bien caracterizado, pero, debido a su naturaleza poco sistemática, presenta graves problemas cuando se busca incluir nuevos criterios de diseño no referentes a la dimensión electromagnética del problema, tales como restricciones en el comportamiento vibro-acústico de la máquina.

En concreto, las máquinas síncronas de imanes permanentes (PMSM por sus siglas en inglés) se han convertido, desde el descubrimiento de los imanes de neodimio hierro-boro (NdFeB), en una interesante opción tanto en las aplicaciones industriales como domésticas. Sirva como ejemplo su relevante presencia en sectores tales como la elevación, aeroespaciales, el vehículo eléctrico o la generación eléctrica. Sus buenas características (elevada eficiencia y alta densidad de potencia, entre otras) hacen de ellos una tecnología emergente y un atractivo campo de estudio, como demuestra la gran cantidad de publicaciones realizadas en los últimos años.

Por ello, el objetivo fundamental de la tesis es el desarrollo de una innovadora metodología que permita realizar diseños de PMSM holísticos, multidisciplinarios y optimizados, considerando en la fase de diseño además de los aspectos convencionales, el comportamiento vibro-acústico de la misma.

Para cumplir con este objetivo se ha desarrollado un completo modelado multidisciplinar y analítico a partir de un detallado estudio de las características electromagnéticas, térmicas y vibratorias de la PMSM prestando una especial atención a las interacciones entre los diferentes dominios físicos.

Estos modelos se han utilizado para desarrollar una innovadora metodología optimizada de diseño basada en la utilización de un novedoso algoritmo heurístico llamado DMS (direct multiseach).

Finalmente un prototipo de máquina síncrona de 75 kW (IkerMAQ) ha sido diseñado y, a través de numerosos test que abarcan todos los dominios físicos citados, se han validado exhaustivamente los modelos analíticos.

Palabras clave: Máquinas eléctricas de imanes permanentes, modelado analítico multifísico, estudio modal vibro-acústico, caracterización experimental, metodología de diseño de máquinas eléctricas.



Laburpena

Energia elektrikoa zibilizazio modernoaren oinarrietako bat da. Gaur egungo kontextuan, makina elektrikoak garrantzi handia daukate zentral elektriko gehienak hauetako bat behar dutelako sorgailu moduan lan egiteko, zentral nuklearretatik haize sorgailuetaraino, besteak beste. Bestalde, gaur egungo sare elektrikoa hornitzen duen % 65a motore elektrikoak inguru industrialetan kontsumitzen dutela estimatu da.

Makina elektrikoak sistema komplexuak dira non fenomeno fisiko ugari gertatzen diren aldi berean; horregatik diseinu egoki batek diziplina anitzeko eredu zehatzak eskatzen ditu. Hala eta guztiz ere, diseinu metodologia eta diseinu tresna gehienak makinaren ezaugarri elektrikomagnetikoetan oinarritzen dira, potentzia, eraginkortasuna eta bolumenaren pisuarekiko erlazio helburu izanik, diseinu egokiak optimoak baino lortuz. Kasurik egokienean, beste domeinu fisikoen ezaugarriak erregela enpirikoen eta meritu figuren bitartez kontsideratzen dira diseinatzailearen esperientzian oinarrituta (dimentsionamendu termikoa adibidez), edo bigarren maila batean kokatzen dira, diseinuaren prozesuan garrantzi txikiagoa emanez (makinaren azterketa bibro-akustikoa esaterako).

Ikuspegi hauek ezagunak diren aplikazioetarako eraginkorrak dira non makinaren portaera oso ondo karakterizatuta dago. Baina metodologia hauek ez direnez naturalki sistematikoa, arazo garrantzitsuak aurkezten ditu makinaren diseinuan irizpide berriak sartu nahi direnean, elektromagnetikoak ez direnak, portaera bibro-akustikoa adibidez.

Zehazki, iman iraunkorreko motoreak (PMSM ingelesez) aukera oso egoki batean bihurtu dira neodimio burdin-borozko (NdFeB) imanak aurkitu direnetik, bai aplikazio industrialetarako zein etxeko aplikazioetarako, industria aeroespazialean, igogailuetan, ibilgailu elektrikoetan edo sorkuntza elektrikoan, esaterako. Motore hauen ezaugarri egokiak (efizientzia eta potentzi dentsitatea handiak, besteak beste) teknologia berria eta ikerkuntzarako alor interesgarria dela erakusten dute, azkenaldian gai honen inguruan agertzen ari diren publikazioen kantitatea ikusita.

Horregatik tesi honen helburu nagusia metodologia berritzaile bat garatzea da, PMSM makinaren diseinua olistikoa, diziplina anitzekoa eta optimizatua eginez. Horrez gain, proposatutako metodologia honek ez du aspektu elektromagnetikoa eta termikoa bakarrik kontutan hartzen, baizik eta makinaren portaera bibro-akustikoa ere.

Helburu hau lortzeko diziplina anitzeko eredu analitiko bat garatu da, PMSM makinaren ezaugarri elektromagnetiko, termiko eta bibro-akustikoen ikerketa zehatza eginda, domeinu haetako bakoitzak besteetan duen eragina zehazki eta arreta bereziarekin aztertuz.

Eredu hauek metodologia ezinhobea eta berritzaile bat garatzeko erabili izan dira, algoritmo heuristikoa berri batean oinarrituta, DMS deitzen dena (direct multiseach ingelesez).

Azkenik, 75 kW-tako makina sinkrono baten prototipoa diseinatu da (IkerMAQ), zeinetan aipatutako domeinuen test kopuru handia gauzatuz, eredu analitikoak zehazki balioztatu dira.

Hitz gakoak: Iman iraunkorreko motorra, ereduztapen analitiko multifisikoa, azterketa bibro-akustiko modala, karakterizazio esperimentalala, PMSM diseinatzeko metodologia.



Contents

Acknowledgements	i
Abstract	iii
Resumen	v
Laburpena	vii
Contents	ix
List of Figures	xiii
List of Tables	xix
Nomenclature	xxii
1 Introduction	1
1.1 Thesis Objectives.....	3
1.2 Background: The Permanent Magnet Synchronous Machine.....	4
1.2.1 Operating Principle.....	5
1.2.2 Permanent Magnets: Features and Evolution	7
1.2.3 PMSM Structure and Classification	10
1.3 Radial SPMSM Design: The Starting Point	14
1.4 Outline of the Document	17
2 Design and Modelling of PMSM: Optimized-Multiphysical Study .	19
2.1 Towards a Design Methodology: State of the Art	21
2.1.1 From a Magnetic to a Multiphysical Approach	23
2.1.2 From a Sizing to an Optimized Approach.....	25
2.1.3 The Global Picture	29
2.2 State of the Art in PMSM Modelling.....	30
2.2.1 Electromagnetic Modelling	31
2.2.2 Thermal Model	38
2.2.3 Vibro-acoustic Model	40
3 Multiphysical Modelling	45
3.1 Introduction	47
3.1.1 SPMSM Geometry	47
3.1.2 Electrical and Mechanical variables	49
3.1.3 Winding Layout: the Star of Slots.....	50
3.2 Magnetic Domain.....	54

3.2.1	Rotor Magnetic Field	55
3.2.2	Slotting Effect: Relative Permeance Function	57
3.2.3	Electro-Motive Force and Stator Flux Induced by the Magnets	61
3.2.4	Armature Reaction and Total Magnetic Field	67
3.2.5	Radial Stator Force and Cogging Torque Calculus.....	74
3.3	Electric Characterization	80
3.3.1	PMSM Coil Inductance	81
3.3.2	PMSM Resistance	89
3.4	Efficiency and Losses Estimation	93
3.4.1	Copper and Iron Losses	93
3.4.2	Magnet Losses	95
3.4.3	Efficiency and other Quality Parameters	100
3.5	Thermal Approach	103
3.5.1	Heat Transfer: Basic Principles	103
3.5.2	Introduction to Lumped Thermal Models	106
3.5.3	Simplified Thermal Network for a SPMSM.....	107
3.5.4	Thermal-Electromagnetic Coupling.....	121
3.6	Vibratory and Acoustic Behaviour	123
3.6.1	Structural and Vibratory Approach	124
3.6.2	Acoustic Calculus	137
3.7	Multiphysical Modelling Validation	141
3.7.1	Electromagnetic Validation	143
3.7.2	Thermal Validation	146
3.7.3	Vibratory Validation	147
4	Experimental Validation	149
4.1	Case of Study: IkerMAQ Q45p5	151
4.1.1	Application and Initial Specifications	151
4.1.2	Design, Manufacture Process and Internal Geometry.....	152
4.2	Laboratory Test-Bench.....	155
4.2.1	Experimental assembly without converter	155
4.2.2	Experimental assembly with converter.....	156
4.3	IkerMAQ Parametrization	158
4.3.1	Permanent Magnets EMF	158
4.3.2	Stator Resistance	159
4.3.3	Stator Inductance and Saliency	160
4.4	Electromagnetic Tests.....	161
4.4.1	Open circuit	162
4.4.2	On load	164
4.4.3	Quality Parameters.....	169
4.5	Thermal Validation.....	171
4.5.1	Thermal Measurements	172
4.5.2	Model fitting and experimental results.....	176
4.6	Vibro-Acoustic Measurement.....	178

4.6.1	IkerMAQ Experimental Modal Analysis.....	179
4.6.2	IkerMAQ Operational Modal Analysis and Acoustic Test	184
4.7	Conclusions	186
5	Optimized Methodology Proposal	187
5.1	The Optimization Process: A Global View.....	189
5.1.1	Design and State Variables	189
5.1.2	Objective and Constraint Functions	191
5.1.3	The DMS Algorithm	193
5.2	Proposed “Two Round Exploratory Algorithm”	194
5.2.1	The Initial Population: Specifications and Pre-Design.....	194
5.2.2	Exploratory Rounds:	202
5.3	Practical Example: Machine Design	205
5.3.1	Selected Application: Specifications and Constraints	205
5.3.2	Methodology Practical Implementation	207
5.3.3	Final Designs and IkerMAQ Q45p5 Comparison	210
5.4	Conclusions	212
6	Conclusions and Future Work	213
6.1	Summary	215
6.2	Contributions	216
6.3	Future Work	217
A	PMSM Analysis: Maxwell Equations	219
A.1	Definition of the Electromagnetic Problem.....	221
A.2	Flux Density Generated by the Magnets	222
A.2.1	Resolution in the airgap	223
A.2.2	Resolution in the magnets.....	224
B	Fourier Series.....	227
B.1	Definition	229
B.2	Main properties	229
B.3	2D-Fourier Series	230
C	Slot Inductance Calculus	235
C.1	Slot Types	237
C.2	Analytical Method.....	237
C.2.1	Uniform single-layer configuration	238
C.2.2	Uniform double-layer configuration	239
C.2.3	Non-uniform single-layer configuration.....	240
C.2.4	Non-uniform double-layer configuration.....	241
C.3	Slot inductances.....	242

D	Elasticity in Continuum Mechanics.....	243
D.1	Cauchy Stress Tensor	245
D.2	Lineal Elastic Bodies: Hooke's Law.....	246
E	Resumen.....	249
E.1	Objetivos de la tesis	251
E.2	Máquina Síncrona de Imanes Permanentes.....	252
E.2.1	Principio de Funcionamiento.....	253
E.2.2	Clasificación y Estructura Interna de los PMSMs	255
E.3	Diseño de una SPMSM Radial: el Punto de Partida	259
E.4	Estructura de la Tesis	261
	Bibliography	263



List of Figures

Figure 1.1. ABB motors. Left, DC motor and right, stator and rotor of an induction ABB motor. [Photos: ABB corporation].....	4
Figure 1.2. Motors basic principles; (a) basic case with magnets and (b) with a electromagnet rotor.	6
Figure 1.3. PMSM configuration; (a) example with one coil and (b) example of a three-phases configuration.	6
Figure 1.4. Hysteresis loop of permanent magnet material.	7
Figure 1.5. Demagnetization curves for N40H magnets at different temperatures. (Arnold® Magnetic Technologies [Arnold 2015]).....	8
Figure 1.6. Characteristic operation line segments and BH curve.	8
Figure 1.7. Evolution timeline of the permanent magnet maximum energy product during the last decades [Rahman 2013].....	9
Figure 1.8. (a)Schematic of a 2-D slice of a radial PMSM. (b)Typical radial PMSM.	11
Figure 1.9. (a) External rotor configuration, (b) Internal rotor configuration.	11
Figure 1.10. (a) SPMSM rotor by [Wu 2015], (b) IPMSM rotor by [Rahman 2013]. ...	12
Figure 1.11. Comparison of distributed (a) and concentrated (b) windings. [Photos: University of Bundeswehr].	13
Figure 1.12. Example of the main PMSM topologies; (a) Radial flux, (b) axial flux and (c) transversal flux [Anyuan 2010].....	14
Figure 1.13. Block diagram of the proposed multiphysics linked models.....	15
Figure 1.14. (a) Main dimensions of the SPMSM and (b) detail of a slot.....	16
Figure 2.1. Classical two-stage flowchart in recent machine design approaches.....	22
Figure 2.2. Example of electromagnetic-thermal loop in PMSM design by [Kazmin 2008-a].	24
Figure 2.3. Physical domains and main possible objectives of a multiphysical design methodology.	25
Figure 2.4. Proposed classifications of the main optimization algorithms applied to PMSM design methodologies.....	28
Figure 2.5. Different model approaches for electromagnetic characterization of PMSM.	32
Figure 2.6. Geometry simplification done in order to obtain airgap flux density.....	33

Figure 2.7. Interaction forces between slots and magnets. The forces acting on the magnets cause the cogging torque.	34
Figure 2.8. 6 th force mode on the stator. This is the fundamental mode induced by the magnets if $p=3$	36
Figure 2.9. Deformation caused by an unbalanced force distribution.....	36
Figure 2.10. SPMSM lumped thermal networks. (a) [Mellor 1991], (b) Motor-CAD® ...	39
Figure 2.11. Noise sources and sound propagation in electrical machines.	41
Figure 2.12. Electromagnetic sound genesis in electrical machines.	42
Figure 2.13. 2 nd to 5 th stator radial modes calculated with ANSYS®. Deflections have been scaled for visual purposes.	43
Figure 3.1. (a) Main dimensions of the SPMSM and (b) detail of a slot.....	47
Figure 3.2. Equivalence between a stator slotting and its star of slots.	52
Figure 3.3. Star of slots method applied to two examples. Top: a single layer winding (Q12p5) and bottom: a double layer layout (Q6p2).	53
Figure 3.4. Example of a double layer winding layout, three coils with six turns each. Each coil belong to a different phase.	54
Figure 3.5. Angle covered by a magnet (α_p) with respect to pole pitch. Radial magnetization.....	57
Figure 3.6. Geometry considered for the calculus of the relative permeance function.....	58
Figure 3.7. Radial component of the magnet flux density in the airgap. The PMSM simulated is a Q3p1 (3 slots and just one pole pair).	59
Figure 3.8. Flux density paths simulated in FEM with FLUX2D®	60
Figure 3.9. Equivalent reluctance circuit for stator yoke magnetic flux calculus.....	64
Figure 3.10. Phase winding example in a fractional slot PMSM. Slots/teeth numbering included.	66
Figure 3.11. Armature reaction caused by one coil in the adjacent teeth.....	68
Figure 3.12. Spatial distribution of the MMF per current unit caused by a single coil. Example from [Almandoz 2008]......	69
Figure 3.13. Spatial distribution of the MMF per current unit caused by a phase conformed by two coils.	70
Figure 3.14. Spatial distribution of the radial magnetic field and the generated force density in the stator boundaries.	75
Figure 3.15. Radial force density over a tooth during an electrical period.....	78

Figure 3.16. Detail of the slot opening surfaces where the forces are applied.	78
Figure 3.17. Phase A PMSM electric model including iron losses effect.....	81
Figure 3.18. Magnetic energy stored in a PMSM due to the armature reaction. FEM simulation in FLUX®	82
Figure 3.19. Example of phase A winding for a Q12p2 machine (a) and its equivalent reluctance circuit (b).....	83
Figure 3.20. Example of the two main cases of slot windings types.....	85
Figure 3.21. IkerMAQ stator, the end-windings at both sides are clearly visible.	87
Figure 3.22. End winding geometry (a) Flux generated in the end-winding region and (b) Top view of a coil inserted in the stator slots.	88
Figure 3.23. Graphic representations of frequency effects: skin effect (a), and proximity effect with current in the opposite directions (b) and in the same direction (c).	90
Figure 3.24. Distribution of wires within a slot.	91
Figure 3.25. Flowchart of the RFe calculus algorithm.	92
Figure 3.26. Example of integration area on the magnet.	96
Figure 3.27. 2-D section of the PMSM geometry under study. Both angular references respect to the stator and the rotor have been included.....	97
Figure 3.28. One pole geometry with three axial slices. Eddy current paths are represented.	98
Figure 3.29. Current density in one of the magnets. Current is nearly constant with r.	100
Figure 3.30. Phase A PMSM electric model.....	101
Figure 3.31. Example of an electrical machine thermal network [Kylander 1995]	106
Figure 3.32. Implemented SPMSM small thermal network model.....	108
Figure 3.33. SPMSM axial 2D-section, main thermal resistances are included.	109
Figure 3.34. Machine 2-D section geometry. Figure from Motor-CAD®	110
Figure 3.35. Stator teeth and slots typical geometry.	113
Figure 3.36. Relation between λ_{slot} and λ_{imp} as a function of the slot fill factor and the manufacture technique. Data from [Kylander 1995].....	115
Figure 3.37. Slot geometry equivalence used in the thermal modelling by [Lindström 1999].....	115

Figure 3.38. Single coil thermal model.	117
Figure 3.39. Global thermal resistance between embedded coils and end-winding. .	117
Figure 3.40. Equivalent end-wind thermal network in its Y and Δ forms [Kylander 1995].	118
Figure 3.41. Electromagnetic-thermal coupling algorithm flowchart.....	123
Figure 3.42. Stresses on a differential element in polar coordinates.	126
Figure 3.43. Example of a stator breathing mode.....	128
Figure 3.44. (a) Strain and dimensions in a ring element and (b) stresses in a ring. ...	129
Figure 3.45. Stator seen as a ring (mean radius R_c and thickness h) with teeth.....	134
Figure 3.46. 1 st to 4 th stator axial modes simulated with ANSYS®. Deflections have been scaled for visual purposes.	136
Figure 3.47. Sound radiation efficiency from mode $n=0$ (blue) to mode $n=6$ (grey). .	140
Figure 3.48. Equal-loudness curves. Standard from [ISO 2003].....	141
Figure 3.49. 2D section of the simulated PMSM (Q12p5).....	142
Figure 3.50. Rotor flux density in the airgap at a time instant.....	143
Figure 3.51. Armature reaction in the airgap at a time instant.	143
Figure 3.52. Total flux density in the airgap at a time instant.	144
Figure 3.53. EMF induced by the magnets in phase A.	144
Figure 3.54. Mutual torque ripple.	144
Figure 3.55. Cogging torque.	145
Figure 3.56. PMSM temperatures calculated by Motor-CAD®.	146
Figure 4.1. IkerMAQ (a) rotor and (b) stator. Notice the thermocouples and test coils.	153
Figure 4.2. IkerMAQ phase B winding blueprint.	153
Figure 4.3. Magnets inset detail. (a) One periodicity 2D cross section, (b) rotor end- cap.	154
Figure 4.4. IkerMAQ (Q45p5), designed by IK4-Ikerlan during 2013 and built by Lancor in 2014	154
Figure 4.5. Laboratory facilities block diagram in the “without converter” configuration	155
Figure 4.6. IkerMAQ and ABB machine connection within test-bench.....	156

Figure 4.7. Laboratory facilities block diagram in the “with converter” configuration	156
Figure 4.8. IkerMAQ supply and control equipment; (a) voltage converter, (b) DC source.	157
Figure 4.9. Phase stator inductance as function of the rotor position. Dotted lines represent the measured values.....	161
Figure 4.10. Open-circuit line EMF (measured in IkerMAQ terminals).....	162
Figure 4.11. Open-circuit EMF induced in a single tooth.	163
Figure 4.12. Open-circuit magnetic flux flowing through a tooth cross section.....	163
Figure 4.13. Measured electric waveforms. Current lines are dotted.	164
Figure 4.14. On load line voltage, measured in machine terminals.....	165
Figure 4.15. On load voltage induced in a single tooth.....	165
Figure 4.16. On load magnetic flux flowing through a tooth cross section.	166
Figure 4.17. On load electromagnetic torque.	167
Figure 4.18. Electric waveforms in converter terminals. Current lines are dotted.....	168
Figure 4.19. Converter test. Voltage induced in a single tooth.....	168
Figure 4.20. Converter test. Magnetic flux flowing through a tooth cross section. ...	169
Figure 4.21. IkerMAQ internal test points. In red K thermocouples, in blue magnetic test coils.....	171
Figure 4.22. IkerMAQ external test points. Measures are carried out through J thermocouples.....	172
Figure 4.23. Temperatures measured during the open circuit test.	173
Figure 4.24. Temperatures obtained in the DC-current test. Dotted lines represent the measured values.....	174
Figure 4.25. Temperatures obtained in nominal conditions with and without converted. Dotted lines represent the measured values.	176
Figure 4.26. IkerMAQ particularized SPMSM small thermal network model.....	177
Figure 4.27. Experimental and analytical results comparison in the four test configuration.	177
Figure 4.28. Classical EMA block diagram.	179
Figure 4.29. Free-free stator tests conditions (a) without coils and (b) wound.	180

Figure 4.30. Example of FEM modal shapes (a) mode (2,0) and (b) mode (2,1). Feet anchored.....	181
Figure 4.31. Stator core. Calculated and measured transfer function.....	182
Figure 4.32. Wound stator. Calculated and measured transfer function.....	182
Figure 4.33. Location of accelerometers on IkerMAQ housing.....	184
Figure 4.34. Maximum vibratory radial displacement as function of frequency. IkerMAQ OMA results and analytical calculus comparison.....	185
Figure 4.35. Sound emission comparison. Experimental and analytical results.....	185
Figure 5.1. PMSM modelling flowchart.....	191
Figure 5.2. PMSM design methodology flowchart.....	195
Figure 5.3. Analytical pre-design stages.....	197
Figure 5.4. Rotor flux density in the airgap.....	198
Figure 5.5. Example of Pareto envelope obtaining in the global search first step.....	203
Figure 5.6. Matlab® tool which implements the proposed methodology.....	204
Figure 5.7. Proposed PMSM solutions generated by the algorithm during its different stages.....	208
Figure 5.8. 2D sections of the PMSM solutions obtained in the different design stages.....	209
Figure 5.9. 2D sections of the considered PMSM design proposals.....	211
Figure 5.10. Final selected design compared with the achieved Pareto-frontier.....	211
Figure B.1. Spatial mode 2 rotating at angular speed πf_e rad/s , (a) clockwise and (b) counter-clockwise.....	232
Figure B.2. IkerMAQ airgap magnets flux density, B_{gm} , and its 2D-FS coefficients...	232
Figure B.3. IkerMAQ armature reaction, B_{ga} , and its 2D-FS coefficients.....	233
Figure B.4. IkerMAQ airgap total flux density, B_g , and its 2D-FS coefficients.....	234
Figure B.5. IkerMAQ magnetic pressure over stator teeth, P_M , and its 2D-FS coefficients.....	234
Figure C.1. Most popular slot types.....	237
Figure C.2. Circular paths chosen in order to apply Ampere's law.....	238
Figure C.3. Example of magnetic field intensity due to armature reaction.....	240
Figure D.1. Example of forces density on a body internal surface.....	245

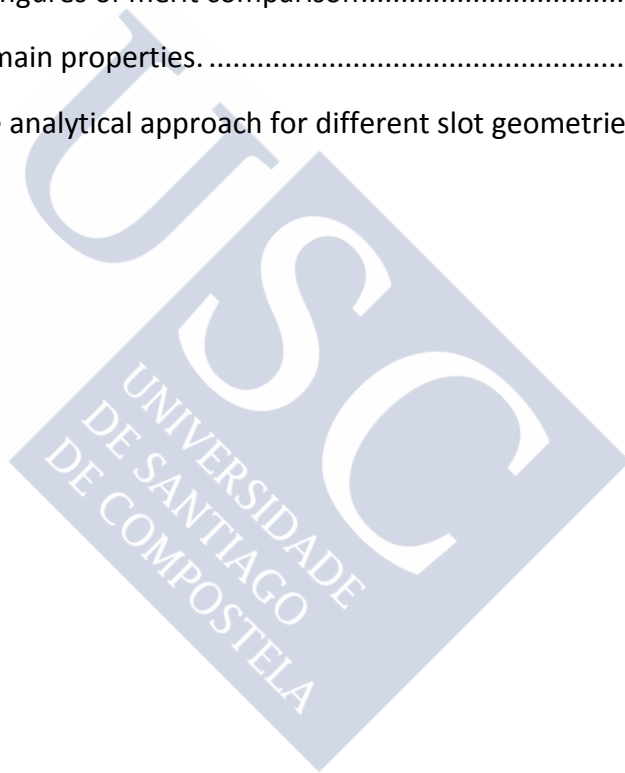
Figura E.1. Motores de ABB. A la izquierda un motor de continua, a la derecha el rotor y el estátor de una máquina de inducción. [Fotos propiedad de la corporación ABB]	252
Figura E.2. Principios básicos del funcionamiento de un motor; (a) sólo con imanes permanentes y (b) con un electroimán en el rotor.	254
Figura E.3. Configuraciones PMSMs; (a) ejemplo con una sola bobina y (b) ejemplo con una configuración trifásica.	255
Figura E.4. (a)Esquema de una sección 2D de una PMSM radial, (b) PMSM radial.	256
Figura E.5. (a) Configuración de rotor exterior. (b) Configuración de rotor interior.	257
Figura E.6. (a) Rotor de una SPMSM [Wu 2015], (b) rotor de una IPMSM [Rahman 2013].	257
Figura E.7. Comparación entre máquinas de bobinado (a) distribuido y (b) concentrado.	258
Figura E.8. Diagrama de bloques y relación entre los diferentes dominios modelados.	259
Figura E.9. (a) Principales dimensiones de una PMSM; (b) detalle de una ranura.	261

List of Tables

Table 2.1. Classification of the PMSM design proposals found in the literature.	29
Table 3.1. Scale factor for the example shown in Figure 3.10	66
Table 3.2. Two layers slot distribution in a three phases PMSM.	86
Table 3.3. Slot inductance analytical approach for different slot geometries.	86
Table 3.4. Analogy between electrical and thermal circuit	107
Table 3.5. PMSM main parameters.	142
Table 3.6. PMSM electrical and quality parameters	145
Table 3.7. Estimated PMSM temperatures.	147
Table 3.8. Simulated and estimated modal static displacements and natural frequencies	147
Table 4.1. IkerMAQ main geometrical and structural features.	152
Table 4.2. ABB load equipment features.	156
Table 4.3. Magna Power DC source characteristics.	157

Table 4.4. Relation between rotor speed and EMF (magnets at 20°C).	159
Table 4.5. Relation between rotor speed and EMF (n=1080 rpm).	159
Table 4.6. End-winding length fitness.	159
Table 4.7. Stator resistance: analytical estimation and measurements.	160
Table 4.8. Stator inductance analytical estimation and measurements.....	161
Table 4.9. Experimental electrical variables. Cold magnets test.....	164
Table 4.10. Experimental electrical variables. Hot magnets test.....	165
Table 4.11. Average electromagnetic torque. Analytical estimation and measurements.	167
Table 4.12. Experimental electrical variables. Converter controlled test.....	168
Table 4.13. Test without converter. Quality parameters analytical estimation and measures.	170
Table 4.14. Test with converter. Quality parameters analytical estimation and measures.	170
Table 4.15. Open circuit test features	173
Table 4.16. DC- current heating test features	174
Table 4.17. Nominal conditions without converter, test features.....	175
Table 4.18. Nominal conditions without converter, test features.....	175
Table 4.19. Thermal resistance experimental fit.....	176
Table 4.20. EMA results. Resonant frequencies and damping factors.	181
Table 4.21. Analytical and EMA static displacements and resonant frequencies. Stator core.....	183
Table 4.22. Analytical and EMA static displacements and resonant frequencies. Wound stator	183
Table 5.1. Design variables.	190
Table 5.2. State variables.....	190
Table 5.3. Design constraints.....	192
Table 5.4. Geometric constraints.	192
Table 5.5. Magnetic constraints.	193
Table 5.6. Electric constraints.....	193

Table 5.7. Thermal and acoustic constraints.....	193
Table 5.8. Stage 0: Design variables assumed values.....	197
Table 5.9. Stage 2: Design variables established values.....	200
Table 5.10. Initial variables selection in analytical pre-design.....	202
Table 5.11. Drive Machine specifications.....	206
Table 5.12. Initial constraint set.	206
Table 5.13. Chosen optimization variables	207
Table 5.14. Final designs, features comparison	210
Table 5.15. Final designs, figures of merit comparison.....	211
Table B.1. Fourier Series main properties.	230
Table C.1. Slot inductance analytical approach for different slot geometries.....	242



Nomenclature

Abbreviations

AC	Alternating Current
AlNiCo	Aluminium Nickel and Cobalt
BEM	Boundary Element Method
CFD	Computational Fluid Dynamics
DC	Direct Current
DMS	Direct MultiSearch
EMA	Experimental Modal Analysis
EMF	ElectroMotive Force
EV	Electric Vehicle
FEM	Finite Element Calculus
FFT	Fast Fourier Transform
FS	Fourier Series
GA	Genetic Algorithm
IPMSM	Interior Permanent Magnet Synchronous Machine
ISO	International Organization for Standardization
MMF	MagnetoMotive Force
NdFeB	Neodymium Iron Boron
OMA	Operational Modal Analysis
PMSM	Permanente Magnet Synchronous Machine
PWM	Pulse Width Modulation
SA	Simulated Annealing
SPMSM	Surface Permanente Magnet Synchronous Machine
SPO	Swarm Particle Optimization
SUMT	Sequential Unconstrained Minimization Techniques

PMSM optimization, configuration and geometric symbols

A_{Cu}	Effective copper area within a slot	$[m^2]$
A_g	Airgap mean area	$[m^2]$
A_s	Slot area	$[m^2]$
C	Material cost	$[\$/kg]$
d_{air}	Equivalent air length enclosed by slot insulation	$[m]$
d_{Cu}	Copper wires diameter	$[m]$
F_f	Slot fill factor	
f_h	Frame fin high	$[m]$
f_{tip}	Frame fin width	$[m]$
f_w	Distance between fins	$[m]$

g	Airgap length	[m]
g_e	Equivalent stator-frame airgap length	[m]
h_0	Tooth-tip height	[m]
h_1	Slot enlargement height	[m]
h_2	Slot height (occupied by down phase turns)	[m]
h_3	Slot insulation width	[m]
h_4	Slot height (occupied by up phase turns)	[m]
inL	Inward coil vector	
h_{fr}	Frame width	[m]
L_e	Stator core effective length	[m]
L_{ew}	End-winding length	[m]
L_{Fe}	Stator core total length	[m]
L_{phase}	Total phase winding length	[m]
L_{wire}	Mean coil length	[m]
l_m	Magnet length	[m]
l_m	Magnet length	[m]
m	Number of phases	[kg]
M_{Cu}	Total copper mass	[kg]
M_{Fe}	Total ferromagnetic stator mass	[kg]
M_{Fes}	Stator yoke mass	[kg]
M_{Fet}	Teeth mass	[kg]
M_m	Magnets mass	[kg]
M_r	Total ferromagnetic rotor mass	[kg]
N_{lay}	Number of layers in a slot	
N_m	Number of magnets in each pole (axial direction)	
N_{para}	Number of parallel paths in a phase	
$outL$	Outward coil vector	
p	Number of pole pairs	
P_{obj}	Objective output power	[W]
phL	Phase coil vector	
Q	Number of slots	
q	Number of slots per phase per pole	[m]
R_m	External magnet annulus radius	[m]
R_r	External rotor radius	[m]
R_s	Internal stator radius	[m]
R_{se}	External stator radius	[m]
R_{shaft}	Shaft radius	[m]
R_{ss}	Superior slot radius	[m]
S	External PMSM surface	[m ²]
S_1	Phase A scale factor	
t_p	Winding periodicity	

w_0	Slot opening width	[m]
w_1	Maximum slot width	[m]
w_2	Minimum slot width	[m]
w_s	Medium slot width	[m]
w_{sy}	Stator yoke width	[m]
w_t	Tooth width	[m]
X	Optimization design variables vector	
Y	Optimization estate variables vector	
Z	Number of turns within a coil	
α_0	Angle covered by a slot opening	[rad]
α_m	Fraction of the coil pitch covered by the magnet	[%]
α_p	Angle covered by a single magnet	[rad]
θ_e	Polar coordinate (electrical reference)	[rad]
θ_m	Polar coordinate (mechanical reference)	[rad]
θ_p	Pole pitch	[rad]
θ_s	Slot pitch	[rad]
θ_t	Tooth arch (including shoes)	[rad]
ξ	Winding factor	
τ_{cp}	Mean coil pitch radius	[m]

Magnetic variables symbols

B	Magnetic induction	[T]
B_g	Total magnetic induction in the airgap (slotless)	[T]
B_g^a	Armature reaction in the airgap (slotless)	[T]
B_g^m	Magnets flux density in the airgap (slotless)	[T]
\widehat{B}_g^m	Magnets flux density in the airgap (maximum, slotless)	[T]
B_g^r	Total magnetic induction in the airgap (rotor frame)	[T]
B_{gs}	Total magnetic induction in the airgap	[T]
B_{gs}^m	Magnets flux density in the airgap	[T]
B_r	Magnet residual induction	[T]
B_s	Total magnetic induction in the stator yoke	[T]
B_s^m	Magnets flux density in the stator yoke	[T]
B_s^a	Armature reaction in the stator yoke	[T]
B_{sat}	Ferromagnetic core saturation magnetic induction	[T]
B_t	Total magnetic induction in the teeth	[T]
B_t^m	Magnets flux density in the teeth	[T]
B_t^a	Armature reaction in the teeth	[T]
$BH _{max}$	Magnet maximum energy product	[J/m ³]
H	Intensity magnetic field	[A/m]
H_c	Magnets coercive magnetic field	[A/m]

k_a	Anomalous or excess loss constant	
k_e	Eddy current loss constant	
k_h	Hysteresis loss constant	
K_r	Magnetization profile factor	
K_{sl}	Relative permeance function	
M	Magnetization vector	[A/m]
φ_g	Airgap permeance	[Wb/A]
α_h	Hysteresis loss exponential factor	
δ	Effective magnetic airgap length	[m]
μ_0	Void magnetic permeability	[H/m]
μ_r	Relative permeability	
φ	Magnetic scalar potential	[A]
ϕ	Magnetic flux	[Wb]
$\phi_{lk}^{m,l}$	Magnets flux linked by phase l	[Wb]
ϕ_s	Total magnetic flux in the stator yoke	[Wb]
ϕ_s^m	Magnets flux in the stator yoke	[Wb]
ϕ_s^a	Armature reaction flux in the stator yoke	[Wb]
ϕ_t	Total magnetic flux in the teeth	[Wb]
ϕ_t^m	Magnets flux in the teeth	[Wb]
ϕ_t^a	Armature reaction flux in the teeth	[Wb]

Electric and power variables symbols

D	Electric displacement field	[C/m ²]
E	Electric field	[V/m]
E	EMF induced voltage	[V]
F	Inductive skin effect factor in round conductors	
F	Magnetomotive Force per current unit	
f_e	Electric frequency	[Hz]
G	Inductive proximity effect factor in round conductors	
I	Electric current	[A]
I_{Fe}	PMSM magnetizing current	[A]
I_{ph}	Electric current in a PMSM phase	[A]
J	Current density	[A/m ²]
k_{ad}	Mechanical losses constant	
L_d	Total phase inductance in d-axis	[H]
L_g	Airgap inductance	[H]
L_g^{si}	Airgap auto-inductance (phase A)	[H]
L_{ph}	Total phase inductance	[H]
L_q	Total phase inductance in q-axis	[H]
L_s	Single slot inductance	[H]

L_{sd}	Slot auto-inductance (bottom layer)	[H]
L_{sm}	Slot mutual inductance	[H]
L_{su}	Slot auto-inductance (top layer)	[H]
$L_{\sigma e}$	Total end-winding leakage inductance	[H]
$L_{\sigma s}$	Total slot leakage inductance	[H]
M_g	Airgap mutual inductance	[H]
MMF	Magnetomotive Force	[A]
P_{ad}	Additional mechanical losses	[W]
P_{Cu}	Copper losses	[W]
P_{elec}	Electrical PMSM power	[W]
P_{Fe}	Iron losses	[W]
P_{in}	PMSM input power	[W]
P_m	Rotor losses in magnets	[W]
P_{mec}	Mechanical PMSM power	[W]
P_{out}	PMSM output power	[W]
P_S	Electrical active power	[W]
pf	Power factor	
q_e	Electrical load	[A/m]
Q_S	Reactive power	[VAr]
R_{Fe}	Ferromagnetic material equivalent resistance	[Ω]
R_{ph}	Total phase resistance	[Ω]
S	Apparent Power	[VA]
T_e	Electric period	[s]
T_m	Mechanical period	[s]
V_{ph}	Electric phase voltage in PMSM terminals	[V]
Δ	Penetration ratio	
δ	Skin depth	[m]
η	Efficiency	[%]
ρ	Electrical resistivity	[Ω m]
φ	Current-voltage phase different	[rad]
ω_e	Angular speed (electrical reference)	[rad/s]
ω_m	Angular speed (mechanical reference)	[rad/s]

Thermal variables symbols

c	Specific heat capacity	[J/K]
G	Thermal conductance matrix	[W/K]
Nu	Nusselt's number	
P	Power losses matrix	[W]
Pr	Prandtl's number	
Q	Dissipated power density	[W/m ³]

q	Transmitted power by surface unit	$[\text{W}/\text{m}^2]$
R_{th}	Thermal resistance	$[\text{K}/\text{W}]$
Re	Reynold's number	
T	Absolute temperature	$[\text{K}]$
T_{∞}	Coolant temperature	$[\text{K}]$
T_{ew}	End-winding temperature	$[\text{K}]$
T_{m}	Magnets temperature	$[\text{K}]$
Ta	Taylor's number	
u_s	Coolant surface speed	$[\text{m}/\text{s}]$
α	Heat transfer coefficient	$[\text{W}/(\text{K m}^2)]$
α_{Cu}	Copper resistivity thermal coefficient	$[\text{K}^{-1}]$
α_{m}	Residual induction thermal coefficient	$[\text{K}^{-1}]$
ε	Emissivity coefficient	
Θ	Relative temperature matrix	$[\text{K}]$
λ	Thermal conductivity	$[\text{W}/(\text{K m})]$
σ	Stefan-Boltzmann constant	$[\text{W}/(\text{K}^4\text{m}^2)]$

Mechanical vibratory and acoustic variables symbols

c	Sound speed in air at 20°C	$[\text{m}/\text{s}]$
E	Young's modulus	$[\text{Pa}]$
f	Maxwell's force	$[\text{N}]$
f_m	Mode m^{th} resonant frequency	$[\text{Hz}]$
I	Acoustic intensity	$[\text{W}/\text{m}^2]$
I_z	Moment of inertia	$[\text{kg}/\text{m}^2]$
L_{dB}	Sound emission	$[\text{dB}]$
$L_{\text{dB(A)}}$	Sound emission A-weighted	$[\text{dB(A)}]$
M	Bending moment	$[\text{N.m}]$
n	Rotor speed	$[\text{rpm}]$
p	Acoustic pressure	$[\text{Pa}]$
P_M	Maxwell's force density	$[\text{Pa}]$
\mathcal{T}	Maxwell stress tensor	$[\text{N}/\text{m}^2]$
T	PMSM torque	$[\text{N.m}]$
T_e	Electromagnetic torque	$[\text{N.m}]$
T_c	Total cogging torque	$[\text{N.m}]$
T_{cs}	Single slot cogging torque	$[\text{N.m}]$
u	Vibratory displacement	$[\text{m}]$
W	Total radiated sound power	$[\text{W}]$
Y_m	Mode m^{th} static displacement	$[\text{m}^3/\text{N}]$
Δ	Mass addition factor	
Δ_{rot}	Mass addition factor for rotation	

ϵ	Differential elongation matrix	
ζ	Damping factor	
λ	Sound wavelength	[m]
ν	Poisson's ratio	
ρ	Density	[kg/m ³]
σ	Sound radiation efficiency	
σ	Stress tensor	[N/m ²]
ω_m	Mode m th resonant pulsation	[rad/s]

Superscript symbols

r	Rotor
m	Magnets
a	Armature reaction
<i>n</i>	Mute index in summary
<i>l</i>	Mute index in summary

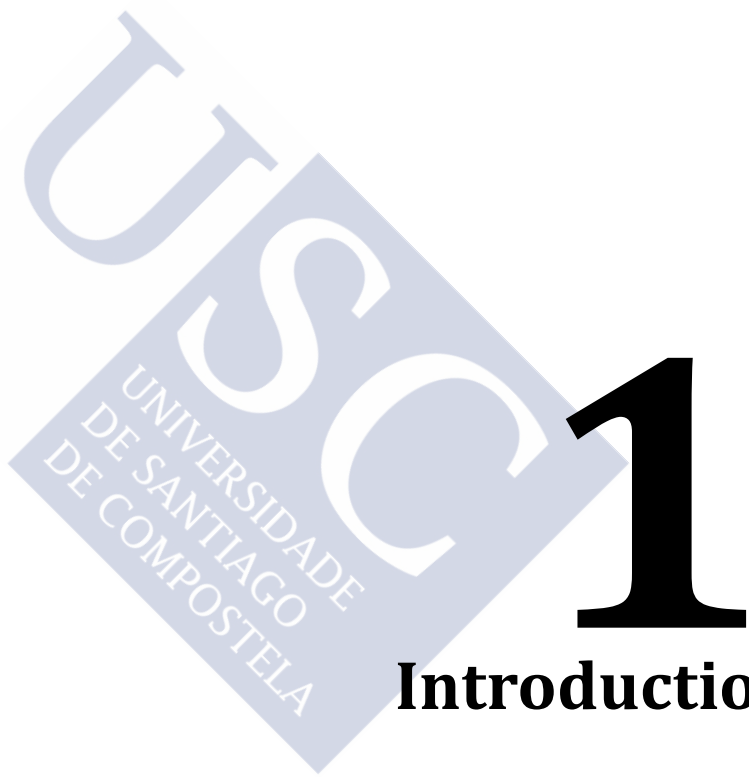
Subscript symbols

A	A-phase
ad	Additional
Al	Aluminium
av	Average
Cu	Copper
DC	Direct current
e	Electric/Effective
ew	End-winding
Fe	Ferromagnetic material
fr	Frame
g	Airgap
Ini	Initial
iter	Iterations
<i>k</i>	Mute index in summary
<i>l</i>	Mute index in summary
lk	Linked
m	Magnets/Mechanical
max	Maximum
min	Minimum
<i>n</i>	Mute index in summary
n	Normal
obj	Objective

p	Pole
ph	Phase
pk	Peak
pk-pk	Peak to peak
r	Rotor/ relative/ r-coordinate
rms	Root Mean Square
s	Stator/Slot
s	Mute index in summary
sat	Saturation
SM	Synchronous machine
t	Tooth/ Tangential
th	Thermal
x,y,z	Cartesian coordinates
θ	Cylindrical θ -coordinate







Introduction



1.1 Thesis Objectives

Nowadays, most of electrical machines design methodologies applied in the industry are based on empirical and semi-heuristic rules that require a lot of personal experience and whose accuracy strongly depends on previous available data, often considered being property of large electrical machines manufacturers [Amrhein 2013]. Moreover, most of the models are only focused on the electromagnetic performance and other important physical fields such as thermal or vibro-acoustics are taken into account through very rough “rules of thumb” or directly treated as an afterthought in best cases.

On the other hand, only a small amount of academic literature devoted to machine methodological design exists, and typically it presents incomplete and partial approaches, difficult to apply and more focused on the improvement of a previous design than in the development of a new, complete and optimized machine [Goss 2013-a].

Both approaches provide a first approximation that needs to be fulfilled with trial and error methods usually supported by time consuming numerical calculus. Thus, these design methodologies are only suitable for very well-known applications or low-performance machines but they are unsystematic by nature and present serious difficulties to extrapolate the obtained results to a new set of specifications or to more demanding applications where more physical domains, such as vibro-acoustics, must be taken into account.

Since electrical machines are complex systems where a great amount of physical phenomena are produced simultaneously, a detailed multidisciplinary approach taking into account the coupling between different physical fields is needed in order to implement a fast, accurate, reliable and optimized design methodology.

Therefore, the main goal of the thesis is to aid to fill the detected gap, developing a multidisciplinary and optimized design methodology for Permanent Magnet Synchronous Machines (PMSM).

In order to achieve the proposed aim the next objectives must be fulfilled:

- 1) Review and summarize the state of the art in design methodologies and modelling strategies of PMSM, paying especial attention to the optimized and multidisciplinary approaches.
- 2) Implement a multiphysical modelling of a PMSM including; electrical, magnetic, thermal, structural and vibro-acoustics domains. The key feature of the model is that it can be completely solved by analytical methods, most of them based on Fourier series, in order to obtain not only a multiphysics simulation but also modular and fast, especially suitable to be used in a subsequent optimized methodology. A summary of the proposed model has been presented in the conference ICEM 2014 [Rodríguez 2014-a].

- 3) Develop a new, improved, multidisciplinary and optimized design methodology for PMSMs coupling the aforementioned models.
- 4) Perform a complete case of study by designing a machine in order to validate the proposed methodology with both, numerical simulations and experimental tests.

1.2 Background: The Permanent Magnet Synchronous Machine

Electric energy is one of the supports of modern civilization. In the actual context, the electrical machines are of capital importance since most of power plants, from nuclear plants to wind turbines, need an electrical machine working as a generator. Moreover, it is estimated that nowadays the 65% of the total energy supplied by the grid is consumed by electric motors [Rahman 2013].

The widespread use in industry of electrical machinery all over the 20th century has led to a great investigation and improvement of its technology. Until the 50's the DC motors were the only available option at a competitive cost, because of the possibility of a simple and precise control, but their use has many drawbacks such as high maintenance requirements, big size and limited reliability.

During the eighties, the electronic advancements allowed a precise control of induction AC machines. In a decade they replaced the DC machines in most of industrial applications due to their smaller size, more robust construction and, overall, their lower maintenance caused by the absence of brushes and commutator [Novotny 1996]. Figure 1.1 shows an example of an induction AC and a DC machine.

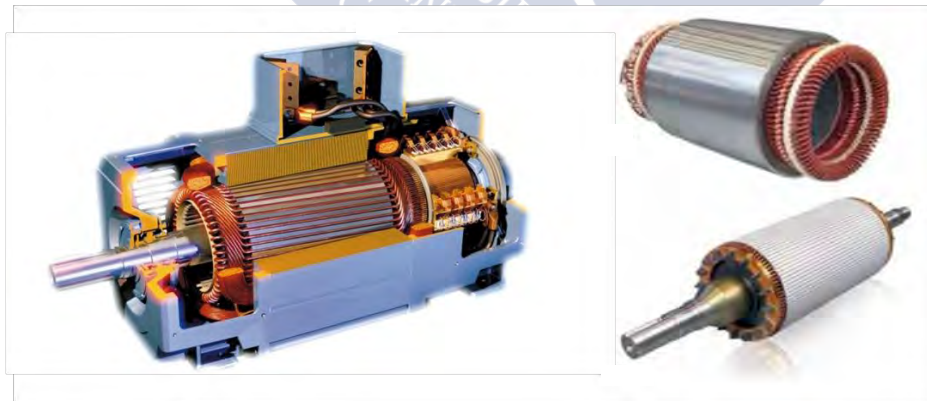


Figure 1.1. ABB motors. Left, DC motor and right, stator and rotor of an induction ABB motor. [Photos: ABB corporation].

In spite of the fact that PMSM technology is well known since the thirties and the presence of practical designs in the literature in dates as early as 1953 [Ginsberg 1953], it is in the nineties when the commercialization of Neodymium Iron Boron (NdFeB) magnets made possible that the PMSMs penetrated into the industry as a suitable choice.

Compared with the induction machine the PMSM has a good amount of advantages such as compactness, no rotor losses, higher power factor, higher power density and better efficiency [Islam 2009]. Like induction machines, PMSMs do not need brushes. Due to these attractive features PMSMs are widely employed in high-power applications such as aircraft industry, elevation, electric vehicle or power generation, where they are a competitive alternative to induction machines.

Two main PMSM drawbacks are the reason why the induction machines continue being the preferred choice in most of the industrial applications: high magnet cost and the risk of permanent magnet demagnetization that means less reliability than induction machines. Moreover, there exist certain risks associated with the fact that the magnets are “permanent”, so magnetic flux is induced no matter there is external excitation or not. This fact may cause that, under fault conditions, it could be troublesome to stop the PMSMs in traction applications, even if the feed currents are removed.

However, a clear trend towards an increasing presence in both, industrial and domestic applications, makes the PMSM an emerging technology and a very active field of study, as it is highlighted by the great amount of publications devoted to that topic in the last years.

For the aforementioned reasons the PMSM is the chosen topology to perform the design methodology proposed in this thesis. In the next section a brief summary of PMSM operating principles, classification, challenges and evolution is included.

1.2.1 Operating Principle

All electrical motors and generators operate with the same principle: the interaction between magnetic fields. In most cases (except in some reluctance machines) there exist two magnetic fields whose interaction transform the electrical energy into mechanical one, or vice versa, by storing it in magnetic fields.

The simplest kind of motor is formed by two external permanent magnets which remain fixed (stator) and an internal one which is free to rotate about its axis (rotor), see Figure 1.2 (a). Of course, the internal magnet tries to align itself with the others generating torque, as far as different poles attract each other and equal poles experiment a repulsion force. The motion ends when the internal magnet is aligned with the other two in an equilibrium position.

If the internal magnet is replaced by an electromagnet its polarity can be reversed inverting the DC current direction through it, in that way it is possible to change the polarity when the electromagnet reaches the equilibrium point, so the motion will continue indefinitely. Figure 1.2 (b) shows an electromagnet under the aforementioned conditions. It is interesting to notice the presence of the brushes and the commutator which allow the current propagation to the rotor during its motion and inverts the current direction, respectively.

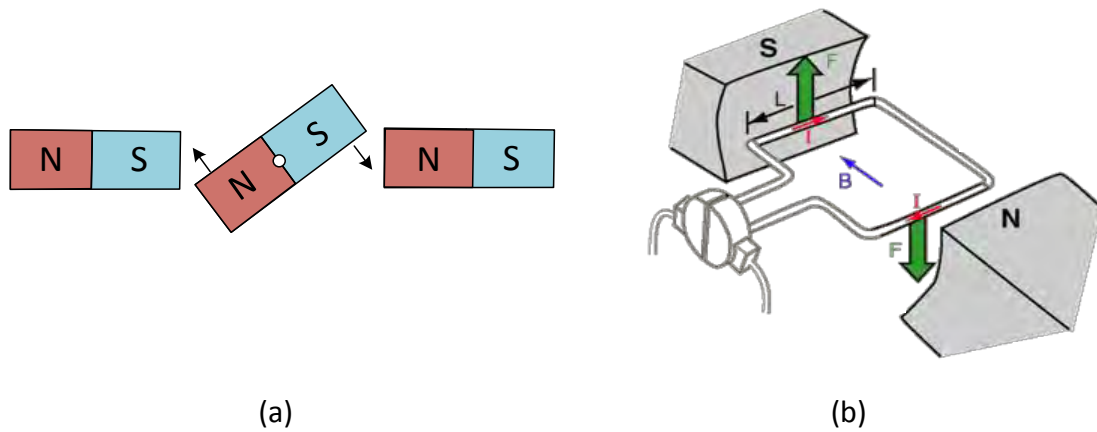


Figure 1.2. Motors basic principles; (a) basic case with magnets and (b) with a electromagnet rotor.

In the case of a PMSM the principles are the same that in the examples presented but some important changes are introduced: usually there are a higher number of magnets (called poles) and they are commonly placed not in the stator but in the rotor, in order to avoid the faults caused by the brushes. On the other hand, the current source is a polyphase AC with one or many coils in each phase (see Figure 1.3), rather than a DC one.

As a general principle, during a normal motor operation, the magnetic field caused by the stator coils (that can be seen as an equivalent electromagnet) leads the rotor motion, causing the magnets to rotate while the rotor magnetic field is lagging the stator one by a constant angle φ that is usually near 90° in order to transfer the maximum energy between the stator and the rotor, i.e. to reach the maximum possible torque.

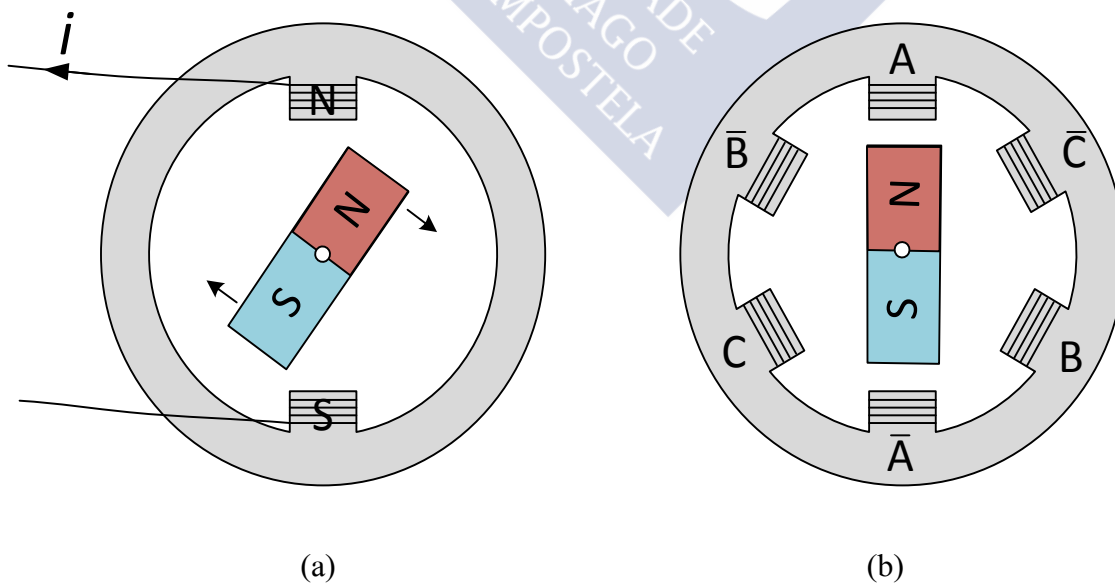


Figure 1.3. PMSM configuration; (a) example with one coil and (b) example of a three-phases configuration.

1.2.2 Permanent Magnets: Features and Evolution

The history of the PMSM is undeniable linked with the features and technical evolution of the permanent magnets. In essence, permanent magnets are magnetic materials with very large hysteresis loop [Hanselman 2012], see Figure 1.4. In order to create a new magnet from an unmagnetized sample of a magnetic material (e.g. ferrite, samarium-cobalt, neodymium-iron-boron, etc.) very large magnetic field intensity is applied by means of external electromagnets and then it is removed. Thus, the relaxed material goes from its unmagnetized point 1 to point 2. Once the external magnetic field is switched off the newly created magnet reach point 3, going through a demagnetization curve different from the magnetization one.

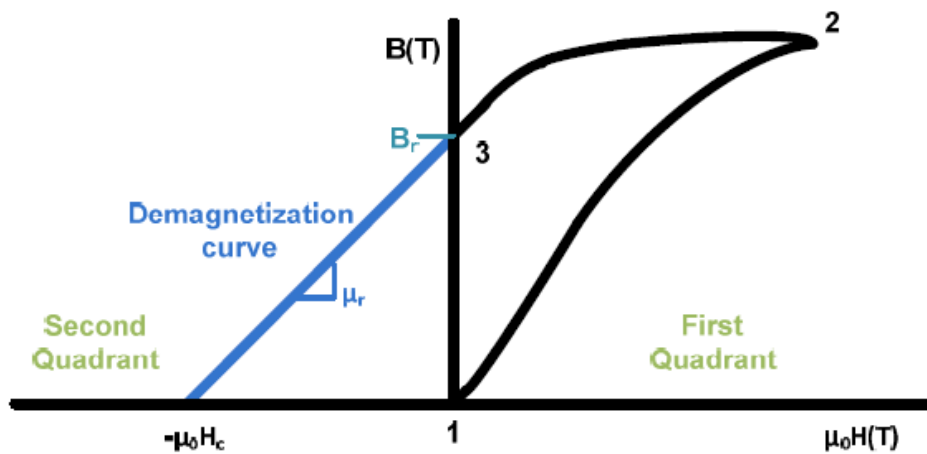


Figure 1.4. Hysteresis loop of permanent magnet material.

Once the magnet has been created, it is expected that its normal operation is not in the first but in the second quadrant, where its operating point depends on both, the reluctance path that the PMSM offers to the magnetic flux and the external magnetic field caused by the stator coils. Generally, three data define the magnet behaviour in a practical machine design: first its residual induction B_r , second its relative permeability μ_r (which is generally very close to unity) and third the reversible temperature coefficient of residual induction $\alpha_m(B_r)$. The first parameter is the origin ordinate and the second the line slope. The third is related with the B_r temperature dependence, because real magnets decrease its residual induction with temperature as it is shown in Figure 1.5. This B_r loss is reversible and it is recovered once the temperature returns to its original value, mathematically $\alpha_m(B_r) = \frac{1}{B_r} \frac{dB_r}{dT}$.

Figure 1.5 shows another important characteristic of permanent magnets; its real demagnetization curve presents a knee in the second quadrant. If the external field intensity H_g is large enough to operate beyond the knee an irreversible demagnetization will occur. Once H_g is removed, the residual induction is not the original B_r one and the recovery line is different to the demagnetization curve leading to a new point B_r' lower than B_r (see the red dotted line in Figure 1.6). So, it is very important to ensure that the magnets do not reach that operation point, not even if a short circuit in the PMSM winding is produced.

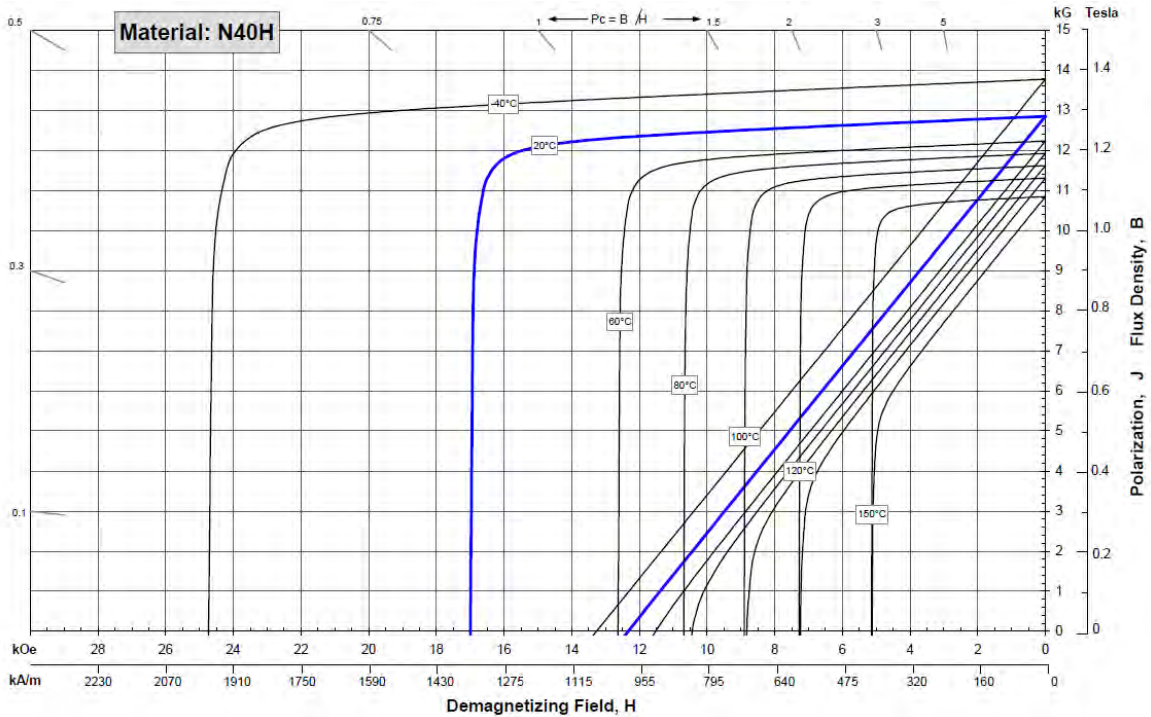


Figure 1.5. Demagnetization curves for N40H magnets at different temperatures. (Arnold[®] Magnetic Technologies [Arnold 2015]).

Another interesting feature of the magnets related with their hysteresis loop is the maximum energy product, which is defined as the maximum achieved BH value. Although this magnitude is a typical figure of merit in magnets comparisons and it has units of energy, it is not, in fact, the stored magnetic energy but rather a qualitative measure of the magnets general performance in a machine [Hanselman 2012]. Figure 1.6 shows an example of this concept. It is important to notice that, though $BH|_{max}$ is the point of maximum efficiency in order to exploit the magnets properties, it is unusual that the PMSM magnets work in that point because of the high risk of demagnetization if the curve knee is reached.

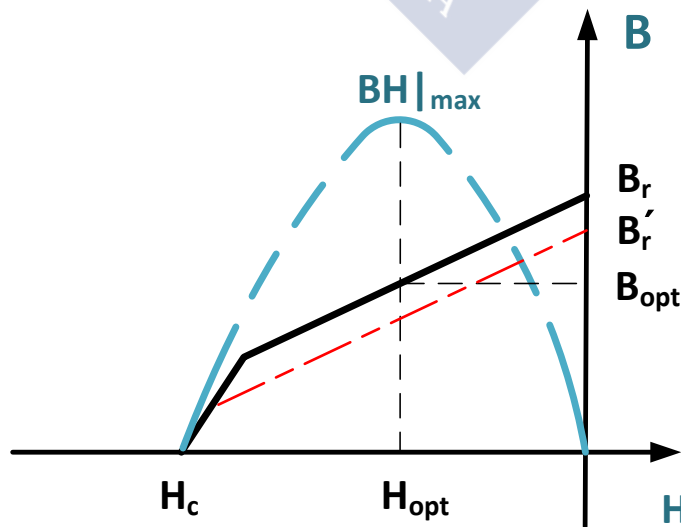


Figure 1.6. Characteristic operation line segments and BH curve.

The general features of permanent magnets have been introduced in the previous paragraphs but each permanent magnet technology has its own advantages and drawbacks related to its energy product, temperature, external field dependences and cost.

Over the past century great improvement of high-energy permanent magnet materials has been done. Figure 1.7 shows the maximum energy product achieved for each magnet technology during the last years.

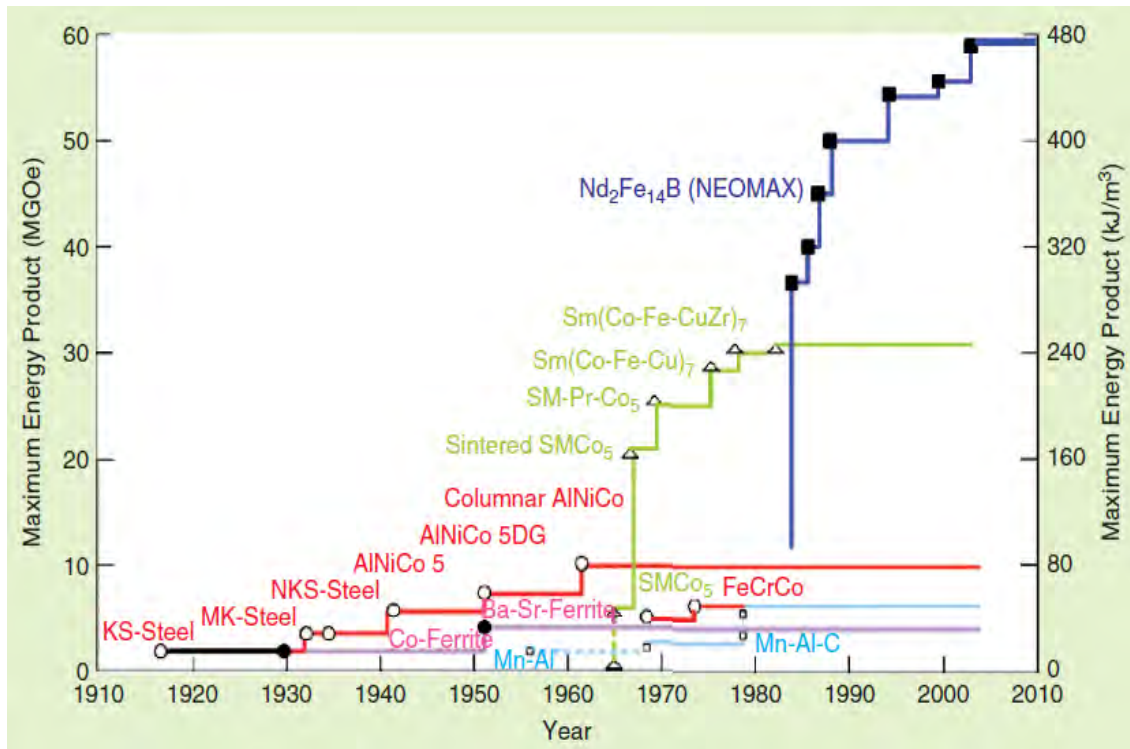


Figure 1.7. Evolution timeline of the permanent magnet maximum energy product during the last decades [Rahman 2013].

In the fifties, ferrite and barium ferrite magnets were the favourite choice for PMSM construction, with energy products from 8 to 30 kJ/m³ [Rahman 2013]; even nowadays ferrite magnets are a suitable option in low power and performance PMSMs, due to their low market price.

In the late fifties, aluminium nickel cobalt magnets (AlNiCo) reached energy products of 40 kJ/m³ and became the best choice for PMSMs until rare-earth magnets appeared in the sixties with samarium cobalt alloys [Rahman 2013].

But it is in the late eighties when the discovery of NdFeB magnets enabled the popularization of the PMSM and a higher integration of this kind of machines in industrial and transport applications due to their good features. These magnets present the higher available energy product in the actual market [Islam 2009], reaching 480 kJ/m³ with a residual induction of 1.3 T.

In spite of that fact, the NdFeB magnets present some important drawbacks, like their high temperature dependence, their poor cooling capabilities and their relative low electrical conductivity that causes higher eddy current losses [Pyrhönen 2012]. However, their main disadvantage is their high and changing price.

The main cause of this high price is that most of the operating rare-earth metals mines are in China (e.g. China controls the 75% of the NdFeB magnet production), therefore it has the ability to modify NdFeB magnets price according to their own needs. For example, in 2010 Chinese government limited to a 60% the rare-earth metal exportation respect to previous years, causing a high increase in its price. Eventually, this fact makes that other potencies, such as the US, are opening new rare-earth mines in their own territory, trying to avoid the excessive dependence from China [Sirvent 2012].

1.2.3 PMSM Structure and Classification

Classical PMSM structure consists of a mobile part or rotor where the permanent magnets are glued or inserted, and a fixed part or stator where the coils are wound, generally in slots located between teeth. Both, the stator and the rotor are constructed with some type of ferromagnetic material in order to lead the magnetic flux in the appropriate direction. Between the rotor and the stator there is a slight layer of air called airgap, where most of the magnetic energy is stored.

The aforementioned components establish the machine magnetic circuit. Figure 1.7 (a) shows a 2D representation of a radial surface PMSM whose magnetic flux flows radially through the airgap and it is only dependent on the circumferential coordinate, so just a 2D slice of the PMSM should be used in order to study its magnetic behaviour. This scheme represents a PMSM, as it is shown in Figure 1.8 (b), where the most important machine parts can be seen, such as the coils end-windings, the housing with its fins or the rotor shaft, all of them playing a major role in the mechanical, thermal, electrical and structural machine features.

The example presented in Figure 1.8 (a) is a cross-section of an interior rotor concentrated winding PMSM, which is one of the commonest PMSM topologies. In this section other possible PMSM topologies will be introduced.

There exist a lot of PMSM valid topologies that can be classified according to the magnets situation in the rotor, the rotor relative position, the wound stator coils or the main direction of the flux through the airgap. The classification presented in this section is the most common but it is far from being exhaustive, mainly because some PMSM topologies were invented in recent dates, challenging old classifications and generating new ones, as far as many of their properties are still unknown.

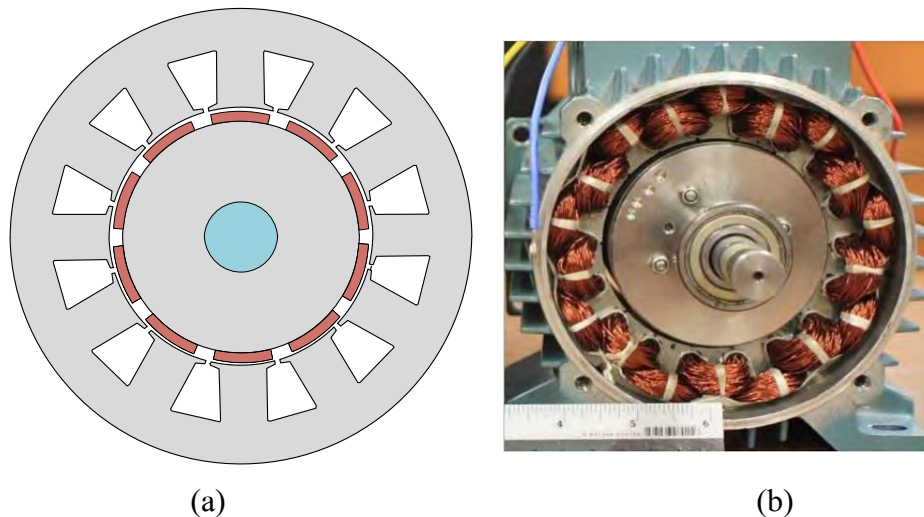


Figure 1.8. (a) Schematic of a 2-D slice of a radial PMSM. (b) Typical radial PMSM.

1.2.3.1 Rotor Relative Position

Two options exist related to the rotor position: internal or external rotor. Figure 1.9 shows both alternatives.

The main advantage of the exterior rotor is that the machine could be designed with larger airgap diameter for the same volume, as far as the magnets height is less than the total stator height, usually determined by the slots. Since the total PMSM power is roughly proportional to the squared airgap diameter, this leads to a design with more power density [Kazmin 2008-b]. Another advantage is that the magnets are closer to the machine surface, being able to evacuate the heat more easily and avoiding the risk of permanent demagnetization due to high temperatures.

On the other hand, the rotor is more exposed in that configuration; this fact can lead to operation failures. Moreover, the stator is known to be the PMSM part where most of the losses are concentrated. Indeed, both iron losses in the core and copper losses in the winding are concentrated into the stator. Due to the stator enclosure in external rotor machines most of the generated heat must be evacuated through the hub which has much less surface than that available in an internal rotor configuration.

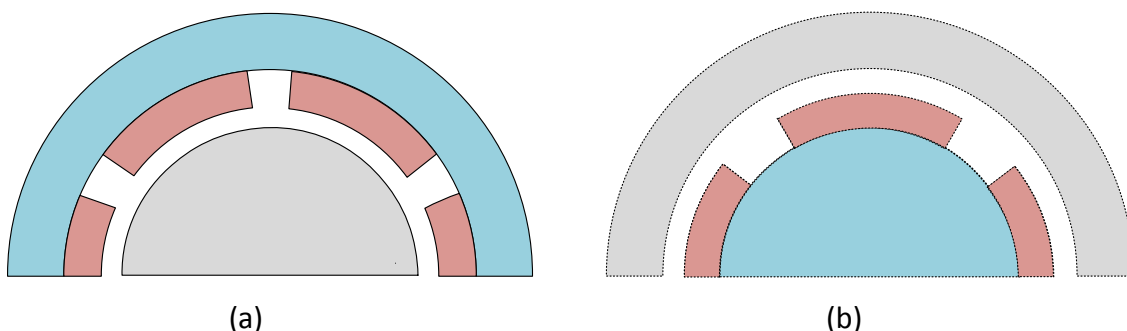


Figure 1.9. (a) External rotor configuration, (b) Internal rotor configuration.

Because of these disadvantages internal rotor configuration is the most common in practical applications.

1.2.3.2 Magnets Situation in the Rotor

Three main configurations can be found in the literature: surface PMSM (SPMSM), internal PMSM (IPMSM) and inset PMSM. In the latter, the magnets are embedded in the rotor, but very near of the airgap. In practical terms, inset PMSM are more similar to IPMSM and their features are very close. An example of an IPMSM rotor and a SPMSM rotor can be seen in Figure 1.10.

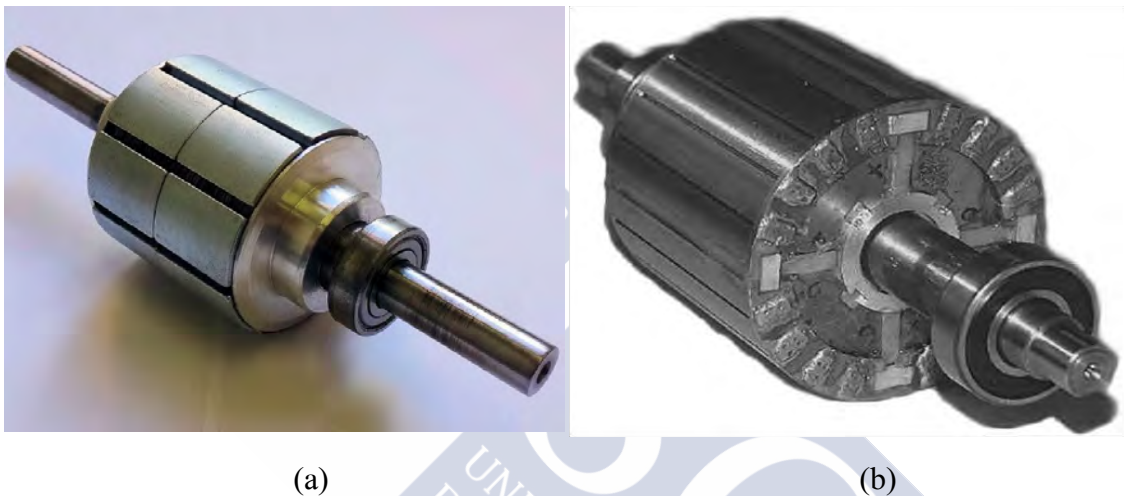


Figure 1.10. (a) SPMSM rotor by [Wu 2015], (b) IPMSM rotor by [Rahman 2013].

The main feature of an IPMSM is that it presents an additional source of torque called reluctance torque, that it is not caused by the rotor and the stator magnetic fields interactions, but just for the interest of the stator electromagnets to align themselves with the lowest reluctance path. The obvious conclusion is that the IPMSM has more torque density and, thus, more power density than a SPMSM.

Another important consequence of having the magnets inside the rotor is that the airgap could be much shorter, since the magnets are no longer a part of it [Kazmin 2008-b]. This means that the magnetic induction is higher than in a SPMSM design, causing higher rotor saturation and a higher risk of magnets demagnetization in case of stator coils short circuit.

As a summary, compared with SPMSM, IPMSM topology presents higher power density and, because of their enclosure, the magnets are more protected from mechanical stress, but it has the drawbacks of more complicated rotor manufacture process, higher level of torque ripple, higher rotor core losses, higher magnet heating and presence of local rotor saturations.

Therefore, the best choice between an IPMSM and a SPMSM mainly depends on the application.

1.2.3.3 Stator Coils Winding

There are two main options when a stator winding is chosen: concentrated or distributed winding. In concentrated windings the coils are wound in consecutive slots, while in distributed ones they are wound in order to maximize the rotor flux linkage, no matter the distance between the connected slots.

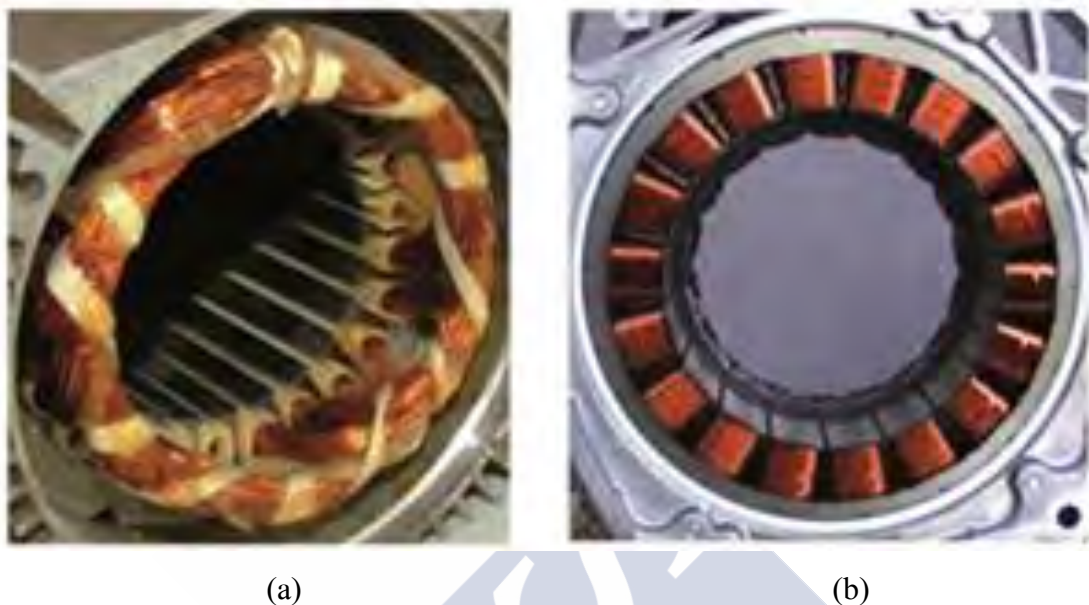


Figure 1.11. Comparison of distributed (a) and concentrated (b) windings. [Photos: University of Bundeswehr].

The main advantages of concentrated windings over the distributed ones are related with their shorter end-winding. In fact, less end-winding means lower copper losses, less total PMSM volume and more effective automated manufacturing.

However, the voltage induced by the magnets in the coils, i.e. the electromotive force (EMF), has more harmonic components, so current and torque ripples are generally higher than those caused by distributed windings [Lee 2009, Patel 2013]. Moreover, concentrated windings machines noise emission and magnetic forces over the stator are usually higher [Chen 2014].

1.2.3.4 Flux Direction

One of the main fields of investigation of PMSM concerns new topologies where the classical airgap magnetic induction orientation in the radial direction is changed in order to achieve better machine performance.

The main flux path in an axial machine is in axial direction, while in a transversal one the flux is directed in both, axial and radial directions. A representation of the three mentioned topologies is shown in Figure 1.12.

Transversal and axial machines are expected to have better performance than classical radial ones. For example, transversal PMSM present a very high power density due to the fact that they are able to increase their power with their pole number but without increasing the ferromagnetic material volume. Another of their features is that they have less copper losses and high efficiency in applications with low speed and high torque.

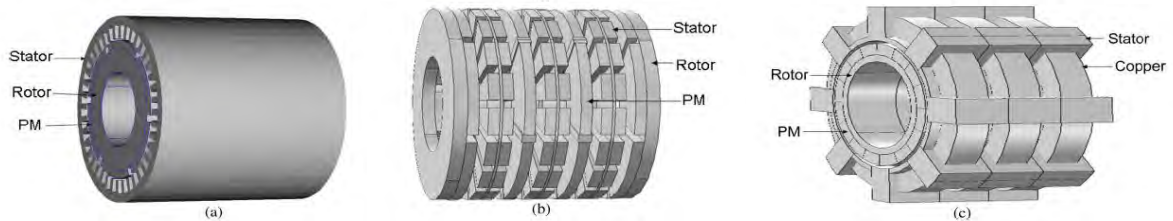


Figure 1.12. Example of the main PMSM topologies; (a) Radial flux, (b) axial flux and (c) transversal flux [Anyuan 2010].

In spite of the aforementioned reasons, radial flux machines are, by far, the most common ones among PMSMs, because of their simpler manufacture process and their much more mature technology.

1.3 Radial SPMSM Design: The Starting Point

The PMSM topology selected in order to implement a complete analytical and multiphysical modelling and a subsequent design methodology is an internal-rotor radial-surface PMSM because it is the more frequent PMSM topology and, therefore, the most used for industrial applications, with good features and well-established manufacture process.

The main features and advantages of this topology in particular and of PMSM in general with respect to other machines are summarized below:

- High compactness.
- High torque and power densities.
- Very low rotor losses. High efficiency.
- No need of brushes or commutator as required by other machines.
- Higher power factor than induction machines.
- Simple and robust rotor construction, no need of internal holes or rotor bars.
- Lower noise and vibration with respect to induction or switched reluctance machines.

Due to the aforementioned characteristics, radial SPMSM became the final election to perform an improved design methodology useful to accomplish a real, complete industrial machine design.

In this section a brief summary of the multiphysics models used to support the optimized design methodology are introduced in order to achieve the necessary overview of the whole process that will be explained in detail along the rest of the document. Figure 1.13 shows the general diagram that will be the backbone of the proposed modelling.

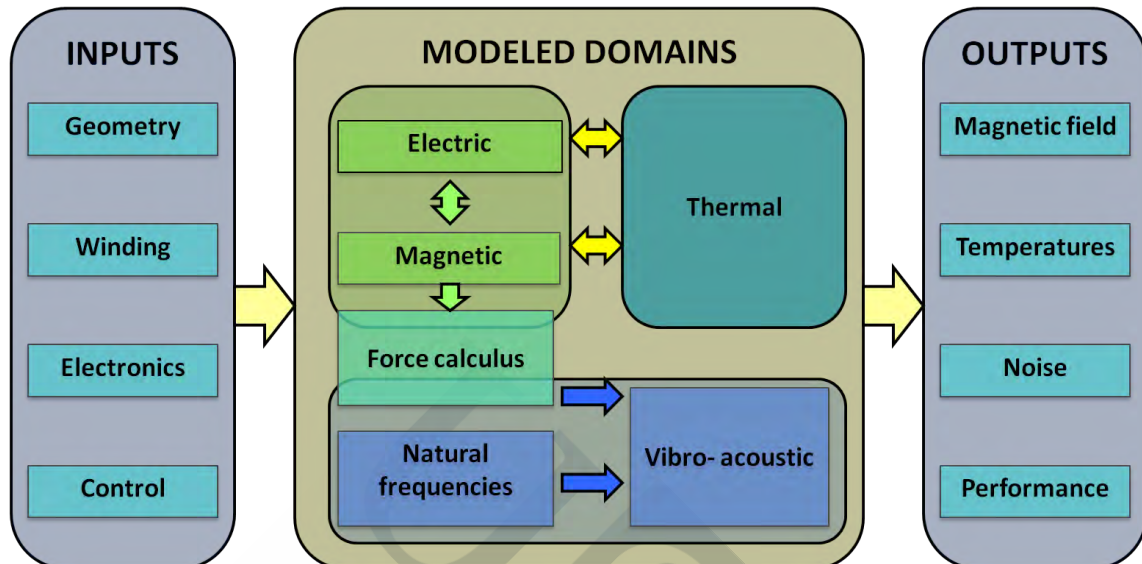


Figure 1.13. Block diagram of the proposed multiphysics linked models.

As it was introduced before, the implemented models are analytical, in order to save computation time. Such analytic methods require the simplifications and assumptions listed below:

- 1) It is assumed that the ferromagnetic material in the rotor and stator cores is infinitely permeable.
- 2) The magnetization profile of the magnet must be radial or parallel.
- 3) The machine has m phases without neutral with a balanced winding spatial distribution.
- 4) It is considered that the machine is rotating anticlockwise, so the teeth and the slots are numbered from 1 to Q in this direction. See Figure 1.14.

The first simplification is especially important because it could lead to a considerable accuracy loss if the ferromagnetic core is saturated. In fact, this entails the main disadvantage of the analytic methods, but the error can be minimized ensuring that the ferromagnetic material is not in the saturated region during the PMSM normal operation mode.

Another important remark is the different nature of the input variables that the model needs in order to obtain the machine behaviour and performances. They can be classified by their origin as geometrical variables, winding and other configuration variables (such as number of poles or slots), electronics variables and control variables, the latter having a major influence in the machine current harmonics. All of them are required by the model and must be established by an external algorithm.

These input variables can also be classified in a more interesting way by their nature. They are divided into three groups:

Design specifications: initially established by the user as a requisite of the desired PMSM. Once the optimization software is running they cannot be changed, not even between different iterations of the model. Examples of design specifications are the revolutions per minute, the nominal mechanical power or the number of machine phases.

Physical constants: They are established by the program itself and cannot be modified, either by the user or the optimization program. Two examples can be the void magnetic permeability or the thermal properties of the copper and the ferromagnetic cores.

Design variables: They are fundamental variables that cannot be modified in an iteration of the model but they are changed between iterations. They are used by the external optimization algorithm in order to find the best solution in terms of an objective function. Geometric variables (number and dimension of the slot in the stator, machine radial dimensions, etc...), configuration variables and most features of the used materials are included here.

Prior to the solving the physical models, a set of secondary variables is obtained from the aforementioned main variables. They can be calculated by direct operation and will not change during an iteration of the code. A good example is the rotor radius R_r which is obtained from the inner stator radius R_s , the magnet length l_m and the airgap g by

$$R_r = R_s - g - l_m. \quad (1.1)$$

For a clear understanding of the geometric variables used during this thesis work, Figure 1.14 is included, showing a cross-section of the PMSM and a detailed view of a slot.

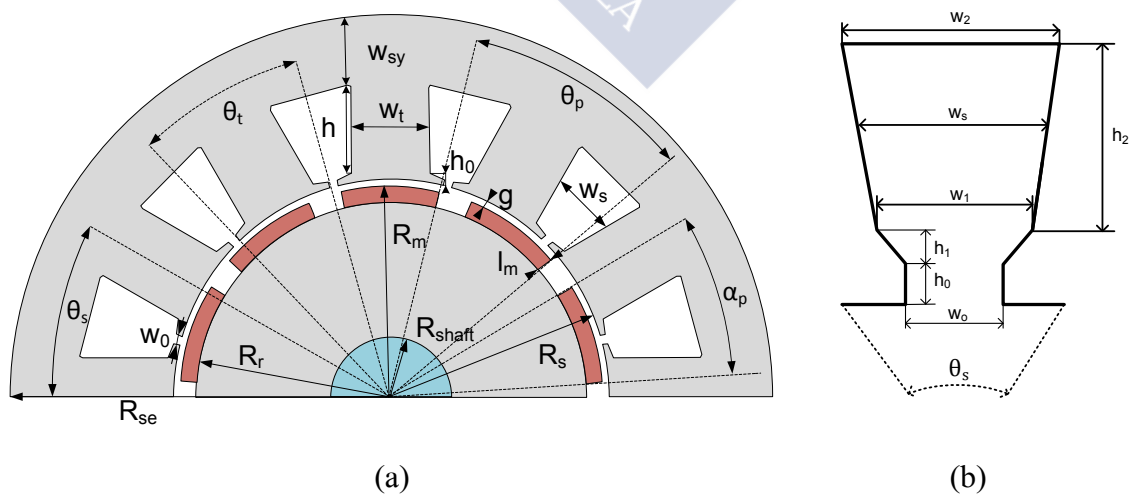


Figure 1.14. (a) Main dimensions of the SPMSM and (b) detail of a slot.

In order to validate the developed models and therefore the design methodology, a tool was programmed in Matlab®. The obtained results will be compared with those achieved using commercial Finite Element Method (FEM) software.

1.4 Outline of the Document

The document contents are summarized as follows:

In this first chapter the objectives of the work, the general context of the problem and the starting point of the thesis are highlighted. Moreover, a brief introduction to the PMSM is included, explaining its operating principle, its different topologies and its historical evolution.

Chapter 2 shows the state of the art and the main technical and scientific contributions in PMSM design and modelling published in the past years, paying an especial attention to the optimized and multiphysical approaches that include two or more of the physical domains of interest, i.e. magnetic, electric, thermal, structural or vibro-acoustic.

Chapter 3 explain the physical models implemented, showing the achieved results and proving their accuracy, usefulness and precision through the comparisons between the developed tool and commercial FEM software (FLUX2D®, ANSYS® and Motor-CAD®).

Specifically, the first parts are devoted to the electromagnetic models and their linkage with main mechanical aspects, such as torque and mechanical power generation, quality parameters and losses estimation methods are also included. Then, a thermal approach based on a lumped thermal network is introduced. Finally, the structural and vibro-acoustic features of a PMSM are analytically deduced.

In chapter 4 a complete experimental validation is carried out by means of a case of study: IkerMAQ (Q45p5), a 75 kW PMSM fully designed in IK4-Ikerlan. The performed experiments are detailed and their results compared and correlated with those obtained by the models exposed in chapter 3.

Once the physical models have been validated in chapter 4, chapter 5 explains their application in the synthesis and implementation of an improved, original, optimized, holistic and fully analytical design methodology. This methodology is programmed in Matlab® in order to generate a proper design tool.

Finally, chapter 6 shows the conclusions and contributions of the thesis and the proposals of future lines of study are highlighted.





**Design and Modelling of PMSM:
Optimized-Multiphysical Study**



SPMSM design is a complex matter, so the development of an extensive state of the art is a difficult task, because many criteria and different approaches should be taken into account. In this chapter, a brief global picture in PMSM design will be presented in order to achieve a summarized but complete insight in the recent developments and global trends in the subject.

The chapter is divided into two main sections, corresponding to the parts of a complete design implementation: the first one introduces the state of the art in PMSM design methodologies and the second one is devoted to the main modelling approaches used in the aforementioned methodologies.

2.1 Towards a Design Methodology: State of the Art

Nowadays, in technical literature many papers and related publications about PMSM design can be found. In spite of this fact, most of them only take into account partial aspects of the global problem and offer unclear and opaque methodologies that are hardly replicable at the best.

Moreover, these approximations are not only incomplete but, generally, use optimization tools and algorithms as a black box, trying to achieve just a satisfactory rather than an optimal design [Goss 2013-a].

In this context, it is common to find methodologies just based on a basic electromagnetic initial sizing, where the main contribution presented is the link of FEM calculus with a blind use of an optimization algorithm which slightly improves a pre-existing design.

On the other hand, in industrial design, most of the used methodologies are focused only on the electromagnetic performance and they estimate the most important features of the machine, such as efficiency, power, and volume to mass ratio, only considering its electromagnetic characteristics [Boglietti 2009]. Thermal sizing is usually reduced to some empirical rules and key aspects, such as maximum winding current density, which provides a first approximation that can be accurate enough in some low-performance, very well-known applications [Amrhein 2013]. Other important physical domains such as mechanics and vibro-acoustics are treated as an afterthought if needed.

This kind of “industrial methodologies”, labelled “sizing models” in [Carlson 2012], relies on basic electromagnetic equations without any optimization process and they usually need a great deal of approximations and “rules of thumb”. This fact supposes that, in a complete design process, many interesting machine possibilities are directly discarded and never modelled at all.

Sizing models are fast and reliable if very similar machines have been previously studied and correct empirical parameters obtained. However, they are unsystematic

by nature and present serious difficulties to extrapolate the obtained results to a new set of specifications or to more demanding applications.

In recent years, especially in the last decade, a different methodological approach based on a deeper insight in the physical PMSM behaviour has been developed. This new modelling allows the implementation of design methodologies which are less dependent on designer experience or empirical rules and, therefore, they are much more reliable for high-performance and new applications.

The interest in these new design methodologies in the academic, and even in the industry world, is endorsed by recent publications, such as [Agamloh 2013], which explains in detail the multiphysical challenges of a holistic induction machine design, [Ombach 2007] which deals with the manufactured tolerances during an industrial design process, [Tsampouris 2013] which develops a software capable of coupling the design and control stages or [Favi 2011] which proposes an online design tool in order to shorten the development time. These works try to bring closer new methodology approaches from a more academic context to the industry, where its practical implementation can suppose more efficient machines at lower cost.

Despite their many advantages these methodologies are far from being widely used in industry because of their novelty and the specific knowledge necessary to analyse the different aspects of a PMSM. Because of the aforementioned drawbacks only some research groups are focusing on the multiphysics machine modelling and design, but the great accuracy and high integration levels of their results explain the increasing interest in these approaches.

Many of these methodologies present a double loop structure, where a first design stage is done with fast analytical sizing equations and a second one with numerical approaches, more accurate but more time consuming. This approach tries to combine the advantages of both techniques. The general flowchart shown in Figure 2.1 is shared with slight modifications by many recent publications [Makni 2007, Elosegui 2008, Tutelea 2010, Wang 2012, Goss 2013-b].

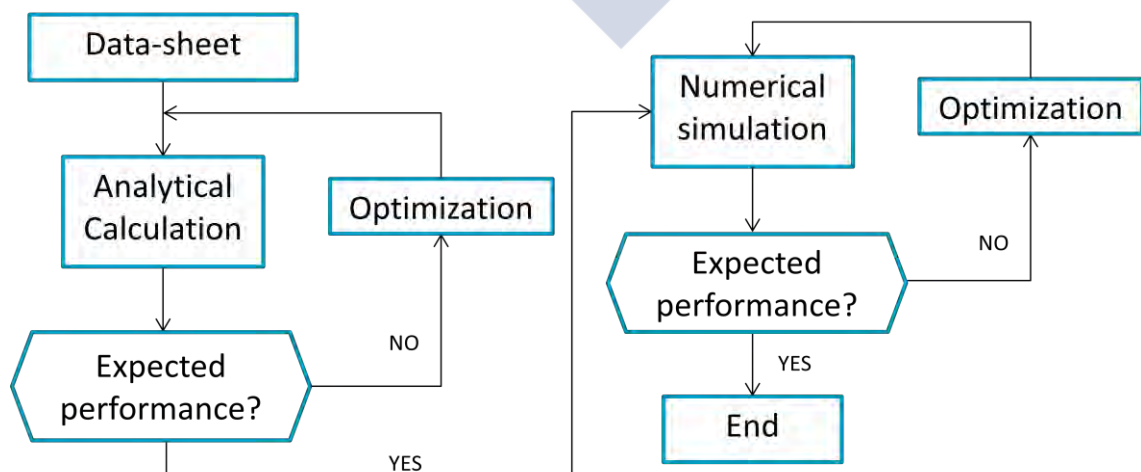


Figure 2.1. Classical two-stage flowchart in recent machine design approaches.

Most of the recent published design methodologies have the presented flowchart with minor modifications; one of these differences is the specific weight of the numerical and analytical calculus (even some of them include only one of the two stages) and the presence or not of an optimization algorithm closing the loop. According to the design criteria the aforementioned methodologies can be classified as follows:

- **Design type:** Two main designs can be performed: the first is a global one, taking into account a high number of design variables and seeking for a holistic and new design; the second is a local one, varying a limited number of design parameters and generally starting from a previous design in order to improve some key features. Examples of global designs are [Bracikowski 2012, Hecker 2013], and local designs are [Mi 2006, Lee 2009].
- **Operation range:** Another major concern is the torque-speed PMSM operation range. Some publications deal with the design problem just in nominal operation conditions [Hecker 2013, Duan 2013-b], i.e. at rated speed and torque, while others are centred in applications, such as electric vehicles, which demand a design based in all the operation range and not just in nominal conditions [Hafner 2011, Wang 2013].
- **Physical domains:** Depending on the number of physical domains studied, the design methodologies can be classified in electromagnetic [Elosegui 2008, Tutelea 2010], magnetic-thermal [Kazmin 2008-a, Legranger 2008] or multiphysics [Semidey 2011, Jannot 2011].
- **Modelling:** According to the kind of modelling used, a methodology can be analytical [Kazmin 2008-a], lumped parameter oriented [Bracikowski 2012], numerical [Giurgea 2008, Van der Giet 2010] or hybrid [Makni 2007, Goss 2013-a].
- **Optimization process:** Another major concern is the use or not of an optimization algorithm in the design process. The methodologies can be optimized [Iles-Klumpner 2004, Sarikhani 2012] or not optimized [Kazmin 2008-a, Saito 2010], the latter being the so called sizing models. Within the optimized methodologies a classification according to the used algorithm and the proposed variables and objectives will be performed below.

Among all the aforementioned features of these design methodologies, two are selected as the key features: their multiphysics nature and the possibility to run optimization algorithms as a part of an eventual design process. The global classification of different design methodologies proposed in the literature will be performed in function of two parameters: their optimization procedure and their multiphysical approach, since this thesis will be especially focused in this two key features.

2.1.1 From a Magnetic to a Multiphysical Approach

When a new PMSM design should be done electromagnetic criteria are the major concern, since the machine main features depend on its electromagnetic behaviour.

Although the final performance and even the safety and reliability of the proposed design are heavily conditioned by thermal considerations, many designs only take into account the electromagnetic domain, oversizing the machine according to heuristic or empirical rules in order to ensure a correct temperature operation in the magnets and windings. Some very recent approaches are only focused on partial or global aspects of the electromagnetic design, ignoring the thermal effect in the design process.

A second kind of design methodology is an electromagnetic-thermal approach; this is a great improvement over the classical design methodology, as far as the thermal behaviour of the machine has a great influence on its electromagnetic performance. In fact, not only the electromagnetic features determine the temperatures in the PMSM through copper and iron losses but those temperatures change the physical characteristics of the magnets and the copper wires, modifying their operation points and, thus, their performance. An example of flowchart containing an iteration loop in order to calculate the thermal and electromagnetic behaviour is shown in Figure 2.2.

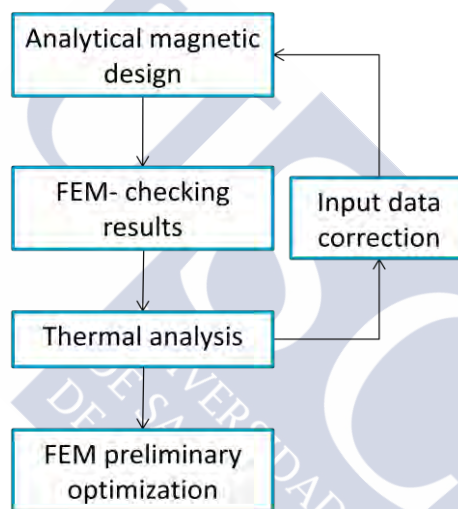


Figure 2.2. Example of electromagnetic-thermal loop in PMSM design by [Kazmin 2008-a].

The third and most complete approach is the multiphysical design methodology, which takes into account not only the electromagnetic and thermal features but also the electric, structural and vibratory ones. This is a much more complete design method as it permits to model the PMSM from a global point of view, achieving an optimum which takes into account much more design goals and features. This is important since the global optimum is not the sum of the partial optima in each discipline. Moreover, it allows to apply optimization algorithms in a more powerful sense, since the results obtained by the physical models can be used not only as objective functions but also as constraints, for example achieving efficient PMSM designs with constraints on their interior temperatures, maximum converter voltage required or radiated noise.

Figure 2.3 shows a graphical representation of the physical domains that a multiphysical design should take into account and the possible goals than can be achieved with this methodological approach.

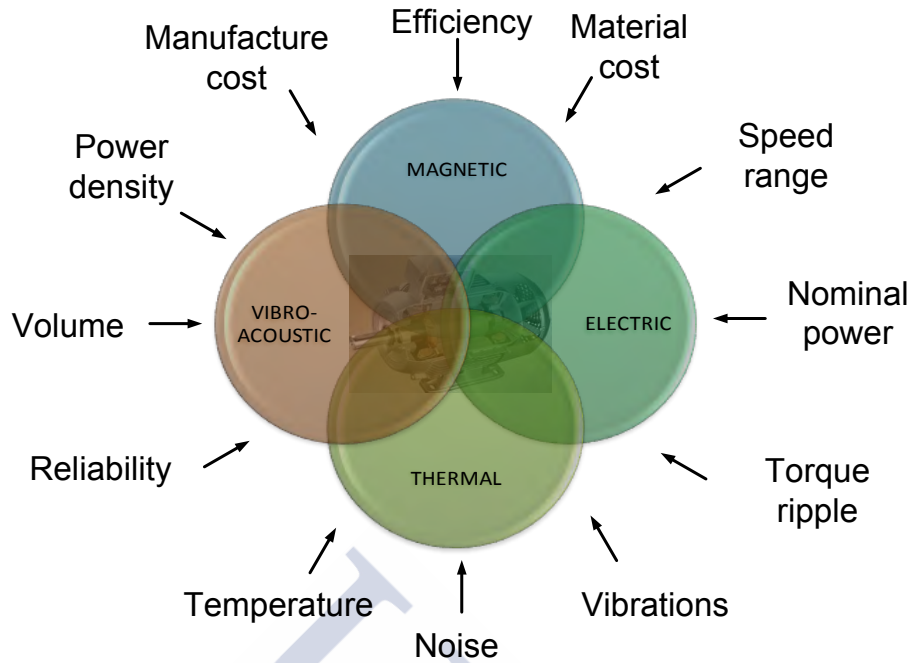


Figure 2.3. Physical domains and main possible objectives of a multiphysical design methodology.

2.1.2 From a Sizing to an Optimized Approach

From a mathematical point of view an optimization process can be defined as a problem where, from an input vector called design variables:

$$X = (x_1, x_2, \dots, x_n) \in \mathbb{R}^n \quad (2.1)$$

and a set of estate variables, calculated from the design ones,

$$Y = (y_1, y_2, \dots, y_m) \in \mathbb{R}^m \quad (2.2)$$

it is possible to define one or more objective functions such that

$$\begin{aligned} f: \mathbb{R}^n &\rightarrow \mathbb{R} \\ X &\rightarrow f(X), \end{aligned} \quad (2.3)$$

and a set of constraints:

$$\begin{aligned} g_i(X, Y) &\leq 0 \quad i = 1, \dots, k \\ h_j(X, Y) &= 0 \quad j = 1, \dots, s \end{aligned} \quad (2.4)$$

that must be satisfied.

The optimization problem is then to find a vector X such as $f(X)$ is a minimum (ideally the global minimum) of f verifying the constraints imposed by $g_i(X, Y)$ and $h_j(X, Y)$.

The external users of any optimization algorithms have the main task to define the design variables X , the state variables Y and also the objective function f and the constraint functions g_i and h_j . Then, the more adequate optimization algorithm to the

proposed problem should be selected. In electrical machine design the variables usually are the machine dimensions and materials, and the objective functions are the maximum efficiency, minimum cost or minimum weight.

The different optimal design methodologies applied to PMSM can be studied and classified according to their objective functions, design variables, constraints and the used optimization algorithm.

2.1.2.1 Objective Functions and Design Variables

Many objectives must be satisfied in a complete PMSM design, among them the commonest are highest efficiency, lowest cost, minimum use of ferromagnetic material and minimum magnets weight. Since many of these objectives can be conflicting, a compromise must be achieved. In recent optimized methodologies multiobjective optimizations with efficiency and cost [Munteanu 2012] or efficiency and weight [Jannot 2011] objectives are very usual.

Other approaches try to optimize more concrete machine features, such as the cogging torque [Cassimere 2009, Wang 2012], the electromagnetic torque [Aydin 2015] the stator structural characteristics, the noise emission [Lee 2009] or the amount of needed magnet material [Wrobel 2006].

One important trend in the last years is the step from just one objective function in which all the proposed goals are contained, to a multiobjective approach, with various objective functions and a Pareto-frontier oriented design. These new approaches have the advantage to provide, not just a single solution but an optimal set of them in order to let the designer choose the most suitable for its application.

The choice of design variables is another major concern in optimization processes. In that sense a clear evolution was performed during the present decade. Ten years ago, only a few geometrical continuous variables were taken into account in the design process, leading to very local approaches that yield to designs very close to a proposed initial prototype. An example of that is [Iles-Klumpner 2004] who only uses seven variables in order to perform the electromagnetic design.

Nowadays, the global trend is to define a big set of design variables, usually more than ten, taking into account both continuous and discrete values and allowing a much more global design, varying not only the physical PMSM dimensions but also the number of pole pairs, the number of slots or the ferromagnetic and magnet materials. This evolution was possible because the powerful software and optimization algorithms developed in the last decades are being applied in the machine design context. Good examples of this trend are [Cassimere 2009] which takes into account seventeen variables, including different core materials and [Kreuawan 2007] which uses twelve variables, including the number of poles and slots.

2.1.2.2 Optimization Algorithm

An important decision in every optimized design methodology is the correct selection of the optimization algorithm. In order to do so, a first step is to know the particularities of the proposed problem. A lot of different optimization algorithms have been used in machine design methodologies and their main features listed in the literature. A global review of the subject can be found in [Duan 2013-a].

To generate an optimal PMSM design it is necessary to take into account that it is a nonlinear and multiobjective optimization problem which involves not only closed-form equations, but several estimations and possible lookup tables and iterative loops where a correct estimation of a derivative function is quite troublesome. These particularities imply that only certain types of optimization algorithms are suitable.

Two different approaches can be done in order to perform a design methodology:

- The first one is the use of surrogate models that capture the relationship between design objectives and inputs. These models are not exactly optimization algorithms but a possible initial step that consists in the reduction of the input vector X by means of mathematical approximations and screening techniques. These methods are very popular because they drastically reduce the number of model evaluations needed, a capital advantage when numerical simulations should be performed. Examples of this approach are the response surface method (RSM) or the Taguchi methods. Many authors apply surrogate models in electrical machine design [Giurgea 2008, Amdouni 2012, Duan 2013-b, Hwang 2013].
- The second is the use of a proper optimization algorithm, further explained in the present section.

Optimal search algorithms can be divided into several categories, so different classifications have been proposed in the literature. Figure 2.4 shows a possible one adapted from [García 2014] which includes the main algorithms used in PMSM design methodologies.

Exhaustive or grid-search methods are the simplest design methodologies, because they are based on performing a discretization of the variables, evaluating the objective functions in every selected point and choosing the best value as the global optimum. In the beginnings of the use of optimization algorithms for electrical machine designs some exhaustive methods were implemented but soon they proved to be unaffordable in that type of methodologies, as far as many variables are involved and the problem complexity scales exponentially with the number of variables. A comparative example between grid-search algorithms and other types of optimization approaches can be found in [Iles-Klumpner 2004].

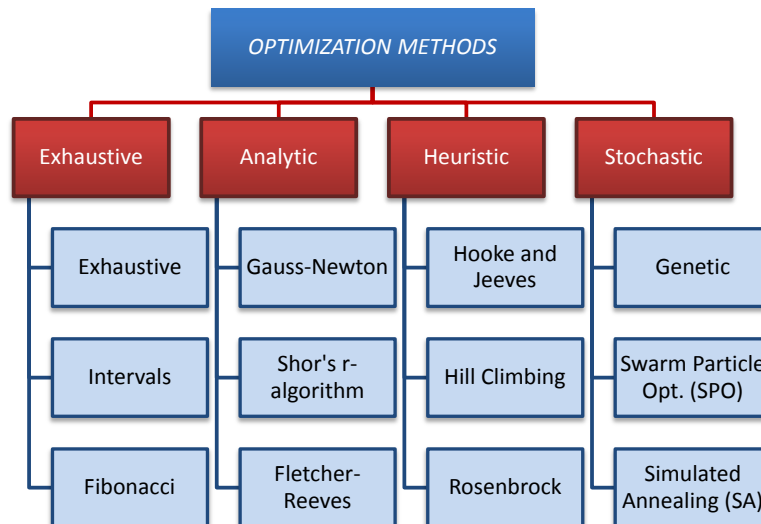


Figure 2.4. Proposed classifications of the main optimization algorithms applied to PMSM design methodologies.

The analytical methods calculate or estimate the derivatives of the objective functions in order to change the design variables in the direction of their gradient. Their main advantage is that they are fast optimization algorithms but firstly they can be caught in local minima and secondly, in some problems, the derivatives are very difficult to obtain. During the nineties, sequential unconstrained minimization techniques (SUMT), an analytical algorithm, were used in order to perform electrical machine design optimization [Wurtz 1996]. Some authors still use that kind of approaches [Wang 2012] but now they are mostly out of use since the advent of more powerful stochastic approaches, such as genetic algorithms (GA) or Particle Swarm Optimization (PSO), where no derivatives are needed.

Heuristics methods have some similarities with the analytical ones but the former are based in the gradient calculus, while in this case the search algorithm is based on performing pattern movements from one or various initial points, and on travelling from these initial points to another one if the objective functions improve. They are slower than the analytical algorithms and equally can be caught in local minima but they have the great advantage of their robustness so they are a very suitable choice to be applied in design methodologies. One heuristic method, the Hooke and Jeeves, is usually applied in machine design [Iles-Klumpner 2004, Tutelea 2010, Amdouni 2012] but it is less popular than stochastic methods.

Both, the analytical and heuristic algorithms are encompassed in a more general classification called the deterministic algorithms, as far as they find the optimum without any kind of stochastic procedure [Duan 2013-a]. In this work, it is considered more useful to divide them in the aforementioned categories, because their application in design methodologies is conditioned by the use or not of derivatives.

The stochastic methods are based on the inclusion of some stochastic operation in order to improve the global search, escaping from local minima and becoming more independent with respect to the starting points. Most of them are based on biological or physical principles, such as natural evolution (GA), the movements of an insect

swarm searching for nectar (PSO) or the particular behaviour within a heating solid (simulated annealing). These methods are very robust and especially suitable in searching global optima in complex problems where they can be easily used as black boxes. Thus, they became very popular in electrical machine design methodologies. In PMSM design GA is the most common choice [Cho 1999, Kreuawan 2007, Jannot 2011, Hecker 2013, Mirahki 2014] but, in recent years, PSO is becoming very popular [Wrobel 2006, Sarikhani 2012]. Other stochastic methods, such as differential evolution [Duan 2013-b, Zhang 2014] or ant colony [Tsampouris 2013], have only a minor use.

Some comparative studies between different optimization algorithms applied to machine design methodology were performed, for example between GA and PSO [Cassimere 2009, Sarikhani 2012] and between GA and Hooke and Jeeves [Tutelea 2010].

2.1.3 The Global Picture

A summary of the studied methodologies is presented in Table 2.1 where the different PMSM design approaches published in the literature are classified according to their multiphysical approach, the used optimization algorithm and the developed type of design (local or global).

Table 2.1. Classification of the PMSM design proposals found in the literature.

		No-optimized	Analytical optimized	Heuristics optimized	Stochastic optimized
Magnetic	Local	[Mi 2006] [Saito 2010]	[Wang 2012]	[Iles-Klump 2004]	[Wrobel 2006] [Zhang 2014]
	Global	[Comanescu 2003] [Elosegui 2008]	[Muetze 2008]	[Tutelca 2010]	[Cassimere 2009] [Sarikhani 2012]
Magnetic-thermal	Local	[Dorrell 2006]	[Legranger 2008]	-	[Cho 2000]
	Global	[Kazmin 2008-a]	-	-	[Goss 2013-a]
Multiphysics	Local	[Marignetti 2006]	-	[Makni 2007]	[Jannot 2011] [Semidey 2011]
	Global	-	-	Proposed methodology	[Bracikowski 2012]

From the point of view of the models used in design methodologies two different trends can be found in the literature: on the one hand, the development of complex and accurate analytical models is performed by an increasing number of researchers. On the other hand, FEM calculus is the most popular option frequently combined with a stochastic optimization algorithm. In order to link the time-consuming FEM model with a GA or PSO algorithms, a surrogate model is usually applied.

Nowadays, it is evident the increasing trend in the use of optimization algorithms in the PMSM design methodologies, especially the stochastic ones. Some research groups go a step forward combining different types of optimization algorithms in order to take advantage of the benefits of a hybrid approach. For example [Amdouni 2012] applies

RMS in order to reduce the problem size, then finds the optimum region by means of a GA and, finally, performs a local search using a Hooke-Jeeves algorithm.

Another major evolution in PMSM design is the increasing number of multiphysical approaches developed. Moreover, most of the multiphysical design methodologies are optimized, in order to maximize the inherent benefits of a multidisciplinary approach. They use their much more powerful insight in the machine behaviour in order to improve several objective functions by means of the optimization algorithm. In fact, in recent publications, the implementation of a multiphysical design without any optimization process is very odd.

Taking into account the aforementioned design approaches, the methodology developed in this thesis is a multiphysical, global and optimized one. The optimization algorithm used will be the direct multi-search (DMS), a novel multiobjective derivative-free heuristics algorithm implemented and first presented by [Custódio 2011]. To the best knowledge of the author, this new algorithm, based on the Hooke and Jeeves one, will be used by the first time in electrical machine design.

As far as it was investigated, no other PMSM multiphysical, global design methodology using heuristics algorithm could be found in the literature, in spite of the fact that the Hooke and Jeeves method obtains very good results in machine design [Tutelea 2010]. This is one of the reasons why it is considered that this new approach is a very interesting path to be investigated.

2.2 State of the Art in PMSM Modelling

As it was explained before, one of the main requirements for the implementation of an optimized design methodology is to develop a model which can represent the complexity of the physical system under study.

This is especially important for a device as complex as a PMSM whose design involves a multidisciplinary approach, including electromagnetic, mechanical, thermal and even structural and acoustic considerations [Bracikowski 2012].

Though many of the aforementioned publications develop multiphysical models in order to include them into different design methodologies, very few explain the correct coupling between physical models, remaining many of the interaction variables and coupling mechanisms unknown. A notable exception to this fact is provided in [Bracikowski 2012], where a complete dissertation about multiphysical coupling in PMSM modelling is performed.

Due to this lack in the consulted literature, this section will be divided into three separate parts, each concerning to a specific physical field applied to the PMSM modelling.

2.2.1 Electromagnetic Modelling

It is well known that electromagnetic characterization is of critical importance in the design of electric machines. Moreover, most of the industrial models are focused only on the electromagnetic performance and they estimate the most important features of the machine only considering its electromagnetic features.

Thus, huge amount of literature have been written about both, the complete electromagnetic modelling of PMSM and the specific aspects of it, such as cogging torque [Zarko 2008], force density [Zhu 2010] or losses in the rotor permanent magnets [Markovic 2007] and its undesirable effects over the magnets, such as local and global irreversible demagnetization [Lee 2015]. Moreover, a lot of studies are focused on the influence of very specific modifications in a PMSM, such as dovetails [Kolehmainen 2010] or arbitrary magnet shapes [Wu 2014].

All these models, both the particular and the global ones, can be classified by its method of calculus in three categories, as shown in Figure 2.5.

- **Numerical methods:** they are based in numerical calculus of the magnetic flux in several points of the machine geometry. Although they reach the most accurate results they are also the most time consuming. The most important methods are the Boundary Elements Methods (BEM) and the FEM; the seconds are, by far, the most common in PMSM electromagnetic modelling. An example of FEM modelling is [Giurgea 2008].
- **Lumped parameters:** this technique is based on a simplification of the machine geometry, represented by a grid of discrete reluctances, i.e. an equivalent magnetic circuit. It can be quite accurate and it is much faster than FEM approach but a very good initial knowledge of the magnetic flux distribution in the machine is required in order to obtain a good reluctance grid which takes into account the geometrical particularities without incurring in prohibitive computation times. Examples of lumped parameters designs can be found in [Lu 2013, Gómez 2014].
- **Analytical:** based on geometrical and physical approximations which permit the simplification of the problem, its formulation in analytical equations can be solved in a short time, but it presents an accuracy loss with respect to the previous methods. In spite of that, several researches [Zhu 1993-a, Proca 2003, Zarko 2006, Liu 2008] had shown that its precision is good enough for a first design stage. Moreover, they have very good accuracy if the ferromagnetic cores are unsaturated or only slightly saturated. An example of recent and complete analytical approach is [Liu 2008].

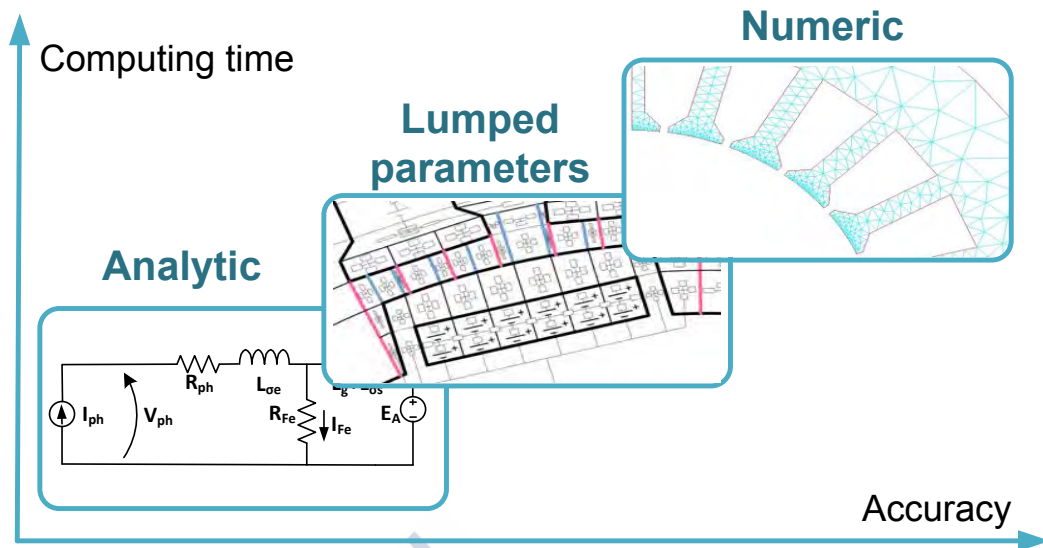


Figure 2.5. Different model approaches for electromagnetic characterization of PMSM.

As it was explained before, in this thesis an analytical approach is used due to its lower computing time. This is a critical advantage in order to implement an optimized methodology, which usually requires running the model many times; this is the main reason why this state of the art will be especially centred in the analytical modelling.

In the literature it is usual to divide the analytical modelling into two main groups: one related to simple and direct size equations and another one based on advanced approaches, which generally used Fourier Series (FS) [Almandoz 2008]. Obviously, the former methods are more straightforward and easier to implement but they are only useful for very rough calculus, so they are usually combined with lumped parameter models or FEM calculations in order to do most of the dimensioning process [Comanescu 2003, Mi 2006, Kazmin 2008-a].

The direct size equation modelling is only useful in the framework of a sizing model design methodology, so the presented work is centred in FS methods, due to their accuracy, their good comparison with FEM results and the existence of robust and reliable Fast Fourier Transform (FFT) developed by many programs toolboxes (e.g. Matlab®).

Next, a brief description of the advanced analytical modelling in the last years, both related to global modelling and to particular aspects, will be included.

2.2.1.1 Global Modelling

Global advanced analytical models are usually centred in the magnetic domain and more precisely in the correct calculus of the magnetic induction in the airgap. That is for a double reason: first, the airgap is the region where most of the energy is magnetically stored during its conversion between electrical and mechanical domains; and second, the airgap magnetic induction is the most critical parameter which

establishes the flux density in the stator core and, thus, PMSM performance and ferromagnetic core saturations [Makni 2007].

One of the major contributions in the airgap magnetic induction estimation was done by [Zhu 1993-a] which solved Maxwell equations in a simplified problem, modelling the PMSM as three concentric cylinders: the rotor, the magnet annulus and the stator (see Figure 2.6). In this way, the magnetic induction in both, the magnets and the airgap was calculated as a closed analytical solution for a slotless PMSM.

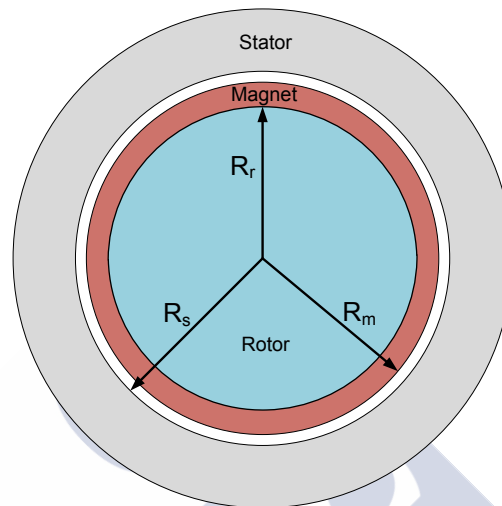


Figure 2.6. Geometry simplification done in order to obtain airgap flux density.

Another major concern about airgap magnetic induction calculus is the accurate modelling of the stator slotting effect. Two different approaches can be found in the literature, both based on the concept of relative permeance.

Carter's coefficient theory is the backbone of the relative permeance concept; it is based on the fact that the magnetic flux has a lower reluctance path under the teeth than under the slots. Hence, it can be established that the equivalent airgap is higher in the circumferential points where the rotor faces a slot. Thus, an equivalent relative permeance θ -function can be defined, where θ represents the angular coordinate [Hanselman 2012, Pyrhönen 2012]. This theory will be further explained in Chapter 3.

The basic Carter's theory is unable to characterize some important aspects of the slotting effect, such as the higher magnetic induction at both sides of a slot opening. Those induction peaks appear because of the accumulation of electric charges in the teeth ends (i.e. the fringe effect). In order to model it a conformal transformation can be used; one of the most complete explanations of this approach applied to a PMSM is found in [Zarko 2006], but many other studies also apply this mathematical technique [Proca 2003].

The conformal transformation method has high accuracy but it is very time consuming as far as some of the required equations do not have a closed form solution and hence must be solved applying numerical methods, such as Newton-Raphson algorithm.

2.2.1.2 Magnetic Forces and Cogging Torque

During the conversion of electric energy into mechanical one or vice versa many parasitic effects may occur. As a consequence, not only the rotor magnets experience a force which causes torque and, therefore, the desired motion but a lot of additional and undesired forces arise both in the rotor and in the stator. Moreover, it has been calculated that the radial forces over the stator are an order of magnitude higher than those causing the motion (the tangential ones) [Weidong 2007].

The estimation methods used in order to calculate and minimize the problems caused by these effects will be further developed in Chapter 3. In this section the causes and main implications will be summarized.

The most important parasitic forces are the stator ones, both in the radial and in the tangential directions. Rotor forces are usually neglected because their enclosure greatly limits the undesired vibrations and noise that they can produce.

The parasitic tangential force component generates the so called cogging torque. As it was previously introduced, the cogging torque is caused by the interaction between the magnets and the slots, as far as the magnets try to align themselves with the maximum amount of ferromagnetic material, i.e. they seek the flux path with least reluctance.

In other words, when a magnet is “leaving” a slot it experiences a positive torque in the direction of the motion, as far as the magnet is decreasing its reluctance path. On the contrary, if a magnet is “entering” into a slot it undergoes a negative torque (opposite to the motion direction) because it is increasing its reluctance path, (see Figure 2.7). It is important to notice two important features of the torque ripple: the first one is that it has a null average and the second that it will exist as far as the PMSM is rotating, even if there is no load and no currents, because it is a consequence of the interaction of the stator and the magnets.

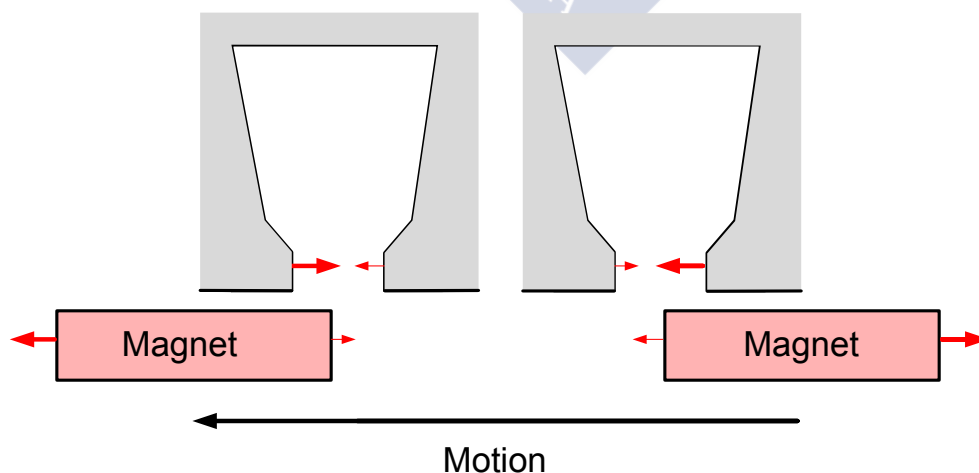


Figure 2.7. Interaction forces between slots and magnets. The forces acting on the magnets cause the cogging torque.

In spite of the null average of the cogging torque, it greatly contributes to the total torque ripple and in many applications severe limits to that ripple are established.

The estimation of the cogging torque can be performed as that of any other magnetic force. There are two ways in order to do so: the virtual work method, based on the principle of energy and co-energy [Lu 2006] and the Maxwell stress tensor method [Zhu 1992, Zarko 2008]. Both principles have similar results. For the sake of simplicity, the second method will be adopted. In this case the total force on a tooth face is estimated as [Almendoz 2008]:

$$f_t = L_e R_s \int_0^{\alpha_0/2} \frac{(B_g^m(\theta))^2}{2\mu_0} d\theta, \quad (2.5)$$

where f_t is the total force on a tooth face, B_g^m the airgap flux density due to the magnets, μ_0 the void permeability, L_e the effective PMSM length, R_s the internal stator radius see Figure 2.6), α_0 the slot opening angle and θ the tangential coordinate. The calculated force is normal and outgoing from the tooth face.

By means of the second Newton law, the cogging torque generated by a single slot (taking into account the two faces of the slot opening) is

$$T_{cs} = L_e R_s^2 \left(\int_0^{\alpha_0/2} \frac{(B_g^m(\theta))^2}{2\mu_0} d\theta - \int_{-\alpha_0/2}^0 \frac{(B_g^m(\theta))^2}{2\mu_0} d\theta \right) \quad (2.6)$$

where T_{cs} is the cogging torque measured in the motion direction.

Another major issue is the normal force applied on the stator teeth, caused by the magnets attraction on the stator core ferromagnetic material. That force can be calculated using the Maxwell stress tensor [Timar 1989]:

$$P_M(\theta) = \frac{(B_g^m(\theta))^2}{2\mu_0} \quad (2.7)$$

where $P_M(\theta)$ is the Maxwell force density as a function of the tangential coordinate.

The mentioned forces are the main cause of the external stator surface radial vibration, which moves the air and emits unpleasant sound. The vibration, and thus the noise, is especially high if the spatial and temporal force frequencies are equal to the natural frequencies of the structure, called resonance frequencies.

Reduction of noise emission is an important goal in many applications, such as elevation, railway traction or electric vehicle, as far as the PMSM is in close contact with passengers, and a silent machine is necessary in terms of final users comfort.

The main component of the exposed force density has a temporal frequency equal to twice the electrical frequency (i.e. $2f_e$) and a spatial frequency (or mode) of p/π (the so called $2p$ mode), where p is the number of rotor poles (i.e. magnets). However, the most important components in terms of noise emission are caused by lower

modes produced by the interaction of the magnet poles and the stator slots [Zhu 2010, Besnerais 2015]. An example of a 6th force mode is shown in Figure 2.8.

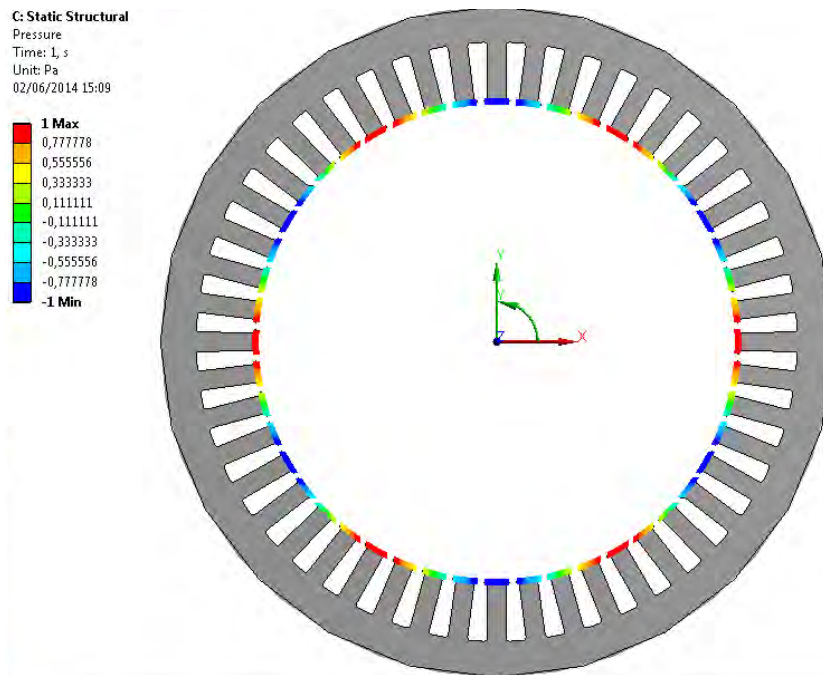


Figure 2.8. 6th force mode on the stator. This is the fundamental mode induced by the magnets if $p=3$.

Many studies have been carried out in order to make the best choice regarding the number of poles (p) / number of slots (Q) in order to achieve a noiseless machine by means of a correct selection [Besnerais 2009, Verez 2015].

Another important problem caused by the stator radial forces is their possible unbalanced distribution, i.e. the total force tries to move the complete stator, which is kept at rest due to the shaft. This force is associated with the first mode and causes a bending deformation (see Figure 2.9). Its effect on a PMSM is especially harmful and should be minimized as far as possible [Islam 2009, Hofmann 2014].

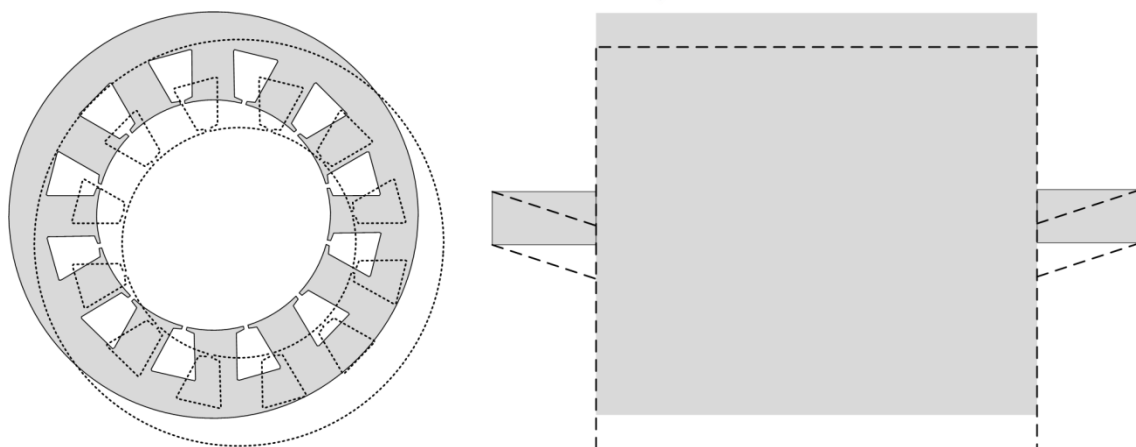


Figure 2.9. Deformation caused by an unbalanced force distribution.

2.2.1.3 Rotor Losses

One of the many advantages of PMSM topology is that the fundamental spatial component of the armature reaction (the magnetic induction generated by the stator coils) rotates in synchronism with the rotor which implies that rotor iron losses are negligible compared with the stator ones. The reason for this effect is that the rotor eddy current losses are proportional to the square temporal derivative of the magnetic induction (this can be shown by using Faraday's law and a constitutive equation).

However, the presence of stator slotting and the spatial and temporal harmonic in armature reaction yields to induction components that rotate at different speeds and are reflected in the rotor with non-null frequency, causing losses that are especially important in the case of high speed and fractional slot machines (machines where the number of slots divided by the number of pole pairs and by the number of phases is not an integer) [Nipp 1999, Ishak 2005].

Among rotor losses, eddy currents are especially relevant in NdFeB magnets which present a moderate conductivity [Pyrhönen 2012]. Although these losses are usually negligible in terms of efficiency, they are of great importance because of their contribution to the magnet heating and the difficulties to evacuate heat through the airgap; in most severe cases they produce magnet demagnetization [Wu 2012]. For the aforementioned reasons the analytical correct estimation of PMSM magnet losses is an important topic that has generated several publications in the last years.

First studies deal with the problem of estimating the losses in a simple manner, supposing the induction on the magnets is spatially constant and introducing formulas to extend a 2D-approximation into a 3D one [Nipp 1999]. Nowadays, some papers propose new methods to estimate 3D eddy currents from 2D analytic methods [Ruoho 2009, Bettayeb 2010, Fadriansyah 2012], and others are centred in the 2D calculus of armature reaction harmonics, both in resistance limited problems (without noticeable skin effect) [Atallah 2000, Ishak 2005, Ede 2007, Wu 2012] and skin limited problems which involve high frequency harmonics in the armature reaction, typically caused by PWM supply [Zhu 2004, Markovic 2007]. Though the difficulties in order to experimentally measured magnet losses, recently some indirect approaches were proposed [Malloy 2015].

Traditionally, induction harmonics causing eddy current losses in the rotor are divided into two groups: permeance harmonics, caused by the stator slotting, and winding harmonics caused by the armature reaction [Pyrhönen 2012]. In turn, the latter are divided into temporal and spatial ones. Usually, the losses due to each group are calculated separately and some of them, especially the permeance ones, are neglected. Since magnet losses are a non-linear phenomenon in its nature, these superposition techniques could yield to large errors [Tessarolo 2012].

In this thesis, a complete, straightforward and analytical model based on Fourier temporal and spatial series, which integrates all the losses in a single formula will be

presented in Chapter 4, allowing for a simple and accurate way to estimate magnet losses.

2.2.2 Thermal Model

A proper thermal modelling of the PMSM is critical because of the great influence of the temperature in the machine performance and operation life. Especially, an accurate estimation of magnets and winding heating is of capital importance. Heating the magnets over their Curie temperature will cause their permanent demagnetization and an excessive temperature in the stator coils can damage their insulation, leading to a remarkable reduction of the PMSM operation life [Kral 2014]. To be more specific, it is estimated that every ten degrees over the insulation class temperature the life time is halved.

Due to the aforementioned reasons the classical empirical rules based on some key parameters, like maximum current density in the coils, are inadequate for high-profile designs and complete thermal models should be used, especially when the machine total size or its efficiency must be optimized [Nerg 2008].

Nowadays, the electrical machine thermal modelling can be divided into three different approaches: analytical lumped circuits, FEM and computational fluid dynamics (CFD), the last two have some common properties as far as both are numerical methods [Boglietti 2009]. The main properties of the three thermal approaches are listed below.

- **Lumped thermal circuit:** similar to a reluctance grid, a lumped thermal circuit is developed as an analogy of an electric network, where losses are treated as current sources and temperatures as voltages. The concepts of thermal resistance for conduction, convection and radiation process are established. Lumped parameter models have proved to be fast and accurate approaches and they have reached a high reliability level after decades of successful use. Moreover, they can be developed only taken into account geometrical and material features and new designs can be easily carried out once the basic geometry circuit is implemented [Mellor 1991]. As usual in lumped methods, its main disadvantages are the troubles associated with the generation of an accurate initial thermal circuit, as far as some thermal resistances are difficult to know due to geometry and material uncertainties such as the gaps across component interfaces or coolant flows over PMSM surfaces. Most of these parameters must be obtained from direct measurement or designer previous experience.
- **FEM:** the main advantage of FEM is its high accuracy obtaining the heat conduction paths in complex geometries. However, it suffers from the same uncertainties as the lumped circuits, needing experimental measures or rough approximations in order to estimate convection and radiation effects. Moreover, FEM is much more time consuming than a thermal network. For these reasons the role played by FEM techniques is to obtain the equivalent

thermal conduction resistance of complex geometries in order to use these data in a lumped model [Boglietti 2009, Bermúdez 2011].

- **CFD:** computational fluid dynamics is a relative new technique in thermal modelling developed in order to calculate the coolant flow rate, speed and distribution through the different machine surfaces and passages. It is very useful in the estimation of the convection process but it has some important disadvantages, such as its high computing time, the high developer previous experience needed to obtain accurate results, the difficulties in defining a suitable mesh and its relative technical immaturity. In spite of the exposed drawbacks, CFD application is an evident growing trend because of the increasing demand of more compact, higher power density machines with especial coolant necessities. A CFD calculus example is [Dong 2014].

Though the previous classification (presented in [Boglietti 2009]) is quite exhaustive, a few authors still using analytical methods based on a direct solving of heat differential equations [Grobler 2015].

As it was exposed, lumped-parameter thermal models suppose a reliable, effective and short-time consuming thermal approach whose accuracy, in most cases, will be enough to estimate the temperature at the critical points of the electrical machine.

Thermal network modelling was a common practice even before the advent of computers, when some designers developed simple thermal circuits in order to obtain a rough approximation of the temperature rise in some critical machine parts, namely, the windings [Boglietti 2009].

In more recent dates some authors have begun to implement new thermal network models representing the machine geometrical paths through which the heat flows. These studies started with the application in a machine thermal analysis of the heat equation in both, the axial and radial directions of a cylinder (see [Pérez 1979]). Based on this work Mellor et al. developed one of the first thermal networks calculated using a computer, its circuitual representation is shown in Figure 2.10 (a) [Mellor 1991]. Since then many other authors have tried, with good results, a small thermal-network as a suitable compromise between computation speed and accuracy [Kylander 1995, Lindström 1999].

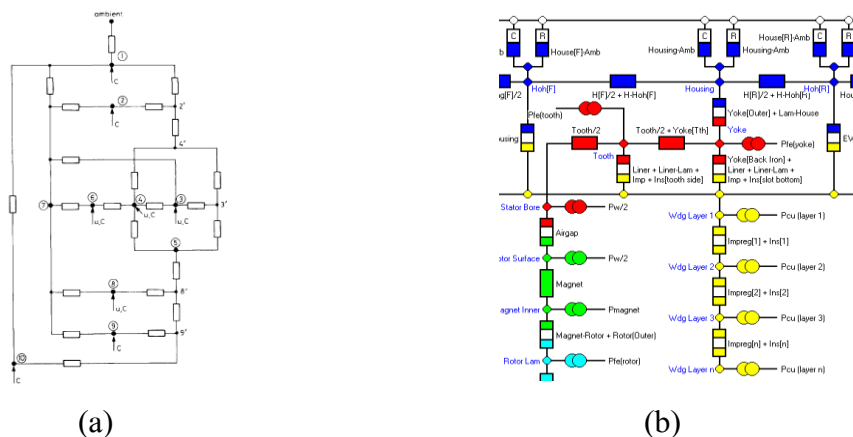


Figure 2.10. SPMSM lumped thermal networks. (a) [Mellor 1991], (b) Motor-CAD®.

The small thermal-networks developed in the nineties are still used, becoming one of the most popular methods to estimate the temperature rising in the machine during the design stage. Numerous PMSM thermal models use slight variations of the thermal circuits developed by the aforementioned authors [Hafner 2008, Vese 2010, Jannot 2011, Bracikowski 2012, Kral 2014].

Nowadays, improvements to these classical approaches are still developed, but the basis of the theory and the main contributions in the modelling of most of the known machine topologies are well established in the literature, as it is proved by the existence of very accurate lumped parameter commercial programs, with a lot of machine topologies implemented and the empirical parameters well-known through years of experimentation. One of the most popular of these software packages is Motor-CAD®; one of its equivalent circuit networks is shown in Figure 2.10 (b).

In the last years, the literature about PMSM lumped thermal models has been devoted to the study of particular aspects, such as the cooling effect of oil or water jackets [Zhang 2015], the thermal influence of the magnets position in an IPMSM [El-Refaire 2004], the particularities of high speed operation [Saari 1998, Dong 2014] or the determination of critical parameters that are usually very difficult to estimate without experimental measures [Boglietti 2008].

2.2.3 Vibro-acoustic Model

Noise has become a major factor in the ambient quality, so a lot of laws and standards have been written in order to limit the total amount of noise to a safe and comfortable level [ISO 2003]. This is not surprising, as far as nowadays there is a high consciousness about the need to keep a non-polluted environment and noise can become an important part of ambient pollution.

This is especially true in an urban context, where people live in close contact with noisy machinery that has greatly increased its presence during the last decades. Among these machinery are the electrical machines like the PMSM, whose application in railway traction, in hybrid and electric vehicles (EV) or in elevators implies that a careful vibratory and acoustical design must be performed in order to avoid passengers and residents annoyance.

Vibro-acoustic modelling is traditionally neglected during the design process and noise problems are only treated like an afterthought, if needed. For the aforementioned reasons this classical approach is no longer efficient and desirable in many applications.

Sound emitted by electrical machines has different sources that are classified by classical literature in the next three types [Timar 1989, Gieras 2006]:

- **Magnetic source:** directly caused by the magnetic field on the machine materials. The Maxwell forces on the ferromagnetic cores and the magnetostriction effects are included in this group.
- **Mechanical source:** associated with the mechanical assembly and mechanical energy transmission, the generated noise is mainly due to bearings, sliding contacts, gears, etc.
- **Aerodynamic source:** noise related to the air flow in the machine. It is mainly caused by the airstream produced by the cooling fan flowing through the machine surface fins or structure vent holes.

Figure 2.11 graphically shows this classification and the acoustic energy propagation process.

The previous sources can generate air-born sound or structure-born sound, more precisely mechanical and magnetic noise sources produce vibrations that, through the housing, propagate their energy into the air, causing noise.

The magnetic noise plays a major role in many PMSM, especially for low and medium-power designs, whereas aerodynamic noise is the main contribution to the total sound in high-power machines cooled by air requiring large fans and multiple vent conducts. In most cases, mechanical sound sources are negligible compared with the magnetic and aerodynamic ones and usually they are not taken into account [Besnerais 2008].

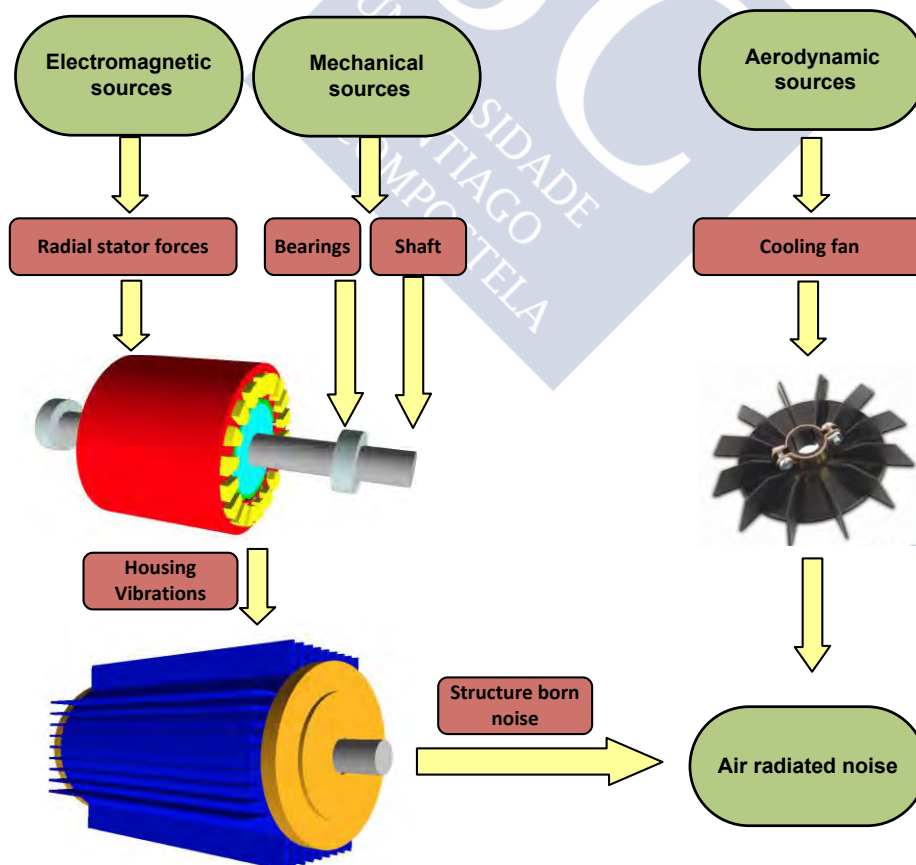


Figure 2.11. Noise sources and sound propagation in electrical machines.

Most studies deal with the electromagnetic noise, especially with the sound generated by the Maxwell forces on the stator, as far as this noise is one of the most intense and annoying in electrical machines; so its study is of great practical interest.

This thesis deals with the electromagnetic noise caused by Maxwell forces whose genesis process is summarized in Figure 2.12.

The complete acoustic study can be divided into different parts: the first one corresponds to the electromagnetic force calculus, the second one to the structural natural vibration modes (i.e. the specific vibration patterns and frequencies more easily induced into the structure due to its mass and stiffness) and the third one to the vibratory and acoustic behaviour of the structure due to the applied forces [Zuo 2015].

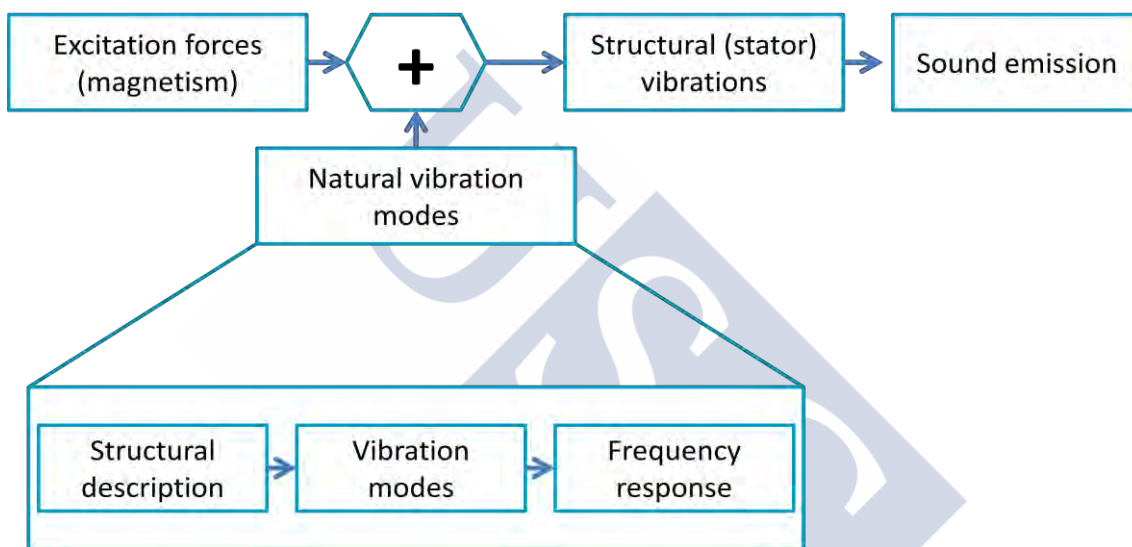


Figure 2.12. Electromagnetic sound genesis in electrical machines.

Both, natural vibration modes and stator vibration and sound response can be calculated by means of numerical methods (FEM and BEM) or analytically. In principle, it is also possible to develop lumped models but this approach is rarely found in the literature devoted to this subject.

The advantages and drawbacks of numerical methods are the same as those listed for electromagnetic and thermal models: they are much more accurate than analytic ones but they are very time consuming and require a complete knowledge not only of the machine dimensions but also of the stator-housing interface, the house fins and anchoring points of the structure. Much of this information is not available during the design stage process and the accuracy of numerical methods decreases dramatically.

Analytical vibratory and acoustic models show low accuracy, especially compared with analytical electromagnetic and even thermal ones. However, they have the advantage of fast calculus and they are capable of correctly estimating the main vibration frequencies emitted by the machine and to establish a good comparison between candidate designs.

As it was introduced, a natural vibration mode is a specific spatial oscillation pattern; in radial machines the most important ones are the radial modes which present a sinusoidal θ dependence, e.g. the second radial mode is associated with a spatial displacement $k(t) \sin(2\theta)$, where t is the time and $k(t)$ is a parameter depending on the magnitude and frequency of the excitation forces and the stator structural features. Examples of different modes are shown in Figure 2.13.

It is important to notice that every spatial mode has an associated natural frequency, defined as the excitation force frequency which generate an infinite displacement (i.e. $k(t)|_{\max} \rightarrow \infty$) in absence of damping. In real machines, where the deformation is usually of some μm , the damping limits the vibration amplitude. In spite of this fact, the natural frequencies are especially dangerous because a modal force with a frequency close to a natural frequency will cause a resonance and the vibrations and the sound would be very high.

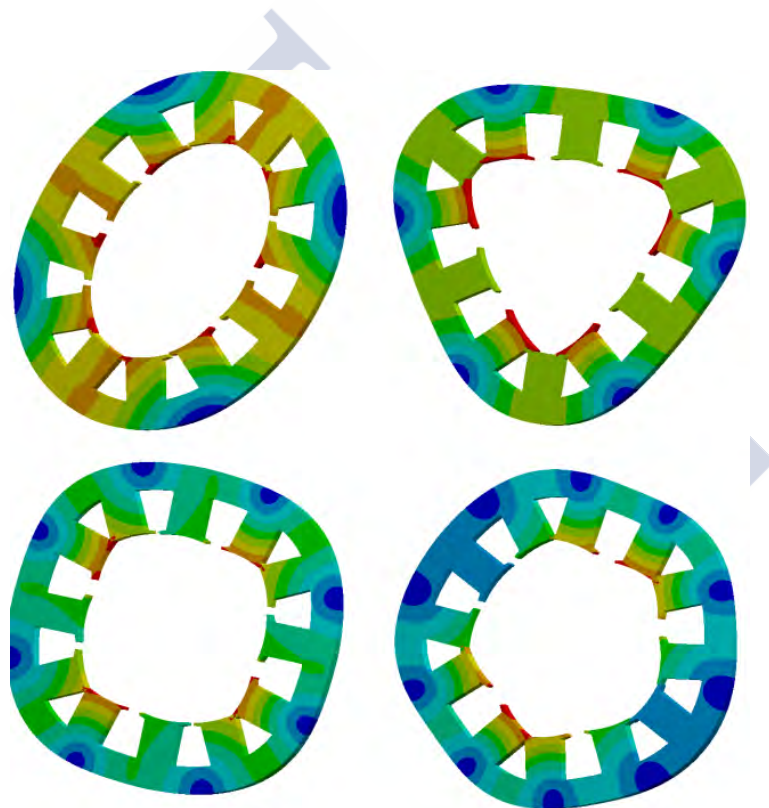


Figure 2.13. 2nd to 5th stator radial modes calculated with ANSYS®. Deflections have been scaled for visual purposes.

Thus, once the structural modes and its natural frequencies are obtained, the excitation forces will be expressed in a mathematical basis conformed by the structural vibration modes. The stator will be treated as a linear system where the forces are the inputs and the displacements (vibrations) the outputs.

Finally, a radiation factor is estimated and the sound power radiated at each frequency is calculated from the surface vibrations (see Figure 2.12).

In the last decades, a lot of effort has been done in order to establish a reliable and accurate method for the estimation of stator natural vibration modes and static displacements (maximum displacement of the structure when a force of the mode corresponding to a frequency of 0 Hz is applied).

During the twenties, first analytical models of a stator were developed and natural frequencies were calculated approximating the stator by a thin ring. In 1950 Jordan published its work, applying the same thin ring approximation but adding the effects of shear, teeth and winding to the model [Jordan 1950]. Jordan's study is still a capital reference and, in the last sixty years, only little advances were done in the analytical calculus of stator natural frequencies.

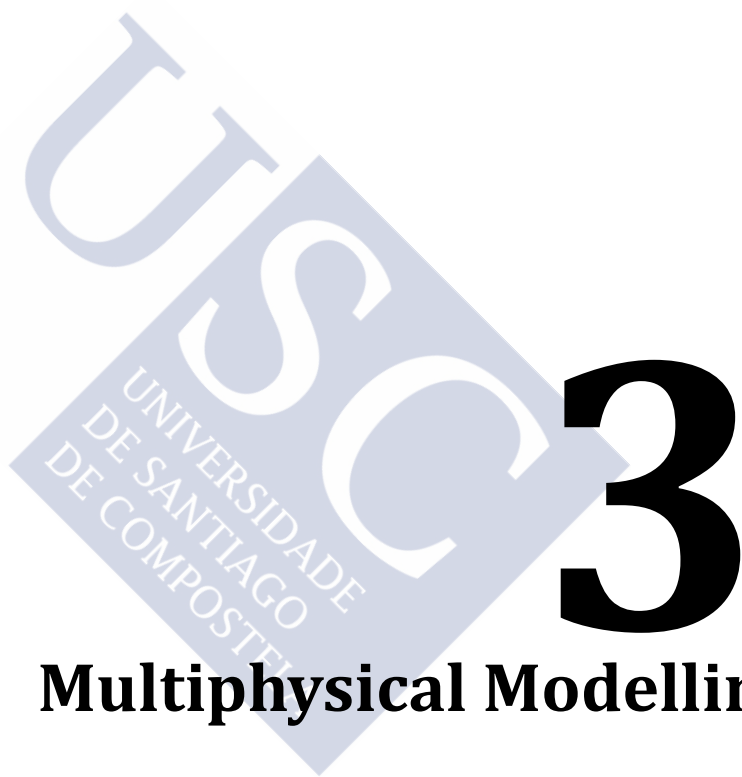
In 1979 Girgis and Verma studied and measured the practical effects that teeth and windings have over the thin ring approach [Girgis 1979] concluding that Jordan analytical approximations reasonably match the experimental results. Another two classical books about the subject [Yang 1981, Timar 1989] rewrite Jordan results adding an additional factor that takes into account the effects of the teeth and winding in rotating inertia and establish the usual form in which these equations can be found in actual literature. A complete review about noise in electric machines [Vijayraghavan 1999] still references Jordan's work equations as the most accurate ones and many recent authors use them with minor modifications [Anwar 2000, Schlensook 2008, Islam 2010, Besnerais 2010, Fiedler 2012, Islam 2014]. Moreover [Weilharter 2012] compares his analytical results with those calculated by Jordan sixty-two years before.

Other approaches developed in the last years calculate the mode features from the estimation of kinetic and potential energies during vibration process [Ishibashi 2003] or estimate the stator vibratory behaviour from its linear properties, obtaining its impulse response from both FEM or experimental measurements [Van der Giet 2010, Torregrossa 2012].

Nowadays, the research efforts seem to be centred in the correct calculus of Maxwell forces from airgap flux density values, especially in cases where these forces are rich in the frequency domain due to both spatial harmonics, caused by winding distribution [Zhu 2010], and temporal harmonics, caused by Pulse Width Modulation (PWM) or control strategies [Besnerais 2010].

[Gieras 2006] offers a complete study that includes most of the recent developments in the calculus of noise emitted by electric machines, including force estimation and aerodynamic and mechanical sources effects.

As far as Jordan's results have proved to have enough accuracy for low order modes during decades of use, and due to its easy implementation and low computing time this approach is adopted in the present thesis.



Multiphysical Modelling



3.1 Introduction

The main goal of this chapter is to present an analytic model allowing a fast and accurate characterization of PMSM behaviour, taking into account its electric, magnetic, thermal and vibro-acoustic features.

As it was aforementioned, the model is fully analytical and based on Fourier series, being its main advantages its fastness, modularity and the easiness of integration between different modelling blocks and with an external optimization algorithm. The different modules and their main interactions will be explained.

In order to achieve a correct understanding of the aforementioned physical domains some considerations about PMSM geometry and their winding layout should be taken into account. Therefore, the present introduction is devoted to them.

3.1.1 SPMSM Geometry

It can be said that all the PMSM features are established by three factors: the used materials, the winding layout and the machine geometry. In this section the main geometrical variables will be introduced and their major implications briefly explained.

It is worthwhile to notice that SPMSM geometry plays a major role in magnetic, electric, thermal and vibro-acoustic behaviour. Figure 1.14 shows the main geometry variables, it is repeated below for the shake of clearness.

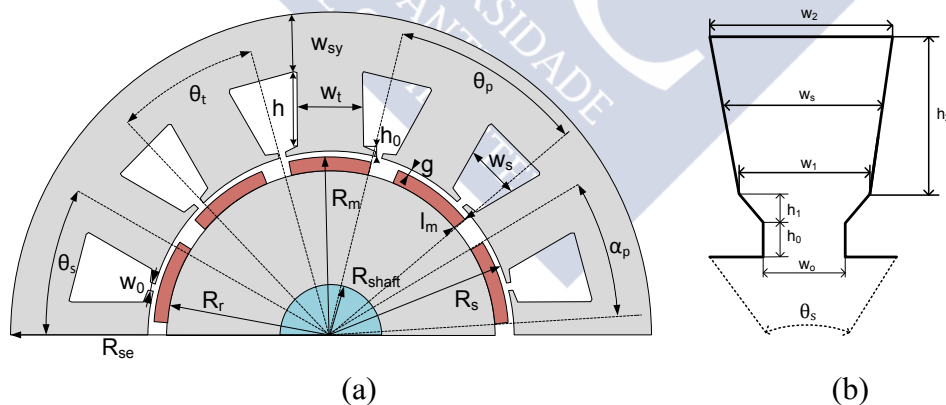


Figure 3.1. (a) Main dimensions of the SPMSM and (b) detail of a slot.

During the present section the variables showed in Figure 3.1 will be listed and introduced. They will be divided in four categories: general, rotor, stator and slot variables.

General variables: They are the “configuration variables” *number of slots* (Q) and *number of pole pairs* (p). A concrete configuration (i.e. a chosen Q and p values) determines the electromagnetic behaviour of the PMSM and, indirectly, the inputs of the thermal (i.e. electromagnetic losses) and vibratory (i.e. magnetic pressures and

forces) models. Therefore, the influence of Q and p is critical in all the studied domains. Moreover, they have such high importance that a concrete machine will be denoted $Q_x p_y$, where x is its number of slots and y its number of pole pairs.

Another important variable is *the effective length* (L_e) which is the axial length of effective core material both, in the stator and in the rotor. It mainly determines the amount of machine power.

Rotor dimensions: The rotor geometry configures most of the machine equivalent magnetic circuit, so it has a great influence over the PMSM magnetic features. It also plays an important role in heat transmission and in the magnetic forces acting over the stator and, through them, over the vibro-acoustic process.

The main rotor geometrical variables are listed below.

- *Shaft radius* (R_{shaft}).
- *Magnet radius* (R_m).
- *External rotor radius* (R_r).
- *Magnets high* (l_m).
- *Airgap length* (g).
- *Magnet pitch* (α_p): Angular distance covered by a magnet, it can be measured both in radians and in meters.
- *Pole pitch* (θ_p): Angular distance covered by a single pole, it can be measured both in radians (π/p rad) and in meters.

Stator geometry: The stator and the winding layout determine the electrical behaviour and, through the armature reaction (i.e. the magnetic field caused by the coil currents), they have an important influence in the PMSM magnetic properties. Stator geometry also has a great relevance in both, the thermal features and in the vibro-acoustic characteristics, because it is the interface between the machine internal parts and the outside world.

From the thermal point of view, most of the losses (both copper and iron ones) are produced in the stator. Moreover, almost all the heat generated crosses through the stator and is evacuated by its external surface.

On the other hand, from the vibro-acoustic perspective the forces are directly exerted in the interior surface of the stator teeth, and stator mass and stiffness fully determines the structural behaviour within the vibratory process.

As a rough simplification, it can be said that the electric, thermal and vibro-acoustic domains are primarily ruled by the stator geometry, while the magnetic physics is mostly governed by the rotor one. By the way, the slots dimensions mainly have an influence over parasite effects. Taking this into account it is not surprising that many of the critical design variables are related with the stator and their windings configuration and geometry.

The main stator geometrical variables are listed below.

- *Internal stator radius* (R_s).
- *External stator radius* (R_{se}).
- *Teeth height* (h).
- *Teeth width* (w_t).
- *Airgap length* (g).
- *Yoke thickness* (w_{sy}).
- *Tooth arch* (θ_t): Angular length covered by a single tooth (including its shoes), it is measured in radians.
- *Slot pitch* (θ_s): Angular distance between two consecutive tooth central points, it can be measured both in radians ($2\pi/Q$ rad) and in meters.

Slotting features: Though the slotting can be seen as a stator “component”, the slots specifically produce and affect over many parasite magnetic and electrical phenomena, so it is worthwhile to consider their geometry independently.

Specifically, slots dimensions play a major role in electrical losses and, through them, in the thermal behaviour, especially in such critical magnitude as winding temperature.

Other critical effect is caused by the slots opening; it is the reduction of the magnetic flux due to the minor flux density under this region. Therefore, slots openings geometry directly affect the PMSM generated voltage and its efficiency and performance.

The main slotting geometrical variables are listed below.

- *Slot height* (h_2).
- *Mean slot width* (w_s).
- *Minimum slot width* (w_2).
- *Maximum slot width* (w_1).
- *Slot opening* (w_0): It can be measured both, in radians and in meters.
- *Tooth-tip height* (h_0).
- *Slot enlargement height* (h_1).

3.1.2 Electrical and Mechanical variables

The concepts of “electrical” and “mechanical” frequencies and its associated variables (i.e. period and angular frequency) are fully established in rotating electrical machines bibliography.

On the one hand, the mechanical period, T_m is the interval of time that the machine inverts in perform a complete turn, i.e. the rotational motion has a frequency $f_m = 1/T_m$ and an angular speed equal to $\omega_m = 2\pi/T_m$.

On the other hand, the electrical frequency f_e is defined as the main harmonic frequency of the electrical variables (e.g. the machine current and voltage frequency).

Obviously, an electrical period $T_e = 1/f_e$ and an electrical angular frequency $\omega_e = 2\pi f_e$ could also be defined.

The relation between the electrical and the mechanical variables is simple and it is established through the machine number of pole pairs, p . Mathematically,

$$f_e = pf_m \quad (3.1)$$

This relation is a direct consequence of the spatial magnets periodicity (equal to $2\pi/p$) which imposes the electrical variables frequency. In other words, if the machine is rotating at fixed frequency f_m and the rotor physical variables has a known spatial periodicity $2\pi/p$ the temporal periodicity of any event for an observer situated in a fixed reference frame (e.g., the stator) is equal to $p/f_m = pT_m$ which is exactly the T_e definition.

This relation imposes that, in order to obtain an equilibrated multiphase system it is necessary winding the stator with a known spatial phase delay between phases equal to $2\pi/(pm)$ radians. It is recalled that m is the number of phases. By far, the most common machines have $m=3$.

In this thesis, in order to avoid ambiguities, frequencies and periods are always identified by the correspond subscript (either e or m). The only exception is angle θ that is always referred to the machine angular displacement (i.e. it is equivalent to θ_m). If an angular electrical variable is used it will be denoted by θ_e .

3.1.3 Winding Layout: the Star of Slots

A PMSM is made up of multiple coils and magnets in close relation with each other through a complex magnetic circuit (namely, the airgap, and the rotor and stator cores). Therefore, as it was previously introduced, in this context it is critical to know how the different coils are wound in the stator slots. This distribution is called “the winding layout” and it mainly depends of the number of phases, poles and slots. There exist several methods intended to obtain a suitable winding layout design which establishes the coils wound in the available stator slotting. Therefore, in order to generate an efficient torque, the phases which are wound in each slot must be chosen, ensuring the design feasibility and a balanced winding spatial distribution.

In technical literature different types of winding layouts are presented:

- As a function of the number of layers (phases wound) in each slot:
 - Single layer winding: when in a slot only one coil is wound.
 - Double layer winding: when in a slot two coils are wound. In a general way, these coils are part of any phase and are wound in any direction.
- As a function of the number of slots per phase per pole:

- Integral slot machines: when the number of slots per phase per pole pair is an integer, i.e. the stator is wound with the same number of spatial periods that pole pairs in the rotor.
- Fractional slot machines: when the number of slots per phase per pole pair is a fraction, so the stator is possibly wound with a number of spatial periods different of the number of pole pairs in the rotor.
- As a function of the winding distribution:
 - Concentrated windings: the coils are wound in consecutive slots, minimizing the end-winding and, thus, the copper losses.
 - Distributed windings: the coils are wound in the most suitable slots in order to obtain the maximum electromotive force (EMF), i.e. the maximum induced voltage.

In a distributed winding layout the main goal is to place the coils having a span such as their pole pitches are as near to 180 electric radians as possible and their midpoints are out of phase 0 electric radians in order to ensure a maximum phase EMF (i.e. place the windings in order to sum in phase their induced voltages). In some simple machines the distribution can be obvious but, in a general manner, the selection of a good winding layout could be a difficult task.

Despite the fact that there are different methods that allow to fulfil the previous goal, in this work one of the most popular of them, the star of slots [Bianchi 2006, Almandoz 2008], is implemented.

The star of slots is a generic method based on a graphical representation of the flux phase in each slot. One of its main advantages is that it is used to design automatically any kind of distributed winding, fractional or integral slot machine, single or double layer, in a straightforward way. A brief description of the method is exposed below.

A parameter q is defined as the number of stator slots per pole and per phase

$$q = \frac{Q}{2pm}, \quad (3.2)$$

where m , p and Q are the number of phases, pole pairs and slots, respectively.

Another important variable is t_p , the winding periodicity: number of the machine periods in the circumferential coordinate. Mathematically, it is defined as the greatest common divisor between Q and p .

$$t_p = \text{GCD}\{Q, p\} \quad (3.3)$$

In the case of an integral slot machine $t_p = p$, but, in a fractional machine, q is a fraction and the winding periodicity could be different from the number of pole pairs. In fact, the number of pole pairs in a winding periodicity (p') is defined as

$$p' = p/t_p \quad (3.4)$$

In a similar way, Q' is the number of slots within a winding periodicity. Obviously, Q' must be multiple of the number of phases (m), otherwise the winding is not feasible.

$$Q' = Q/t_p \quad (3.5)$$

Two consecutive slots are out of phase between them a number of electric radians

$$\alpha_z = \frac{2\pi p'}{Q'}. \quad (3.6)$$

The first step to perform the winding layout is to plot a star of slots with Q' vectors equally spaced. Obviously, the geometrical angle between them will be equal to

$$\alpha_n = \frac{2\pi}{Q'}. \quad (3.7)$$

These vectors are numerated from 1 to Q' . One of them is chosen as the initial one and then the others are enumerated considering a constant pitch equal to α_z . This number determines the physical slot associated with the selected vector. For example, if the second vector of the star is numerated as eight that means that its physical slot is the 8th within a machine periodicity (see Figure 3.2).

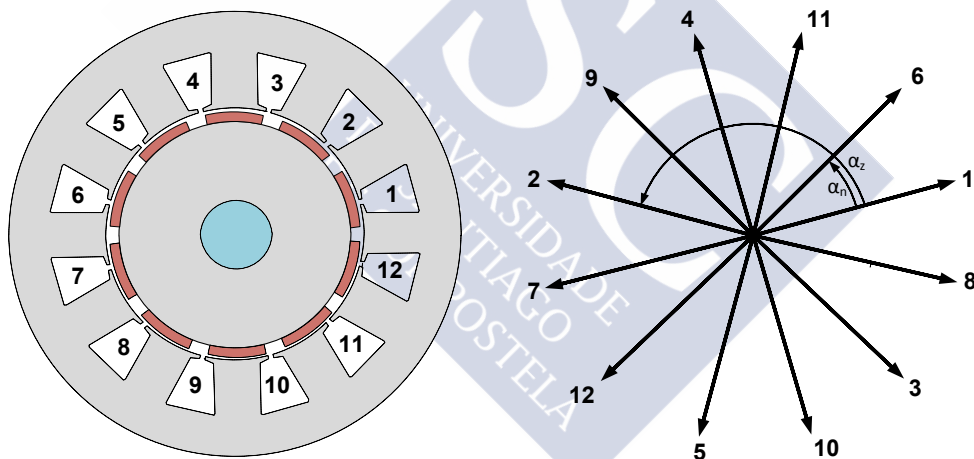


Figure 3.2. Equivalence between a stator slotting and its star of slots.

As it was introduced, the winding layout could be single or double layer. If Q'/m ratio is even a single layer winding is performed. The coils are placed beginning at the first vector and following a fixed sequence. In a three-phase machine, the sequence will be A+C-B+A-C+B-. It must be taken into account that coils of the same phase and direction, if they exist, are emplaced in consecutive vectors.

For example, if $Q'=12$ and $m=3$, four slots are assigned to each phase within a machine periodicity. Therefore, the assignation sequence will be A+A-C-C-B+B-A-A-C+C-B-B-.

If Q'/m ratio is odd, a double layer coil distribution is required in order to obtain a feasible winding. The procedure is almost the same as in the single layer case, but two

“rounds” are needed because there are two coils in each slot. In the first round an extra inward coil is wound in each phase, while in the second an extra outward coil is emplaced.

For example, if $Q'=9$ and $m=3$ in the first layer of the winding the sequence will be: A+A+C-B+B+A-C+C+B-, while in the second it will be A+C-C-B+A-A-C+B-B-. Thus, two coils are assigned to each vector.

Once the coils are associated with the vectors, the relation among them and their physical slots is used for a proper winding layout. That is, if the 12th vector is numbered as 12th and contains an A+ coil and a C- coil that means that the 12th real slot is wounded with an A+ and a C- coils. Figure 3.3 shows the final winding layouts for two examples.

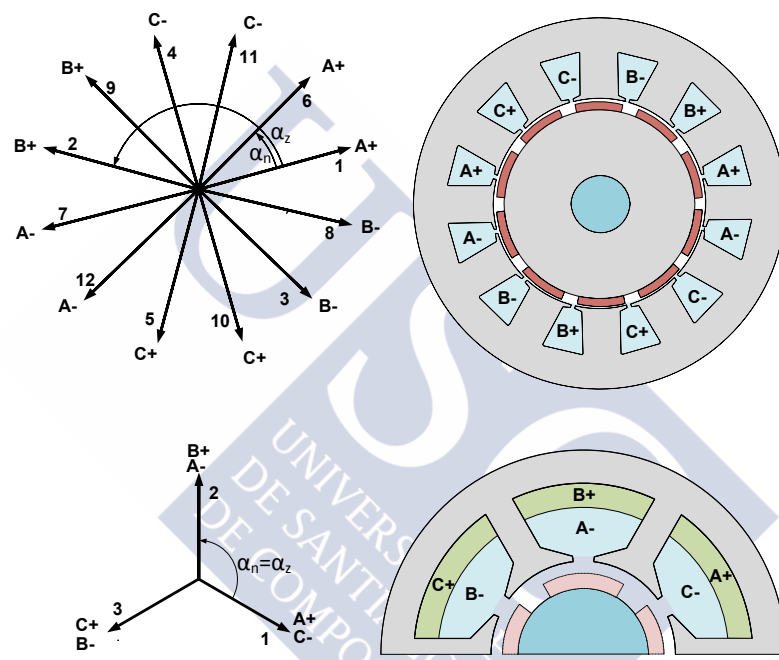


Figure 3.3. Star of slots method applied to two examples. Top: a single layer winding (Q12p5) and bottom: a double layer layout (Q6p2).

A program which implements the star of slot method has been developed. It is important that any kind of feasible stator winding can be performed by the proposed winding method, because both, the star of slots and the routine implemented, are completely generic.

A final remark in order to understand the winding layout, is that there exists some controversy in order to correctly refer to the winding distributions and terms such as “winding”, “layer”, “coils” or “turns” are frequently used indistinctly. In this thesis and from this point forward, the precise signification of these words will be the following:

- Winding: Generic word referred to all the conductive material (e.g. copper) used in the PMSM; additionally, the conductive material used in a specific phase of the motor, i.e. “a phase winding”.

- Coil: It is the part of a phase winding that links two specific slots, crossing through them. Coils are the individual pieces that conform a phase winding.
- Layer: Number of coils present in a single slot, noted as N_{lay} . In a single layer winding, each slot has just one coil of one determined phase. However, in a double layer winding, each slot has two coils that may belong to different phases.
- Turns: Each coil consist of a set of wires connected in series, i.e. turns. This parameter, noted as Z , is critical because it scales the total amount of armature reaction and the magnetic flux embraced by the coils (i.e. if Z is doubled, the magnets flux embraced by the coils is doubled too and the generated electro-motive forces is twice the original one).

In other words, a phase winding is formed by a number of coils (exactly $QN_{lay}/(2m)$ coils) and every coil has a fixed number of turns Z .

A graphical explanation is shown in Figure 3.4, where three slots with double layer configuration contain a total of three coils, each coil is formed by six turns. Different coils are identified by their colours. In this example each coils belongs to a different phase.

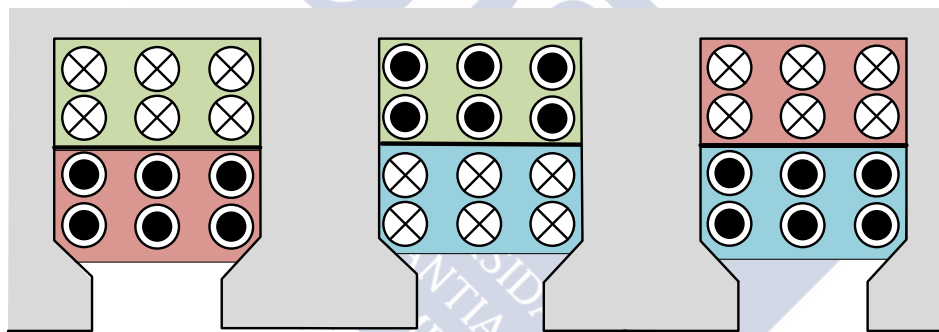


Figure 3.4. Example of a double layer winding layout, three coils with six turns each. Each coil belong to a different phase.

3.2 Magnetic Domain

The objective of the magnetic model is to estimate the magnetic field value in some key parts of the machine (e.g. airgap, stator yoke, stator teeth, etc.) and the physics variables directly related with it such as the electromotive force (EMF) or the cogging torque.

An important feature of most of the variables exposed within this section is their periodicity, which can be spatial, temporal or both. This is a very important issue since it is possible to work with their Fourier Series (FS) coefficients instead of their time domain values. In this work, this approach will be used due to its good features.

Every time a FS is performed it will be clarified whether it is a temporal or a spatial one and, in the second case, which kind of period (electrical period, mechanical period or slot pitch) is taking into account.

3.2.1 Rotor Magnetic Field

In a PMSM, the rotor magnetic field is the most common name for the field created by the rotor magnets in the airgap. A first step in its calculus is to solve the canonical magnetic problem shown in Figure 2.6, where three concentric cylinders are considered: the stator, the magnets and the rotor. Due to the symmetry of the problem it is enough to take into account just a cross-section of the cylinders, simplifying the 3-D formulation into a 2-D one. Moreover, the magnetic field only has radial component which only depends on the tangential coordinate and time.

Thus, neglecting the effect of the stator slotting, the FS of the airgap flux density (i.e. at $r = R_s$) can be obtained [Zhu 1993-a]. It should be highlighted that, since the angular speed of the rotor is considered as a known constant, it is possible to deduce the spatial FS of the magnetic flux density at every instant of time from its FS at $t=0$. More precisely, if

$$B_g^m(\theta, 0) = \sum_{k=-\infty}^{\infty} B_{g,k}^m(0) e^{jkp\theta}, \quad (3.8)$$

then,

$$B_g^m(\theta, t) = B_g^m(\theta - \omega_e t/p, 0) = \sum_{k=-\infty}^{\infty} B_{g,k}^m(0) e^{jk(p\theta - \omega_e t)}, \quad (3.9)$$

where the rotor is supposed to be turning counter clockwise with a constant angular speed $\omega_m = \omega_e/p$. $B_g^m(\theta, t)$ is the rotor magnetic field at the airgap at time "t" and angle "θ". For the sake of simplicity $B_{g,k}^m(0)$ will be denoted as $B_{g,k}^m$. From (3.8) and (3.9) it is concluded that the FS coefficients are the same at any time except for an angular delay. More precisely

$$B_{g,k}^m(t) = B_{g,k}^m e^{-jk\omega_e t}. \quad (3.10)$$

In the simplified problem shown in Figure 2.6, Maxwell equations can be analytically solved [Zhu 1993-a, Hanselman 2012] in order to obtain the FS coefficients $B_{g,k}^m$.

In a general case, the airgap flux density has both, radial and tangential components and it is dependent not only on the tangential coordinate but also on the radial one. In the above simplified model only the radial component is taking into account and the radial dependence will be neglected.

In order to carry out the proposed approximations without significant accuracy loss, the airgap flux density is obtained just on the boundary between the airgap and the

stator ($r = R_s$), where the radius is fixed and the flux density tangential component is close to zero due to the high permeability of the stator core.

If the ferromagnetic material is unsaturated and the stator slotting effect is neglected it can be proved that the FS coefficients of the flux density are given by [Zhu 1993-a]

$$B_{g,k}^m = \frac{2}{\mu_r} B_r K_{r,k} \frac{kp}{kp^2 - 1} R_s^{kp-1} \frac{\Gamma_k}{\Delta_k} \quad (3.11)$$

where

$$\Gamma_k = R_m^{-kp+1} \left((kp - 1)R_m^{2kp} + 2R_r^{kp+1}R_m^{kp-1} - (kp - 1)R_r^{2kp} \right), \quad (3.12)$$

$$\Delta_k = (\mu_r + 1)(R_s^{2kp} - R_r^{2kp}) - (\mu_r - 1) \left(R_m^{2kp} - \left(\frac{R_s R_r}{R_m} \right)^{2kp} \right), \quad (3.13)$$

μ_r is the magnets relative permeability and R_m is the magnets radius (see Figure 2.6).

The previous equations are valid for every k except when $kp = \pm 1$. In fact, equation (3.11) is indeterminate when the fundamental airgap spatial harmonic is calculated in a one pole pair PMSM. To solve this problem, another equation is proposed for this especial case. Thus, when $p = 1$:

$$B_{g,1}^m = \frac{B_r K_{r,1}}{\mu_r} \frac{\left(\frac{R_m}{R_s} \right)^2 - \left(\frac{R_r}{R_s} \right)^2 + 2 \left(\frac{R_r}{R_s} \right)^2 \ln \left(\frac{R_m}{R_r} \right)}{(\mu_r + 1) \left(1 - \left(\frac{R_r}{R_s} \right)^2 \right) - (\mu_r - 1) \left(\left(\frac{R_m}{R_s} \right)^2 - \left(\frac{R_r}{R_m} \right)^2 \right)} \quad (3.14)$$

In expressions (3.11) and (3.14) $K_{r,k}$ are the magnetization vector FS coefficients and thus dependent of the magnets magnetization profile and their geometric position in the rotor. The mathematical expression of most of these magnetization profiles can be found in [Hanselman 2012].

The most common magnetization profiles used in surface magnets PMSM, are the radial and the parallel ones; these cases are implemented in the proposed model. As an example, the mathematical expression in the radial case (see Figure 3.5) is included:

$$K_{r,k} = \begin{cases} \alpha_m \operatorname{sinc}((k\alpha_m\pi)/2) & \text{for } k \text{ odd} \\ 0 & \text{for } k \text{ even} \end{cases} \quad (3.15)$$

where α_m is the fraction of the electrical semi-period covered by the magnet, as it is shown in Figure 3.5, and $\operatorname{sinc}(x) = \sin(x)/x$. It is important to notice that a very low value of α_m supposes an inefficient use of the rotor space but a very large one can lead to an important decrease of the flux linkage, as far as many flux lines cross the space between magnets instead of flowing into the stator through the airgap.

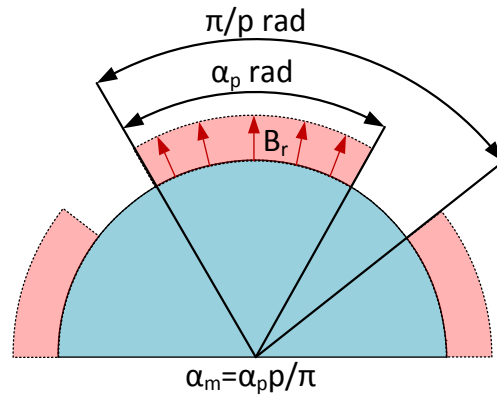


Figure 3.5. Angle covered by a magnet (α_p) with respect to pole pitch. Radial magnetization.

3.2.2 Slotting Effect: Relative Permeance Function

Once the magnetic flux density in the airgap with slotless stator is obtained the next obvious step is to calculate the effect of the slot in its spatial distribution.

Obtaining an analytical solution could be a challenging problem and the use of a numerical algorithm, like FEM, is not desirable as it is very time consuming. Thus, most authors [Zarko 2006, Almandoz 2008, Hanselman 2012] start from the canonical problem solution studied above and define a correction factor $K_{sl}(\theta)$ such that

$$B_{gs}^m(\theta, t) \approx B_g^m(\theta, t) K_{sl}(\theta), \quad (3.16)$$

where B_{gs}^m is the magnet flux density in the airgap with slotting effect, and it is recalled that B_g^m is the canonical problem solution (with slotless stator).

The factor K_{sl} has different names in the literature (slot correction factor in [2012 Hanselman], relative permeance function in [Zarko 2006], etc.). In this work it will be called relative permeance function, since the flux density in the airgap is closely related with its apparent permeance as it will be explained.

A lot of approximations for K_{sl} are proposed but all of them are based on the same idea: under a slot opening the apparent length of the airgap (g) is increased, so the length of the airgap is no longer a constant but a variable which depends on the tangential coordinate θ and has a periodicity of $2\pi/Q$ mechanical radians.

As far as the airgap length is variable the reluctance is no longer a constant, since it is increased under the slots. This higher reluctance supposes less flux density under the slots.

Therefore, $K_{sl}(\theta)$ is the relation between the airgap permeance with slotless stator (\wp_g) and the real permeance taking into account the slotting effect ($\wp_g(\theta)$).

$$K_{sl}(\theta) = \frac{\wp_g(\theta)}{\wp_g} \quad (3.17)$$

The airgap permeance depends on its length and is given by [Hanselman 2012]

$$\wp_g = \mu_0 \frac{A_g}{\delta}, \quad (3.18)$$

where A_g is the cross-sectional area covered by the considered airgap fraction, δ is its effective length, i.e. $\delta = g + l_m/\mu_r$, and μ_0 is the vacuum magnetic permeability.

It is possible to combine (3.17) and (3.18) to obtain a simple, straightforward relation between $g(\theta)$ and $K_{sl}(\theta)$, namely,

$$K_{sl}(\theta) = \frac{\wp_g(\theta)}{\wp_g} = \frac{\mu_0 A_g / (g(\theta) + \frac{l_m}{\mu_r})}{\mu_0 A_g / (g + \frac{l_m}{\mu_r})} = \frac{g + \frac{l_m}{\mu_r}}{g(\theta) + \frac{l_m}{\mu_r}}. \quad (3.19)$$

A lot of approximations for $g(\theta)$ are available; in this model the equivalence proposed by [Hanselman 2012] is adopted. It is based on the application of the well-known Carter's coefficient in order to estimate the trajectory of the flux in front of a slot opening. Mathematically,

$$g(\theta) = \begin{cases} g & \text{if } |\theta| \leq \frac{\theta_t}{2} \\ g + \frac{\pi R_s}{2} \left(|\theta| - \frac{\theta_t}{2} \right) & \text{if } \frac{\theta_t}{2} < |\theta| \leq \frac{\theta_s}{2} \end{cases} \quad (3.20)$$

It should be noticed that $g(\theta)$ is periodic, with period θ_s . The dimensions and angles used in equation (3.20) are shown in Figure 3.6.

Once the expression of the relative permeance is obtained, it is possible to calculate its spatial FS, taking into account a signal period of $2\pi/Q$ radians.

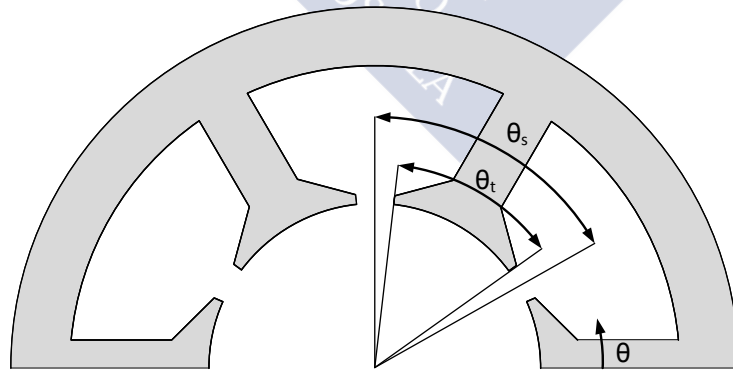


Figure 3.6. Geometry considered for the calculus of the relative permeance function.

3.2.2.1 Relative Permeance Function Limitations

Although the use of the relative permeance function supposes an elegant, straightforward and quite accurate solution which can model the effect of stator slotting in an electric machine, it has some drawbacks that should be corrected. In

order to explain these problems Figure 3.7 is included; it shows the flux density in the airgap calculated both, with the analytical model and using the FEM software FLUX®.

Two main characteristics are shown in Figure 3.7: the first one is that the analytically estimated magnetic field seems to be not solenoidal and the second one is that flux density increases at both sides of a slot opening. Both effects and its main implications will be widely commented.

About the first problem it can be deduced that, for odd relations of Q/t_p ratio, the flux density estimated by the analytical approach is not solenoidal, i.e. the rotor acts like a source or like a sink of field lines. In the example of Figure 3.7, the rotor at the chosen instant is a source because there is a slot in front of the magnet south pole but none in front of the north pole. As far as the total magnetic flux density leaving a close region is not null its divergence is different from zero and one of the Maxwell equations is not fulfilled.

This important error is a direct cause of equation (3.16). Obviously, the canonical solution (B_g^m) is solenoidal because it is obtained by direct resolution of Maxwell equations, but the estimated one with the slotting effect (B_{gs}^m) is no longer solenoidal when there is an odd number of slots in a winding periodicity because of the asymmetry of the relative permeance function.

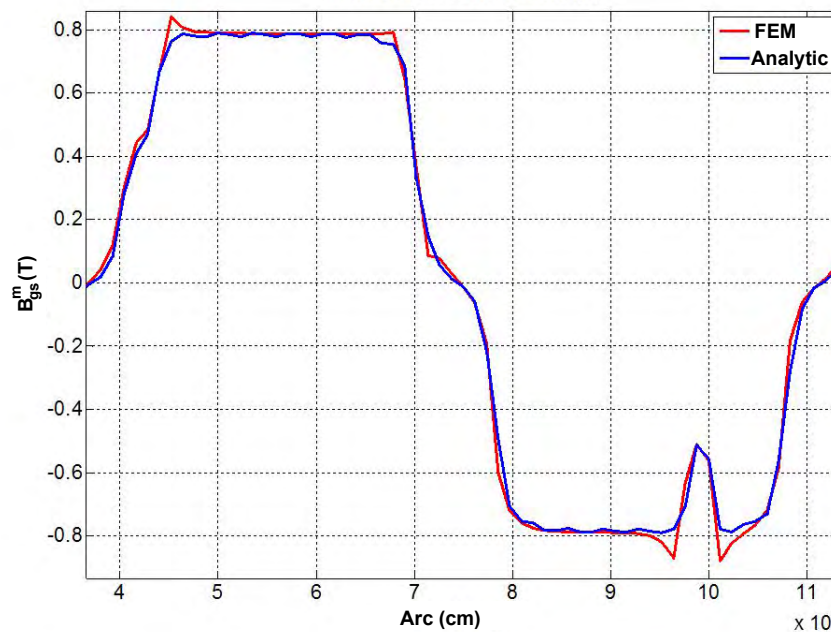


Figure 3.7. Radial component of the magnet flux density in the airgap. The PMSM simulated is a Q3p1 (3 slots and just one pole pair).

The direct consequence of this error is that the total sum of the magnetic flux which goes through each tooth is not equal to zero, so a correct estimation of all the parameters which depends on that flux, such as the electromagnetic force (EMF) or power losses, is impossible.

It is desirable to keep the same $K_{s1}(\theta)$ approximation since it is capable of predicting the flux density quite accurately. A correction based on the study of the spectrum of the magnet flux in the teeth has been demonstrated and implemented with good results. This approach has proved to be very suitable as far as it corrects the previous error. Its development will be explained later in this section.

The second problem is that there exist flux density “peaks” emplaced at both sides of a slot opening. The used analytical approximation is incapable of modelling such phenomenon because its main assumption is that the flux density is completely radial under the teeth but it neglects additional effects occurring at the “tooth-tips”, due to the flux lines concentration.

As can be seen in Figure 3.8 the flux density is nearly radial under the teeth but it is not in the proximities of a slot opening, because it curves in order to avoid the opening and enters into the tooth following the minimum reluctance path. This effect leads to a higher flux density in the tooth tips near the slot opening, as predicted by FEM simulations.

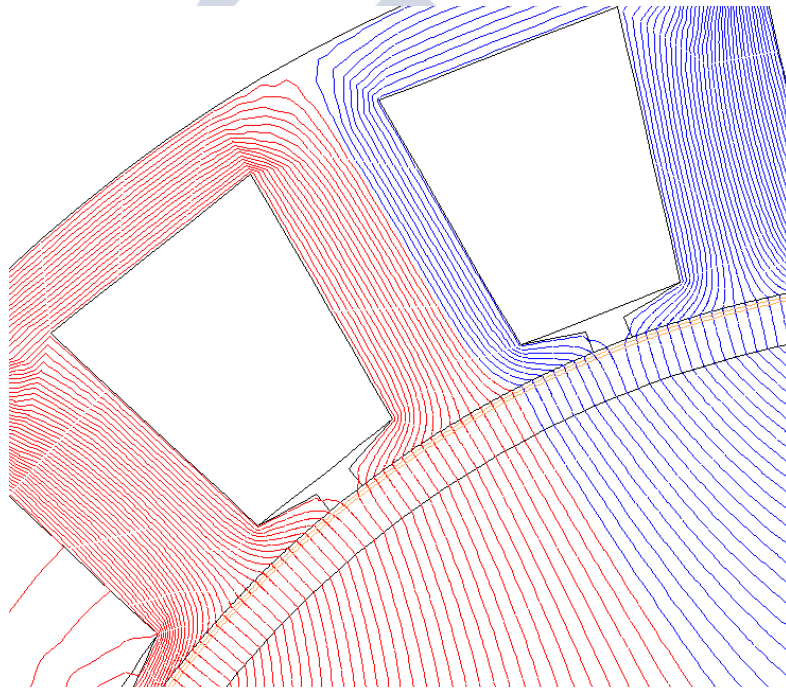


Figure 3.8. Flux density paths simulated in FEM with FLUX2D®.

In most cases, this effect has little influence in the subsequent calculus of the flux and the EMF, especially because the tooth-tip is the first stator part to become saturated, limiting this fringe effect.

An interesting approach to this problem is proposed by [Zarko 2006] who used the conformal transformation in order to calculate $K_{s1}(\theta)$ defining an equivalent problem in a more suitable “equivalent geometry”. Its method is a good candidate to be implemented in a later version of the magnetic model because it allows solving in a straightforward manner the two problems addressed here: the possible non-solenoidal field and the increment of the flux density in the proximities of a slot opening.

3.2.3 Electro-Motive Force and Stator Flux Induced by the Magnets

One of the main variables in any electric machine is the EMF generated in the coils, because through this voltage the magnetic energy is converted into electrical one.

In this section the calculus of the flux densities in the stator core of a PMSM will be explained, as well as the method to obtain the EMF once the fluxes are known.

3.2.3.1 Magnet Flux Density in the Stator Teeth

The magnetic flux induced in the stator teeth by the magnets has a great interest not only for the estimation of the core possible saturation level but also for its direct influence in the generation of the EMF.

In [Hanselman 2012] a mathematical procedure in order to obtain the magnet flux induced in one arbitrary stator tooth ($\phi_t^{m,1}$, the subindex t denotes the flux location, i.e. a tooth and the superindex 1 indicates the tooth number) is proposed. It is supposed without generality loss, that at $t = 0$ the tooth centre is aligned with a magnet centre and that the rotor is turning counter-clockwise at fixed speed ω_m .

In the next equations all the angles are expressed in mechanical radians except otherwise specified.

$$\phi_t^{m,1}(t) = \int_{-L_e/2}^{L_e/2} \int_{-\theta_s/2}^{\theta_s/2} K_{sl}(\theta) B_g^m(\theta, t) R_s d\theta dz = L_e R_s \int_{-\theta_s/2}^{\theta_s/2} K_{sl}(\theta) B_g^m(\theta - \omega_e t, 0) d\theta \quad (3.21)$$

where L_e is the PMSM active length and θ_s is the tooth pitch.

As it is known, B_g^m and K_{sl} can be expressed as their respective FS, but their period difference must be taken into account. B_g^m has a period of $2\pi/p$ radians while K_{sl} has a $2\pi/Q$ radians periodicity.

Having these features in mind it is possible to prove that [Hanselman 2012]:

$$\phi_t^{m,1}(t) = \frac{2\pi L_e R_s}{Q} \sum_{k=-\infty}^{\infty} \sum_{n=-\infty}^{\infty} B_{g,k}^m K_{sl,n} \text{sinc}\left(\left(n + \frac{kp}{Q}\right)\pi\right) e^{-jk\omega_e t}. \quad (3.22)$$

Equation (3.22) could be rewritten as:

$$\phi_t^{m,1}(t) = \frac{2\pi L_e R_s}{Q} \sum_{k=-\infty}^{\infty} e^{jk\omega_e t} B_{g,-k}^m \sum_{n=-\infty}^{\infty} K_{sl,n} \text{sinc}\left(\left(n - \frac{kp}{Q}\right)\pi\right). \quad (3.23)$$

A key FS feature is that, because B_g^m is real, $B_{g,-k}^m = (B_{g,k}^m)^*$, where $*$ denotes the conjugate. This characteristic can be used in order to obtain the temporal FS coefficients of $\phi_t^{m,1}$ from (3.23).

$$\phi_{t,k}^{m,1} = \frac{2\pi L_e R_s}{Q} B_{g,-k}^m \sum_{n=-\infty}^{\infty} K_{sl,n} \operatorname{sinc}\left(\left(n - \frac{kp}{Q}\right)\pi\right). \quad (3.24)$$

It is very important to notice that $\phi_t^{m,1}$ has a periodicity equal to $1/f_e$, being f_e the electrical frequency. That is why the magnets (and, therefore the offset α) pass through an entire period in a time equal to $1/f_e$.

With the previous equations the flux in a specific tooth is obtained. The flux in any other tooth will be the same except for a delay. If the first tooth is the reference, the n^{th} one will have FS coefficients given by

$$\phi_{t,k}^{m,n} = \phi_{t,k}^{m,1} e^{-j(n-1)kp\theta_s}. \quad (3.25)$$

As it will be explained in 3.2.2.1 an anomalous case exists if Q/t_p is odd, condition that only some fractional slot machines satisfy.

As it was introduced, in this case the presence of K_{sl} causes that the magnetic flux density calculated in the airgap is not solenoidal, unfulfilling Maxwell equations. It is necessary to correct that error in order to obtain a suitable approximation of important variables, such as the EMF. It is possible to correct this problem carrying out a detailed analysis of the temporal harmonics of the magnet tooth flux.

The flux in each tooth is calculated by means of equation (3.25). The sum all over a spatial periodicity must be null for any instant of time in order to fulfil Maxwell equations, so

$$\sum_{n=1}^Q \sum_{k=-\infty}^{\infty} \phi_{t,k}^{m,1} e^{j\omega_e kt} e^{-j(n-1)k 2\pi p/Q} = 0 \quad \forall t. \quad (3.26)$$

A necessary and sufficient condition to ensure that the above sum is null is that all temporal harmonics of order $k = sQ/p \quad \forall s \in \mathbb{Z}$ are null, i.e. (3.26) is fulfilled if, and only if

$$\phi_{t,sQ/p}^{m,1} = 0 \quad \forall s \in \mathbb{Z}. \quad (3.27)$$

In order to demonstrate this double implication, (3.26) would be rewritten as:

$$\sum_{k=-\infty}^{\infty} \left(\phi_{t,k}^{m,1} e^{j\omega_e kt} e^{-j(n-1)k 2\pi p/Q} \sum_{n=1}^Q e^{-j(n-1)k 2\pi p/Q} \right) = 0 \quad \forall t. \quad (3.28)$$

where it is clear that the expression in brackets could be seen as the FS coefficients of a null function.

The demonstration in both directions is trivial. That (3.26) implies (3.27) can be proved through “reductio ad absurdum”. In order to ensure that (3.26) is the FS of a null functions, all its coefficients must be null.

If some $\phi_{t,sQ/p}^{m,1}$ were not null, the total amplitude of the FS coefficient $k = sQ/p$ would be equal to Q times the amplitude of $\phi_{t,sQ/p}^{m,1}$, because every tooth flux will be summing in phase and $\sum_{n=1}^Q e^{-j(n-1)k 2\pi p/Q}$ is just equal to Q . As far as $\phi_{t,1sQ/p}^{m,1}$ can adopt any value, the defined FS is not null and the flux density could not be solenoidal.

That (3.27) implies (3.26) is also easy to prove and it is limited to demonstrate that if (3.27) is fulfilled all FS coefficients in (3.28) are null. It is obvious that all coefficients with index $k = sQ/p$ are null (because $\phi_{t,sQ/p}^{m,1}$ is zero). That the other coefficients are also null can be proved considering the sum $\sum_{n=1}^Q e^{-j(n-1)k 2\pi p/Q}$ as a geometric progression with common ratio $e^{-jk 2\pi p/Q}$, thus, equal to

$$\sum_{n=1}^Q e^{-j(n-1)k 2\pi p/Q} = \frac{e^{-jk 2\pi p} - 1}{e^{-jk 2\pi p/Q} - 1} = \frac{0}{e^{-jk 2\pi p/Q} - 1}; \quad (3.29)$$

it is trivial that, if $k \neq sQ/p$ where $s \in \mathbb{Z}$ the denominator is not null and, thus, the sum in (3.29) is null; so, (3.26) is fulfilled.

Hence, in order to preserve K_{s1} definition and perform a correct calculus of the EMF and the rest of machine variables, a correction of (3.23) is needed. As it was previously exposed, this modification consists in the elimination of all tooth flux FS terms with k multiple of Q/t_p , i.e.:

$$\phi_{t,sQ/p}^{m,1} = 0 \quad \forall s \in \mathbb{Z}. \quad (3.30)$$

Once the magnet flux in the teeth is obtained and corrected, it is possible to get its magnetic induction, B_t^m , assuming that the flux is uniform on a cross-section of them:

$$B_t^{m,n}(t) = \frac{\phi_t^{m,n}(t)}{L_e w_t}, \quad (3.31)$$

$$B_{t,k}^{m,n} = \frac{\phi_{t,k}^{m,n}}{L_e w_t}, \quad (3.32)$$

where w_t is the teeth width.

3.2.3.2 Magnet Flux Density in the Stator Yoke

The magnetic flux induced by the magnets in the stator yoke is less important than the one induced in the teeth, because it has no direct influence in either EMF generation or in the conversion of electric into mechanical energy.

However, the magnet flux density in stator yoke must be taking into account in order to avoid the saturation of the iron core. In most design procedures this induction determines yoke height, w_{sy} , and, therefore, the stator external radius.

In order to estimate the magnetic induction in the stator yoke, [Hanselman 2012] proposed a direct and straightforward model based on a reduced reluctance circuit. The main assumptions used in this approach are:

- Teeth are modelled as flux sources of value ϕ_t^{mn} .
- The stator yoke portion between two teeth is established as a reluctance of constant value R.
- Indirectly, the model supposes that the flux lines are normal to the rz-plane at each point.

Figure 3.9 shows the reluctance circuit supposed by the model. Obviously, the presented approach is far from being as accurate as the teeth flux calculus, since it is much simpler and its assumptions rougher. However, its accuracy is enough to obtain a suitable approximation of the maximum magnetic induction in the stator yoke, which is the only important parameter in order to estimate the magnetic saturation.

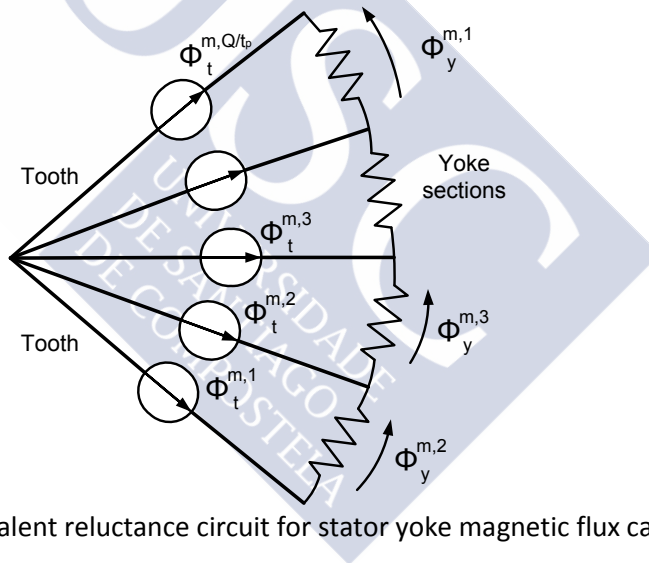


Figure 3.9. Equivalent reluctance circuit for stator yoke magnetic flux calculus.

The magnetic flux in stator yoke section 2 (see Figure 3.9) can be calculated as [Hanselman 2012]:

$$\phi_s^{m,2}(t) = \frac{t_p}{Q} \sum_{n=1}^{Q/t_p} \left(\frac{Q}{t_p} - n \right) \phi_t^{m,n+1}(t) \quad (3.33)$$

Where $\phi_s^{m,2}(t)$ is the stator yoke flux between the first and the second tooth. The general form of this notation establishes that $\phi_s^{m,n}(t)$ is the stator yoke flux between the n^{th} and the $(n-1)^{\text{th}}$ teeth. It should be noticed that the summation is limited to just a winding period due to the stator symmetry.

It is quite simple to modify equation (3.33) in order to obtain the temporal FS coefficients of the yoke flux from the teeth flux temporal FS. If the superposition principle is applied it is obtained

$$\phi_{s,k}^{m,2} = \frac{t_p}{Q} \sum_{n=1}^{Q/t_p} \left(\frac{Q}{t_p} - n \right) \phi_{t,k}^{m,(n+1)}. \quad (3.34)$$

Obviously, the fluxes and magnetic induction in any other stator yoke portion can be obtained from the previous equations taking into account the temporal delay with respect to the reference section, just as it is done in teeth flux calculus.

$$\phi_{s,k}^{m,n} = \phi_{s,k}^{m,2} e^{-j(n-2)kp\theta_s} \quad (3.35)$$

From the fluxes, the magnetic induction in the stator yoke can be obtained in a direct way from

$$B_s^{m,n}(t) = \frac{\phi_s^{m,n}(t)}{L_e w_{sy}}, \quad (3.36)$$

3.2.3.3 Induced EMF

The electro-motive force is one of the main variables in a machine design because it is the critical parameter through which energy is converted from the magnetic domain to the electric one, by applying Faraday's law. Many calculus methods to obtain this variable are proposed in technical literature.

Several authors [Almandoz 2008, Pyrhönen 2008] proposed a model which will be referred to as the classical approach. This approach is based on the calculus of a winding factor (ξ_n), which establishes an equivalence between the EMF created by one coil (with just an inward slot and an outward one) and the EMF of all coils wound in the stator core. This factor takes into account the coil offset angles and the effect of coil pitch.

The classical method is very suitable when the coil EMF is assumed to have a sinusoidal dependence with respect to time or when the current harmonics are negligible. However, since the design methodology proposed is general and the current can contain temporal harmonics the interest of the classical approach is very low [Hanselman 2012]. Thus, a different approach proposed by [Hanselman 2012] will be implemented.

The basis of this method consists in obtaining the total magnet flux linked by a phase winding. In order to do so m "scale factor" vectors (one for each phase, noted S^l) are defined. Their length is Q/t_p , i.e. the number of teeth contained in a winding periodicity.

The n^{th} position within vector S^l defines the number of phase A coils that are linked by the n^{th} tooth and its sign (positive or negative according to the “right-hand rule”). For example, for the phase winding shown in Figure 3.10 the S^1 vector will be

Table 3.1. Scale factor for the example shown in Figure 3.10

Tooth	1	2	3	4	5	6	7	8	9	10	11	12	13	14	15
S^1	1	1	1	0	-1	-1	-1	1	2	2	1	-1	-1	-1	0

Once vectors S^l have been established the total flux linked by any phase, $\phi_{lk}^{m,l}(t)$ in a spatial periodicity is equal to

$$\phi_{lk}^{m,l}(t) = \sum_{n=1}^{Q/t_p} S_n^l \phi_t^{m,n}(t). \quad (3.37)$$

As it has been proved, the flux induced by the magnets is the same in every tooth, except for a temporal delay, so the FS coefficients of the above sum can be written as

$$\phi_{lk,k}^{m,l} = \phi_{t,k}^{m,1} \sum_{n=1}^{Q/t_p} S_n^l e^{-jk(n-1)p\theta_s}. \quad (3.38)$$

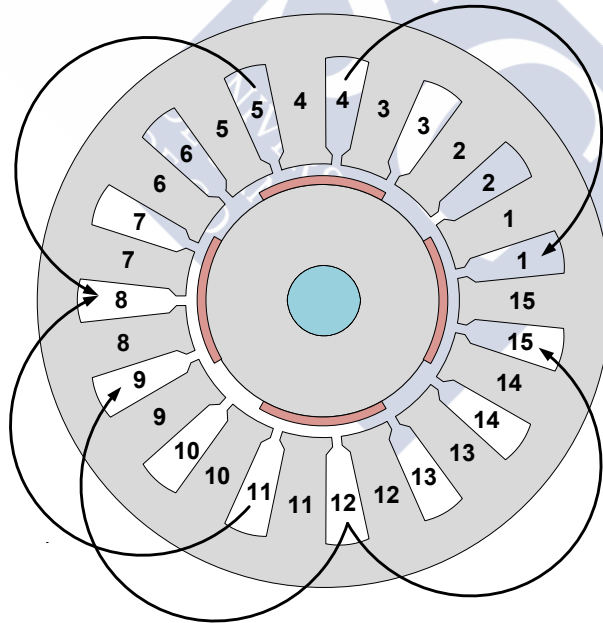


Figure 3.10. Phase winding example in a fractional slot PMSM. Slots/teeth numbering included.

Faraday’s law establishes that the voltage induced is equal to:

$$E_p^1(t) = -Z \frac{d\phi_{lk}^{m,1}(t)}{dt}, \quad (3.39)$$

where $E_p^1(t)$ is the EMF induced in phase 1 (i.e. phase A) in one winding periodicity, and Z the number of turns in each coil. Equation (3.39) can be expressed in the spectral domain as follows:

$$E_p^1(t) = -Z \sum_{k=-\infty}^{\infty} \phi_{t,k}^{m,1} \frac{de^{jk\omega_e t}}{dt} \sum_{n=1}^{Q/t_p} S_n^1 e^{-jk(n-1)p\theta_s}. \quad (3.40)$$

Therefore, the FS coefficients of the induced electro-motive force FS are equal to:

$$E_{p,k}^1 = -jZ\omega_e k \phi_{t,k}^{m,1} \sum_{n=1}^{Q/t_p} S_n^1 e^{-jk(n-1)p\theta_s}. \quad (3.41)$$

The sign of the voltage will be established according to Lenz's law. Thus, the positive voltage reference is in the outward winding slot as can be seen in Figure 3.10.

It is very important to notice that, throughout the developed procedure, the EMF corresponding to a winding periodicity has been obtained. If we assumed that all the coils in one phase are connected in series the total EMF will be t_p times higher:

$$E_k^1 = -jZt_p \omega_e k \phi_{t,k}^{m,1} \sum_{n=1}^{Q/t_p} S_n^1 e^{-jk(n-1)p\theta_s}. \quad (3.42)$$

This case is the most common in electric machines [Hanselman 2012] but other connections are available. The total EMF will depend on the particular combination of series and parallel connections of the windings periodicities. For a generic connection the induced EMF will be

$$E_k^1 = -jZ \frac{t_p}{N_{para}} \omega_e k \phi_{t,k}^{m,1} \sum_{n=1}^{Q/t_p} S_n^1 e^{-jk(n-1)p\theta_s}. \quad (3.43)$$

where N_{para} is the number of groups connected in parallel.

The same procedure can be performed in order to obtain the EMF induced in other phases, but it is not necessary as far as the PMSM is supposed to have a balanced winding distribution and the induced EMF in the phases must be equal except for a phase delay of $360/m$ degrees.

3.2.4 Armature Reaction and Total Magnetic Field

The flux density induced by the stator coils current is known as "armature reaction". The armature reaction is of minor importance in the global behaviour of a PMSM, because it is usually an order of magnitude lower than the magnet induction. In spite of this fact, it is useful to obtain it because it is added to the magnet flux density, so it can have an influence in the losses, and in the non-linearities associated with the core saturation level and the electromagnetic force calculus.

3.2.4.1 Armature Reaction in the Airgap

The literature offers different methods for the analytic calculus of the armature reaction in the airgap [Zhu 1993-b, Almandoz 2008]. Most of them have the main assumption that the ferromagnetic materials can be supposed to be infinitely permeable, so the flux density can be considered as radial, both in the airgap and in the stator core. Figure 3.11 shows the flux lines caused by just one stator coil.

The armature reaction model implemented is based on the estimation of the flux density spatial FS from the stator winding distribution [Almandoz 2008]. In a first stage the magneto-motive force (MMF) generated by coil n is calculated; its spatial FS can be defined as

$$\text{MMF}^n(\theta, t) = F^n(\theta)I^s(t) = I^s(t) \sum_{k=-\infty}^{\infty} F_k^n e^{jkt_p\theta}, \quad (3.44)$$

where $F^n(\theta)$ is the coil n magneto-motive force induced per current unit and $I^s(t)$ is the current flowing through phase s . It is important to notice that coil is defined as the set of turns linking a slot with another and, thus, generating an effective MMF. It is supposed that the generic coil n belongs to phase s .

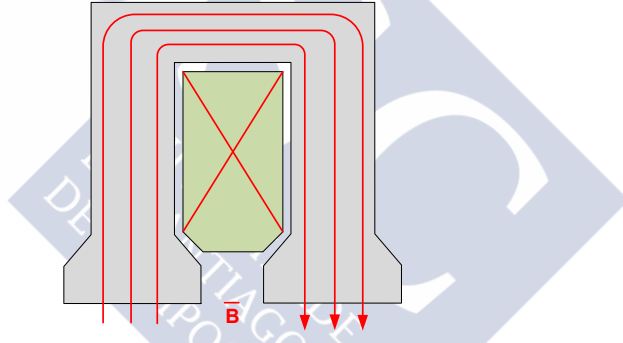


Figure 3.11. Armature reaction caused by one coil in the adjacent teeth.

The spatial waveform of the armature reaction caused by a single coil can be characterized by three parameters: its pitch angle β_n , its central angle ϕ_n and its slot opening α_n (see Figure 3.12), where the subindex n identifies the coil number.

It is possible to obtain the three aforementioned parameters for a particular coil from its “inward” and “outward” slots, i.e. for coil n :

$$\phi_n = \pi \frac{\text{out}L_n + \text{in}L_n - 3}{Q}, \quad (3.45)$$

$$\alpha_n = w_0/R_s, \quad (3.46)$$

$$\beta_n = \frac{2\pi}{Q} (\text{out}L_n - \text{in}L_n) - \alpha, \quad (3.47)$$

where w_0 is the slot opening, and out_n and in_n are, respectively, the outward and inward slot that identifies the coil pitch, i.e. the coil pitch is equal to $\text{out}_n - \text{in}_n$. In the

previous equations the 0 rad reference is at the centre of the first tooth, situated anticlockwise adjacent to the first slot, i.e. a coil which enters by the first slot and leaves by the second is centred in $\phi = 0$ rad (see Figure 3.10).

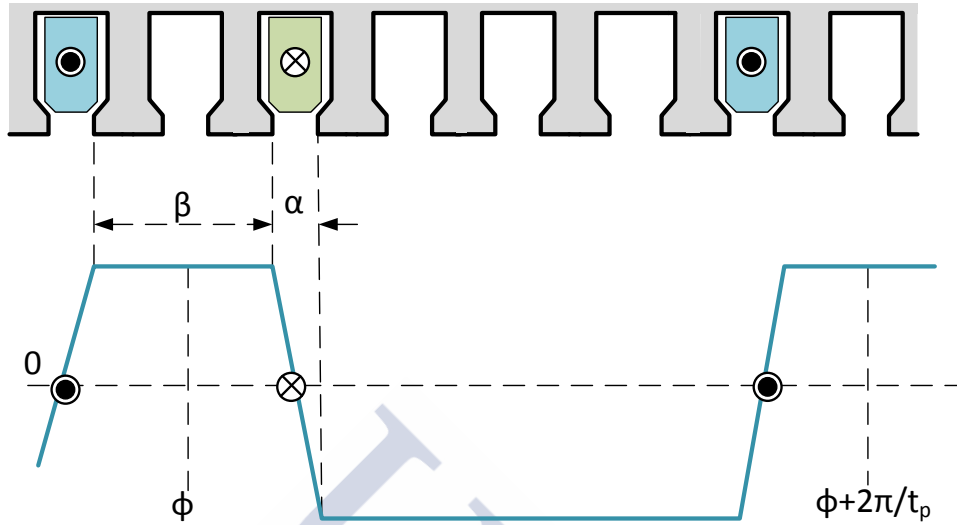


Figure 3.12. Spatial distribution of the MMF per current unit caused by a single coil. Example from [Almandoz 2008].

With the previous values obtained from the coil configuration it is possible to perform the spatial FS of the trapezoidal form adopted by the armature reaction [Almandoz 2008]:

$$F_k^n = \frac{Z}{t_p \alpha_n \pi k^2} \left[\cos \left(kt_p \frac{\beta_n}{2} \right) - \cos \left(kt_p \left(\frac{\beta_n}{2} + \alpha_n \right) \right) \right] e^{-jkt_p \phi_n}. \quad (3.48)$$

Once all the armature reactions of the coils are obtained individually it is possible to calculate the armature reaction caused by one phase, adding all the individual contributions:

$$F_{ph,k} = \sum_{n=1}^{QN_{lay}/(2m)} F_k^n, \quad (3.49)$$

where N_{lay} is the number of layers in a single slot (usually one or two), n is an index which numerates every coil within a phase and F_{ph} is the MMF per unit current in the phase of reference, i.e. phase A. Figure 3.13 shows a typical armature reaction of a phase with two coils at an instant of time.

As far as the PMSM has a spatial balanced winding, all the phases have the same armature reaction waveform up to a phase difference of $2\pi/(mp)$ mechanical radians with respect to the previous phase; hence, the calculus of just one phase armature reaction is enough. The complete magneto-motive force will be

$$\text{MMF}_k^a(t) = F_{\text{ph},k} \sum_{s=0}^{m-1} e^{-\frac{j2\pi sk}{m}} I^s(t), \quad (3.50)$$

where index s represents the phase, and $I^s(t)$ is the current flowing through the s phase at instant t .

Once the magneto-motive force is obtained and applying the approach of an infinitely permeable magnetic core the armature reaction in the airgap is related with MMF_k^a through

$$B_{g,k}^a(t) = \frac{\mu_0 \text{MMF}_k^a(t)}{\delta}. \quad (3.51)$$

where the numerator can be seen as the difference of magnetic potential along the airgap; i.e. $\text{MMF}^a(t)/\delta$ is an approximation of the magnetic intensity field $H(t)$.

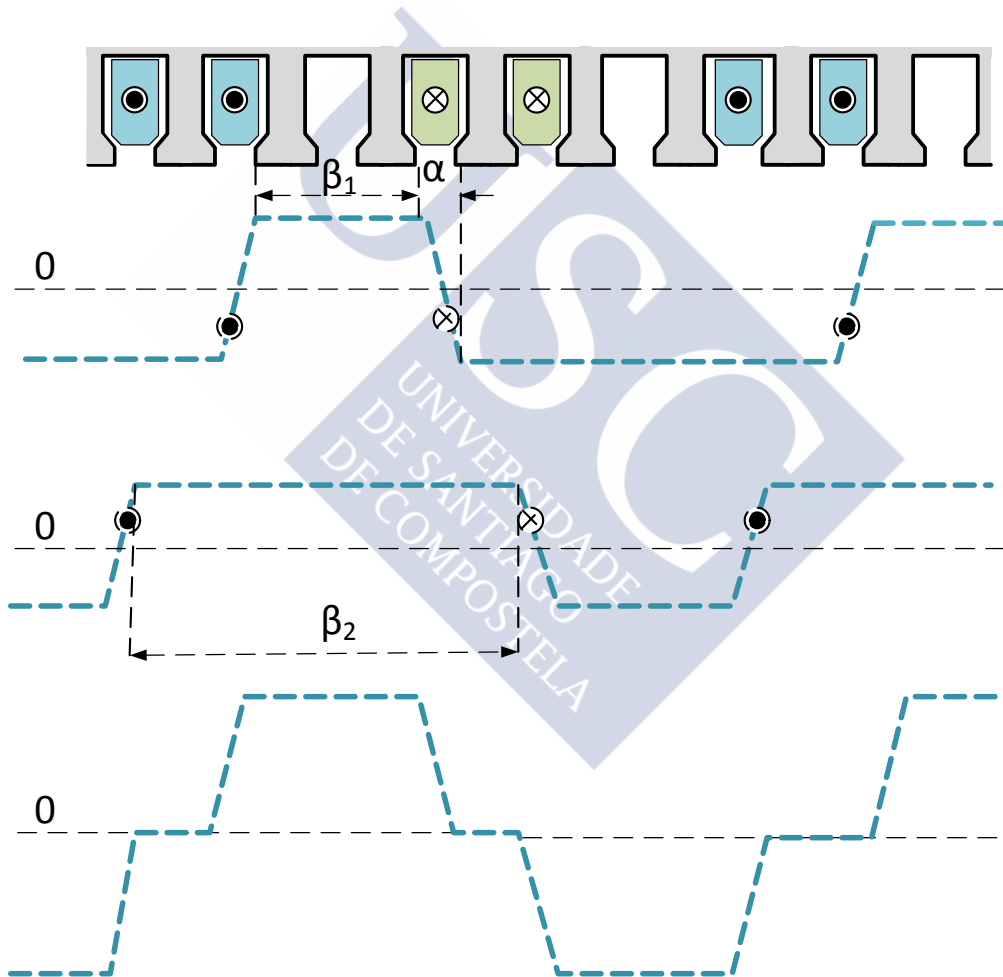


Figure 3.13. Spatial distribution of the MMF per current unit caused by a phase conformed by two coils.

A very important feature of that model is that, since the temporal and spatial variables are independent, it is possible to perform a double FS with respect to both magnitudes. Thus, the final expression of the the double FS of the armature reaction in the airgap will be:

$$B_g^a(\theta, t) = \frac{\mu_0}{\delta} \sum_{k=-\infty}^{\infty} \sum_{l=-\infty}^{\infty} \left(\sum_{s=0}^{m-1} e^{-j2\pi s(k+l)/m} \right) F_{ph,k} I_l^1 e^{j(kt_p\theta + l\omega_e t)}, \quad (3.52)$$

the sum through the phases (i.e. in s) could be computed consider that it is a geometric progression with common ratio $e^{-j2\pi(k+l)/m}$, thus, equal to

$$\sum_{s=0}^{m-1} e^{-j2\pi s(k+l)/m} = \frac{e^{-j2\pi(k+l)} - 1}{e^{-j2\pi(k+l)/m} - 1}; \quad (3.53)$$

this sum is null if $k + l$ is not multiple of m . On the contrary, with $k + l$ multiple of m the sum is equal to m , i.e. the unity is summed m times. Thus, (3.52) can be rewritten in a more compact form as:

$$B_g^a(\theta, t) = \frac{\mu_0}{\delta} \sum_{k=-\infty}^{\infty} \sum_{l=-\infty}^{\infty} m \delta_{0, \text{mod}(m, k+l)} F_{ph,k} I_l^1 e^{j(kt_p\theta + l\omega_e t)} \quad (3.54)$$

where δ is the Kronecker delta and mod the modulus function. In the spectral domain,

$$B_{g,kl}^a = \frac{\mu_0}{\delta} F_{ph,k} I_l^1 m \delta_{0, \text{mod}(m, k+l)}. \quad (3.55)$$

3.2.4.2 Armature Reaction in the Stator Core

Once the flux density in the airgap is obtained it is possible to calculate its value both in the stator teeth and in the stator yoke. In order to achieve these results it is possible to apply a procedure quite similar to that exposed in 3.2.3.1. The flux caused by the stator coils in an arbitrary reference tooth, noted $\phi_t^{a,1}(t)$, will be equal to

$$\phi_t^{a,1}(t) = \int_{-L_e/2}^{L_e/2} \int_{-\theta_s/2}^{\theta_s/2} K_{sl}(\theta) B_g^a(\theta, t) R_s d\theta dz. \quad (3.56)$$

It is interesting to notice that, for a fixed tooth, the armature reaction $B_g^a(\theta, t)$ can be considered as constant, approximating its trapezoidal form for a rectangular one. Thus, (3.56) can be expressed as:

$$\phi_t^{a,1}(t) = L_e R_s B_g^a(t) \int_{-\theta_s/2}^{\theta_s/2} K_{sl}(\theta) d\theta, \quad (3.57)$$

which leads to a temporal FS coefficients

$$\phi_{t,k}^{a,1} = \frac{L_e R_s}{p} B_{g,k}^a \sum_{n=-\infty}^{\infty} K_{sl,n} \text{sinc}(n\pi). \quad (3.58)$$

For any other tooth the same procedure is applied, establishing the proper limit in the integral along θ . It is very important to realize that, in contrast to what happens with the magnets flux, the flux induced by the armature reaction is not equal in every

tooth. In fact, as far as the scale factors S are different for each tooth it is quite possible that some of them have a flux waveform quite different from the others.

From the armature reaction of the teeth it is quite simple to obtain the flux in the stator yoke by using the equations (3.33) and (3.34) proposed in section 3.2.3.2, just replacing the variable $\phi_{t,k}^{m,n}$ by $\phi_{t,k}^{a,n}$. The final results of that section are repeated for sake of completeness. It is worthwhile to notice that the superindex n identifies the tooth (and, equivalently, l is the stator yoke section) where the flux is obtained.

$$\phi_{s,k}^{a,2} = \frac{t_p}{Q} \sum_{n=1}^{Q/t_p} (Q - n) \phi_{t,k}^{a,(n+1)}, \quad (3.59)$$

so, the magnetic induction in the stator yoke can be approximated by:

$$B_s^{a,2}(t) = \frac{\phi_s^{a,2}(t)}{L_e W_{sy}}. \quad (3.60)$$

Magnetic fluxes and inductions in any other stator yoke section can be obtained from the previous equations. In practice, calculating these values will be more time consuming than in the case of the magnet fluxes, because the teeth fluxes are no longer equal in the case of the armature reaction.

The armature reaction for a generic stator yoke section l will be

$$\phi_{s,k}^{a,l} = \frac{t_p}{Q} \sum_{n=1}^{Q/t_p} (Q - n) \phi_{t,k}^{a,\text{mod}(n+l, Q/t_p)}, \quad (3.61)$$

where $\text{mod}(x, y)$ is the remainder in the integer division x/y .

3.2.4.3 Total Magnetic Field in the Stator Core

An accurate expression of the total magnetic field, both in the airgap and in the stator core, is needed in order to obtain some physical variables that are of main relevance for the calculus of the efficiency and the thermal and vibratory behaviour of the PMSM.

More precisely, the magnetic field in the airgap causes electromagnetic forces that produce vibrations in the stator cores, vibrations that are transmitted through the housing and are propagated into the air producing undesirable noise. On the other hand, total flux density in the stator core causes iron losses which are critical in the calculus of the overall machine efficiency and its temperature. Moreover, an excessive magnetic induction can cause the ferromagnetic material saturation, worsening its electromagnetic behaviour and entailing an important loss of accuracy in the analytical model implemented.

In some studies, the influence of the armature reaction is neglected because it is estimated that, in most occasions, its value is an order of magnitude lower compared with the magnet flux. In spite of this fact, complete magnetic induction estimation is preferred as far as, during this work, it has been proved that the forces and iron losses are notably modified by the armature reaction.

Firstly, the induced flux in a stator tooth will be calculated. Due to the fact that both individual contributions have been obtained previously it is enough to sum its values:

$$\phi_{t,k}^n = \phi_{t,k}^{a,n} + \phi_{t,k}^{m,n}, \quad (3.62)$$

where superindex n identifies the tooth and k the temporal FS harmonic.

From (3.24) and (3.58), the total n^{th} tooth flux expressed in terms of its temporal FS coefficients will be equal to:

$$\phi_{t,k}^n = L_e R_s \frac{2\pi}{Q} \left(B_{g,k}^a \sum_{n=-\infty}^{\infty} K_{sl,n} \text{sinc}(n\pi) + B_{g,k}^m \sum_{n=-\infty}^{\infty} K_{sl,n} \text{sinc}\left(\left(n + \frac{kp}{Q}\right)\pi\right) \right). \quad (3.63)$$

Finally the FS coefficients of the total flux density of the n^{th} tooth will be

$$B_{t,k}^n = \frac{\phi_{t,k}^{a,n} + \phi_{t,k}^{m,n}}{L_e w_t}. \quad (3.64)$$

It is important to notice that, while $B_{g,k}^{m,n}$ is the same for all teeth (i.e. for all n) except for a temporal delay, it is not the case of $B_{g,k}^{a,n}$ which can be different for each tooth depending on the particular stator winding. Despite of this fact, for the saturation and losses estimation, it will be considered that all the stator teeth have the same armature reaction (i.e. the same $B_{g,k}^a$) equal to the maximum tooth flux calculated. Hence, it is not necessary the exhaustive calculus of the total flux density in each part of the stator core. This simplification is quite time saving and it establishes a security factor in the iron losses estimation.

The stator yoke total flux can be estimated in a similar fashion, the FS temporal coefficients in a generic yoke section l are given by

$$\phi_{s,k}^l = \frac{t_p}{Q} \sum_{n=1}^{Q/t_p} (Q - n) \phi_{t,k}^{\text{mod}\left(n+l, \frac{Q}{t_p}\right)}, \quad (3.65)$$

$$B_{s,k}^l = \frac{\phi_{s,k}^l}{L_e w_{sy}}. \quad (3.66)$$

In this case, in order to calculate the ferromagnetic losses in the stator yoke, the same approximations as those applied for the teeth will be used. Thus, it will be considered that $\phi_{s,k}^l$ is equal in every yoke region.

3.2.4.4 Total Magnetic Field in the Airgap

The total magnetic field in the airgap is an important variable, on the one hand because it establishes the flux in the stator core, on the other hand because the radial magnetic forces are proportional to its square value.

The expression of the magnet airgap flux density in a slotless machine has been obtained in section 3.2.1, the previously obtained expression is:

$$B_g^m(\theta, t) = \sum_{k=-\infty}^{\infty} B_{g,k}^m e^{jk(p\theta - \omega_e t)}. \quad (3.67)$$

It is worthwhile to notice that it can be reinterpreted as a double FS respect time and space. The double sum is transformed into a single one due to the constant rotating speed which links t and θ

While the FS of the armature reaction in the airgap is equal to

$$B_g^a(\theta, t) = \frac{\mu_0}{\delta} \sum_{k=-\infty}^{\infty} \sum_{l=-\infty}^{\infty} m \delta_{0, \text{mod}(m, k+l)} F_{A,k} I_{A,l} e^{j(kt_p \theta + l\omega_e t)}. \quad (3.68)$$

Thus, double FS of the total airgap induction in a slotless machine is equal to their sum

$$B_g(\theta, t) = \sum_{k=-\infty}^{\infty} \left(B_{g,k}^m e^{jk(p\theta - \omega_e t)} + \sum_{l=-\infty}^{\infty} \frac{\mu_0}{\delta} m \delta_{0, \text{mod}(m, k+l)} F_{A,k} I_{A,l} e^{j(kt_p \theta + l\omega_e t)} \right). \quad (3.69)$$

The most direct form of including the effect of the stator slotting is using the relative permeance factor. Thus, the total magnetic induction, taking into account the slots effect will be:

$$B_{gs}(\theta, t) = K_{sl}(\theta) \left(B_g^m(\theta, t) + B_g^a(\theta, t) \right). \quad (3.70)$$

This is the magnetic induction value that will be used by the methodology in order to estimate the radial forces.

3.2.5 Radial Stator Force and Cogging Torque Calculus

The presence of a magnetic field in the boundary between the airgap and the stator ferromagnetic core generates a surface force due to the abrupt change in the magnetic permeability. These forces are produced by the interaction of the rotor magnetic fields caused by the magnets and the stator fields induced by the currents flowing through the coils. As it was explained during the torque calculus, these magnets and electromagnets are attracted to each other (generating mutual torque) and to the ferromagnetic cores (producing the cogging and reluctance torques). The magnetic field and the forces on the stator core are represented in Figure 3.14.

There exists a great controversy about the best form to estimate the electromagnetic forces, so many approaches have been proposed and implemented in order to perform this calculus. All the aforementioned methods are encompassed in two main categories; the virtual work principle [Sanchez 2006, Bossavit 2014] and the Maxwell stress tensor method [Bermúdez 2014]. Comparisons between them have been carried out [Bossavit 2011].

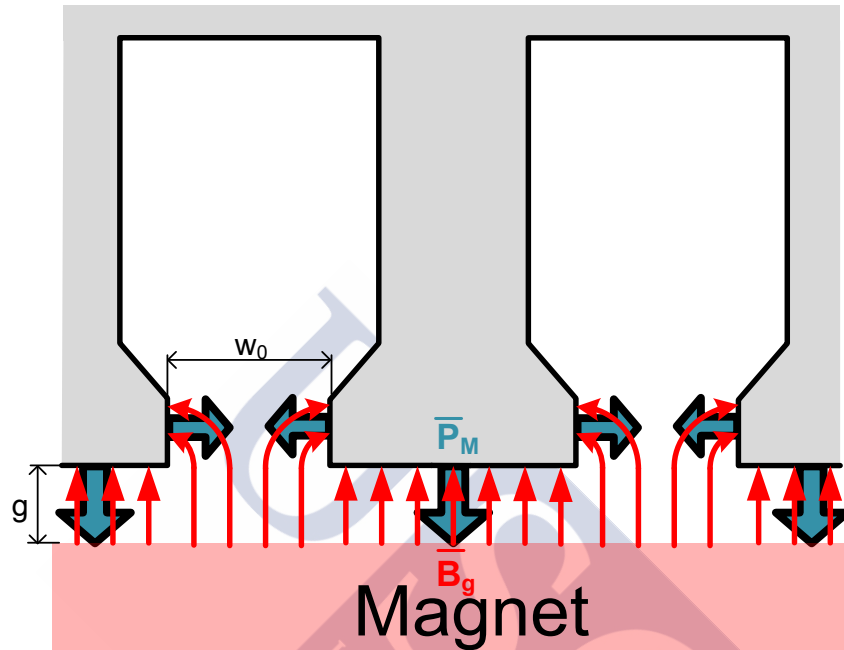


Figure 3.14. Spatial distribution of the radial magnetic field and the generated force density in the stator boundaries.

Let be \mathbf{E} and \mathbf{D} the electric field and the electric flux density vectors, respectively and let be \mathbf{H} and \mathbf{B} the magnetic field intensity and the magnetic flux density vectors. When \mathbf{E} and \mathbf{D} and \mathbf{H} and \mathbf{B} are collinear the Maxwell stress tensor is (see, for example, [Bermúdez 2014])

$$\mathcal{T} = \mathbf{E} \otimes \mathbf{D} + \mathbf{B} \otimes \mathbf{H} - \frac{1}{2} (\mathbf{E} \cdot \mathbf{D} + \mathbf{B} \cdot \mathbf{H}) \mathbf{I} \quad (3.71)$$

where \otimes denotes the tensor product, \mathcal{T} is the Maxwell stress tensor and \mathbf{I} the identity tensor.

In the particular case of a PMSM the electric field and its associated forces can be neglected with respect to the magnetic ones and (3.71) is simplified to:

$$\mathcal{T} = \mathbf{B} \otimes \mathbf{H} - \frac{1}{2} (\mathbf{B} \cdot \mathbf{H}) \mathbf{I} \quad (3.72)$$

The electromagnetic force is given by the divergence of the Maxwell electromagnetic stress tensor:

$$\mathbf{f} = \text{div} \mathcal{T} \quad (3.73)$$

It is important to notice that the divergence operator must be understood in the sense of distributions, because the magnetic fields may present discontinuities on across surfaces. In the present case it can be proved that this divergence is null all over the stator except just in its boundary with the airgap. More precisely, it is the distribution defined by

$$\langle \mathbf{f}, \boldsymbol{\gamma} \rangle = - \int_S \left([\mathbf{H} \cdot \mathbf{nB}] - \frac{1}{2} [(\mathbf{B} \cdot \mathbf{H})\mathbf{n}] \right) \cdot \boldsymbol{\gamma} \, dS \quad (3.74)$$

where \mathbf{n} is the normal outward surface vector (see Figure 3.14), and $\boldsymbol{\gamma}$ is any smooth vector field. The convention adopted for $[\mathbf{a}]$ is

$$[\mathbf{a}] = \mathbf{a}_{\text{Fe}} + \mathbf{a}_g, \quad (3.75)$$

where \mathbf{a} is a vector field which adopts a value \mathbf{a}_{Fe} in the stator core and a value \mathbf{a}_g in the airgap.

It must be taken into account that the boundary between the stator core and the airgap is free of surface currents, those implies that, in order to fulfil Maxwell equations, the tangential component of the magnetic intensity must be equal at both sides of the boundary. Additionally, Maxwell equations also impose the normal component of the flux density is also equal at both sides of the boundary.

$$H_{\text{Fe}}^t = H_g^t \quad (3.76)$$

$$B_{\text{Fe}}^n = B_g^n \quad (3.77)$$

where superscript t and subscript n refer to the tangential and normal component of the field, respectively. Taking this fact into account, is not difficult to obtain that

$$[\mathbf{H} \cdot \mathbf{nB}] = |\mathbf{B}_{\text{Fe}} \cdot \mathbf{n}_{\text{Fe}}|^2 \mathbf{n}_{\text{Fe}} \left(\frac{1}{\mu_{\text{Fe}}} - \frac{1}{\mu_0} \right) \quad (3.78)$$

$$[(\mathbf{B} \cdot \mathbf{H})\mathbf{n}] = |\mathbf{B}_{\text{Fe}} \cdot \mathbf{n}_{\text{Fe}}|^2 \mathbf{n}_{\text{Fe}} \left(\frac{1}{\mu_{\text{Fe}}} - \frac{1}{\mu_0} \right) + \mathbf{n}_{\text{Fe}} |H^t|^2 (\mu_{\text{Fe}} - \mu_0). \quad (3.79)$$

Assuming that the ferromagnetic material is infinitely permeable equations (3.78) and (3.79) yield

$$[\mathbf{H} \cdot \mathbf{nB}] = \frac{-|\mathbf{B}_{\text{Fe}} \cdot \mathbf{n}_{\text{Fe}}|^2}{\mu_g} \mathbf{n}_{\text{Fe}} = \frac{-|B_{\text{gs}}|^2}{\mu_0} \mathbf{n}_{\text{Fe}}, \quad (3.80)$$

$$[(\mathbf{B} \cdot \mathbf{H})\mathbf{n}] = \frac{-|\mathbf{B}_{\text{Fe}} \cdot \mathbf{n}_{\text{Fe}}|^2}{\mu_g} \mathbf{n}_{\text{Fe}} = \frac{-|B_{\text{gs}}|^2}{\mu_0} \mathbf{n}_{\text{Fe}}, \quad (3.81)$$

where it is taken into account that \mathbf{H} is null in the ferromagnetic core, because of its high permeability. B_{gs} is the magnetic flux density in the airgap previously obtained in (3.70).

Thus, the final expression of integral (3.74) will be

$$\langle \mathbf{f}, \boldsymbol{\gamma} \rangle = \int_S \frac{|\mathbf{B}_{gs}|^2}{2\mu_0} \mathbf{n}_{Fe} \cdot \boldsymbol{\gamma} dS, \quad (3.82)$$

Roughly speaking, it means that the modulus of the surface force density is equal to

$$d\mathbf{f}(\theta, t) = P_M(\theta, t) = \frac{|\mathbf{B}_g^n(\theta, t)|^2}{2\mu_0}. \quad (3.83)$$

P_M is called the Maxwell magnetic pressure (i.e. force density).

This is the expression of the surface force density at each point and time that can be used to calculate both, the stator vibrations and the cogging torque.

As it can be seen, the magnetic pressure is applied in two directions, causing different effects.

- If it is applied on the tooth top, it generates a radial force that is transmitted to the air through the housing and causes vibration and noise.
- If it is applied on the tooth shoes, i.e. on the boundaries of a slot opening, the forces cause a torque that, by mean of the second Newton's law, is reflected on the rotor generating the so called cogging torque.

Many authors try to link both phenomena as they are consequence of the same cause, i.e. the electromagnetic forces. The aim of these studies is to predict the machine vibratory behaviour from its cogging torque. However, recent studies have demonstrated that a higher amount of cogging torque is not directly associated with a worse vibratory behaviour [Gieras 2007, Islam 2010], so the two phenomena are studied separately in this thesis in order to achieve a proper PMSM design.

3.2.5.1 Radial Forces

The radial Maxwell forces can be calculated applying (3.82) in the tooth top. The obtained magnetic pressure presents a temporal and a spatial dependence, so a double FS with respect to both, the space and the time, can be performed:

$$P_M(\theta, t) = \frac{|\mathbf{B}_g(\theta, t)|^2}{2\mu_0} = \sum_{k=-\infty}^{\infty} \sum_{l=-\infty}^{\infty} P_{M,kl} e^{jk\omega_e t} e^{jlt_p\theta}. \quad (3.84)$$

The spatial component of the FS is associated with the radial mode excited in the stator structure, while its temporal component provides the excitation frequency. The mechanical vibratory effect caused by the force will be further developed and examples of forces and flux densities double FS can be found in Appendix B. Figure 3.15 shows the Maxwell pressure over a tooth during an electric period (i.e. $2\pi/\omega_e$) magnets and armature reactions contribution can be observed.

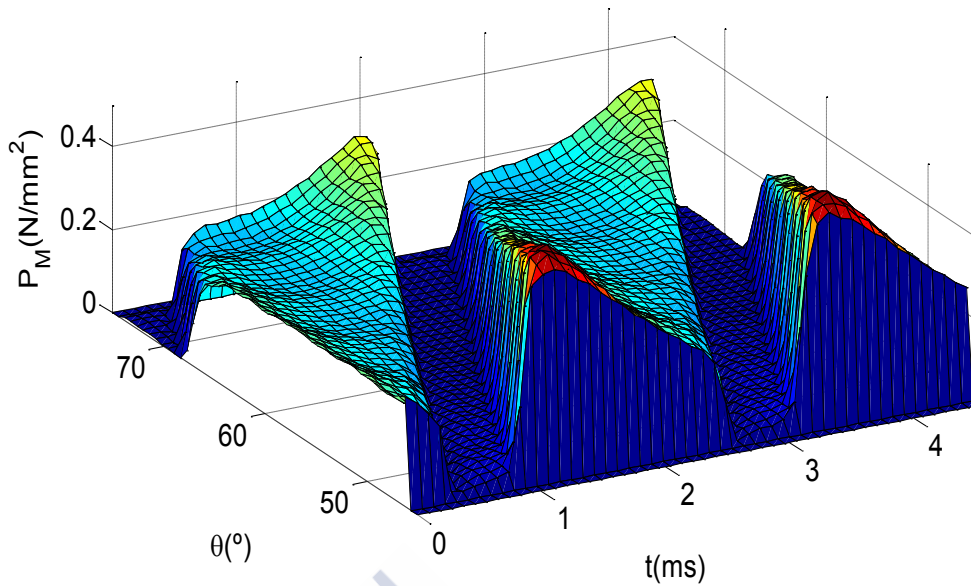


Figure 3.15. Radial force density over a tooth during an electrical period.

3.2.5.2 Cogging Torque

The cogging torque also has an important influence in the machine performance, since an excessive torque ripple can cause important mechanical faults depending on the final applications, as diverse as hard disk drives and industrial elevators.

There are many methods in order to calculate the cogging torque, the simplest one being to apply a direct integration in order to obtain the torque caused by just one slot and then to extrapolate it to the complete machine. Despite its accuracy limitations, the direct integration approach has been selected in the developed model because of its simplicity and easiness of implementation once the rotor flux density is estimated. The strategy is used by many authors [Zhu 1992, Proca 2003, Almandoz 2008] who propose several variations to the basic method in order to improve its accuracy maintaining its easiness. It is assumed that the magnetic induction caused by the rotor magnets follows a circumferential arc into the slot openings, causing a tangential force and, thus a cogging torque (see Figure 3.16).

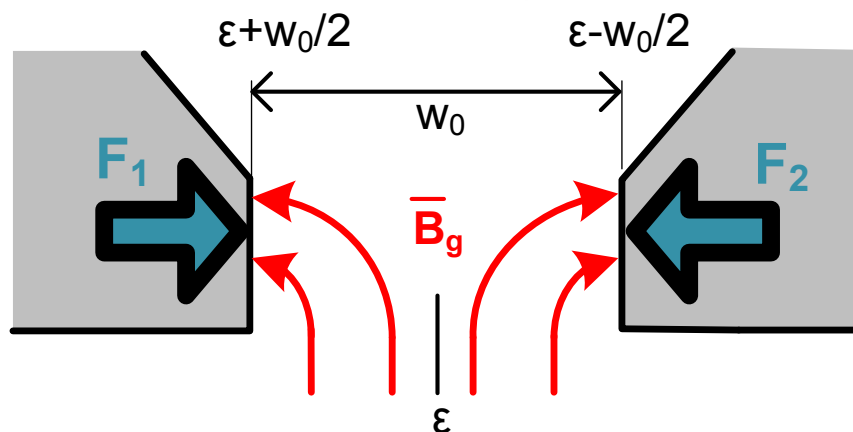


Figure 3.16. Detail of the slot opening surfaces where the forces are applied.

The total cogging torque due to a single slot can be calculated supposing that \mathbf{n}_{Fe} in a slot opening edge can be approximated by the tangential unitary vector \mathbf{e}_θ in that surface. The torque respect to the machine centre exerted in the slot opening can be calculated as the surface integral of the vectorial product of the position vector and the normal component of the magnetic pressure, i.e. the cogging torque in a single slot, noted T_{cs} , is estimated as:

$$T_{cs}(t) = \int_{S_l, S_r} P_M^m(\theta, t) (\mathbf{r} \mathbf{e}_r \times \mathbf{n}_{Fe}) dS \approx R_s \left(\int_{S_r} P_M^m(\theta, t) \mathbf{e}_z dS - \int_{S_l} P_M^m(\theta, t) \mathbf{e}_z dS \right) \quad (3.85)$$

where $P_M^m(\theta, t)$ is the magnetic pressure caused by the magnets (i.e. the pressure in no-load conditions), S_r and S_l denote, respectively, the right and the left slot opening surfaces, \mathbf{e}_r and \mathbf{e}_z are the radial and the axial unitary vector, respectively, and r is the position vector modulus. So, the cogging torque can be expressed as:

$$T_{cs}(t) = -R_s^2 \int_{\varepsilon - \frac{w_0}{2}}^{\varepsilon + \frac{w_0}{2}} \int_{-\frac{L_e}{2}}^{\frac{L_e}{2}} P_M^m(\theta, t) (\mathbf{e}_r \times \mathbf{n}_{Fe}) dz d\theta, \quad (3.86)$$

where ε and w_0 are both measured in radians. From (3.86) and (3.84) it can be deduced T_{cs} as a function of the magnets flux density in the airgap.

$$T_{cs}(t) = \frac{-R_s^2 L_e}{2\mu_0} \left[\int_{\varepsilon - w_0/2}^{\varepsilon} (B_g^m)^2(t, \theta) K_{sl}^2(\theta) d\theta - \int_{\varepsilon}^{\varepsilon + w_0/2} (B_g^m)^2(t, \theta) K_{sl}^2(\theta) d\theta \right] \mathbf{e}_z \quad (3.87)$$

For simplicity, from this point forwards T_{cs} should be treated as a scalar because its direction is always constant and equal to \mathbf{e}_z .

Obviously, K_{sl}^2 takes into account the effect of the stator slotting which, in fact, causes the cogging torque. In order to obtain the global cogging torque as a function of time it is necessary to compute the integral in θ for each instant.

A lot of computational effort could be saved if (3.87) is solved in the spectral domain, using the spatial FS of the magnetic induction and the relative permeance function, both squared. Namely,

$$(B_g^m)^2(t, \theta) = \sum_{k=-\infty}^{\infty} B_{g,k}^{m'} e^{j2pk(\theta - \omega_m t)} \quad \text{and} \quad (3.88)$$

$$K_{sl}^2(\theta) = \sum_{z=-\infty}^{\infty} K'_{sl,z} e^{jQz\theta}. \quad (3.89)$$

It should be noticed that the spatial period of K_{sl}^2 is $2\pi/Q$ rad (it has one slot pitch periodicity) while the spatial period of B_g^{m2} is just a pole pitch, i.e. π/p (remember that B_g^m has a periodicity of two pole pitches and that it is an odd function).

Applying (3.88) and (3.89) in (3.87) and computing the integrals it is obtained

$$T_{cs}(t) = \frac{-R_s^2 L_e}{2\mu_0} \sum_{k=-\infty}^{\infty} B_{g,k}^{m'} e^{-j2pk\omega_m t} \sum_{z=-\infty}^{\infty} K'_{sl,z} \frac{4e^{j\epsilon(2pk+Qz)} \sin^2\left(\frac{W_0}{4}(2pk+Qz)\right)}{j(2pk+Qz)} \quad (3.90)$$

By direct inspection of the temporal FS $T_{cs}(t)$ is:

$$T_{cs}(t) = \sum_{k=-\infty}^{\infty} T_{cs,k}^* e^{-jk2p\omega_m t} = \sum_{k=-\infty}^{\infty} T_{cs,k} e^{jk2p\omega_m t}, \quad (3.91)$$

$$T_{cs,k}^* = \frac{-R_s^2 L_e}{2\mu_0} B_{g,k}^{m'} \sum_{z=-\infty}^{\infty} K'_{sl,z} \frac{4e^{j\epsilon(2pk+Qz)} \sin^2\left(\frac{W_0}{4}(2pk+Qz)\right)}{j(2pk+Qz)}, \quad (3.92)$$

where the super-script * denotes the conjugate.

Once the temporal FS of a single slot torque is obtained it is possible to apply the superposition principle and calculate the total cogging torque. All the slots have the same torque except for a known phase delay, so its sum is given by

$$T_{c,k} = T_{cs,k} \sum_{n=1}^Q e^{-j(n-1)2pk\theta_s} = T_{cs,k} t_p \sum_{n=1}^{Q/t_p} e^{-j(n-1)2pk\theta_s}, \quad (3.93)$$

where θ_s is the slot pitch measured in mechanical radians. Due to the properties of the exponential, this sum will be non-null only for those k multiple of Q , so only these harmonics should be calculated.

Applying the previous expression the cogging torque is calculated and its value can be used in an optimization algorithm. If its temporal expression is required it is enough to perform the inverse FS.

3.3 Electric Characterization

From an electrical point of view a PMSM can be seen as an EMF voltage connected in series with an equivalent impedance, as it is shown in Figure 3.17. The aim of the electric model is to calculate the impedance values in order to solve the circuit and obtain the interaction variables between the PMSM and its power supply converter, i.e. power factor, consumed power, efficiency, etc.

As far as a detailed study of the power interface between the grid and the machine is beyond this thesis aims the combined effect of the grid and the power converter is approximated by a current source with known current value $I_{ph}(t)$, where ph denotes a single phase. It should be noticed that, except this current source all the electric components in Figure 3.17 are part of the PMSM model.

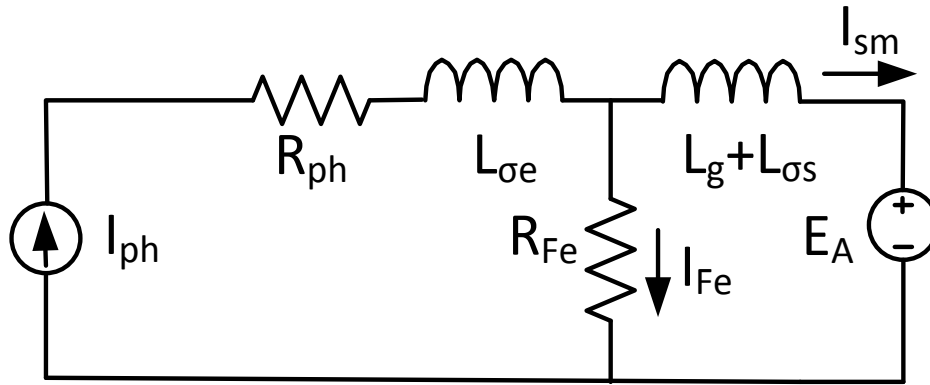


Figure 3.17. Phase A PMSM electric model including iron losses effect.

As it was mentioned, the EMF can be calculated using the proposed magnetic model, while the main goal in the electric domain is the estimation of the impedance values. This impedance has three main components:

- Inductance. It is the physical inductance presented by the stator coils, by means of its ability to store magnetic energy. Taking into account that the amount of magnetic energy in the ferromagnetic core is nearly null (in the ideal case of infinite permeability it will be exactly 0), three regions are capable to store this energy: the end-winding, the airgap and the stator slots, the associated inductances are, respectively, $L_{\sigma e}$, L_g and $L_{\sigma s}$.
- Copper resistance. It is the electrical resistance that the stator coils oppose to the current flowing through it, noted R_{ph} .
- Iron resistance. It is a fictitious parallel resistance that represents the losses in the ferromagnetic cores, noted R_{Fe} . It is just an equivalent impedance used in order to include all the losses in the proposed circuit.

In the next sections the calculus of the different impedance elements will be explained in detail. In order to do so it will be supposed, without loss of generality, that all the winding periodicities are connected in series.

3.3.1 PMSM Coil Inductance

The stator structure consists of a core of ferromagnetic material and copper coils wound around it; therefore, it is obvious that a PMSM behaves as an inductance in series with a voltage source (the EMF). The calculus of this inductance is not an easy task as far as many geometrical features must be considered. Traditionally, the calculus of an electrical machine inductance is subdivided according to the physical region where the magnetic energy is stored: the airgap inductance, the slot inductance and the end-winding inductance.

Figure 3.18 shows an example of magnetic energy stored in the slots and the airgap by means of the armature reaction. As it can be seen, the slots openings and the airgap store most of the energy, so their contribution to the total inductance will be high.

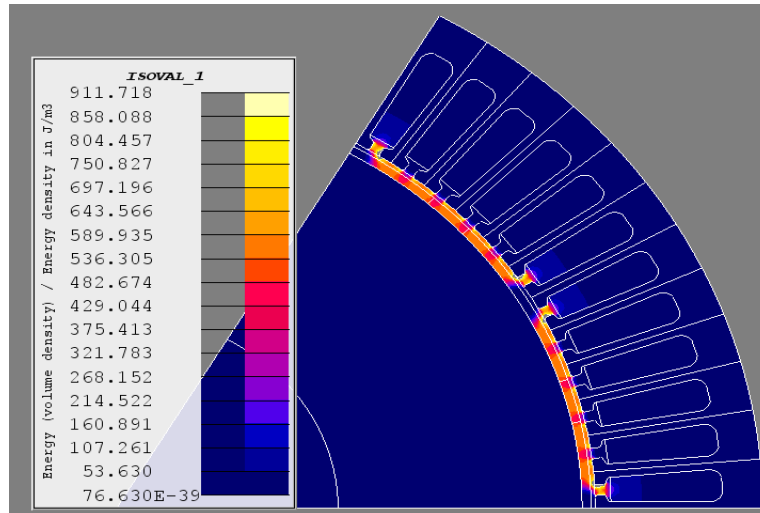


Figure 3.18. Magnetic energy stored in a PMSM due to the armature reaction. FEM simulation in FLUX®.

3.3.1.1 Airgap Inductance

The airgap is one of the main regions where magnetic energy induced by the armature reaction is stored. This is logical as far as the main flux path flows through the airgap in order to perform energy conversion.

In the literature, several airgap inductance estimation methods have been developed, a comparative study of them is included in [Rodríguez 2013]. In the present work an improvement of the approach done by [Hanselman 2012] is applied.

It is very important to notice that the airgap is shared by coils of m phases. Due to this fact, each phase undergoes not only an inductance due to its own flux (the so called self-inductance) but an inductance due to the flux induced by the other phases (the mutual inductance).

For a PMSM with m phases without neutral, the sum of all currents must be 0 and the mutual inductances between phases are all the same and equal to M_g due to geometrical symmetries. Taking this into account it can be shown that

$$L_g = L_g^{si} - M_g, \quad (3.94)$$

where L_g is the airgap total inductance, L_g^{si} the airgap self-inductance and M_g the mutual inductance.

Using the concept of scale factor (S^l) a reluctance equivalent circuit is defined (see Figure 3.19).

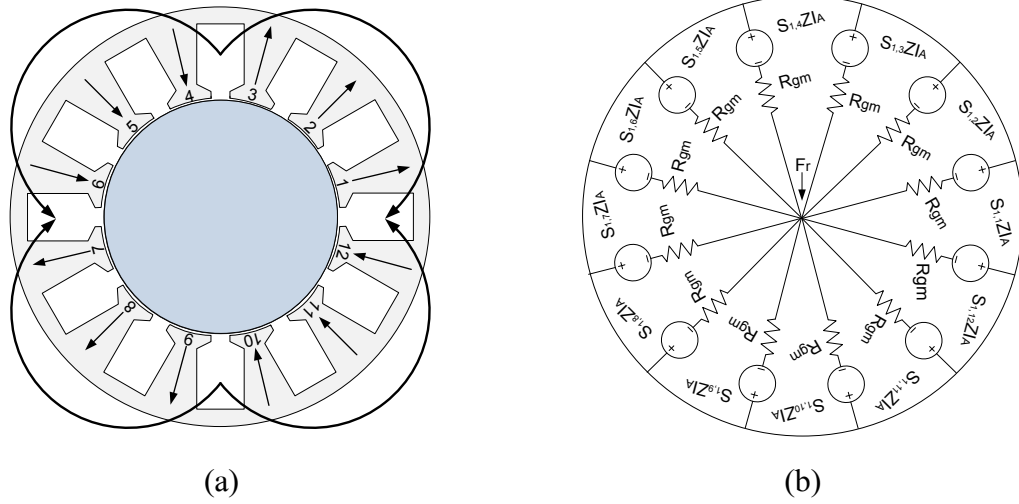


Figure 3.19. Example of phase A winding for a Q12p2 machine (a) and its equivalent reluctance circuit (b).

The proposed reluctance circuit has one branch for each tooth within a spatial periodicity (t_p). R_{gm} is the sum of the airgap and the magnet reluctances seen by each tooth. The solution of the above magnetic circuit for one phase (e.g. phase A) is

$$\text{MMF}_n^1(t) = Z(S_n^1 + F_r)I^1(t) = Z\left(S_n^1 - \frac{1}{Q}\sum_{l=1}^Q S_l^1\right)I^1(t), \quad (3.95)$$

where MMF_n^1 is the MMF generated by phase A in tooth n , I^1 is the phase A current, S_n^1 is the phase A scale factor in tooth n and $ZF_r I^1(t)$ is the fictitious magnetic potential at the centre of the machine. F_r has critical relevance since it is established in order to ensure that the magnetic intensity field associated with the generated MMF is solenoidal and fulfils Maxwell equations, i.e. that its surface integral through the airgap is null.

Once the MMF_n^1 is known, it is possible to calculate the magnetic flux density and the flux under each tooth:

$$\phi_{g,n}^{a,1}(t) = \frac{\mu_0}{\delta} \text{MMF}_n^1(t) \frac{L_e 2\pi R_s}{Q}. \quad (3.96)$$

The airgap self-inductance is defined as the flux $\phi_{g,n}^{a,1}$ linked by phase A divided by its current I^1 .

$$L_g^{si} = Z t_p \sum_{n=1}^{Q/t_p} S_n^1 \frac{\phi_{g,n}^{a,1}(t)}{I^1(t)} = Z^2 t_p \frac{\mu_0 L_e 2\pi R_s}{\delta} \sum_{n=1}^{Q/t_p} S_n^1 \left(S_n^1 - \frac{t_p}{Q} \sum_{l=1}^{Q/t_p} S_l^1 \right). \quad (3.97)$$

It is possible to generalize the result obtained in order to calculate the flux generated by phase A and linked by any other phase (e.g. phase B), obtaining the mutual inductance. In this case, the mutual inductance is equal to

$$M_g = Z t_p \sum_{n=1}^{Q/t_p} S_n^2 \frac{\Phi_{g,n}^{a,1}(t)}{I^1(t)} = Z^2 t_p \frac{\mu_0 L_e 2\pi R_s}{\delta Q} \sum_{n=1}^{Q/t_p} S_n^2 \left(S_n^1 - \frac{t_p}{Q} \sum_{l=1}^{Q/t_p} S_l^1 \right). \quad (3.98)$$

Thus, the total airgap inductance is

$$L_g = Z t_p \sum_{n=1}^{Q/t_p} (S_n^1 - S_n^2) \frac{\Phi_{g,n}^{a,1}(t)}{I_A(t)} = Z^2 t_p \frac{\mu_0 L_e 2\pi R_s}{\delta Q} \sum_{n=1}^{Q/t_p} (S_n^1 - S_n^2) \left(S_n^1 - \frac{t_p}{Q} \sum_{l=1}^{Q/t_p} S_l^1 \right). \quad (3.99)$$

The method introduced above assumes that the airgap effective length (δ) is constant along the tangential direction. However, δ depends on the tangential coordinate θ due to the existence of stator slotting. In many PMSM the effect of the slots in the airgap inductance cannot be neglected without considerable accuracy loss.

In [Rodríguez 2013] the slot correction factor defined in (3.20) is used in order to take into account that dependence. Therefore $\delta(\theta)$ is defined as

$$\delta(\theta) = g(\theta) + \frac{l_m}{\mu_r} \quad (3.100)$$

and (3.99) should be rewritten as

$$L_g = Z^2 t_p \frac{\mu_0 L_e 2\pi R_s}{Q} \int_{-\theta_s}^{\theta_s} \frac{1}{\delta(\theta)} d\theta \sum_{n=1}^{Q/t_p} (S_n^1 - S_n^2) \left(S_n^1 - \frac{t_p}{Q} \sum_{l=1}^{Q/t_p} S_l^1 \right). \quad (3.101)$$

Due to the better results achieved and the negligible increase in the computation time, (3.101) is preferred to (3.99), so it will be used in the present work.

3.3.1.2 Slot Inductance

The coils generate a magnetic field not only in the airgap and in the ferromagnetic cores but also in the same slots where they are wound. Since a magnetic field exists in the slots air and copper, a non-negligible inductance will appear, especially in the slots openings, as far as they are a low reluctance flux path.

This inductance presents a high dependence of the winding type, single or double layer, so the two configurations will be separately studied. Figure 3.20 shows the typical slot for both winding options.

A slot inductance analytic model could be performed solving equation (3.102) for single layer slots and (3.103) for double layer slots.

$$\frac{1}{2} L_s I^2 = \frac{1}{2} \mu_0 \int_V H(x)^2 dV \quad (3.102)$$

where L_s is the inductance due to a single slot and V is the slot total volume.

$$\frac{1}{2}L_{su}I_u^2 + \frac{1}{2}L_{sd}I_d^2 + L_{sm}I_uI_d = \frac{1}{2}\mu_0 \int_V H(x)^2 dV. \quad (3.103)$$

As it is shown in (3.103), as far as two different coils are wound in the same slot not one but three different inductances will appear: the self-inductance of the “up” coil (L_{su}), the self-inductance of the “down” coil (L_{sd}) and the mutual inductance (L_{sm}). It is important to notice that these self-inductances are not equal, as far as the geometrical situation of the coils is not the same.

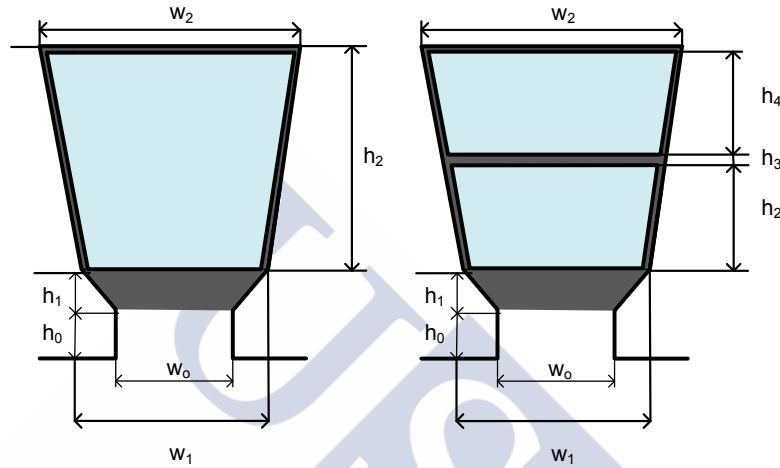


Figure 3.20. Example of the two main cases of slot windings types.

There exists a huge amount of slot geometries with their own analytical approximations, some of them are listed in [Pyrhönen 2008]. However, a more detailed study is carried out for the most common slot geometries: the uniform and the non-uniform one (a slot which area increases with the radius). A complete deduction of their values, based in (3.102) and (3.103) is included in Appendix B. Here the final results of the appendix are included in Table 3.3 in order to show the associated slot inductance for the main slot geometries.

Once a single slot inductance has been obtained the total slot inductance in the PMSM ($L_{\sigma s}$) should be deduced. In the case of a single layer machine it is quite straightforward to deduce

$$L_{\sigma s} = \frac{Q}{m} L_s, \quad (3.104)$$

where L_s is chosen depending on the slot geometry (see Table 3.3).

The case of a double layer machine can be much more complicated since the number of slots shared with the other phases and the slot region occupied by the phase coils must be taken into account in order to obtain $L_{\sigma s}$. Thus, each case has to be analyzed independently.

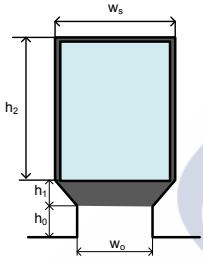
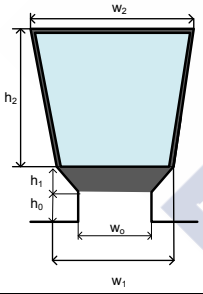
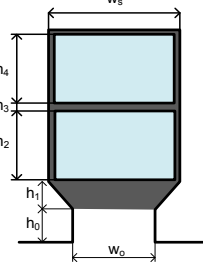
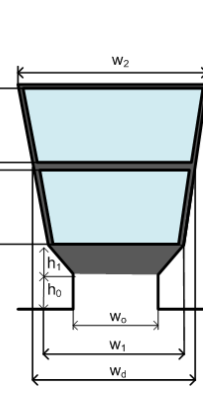
However, in the particular case of a three-phase machine wound in the star of slots it is possible to find an empirical rule in order to obtain $L_{\sigma s}$. As far as this type of winding is the most common, this approach will be used.

It should be noticed that, in every winding periodicity there are exactly three slots in which two different phase coils are emplaced. Moreover, these slots are equally spaced and wound according to Table 3.2.

Table 3.2. Two layers slot distribution in a three phases PMSM.

	Slot 1	Slot 2	Slot 3
Up region	Phase A ⁺	Phase B ⁺	Phase C ⁺
Down region	Phase C ⁻	Phase A ⁻	Phase B ⁻

Table 3.3. Slot inductance analytical approach for different slot geometries.

Type	Geometry	Inductance
Single layer, uniform		$L_s = \mu_0 Z^2 L_e \left[\frac{h_2}{3w_s} + \frac{h_1}{w_s - w_0} \ln \left(\frac{w_s}{w_0} \right) + \frac{h_0}{w_0} \right] \quad (3.105)$
Single layer, non-uniform		$L_s = \mu_0 Z^2 L_e \left[\frac{h_0}{w_0} + \frac{h_1}{w_1 - w_0} \ln \left(\frac{w_1}{w_0} \right) + \frac{h_2}{(w_1 + w_2)^2} K_w \right] \quad (3.106)$ $K_w = \left(\frac{w_1 + 3w_2}{4} - \frac{w_2^2}{2(w_2 - w_1)} - \frac{w_2^3}{(w_2 - w_1)^2} + \frac{w_2^4}{(w_2 - w_1)^3} \ln \left(\frac{w_2}{w_1} \right) \right) \quad (3.107)$
Double layer, uniform		$L_{su} = \mu_0 L_e Z^2 \left(\frac{h_4}{3w_s} + \frac{h_2 + h_3}{w_s} + \frac{h_1}{w_s - w_0} \ln \left(\frac{w_s}{w_0} \right) + \frac{h_0}{w_0} \right) \quad (3.108)$ $L_{sd} = \mu_0 L_e Z^2 \left(\frac{h_2}{3w_s} + \frac{h_1}{w_s - w_0} \ln \left(\frac{w_s}{w_0} \right) + \frac{h_0}{w_0} \right) \quad (3.109)$ $L_{sm} = \left(\frac{h_2}{2w_s} + \frac{h_1}{w_s - w_0} \ln \left(\frac{w_s}{w_0} \right) + \frac{h_0}{w_0} \right) \quad (3.110)$
Double layer, non-uniform		$L_{su} = \mu_0 Z^2 L_e \left[\frac{h_0}{w_0} + \frac{h_1}{w_1 - w_0} \ln \left(\frac{w_1}{w_0} \right) + \frac{h_2 + h_3}{w_d - w_1} \ln \left(\frac{w_d}{w_1} \right) + \frac{h_4}{(w_d + w_2)^2} K_{wu} \right] \quad (3.111)$ $L_{sd} = \mu_0 Z^2 L_e \left[\frac{h_0}{w_0} + \frac{h_1}{w_1 - w_0} \ln \left(\frac{w_1}{w_0} \right) + \frac{h_2}{(w_1 + w_2)^2} K_{wd} \right] \quad (3.112)$ $L_{sm} = \mu_0 Z^2 L_e \left[\frac{h_0}{w_0} + \frac{h_1}{w_1 - w_0} \ln \left(\frac{w_1}{w_0} \right) + \frac{h_4}{(w_d + w_1)} K_{wm} \right] \quad (3.113)$ $K_{wu} = \left(\frac{w_d + 3w_2}{4} - \frac{w_2^2}{2(w_2 - w_d)} - \frac{w_2^3}{(w_2 - w_d)^2} + \frac{w_2^4}{(w_2 - w_d)^3} \ln \left(\frac{w_2}{w_d} \right) \right) \quad (3.114)$ $K_{wd} = \left(\frac{w_1 + 3w_d}{4} - \frac{w_d^2}{2(w_d - w_1)} - \frac{w_d^3}{(w_d - w_1)^2} + \frac{w_d^4}{(w_d - w_1)^3} \ln \left(\frac{w_d}{w_1} \right) \right) \quad (3.115)$ $K_{wm} = \left(0.5 - \frac{w_d}{w_d - w_1} + \frac{w_d^2}{(w_d - w_1)^2} \ln \left(\frac{w_d}{w_1} \right) \right) \quad (3.116)$

An important advantage of that configuration is that all the phases see the same inductance, as far as they have the same number of coils wound in the upper and in the lower region of the slot.

Thus, taking this fact into account the total inductance will be given by

$$L_{\sigma s} = \left(\frac{2Q}{3} - 2t_p \right) L_s + t_p (L_{su} + L_{sd} + L_{sm}), \quad (3.117)$$

where L_s , L_{su} , L_{sd} and L_{sm} are chosen from Table 3.3 depending on the slot geometry.

3.3.1.3 End-Winding Inductance

The coils have a part that goes through the core following its axial direction; this region is where the EMF is generated. In order to do so, another coil region is necessary to connect an axial section with the next one; this region is called the end-winding. Figure 3.21 shows the stator of the IkerMAQ PMSM, a prototype fully designed and tested in IK4-Ikerlan and manufactured by LANCOR (see chapter 4). It is worthwhile to notice the remarkable end-winding region.



Figure 3.21. IkerMAQ stator, the end-windings at both sides are clearly visible.

The end-winding region presents its own inductance as far as a flux is generated by the current flowing through it, see Figure 3.22 (a).

The real end-winding geometry is unknown due to the uncertainties related with its real form and the randomness of the wires distribution, emplaced during the manufacturing process. In this context, the estimation of the end-winding induction is a very difficult task. Fortunately, as far as the end-winding region is formed by non-magnetic materials, the inductance is generally one order of magnitude below the slot and airgap ones, so a very rough estimation is enough in order to perform an initial design sizing.

In order to model the end-winding geometry, some authors approximate the coil by a straight line linked with the stator by two arcs [Almandoz 2008, Pyrhönen 2008], while other authors model the end-winding like a single circumferential arc [Hanselman 2012]. In this work, the latter will be used and the coil geometry shown in Figure 3.22 (b) will be adopted.

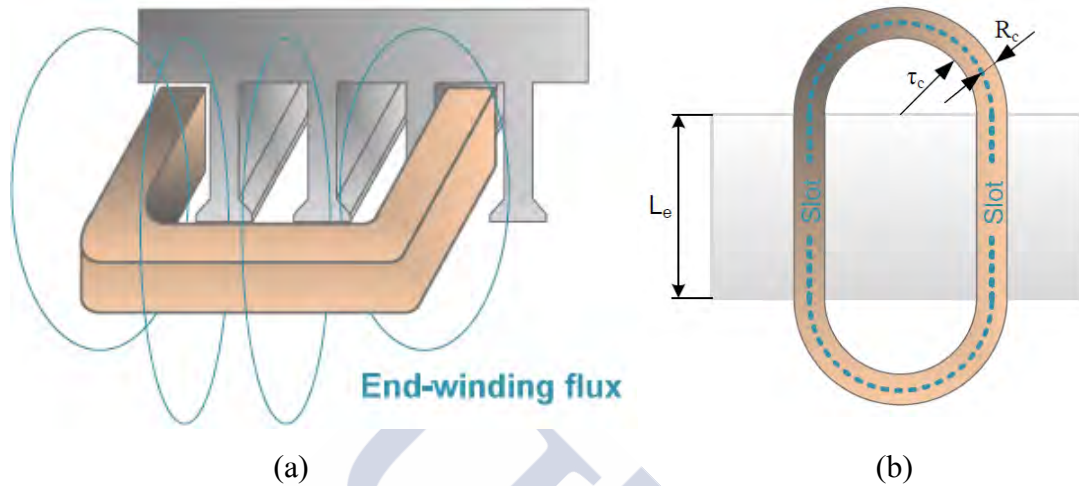


Figure 3.22. End winding geometry (a) Flux generated in the end-winding region and (b) Top view of a coil inserted in the stator slots.

The coils crossing the end-winding from a slot to another are modelled like a single wire with radius R_c following a circumference with radius τ_c (see Figure 3.22 (b)). R_c is estimated from the copper area of an individual wire (A_{Cu}) by

$$A_{Cu} = \frac{F_f A_s}{Z N_{lay}} \quad (3.118)$$

$$R_c = \sqrt{\frac{Z A_{Cu}}{\pi}} = \sqrt{\frac{A_s F_f}{\pi N_{lay}}} \quad (3.119)$$

where N_{lay} is the number of layers within a slot (i.e. the number of coils inside it), A_s is the slot cross-sectional area and F_f is the fill factor, defined as the ratio between A_s and the total copper area in a slot (see Figure 3.24). Generally the fill factor is imposed by manufacturing limitations and geometric reasons, because a rectangular slot cannot be completely filled with circular wires, F_f typical values are about 0.4 or 0.5.

The inductance L generated by a straight wire of finite length (l) and radius R_c can be approximated by [Hanselman 2012]:

$$L = \frac{\mu_0 l Z^2}{2\pi} \ln\left(\frac{l}{R_c}\right) \quad (3.120)$$

In the proposed problem l is equal to $\pi\tau_c$ with τ_c equal to half the mean coil pitch (τ_{cp})

$$\tau_c = \tau_{cp}/2, \quad (3.121)$$

so the total end-winding inductance is

$$L_{\sigma e} = \frac{QN_{lay}}{m} \frac{\mu_0 \tau_{cp} Z^2}{4} \ln \left(\frac{\tau_{cp}}{2R_c} \right), \quad (3.122)$$

where the factor QN_{lay}/m represents the total end-winding coils in one phase.

It is important to notice the meaning of τ_{cp} as the mean coil pitch. It can be calculated as

$$\tau_{cp} = \frac{1}{QN_{lay}} \sum_{l=1}^{QN_{lay}} |\text{in}L_l - \text{out}L_l| \theta_s R_s, \quad (3.123)$$

where $\text{out}L_l$ and $\text{in}L_l$ are the outward and inward slot where coil l was wound. The geometric meaning of θ_s and R_s are shown in Figure 3.1.

The aforementioned estimations are very rough as far as they are based in geometrical approximations that could be quite far from the real end-winding distributions. Moreover, between different phases magnetic coupling can arise, generating mutual inductances which value strongly depends on the random coil distribution. In spite of that it is supposed that the proposed calculus is accurate enough in order to estimate an approximate value of the end-winding inductance.

3.3.2 PMSM Resistance

3.3.2.1 Copper Resistance

Every material presents an opposition to the current flowing through it; this physical property is called electrical resistance. Conducting materials, such as copper and aluminium, present a low resistance. The coil resistance in an electrical machine is generally undesirable, because it generates losses proportional to the squared current flowing through it.

In this section the total winding resistance will be estimated taking into account the resistance behaviour with respect to both thermal and frequency phenomena.

If the wires have circular section, their diameter is

$$d_{Cu} = 2 \sqrt{\frac{A_{Cu}}{\pi}} = 2 \sqrt{\frac{F_f A_s}{ZN_{lay} \pi}}. \quad (3.124)$$

The mean wire length per turn in a phase can be estimated from the total stator axial length (L_{Fe}) and the mean coil pitch in the end-winding (τ_{cp}):

$$L_{wire} = 2(L_{Fe} + \pi \tau_{cp}/2), \quad (3.125)$$

so the total wire length in a phase is the mean wire length per turn multiplied by the number of turns:

$$L_{\text{phase}} = Z \frac{Q N_{\text{lay}}}{2m} L_{\text{wire}}. \quad (3.126)$$

Therefore, the resistance seen by the PMSM equivalent circuit (see Figure 3.17) and a direct current (DC) at 20°C is

$$R_{\text{DC},20^\circ} = \rho_{\text{Cu},20^\circ} \frac{L_{\text{phase}}}{A_{\text{Cu}}}, \quad (3.127)$$

where $\rho_{\text{Cu},20^\circ}$ is the copper resistivity at 20°C.

It is typical to assume that copper resistivity has a lineal dependence with temperature on a wide range of temperatures:

$$\rho_{\text{Cu}} = \rho_{\text{Cu},20^\circ} (1 + \alpha_{T_{\text{Cu}}} (T_{\text{Cu}} - 293.15\text{K})), \quad (3.128)$$

$$R_{\text{DC}} = R_{\text{DC},20^\circ} (1 + \alpha_{T_{\text{Cu}}} (T_{\text{Cu}} - 293.15\text{K})). \quad (3.129)$$

where ρ_{Cu} is the copper resistivity at temperature T_{Cu} measured in Kelvin, while $\alpha_{T_{\text{Cu}}}$ is the copper thermal coefficient generally assumed to be $\alpha_t = 0.0039\text{K}^{-1}$.

The resistance also presents an important dependence with respect to the frequency. Two physical phenomena cause resistance variation with frequency: the skin effect and the proximity effect.

- The skin effect is caused by Faraday's law, if the currents have high frequency, the temporal derivative of the magnetic field generated is high, so a voltage which opposes that change will appear inside the wire. This voltage directs the current to the conductor surface, avoiding its centre. The global effect is that the effective conductor cross-section is smaller than the physical one and, therefore, its resistance is higher.
- The proximity effect is equally caused by Faraday's law but, in this case, the magnetic field is generated by a wire in the neighbour of the considered one. If both wires have currents flowing in opposite directions the current density is higher close to the other conductor, while if the currents are flowing in the same directions the current density is higher in the surface away from the other wire.

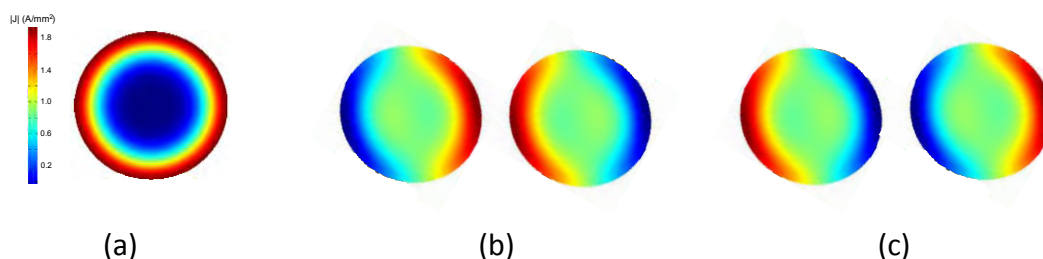


Figure 3.23. Graphic representations of frequency effects: skin effect (a), and proximity effect with current in the opposite directions (b) and in the same direction (c).

Frequency effects in wires have been widely studied in both, rotator and static electrical machines [Villar 2010, Hanselman 2012] here the main results will be presented.

Within a slot, the turns distribution shown in Figure 3.24 is supposed, where n_d is the number of turns uprightly distributed (in the case shown in Figure 3.24 $n_d = 4$).

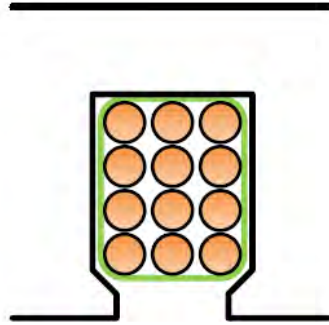


Figure 3.24. Distribution of wires within a slot.

For each positive angular frequency, $k\omega_e$, the skin depth δ_k , is defined as the distance where the density current is reduced at a 37% of its maximum value. It is possible to demonstrate that

$$\delta_k = \sqrt{\frac{2\rho_{Cu}}{k\omega_e\mu_{Cu}}}, \quad (3.130)$$

μ_{Cu} being the copper magnetic permeability (very close to that of the void μ_0).

The resistance for each harmonic can be calculated as [Villar 2010]

$$R_{ph,k} = R_{DC} \left[\Delta_k F(\Delta_k) + \frac{2}{3} (n_d^2 - 1) \Delta_k G(\Delta_k) \right], \quad (3.131)$$

where $F(\Delta_k)$ models the skin effect and $G(\Delta_k)$ the proximity one. These functions are given by

$$\Delta_k = \frac{d_{Cu}}{\delta_k}, \quad (3.132)$$

$$F(\Delta_k) = \frac{\sinh(2\Delta_k) + \sin(2\Delta_k)}{\cosh(2\Delta_k) - \cos(2\Delta_k)}, \quad (3.133)$$

$$G(\Delta_k) = \frac{\sinh(\Delta_k) - \sin(\Delta_k)}{\cosh(\Delta_k) + \cos(\Delta_k)}. \quad (3.134)$$

It is important to notice that the obtained resistance is not a single value but an array with one element for each current harmonic. This must be taken into account in order to calculate the copper losses, as far as the current may be contaminated by non-negligible harmonics.

3.3.2.2 Iron Resistance

As it was aforementioned the iron resistance is a fictitious quantity in order to take into account the magnetic iron losses in the PMSM equivalent circuit (see Figure 3.17).

This technique is the most popular in order to include the magnetic losses in the electric analysis.

It is supposed that the inverter behaves as an ideal current source, i.e. its current is independent of the connected PMSM and its temporal FS is known.

From an electric point of view all the magnetic losses, from both the ferromagnetic core and the magnets, are dissipated in R_{Fe} . Thus, the circuit can be solved as

$$R_{Fe} = \frac{m}{2(P_{Fe} + P_m)} \sum_{k=1}^{\infty} \left(2E_{A,k} + 2I_{sm,k}j\omega_e k(L_{\sigma s} + L_g) \right)^2, \quad (3.135)$$

where P_{Fe} and P_m are, respectively, the ferromagnetic core and magnets losses, and $E_{A,k}$ and $I_{sm,k}$ are the k^{th} harmonic of the voltages and currents represented in Figure 3.17.

From the R_{Fe} value it is possible to estimate $I_{sm,k}$ as

$$I_{sm,k} = \frac{R_{Fe}I_{ph,k} - E_{A,k}}{R_{Fe} + j\omega_e k(L_{\sigma s} + L_g)}. \quad (3.136)$$

In order to solve the previous equations an iterative algorithm is needed, because the calculus of R_{Fe} requires to know the magnetic losses, P_{Fe} and P_m . Since these losses are I_{sm} dependent, then the value of R_{Fe} is needed in order to obtain them. The proposed iterative loop is shown in Figure 3.25.

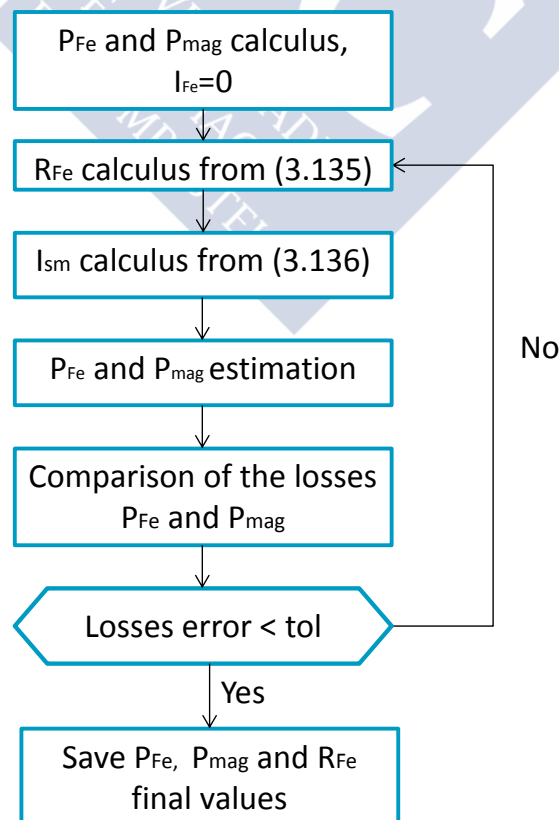


Figure 3.25. Flowchart of the R_{Fe} calculus algorithm.

If an adequate tolerance (tol) value is used (e.g. with 1% maximum error) the above algorithm converges in very few iterations as far as the initial iteration point, where the losses are estimated supposing $R_{Fe} \rightarrow \infty$, is close to the final solution.

Once R_{Fe} is obtained a complete electrical model is achieved. The proposed circuit will be used in the next section in order to estimate efficiency, losses and other important parameters related with the machine behaviour and its interaction with the inverter.

3.4 Efficiency and Losses Estimation

In this section the circuit shown in Figure 3.17 will be solved and the PMSM losses estimated in order to obtain the PMSM figures of merit, such as its efficiency, power factor, electric loading or total electrical and mechanical power.

3.4.1 Copper and Iron Losses

In order to obtain the copper losses, the converter and the grid are modelled as an ideal current source, whose temporal FS is equal to:

$$I_{ph}(t) = \sum_{k=-\infty}^{\infty} I_{ph,k} e^{jk\omega_e t}. \quad (3.137)$$

Applying the superposition principle and the properties of orthogonality of the FS (see Appendix B), the mean copper losses due to the Joule effect will be equal to:

$$P_{Cu} = 2m \sum_{k=1}^{\infty} |I_{ph,k}|^2 R_{ph,k}, \quad (3.138)$$

where $R_{ph,k}$ is calculated according to (3.131).

The iron losses are induced by the temporal dependence of the magnetic field in the ferromagnetic core. An accurate estimation of these losses is not an easy task, as they are caused by many physical phenomena within the microscopic ferromagnetic core structure.

It is well known that the rotor iron losses are negligible in PMSM, because the magnetic field is rotating in synchronism with the rotor [Hanselman 2012], so the rotor core sees a quasi-steady magnetic field and the losses generated are neglected for the sake of calculus efficiency. However, rotor losses can play a major role in the magnets heating so their consequences will be studied in a subsequent section.

The stator losses will be estimated using the classical Bertotti's approach [Bertotti 1988] which classifies them in three main contributions:

- **Eddy current losses:** due to the voltages induced in the iron by means of Faraday's law. The voltages generate Foucault (or eddy) currents causing losses in the ferromagnetic material.
- **Hysteresis losses:** due to the energy necessary to orientate the magnetic domains within the core. They are associated with the material hysteresis loop because this energy is proportional to the area enclosed by its BH curve.
- **Additional losses (or excess eddy current losses):** extra losses generated in the material due to the magnetic intensity temporal variation. Some authors propose that they are caused by new magnetic fields induced by the eddy currents.

An integrated formula taking into account all these phenomena in a laminated core for sinusoidal magnetic excitation is presented, for instance, in [Chen 2002]

$$P_{Fe} = M_{Fe} \left(k_h f_e B_{pk}^{\alpha_h} + k_e f_e^2 B_{pk}^2 + k_a f_e^{1.5} B_{pk}^{1.5} \right), \quad (3.139)$$

where P_{Fe} are the total iron losses, M_{Fe} the ferromagnetic material weight, f_e the magnetic field frequency (i.e. the electrical frequency) and B_{pk} is the flux density peak value in the material. Coefficients α_h , k_h , k_e and k_a depend on the core material. In the presented model they are calculated from the manufacturer datasheet by the least square method. In (3.139) the first term represents the hysteresis losses, the second the eddy current ones and the third the additional ones.

It is possible to extend (3.139) for a generic flux density waveform [Bertotti 1988]:

$$P_{Fe} = M_{Fe} \left(k_h f_e B_{pk}^{\alpha_h} + \frac{k_e}{2\pi^2} \left\langle \left| \frac{dB}{dt} \right|^2 \right\rangle + \frac{k_a}{8.763} \left\langle \left| \frac{dB}{dt} \right|^{1.5} \right\rangle \right), \quad (3.140)$$

where $\langle A \rangle$ denotes the mean value of the variable A during a period.

In order to obtain the iron losses, the stator core is divided in two regions: the teeth and the yoke, where the flux density has been previously calculated. The expressions of their temporal FS were presented in equations (3.64) and (3.66), respectively. The iron losses are given by

$$P_{Fet,n} = M_{Fet} \frac{t_p}{Q} \sum_{n=1}^{Q/t_p} \left(k_h f_e B_{tpk,n}^{\alpha_h} + \frac{k_e}{2\pi^2} \left\langle \left| \frac{dB_{t,n}}{dt} \right|^2 \right\rangle + \frac{k_a}{8.763} \left\langle \left| \frac{dB_{t,n}}{dt} \right|^{1.5} \right\rangle \right), \quad (3.141)$$

$$P_{Fes} = M_{Fes} \frac{t_p}{Q} \sum_{n=1}^{Q/t_p} \left(k_h f_e B_{spk,n}^{\alpha_h} + \frac{k_e}{2\pi^2} \left\langle \left| \frac{dB_{s,n}}{dt} \right|^2 \right\rangle + \frac{k_a}{8.763} \left\langle \left| \frac{dB_{s,n}}{dt} \right|^{1.5} \right\rangle \right), \quad (3.142)$$

$$P_{Fe} = P_{Fet} + P_{Fes}, \quad (3.143)$$

where subscript n numerates the geometric period where teeth and yoke sections are contained, M_{Fet} is the total tooth mass, M_{Fes} the total yoke mass and B_t and B_s are the magnetic fields in the teeth and in the yokes, respectively. It is important to notice that the amplitude of these fields, and even their waveforms, change in each stator

teeth and yoke section, due to the armature reaction. Therefore, a summation of the losses in each tooth and yoke section should be carried out in order to calculate the total iron losses.

The teeth and yoke total mass (M_{Fet} and M_{Fey}) are calculated from the stator geometrical dimensions:

$$M_{Fet} = \rho_{Fe} Q h_t w_t L_e \quad (3.144)$$

$$M_{Fes} = \rho_{Fe} L_e w_{sy} \pi (2R_{se} - w_{sy}) \quad (3.145)$$

where ρ_{Fe} is the stator core density and R_{se} the external stator radius

3.4.2 Magnet Losses

As it was previously introduced rotor losses are not important in terms of the total energy consumption, so they can be neglected in the efficiency calculus. However, an important part of these losses are concentrated in the magnets, causing their heating and, in very severe cases, leading to permanent demagnetization.

In this section an approach in order to take into account the magnet losses caused by the MMF temporal and spatial harmonics will be presented. A more detailed study, including the stator slotting effect and a validation example was previously presented in [Rodríguez 2014-b].

In the proposed model, in addition to the general approximations explained in 1.3, the following assumptions are made:

1. The PMSM is a polyphase AC machine with balanced winding distribution.
2. Firstly, only the radial component of the magnetic induction in the magnets is taken into account. The flux density is supposed to be constant along the radial dimension of the magnet. This leads to a simple model without significant loss of accuracy in most of the PMSMs of practical interest.
3. The problem is considered resistance-limited; i.e. the magnetic reaction of eddy current is neglected.
4. Magnets end-effect is supposed to be negligible in the problem formulation. It will be taken into account in the final result with a 2-D to 3-D correction factor.
5. The magnets are relatively thin, so the radial coordinate r could be taken equal to R_m (see Figure 3.27)
6. The magnets are supposed to be homogenous and isotropic with electrical conductivity σ_m and relative magnetic permeability μ_{rm} .

3.4.2.1 Eddy Current Loss Estimation Method

The basis of the study is Faraday's equation and Ohm's law:

$$\nabla \times \mathbf{E} = -\frac{\partial \mathbf{B}}{\partial t}, \quad (3.146)$$

$$\mathbf{J} = \sigma_m \mathbf{E}, \quad (3.147)$$

where \mathbf{B} , \mathbf{E} and \mathbf{J} are the magnetic flux density, the electric field strength and the current density vectors, respectively. A graphical representation of the basic studied geometry is shown in Figure 3.27.

Equation (3.146) integration on surface S (see Figure 3.26) and Stoke's theorem yields

$$\oint \mathbf{E}(t, \theta_R) \cdot d\mathbf{l} = - \iint_S \frac{\partial \mathbf{B}(t, \theta_R)}{\partial t} \cdot \mathbf{n} \, dz \, d\theta_R, \quad (3.148)$$

the integration path on the left-hand side is the oriented closed-curve surrounding S .

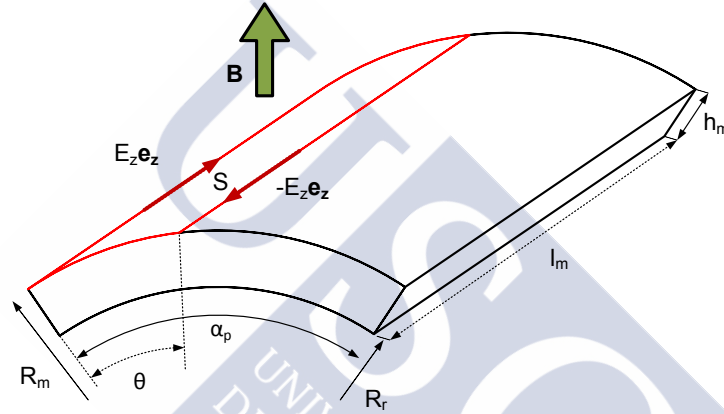


Figure 3.26. Example of integration area on the magnet.

If the PMSM axial dimension (in the z -axis) is much longer than its magnet pitch (the arch length covered by a magnet, $R_m \cdot \alpha_p$), i.e. if the length of the magnet is much higher than its width, a 2-D approximation can be used and Stoke's theorem leads to

$$(E_z(t, \theta) - E_z(t, 0))l_m = \int_0^\theta \int_0^{l_m} \frac{\partial B_g^r(t, \theta_R)}{\partial t} R_m \, dz \, d\theta_r, \quad (3.149)$$

where r , z and θ_R are the radial, the axial and the circumferential coordinates of the cylindrical system with respect to the rotor frame, $B_g^r(t, \theta_r)$ is the armature reaction in the rotor frame, l_m is the axial length of one magnet, and 0 rad is considered as the rotor position where the magnet edge is emplaced for $t = 0$.

If the simplified magnet geometry shown in Figure 3.26 is assumed and with the approximations previously made, equations (3.147) and (3.149) can be combined leading to [Madina 2011]:

$$J_z(t, \theta) = \sigma_m \int_0^\theta \frac{\partial B_g^r(t, \theta_r)}{\partial t} R_m \, d\theta_r + C(t), \quad (3.150)$$

where J_z is the axial component of the eddy current (the only considered not negligible), $B_g^r(t, \theta_r)$ is the radial component of the armature reaction with respect to

the rotor frame (thus, the main cause of rotor losses) and $C(t)$ is an integration constant equal to $\sigma_m E_z(t, 0)$. The value for this spatial constant is calculated taking into account that the total current in a magnet is 0 at any moment (particularization of the Maxwell's equation which states $\nabla \cdot \mathbf{E} = 0$ in absence of free charges), i.e.

$$\int_{\theta_0}^{\theta_0 + \alpha_p} J_z(t, \theta_r) d\theta_r = 0 \quad \forall t. \quad (3.151)$$

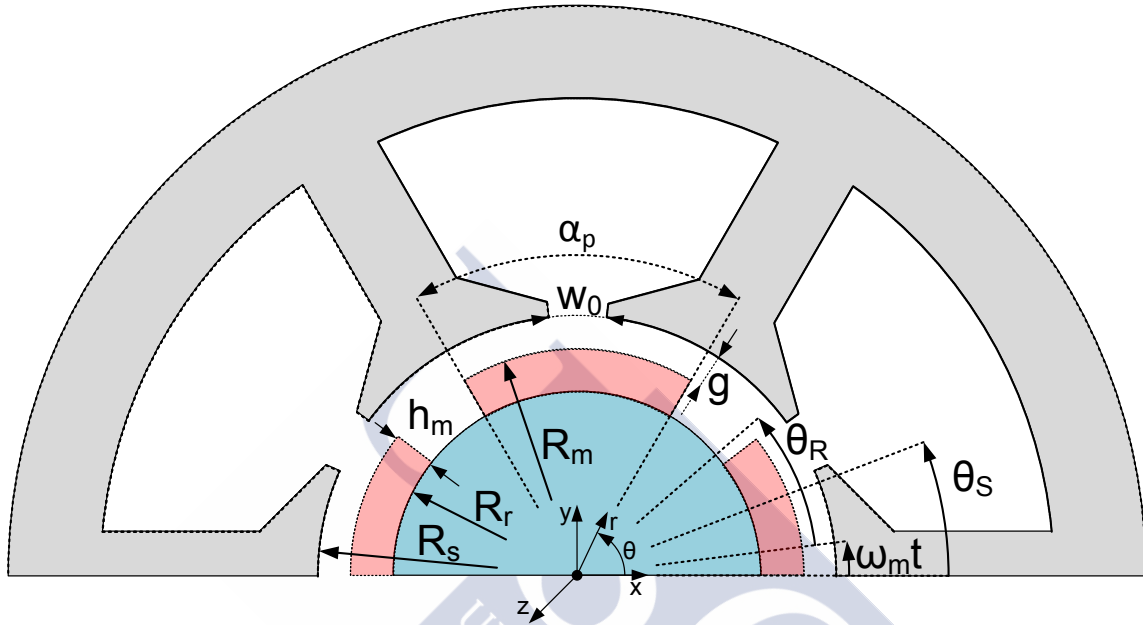


Figure 3.27. 2-D section of the PMSM geometry under study. Both angular references respect to the stator and the rotor have been included.

Once the current has been obtained, the next step is to calculate the mean power dissipated in the magnets which is equal to:

$$P_m = \frac{2 p K_{3D} l_m}{T} \int_{t=0}^T \int_{\theta_r=\theta_0}^{\theta_0 + \alpha_p} \int_{r=R_r}^{R_m} \frac{J_z^2(t, \theta_r)}{\sigma_m} r dr d\theta_r dt. \quad (3.152)$$

where T is the mechanical period (i.e. $T = p/f_e$), P_m is the main power dissipated by the magnets and K_{3D} is a correction factor proposed by [Ruoho 2009] which takes into account the end-effects and the axial segmentation of the magnets:

$$K_{3D} = N_m \frac{3}{4} \frac{l_m^2}{w^2 + l_m^2}, \quad (3.153)$$

where N_m is the number of magnet pieces in the axial direction and w is the equivalent width of the magnet, i.e.:

$$N_m = L_{Fe}/l_m \quad \text{and} \quad (3.154)$$

$$w = \alpha_p (R_m + R_r)/2. \quad (3.155)$$

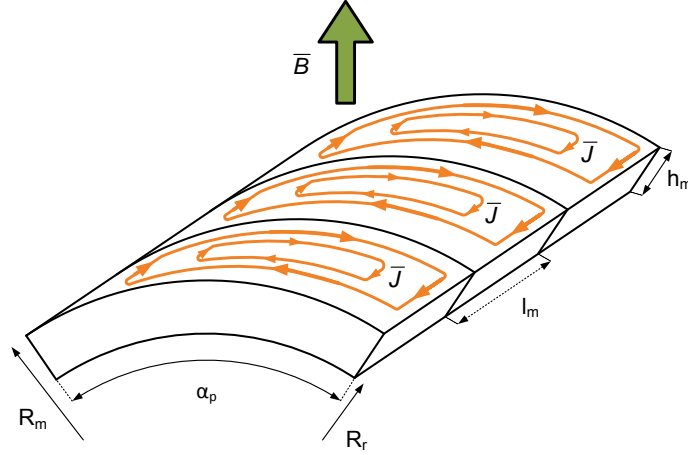


Figure 3.28. One pole geometry with three axial slices. Eddy current paths are represented.

Equations (3.150)-(3.153) completely describe the calculus of eddy current losses; only two variables need to be obtained in order to fulfil the analysis. The first one is the derivative of the magnetic induction with respect to time which mainly depends on the armature reaction MMF. The second one is the integration constant which mainly depends on the magnet pitch.

The full process implemented in order to obtain these two critical variables is described below.

3.4.2.2 Magnetic Induction in the Rotor Reference Frame

It is well known that the main cause of eddy-current losses in the magnets is the MMF spatial and temporal harmonics which are not in synchronism with the rotor. An expression for $B_g^a(t, \theta)$ referred to the stator reference frame was previously obtained in (3.52). The final results will be included for the sake of clarity:

$$B_g^a(\theta, t) = \frac{\mu_0}{\delta} \sum_{k=-\infty}^{\infty} \sum_{l=-\infty}^{\infty} m \delta_{0, \text{mod}(m, k+l)} F_{ph, k} I_l^1 e^{j(k t_p \theta + l \omega_e t)}, \quad (3.156)$$

where the superindex is referred to phase A, phase A is assumed to be the temporal angular reference so its phase angle is taken equal to 0 rad. It is important to notice that the harmonics in (3.156) are only different from 0 when the sum $k + l$ is a multiple of m .

It is quite clear that, in the rotor reference frame, the circumferential coordinate θ is given by

$$\theta = \theta_r + \omega_m t, \quad (3.157)$$

where θ_r is the tangential coordinate referred to the rotor reference frame and ω_m the mechanical angular speed, related with the electrical pulsation by

$$\omega_m = \omega_e / p. \quad (3.158)$$

It is quite straightforward to refer the armature reaction to the rotor reference frame by replacing (3.158) in (3.156):

$$B_g^r(\theta_r, t) = \frac{\mu_0}{\delta} \sum_{k=-\infty}^{\infty} \sum_{l=-\infty}^{\infty} m \delta_{0, \text{mod}(m, k+l)} e^{j(k t_p \theta_r)} F_{ph, k} I_l^1 e^{j\omega_m t (k t_p + l p)}, \quad (3.159)$$

where $B_g^r(\theta_r, t)$ is the radial component of the armature reaction with respect to the rotor frame and I_l^1 the phase A current. The temporal derivative of the armature reaction can be obtained from (3.159) as

$$\frac{\partial B_g^r(\theta_r, t)}{\partial t} = j\omega_m \sum_{k=-\infty}^{\infty} \sum_{l=-\infty}^{\infty} (k t_p + l p) B_{g, kl}^r(\theta_r) e^{j\omega_m t (k t_p + l p)}, \quad (3.160)$$

where $B_{g, kl}^r$ is seen as a multivariable Fourier coefficient given by

$$B_{g, kl}^r(\theta_r) = \frac{\mu_0}{\delta} m \delta_{0, \text{mod}(m, k+l)} e^{j(k t_p \theta_r)} F_{ph, k} I_l^1. \quad (3.161)$$

This general formulation allows us a simple, precise calculus of the temporal derivative of the armature reaction field in the rotor. An especially important case arises when the PMSM current is considered perfectly sinusoidal, i.e.

$$I_l^1 = 0 \Leftrightarrow l \neq \pm 1 \quad (3.162)$$

This assumption yields a great simplification of (3.159) into

$$B_g^r(\theta_r, t) = \frac{3}{2} \frac{\mu_0}{\delta} I_1^1 \left(\sum_{k=[\dots-1, 2, 4, \dots]}^{\infty} F_{ph, k} e^{j k t_p \theta_r} e^{j\omega_m t (k t_p + p)} + \sum_{k=[\dots-2, 1, 4, \dots]}^{\infty} F_{ph, k} e^{j k t_p \theta_r} e^{j\omega_m t (k t_p - p)} \right), \quad (3.163)$$

where I_1^1 is the only term in the current temporal FS and it is equal to the half of the peak value of phase A current. The transformation of (3.159) into (3.163) and its implications are fully included in [Rodríguez 2014-b].

3.4.2.3 Total Current Density in the Magnets

Once the temporal derivative of the magnetic induction has been estimated, the next step is the calculus of the total current density in the magnets. From (3.150) and (3.151) it is given by

$$\int_{-\alpha_p/2}^{\alpha_p/2} \left(\sigma_m \int_{\theta=-\alpha_p/2}^{\theta_r} \frac{\partial B_g^r(t, \theta)}{\partial t} R_m d\theta + C(t) \right) d\theta_r = 0. \quad (3.164)$$

Direct inspection of (3.160) shows that the derivative term can be expressed as a spatial FS with respect to the rotor angular coordinate θ_r as follows:

$$\frac{\partial B_g^r(t, \theta_r)}{\partial t} = \sum_{k=-\infty}^{\infty} B_k'(t) e^{j k t_p \theta_r}, \quad (3.165)$$

where $B'_k(t)$ is a t dependent spatial Fourier index given by

$$B'_k(t) = j\omega_m \frac{\mu_0}{\delta} \sum_{l=-\infty}^{\infty} (kt_p + lp) j\omega_m m \delta_{0, \text{mod}(m, k+l)} F_{ph, k} I_l^1 e^{j\omega_m t (kt_p + lp)}. \quad (3.166)$$

By direct integration of (3.164) it is obtained [Rodríguez 2014-b]

$$C(t) = \frac{\sigma_m R_m}{\alpha_p} 2 \sum_{k=-\infty}^{\infty} j \frac{B'_k(t)}{k^2} \sin(k\alpha_p/2). \quad (3.167)$$

Thus, the complete expression of the current density in the magnets is

$$J_z(t, \theta_r) = \sigma_m R_m j \sum_{k=-\infty}^{\infty} \frac{B'_k(t)}{k} \left(e^{jk\theta_r} - \text{sinc}(k\alpha_p/2) \right). \quad (3.168)$$

These calculations can be directly used in (3.152) in order to obtain the mean power dissipated in the magnets. Notice that properties of the Fourier series can be applied in the calculation of the temporal integral, while the spatial one (with respect to θ_r) can be computed numerically. Figure 3.29 shows a typical eddy current distribution over a magnet; the numerical simulation was made with the commercial software FLUX2D®.

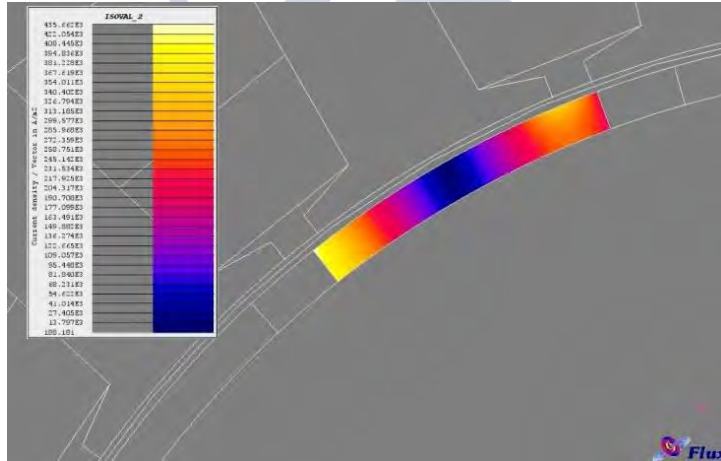


Figure 3.29. Current density in one of the magnets. Current is nearly constant with r .

3.4.3 Efficiency and other Quality Parameters

In order to accurately estimate the efficiency and other critical quality parameters, such as the power factor, the equivalent PMSM circuit must be solved. For the sake of completeness, the circuit scheme is included in Figure 3.30.

The impedance value was calculated in section 3.3, while I_{ph} is considered as a sinusoid, polluted with harmonics, but with a known amplitude and delay with respect to the EMF (E_A), i.e. it is supposed that the PMSM control system is fast and accurate enough for correctly provide the needed current supply.

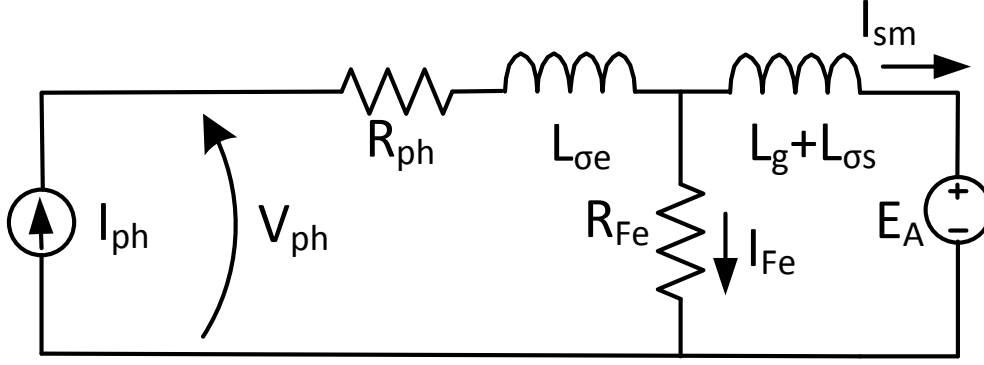


Figure 3.30. Phase A PMSM electric model.

Thus, in order to solve the circuit, the values of V_{ph} and I_{SM} should be obtained. It must be taken into account that the circuit values are frequency dependant so a phasor analysis will be performed.

The temporal FS of V_{ph} and I_{SM} are respectively given by

$$I_{sm,k} = \frac{I_{ph,k} R_{Fe} - E_{A,k}}{jk\omega_e(L_g + L_{\sigma s}) + R_{Fe}} \quad \text{and} \quad (3.169)$$

$$V_{ph,k} = (R_{ph} + jk\omega_e L_{\sigma e}) I_{ph,k} + jk\omega_e (L_g + L_{\sigma s}) I_{sm,k} + E_{A,k}. \quad (3.170)$$

The next study will be performed, without generality loss, supposing PMSM generator operation.

3.4.3.1 Power, Torque and Efficiency

The mean electrical output power is

$$P_{elec} = 2m \sum_{k=1}^{\infty} \text{real}(V_{ph,k} I_{ph,k}^*), \quad (3.171)$$

where $I_{ph,1}^*$ denotes the conjugate of $I_{ph,1}$. The total mechanical power in the shaft is

$$P_{mec} = \omega_m \bar{T}, \quad (3.172)$$

where \bar{T} is the mean torque developed by the PMSM.

From a power balance it is possible to obtain the temporal values of the torque, namely,

$$T(t) = \frac{1}{\omega_m} \left(\sum_{l=1}^m E_{A,l}(t) I_{sm,l}(t) + P_{ad} \right) \quad (3.173)$$

where $T(t)$ is the instantaneous torque, $E_{A,s}(t)$ and $I_{SM,s}(t)$ are the EMF and machine current in phase s and P_{ad} is an estimation of the mechanical losses caused by the friction in the bearings and other moving parts. In [Almandoz 2008] these losses are estimated as

$$P_{ad} = K_{ad} M_r n, \quad (3.174)$$

where n is the rotation speed in revolutions per minute, M_r the total rotor mass and K_{ad} is an experimental coefficient which value is close to $1.5 \cdot 10^{-3}$.

Thus, the efficiency (η) will be defined as

$$\eta = \frac{P_{elec}}{P_{mec}} \quad (3.175)$$

or, equivalently,

$$\eta = \frac{P_{elec}}{P_{elec} + P_{Fe} + P_{Cu} + P_{ad}}. \quad (3.176)$$

3.4.3.2 Electric Quality Parameters

Another important quality parameters are related with the power factor (pf), i.e. the delay between the main harmonics of the inverter voltage and the current.

$$pf = \cos \varphi \quad (3.177)$$

where φ is the phase delay of the current with respect to the voltage. A high absolute value of the power factor is generally preferred, since a system with higher power factor may generate the same amount of power with less current flowing through the wires; this save both, losses and copper material.

The pf calculus in the phasor theory requires the definition of the concepts of real, apparent and reactive powers. The apparent power provided by the inverter (S) is defined as

$$S = 2mV_{ph,1}I_{ph,1}^* \quad (3.178)$$

The real (P_s) and the reactive (Q_s) powers are defined as the real and the imaginary part of S , respectively, i.e.

$$P_s = 2m \operatorname{real}(V_{ph,1}I_{ph,1}^*) \quad \text{and} \quad (3.179)$$

$$Q_s = 2m \operatorname{imag}(V_{ph,1}I_{ph,1}^*). \quad (3.180)$$

It is important to notice that P_s is just the mean power provided by the main harmonic of the electric supply. Once S is defined, pf is obtained as

$$pf = \frac{P_s}{|S|}. \quad (3.181)$$

Other interesting quality parameter is the electrical load (q_e), which relates the machine heating in relation with the copper losses. This value is useful in the first part of the design stage in order to obtain a rough estimation of the machine dimensions. The electrical load is equal to [Almandoz 2008]

$$q_e = \frac{N_{lay} QZ |I_{ph,1}|}{2 \pi R_s}. \quad (3.182)$$

It should be noticed that both, the power factor and the electrical load, are interesting figures of merit in order to be included as constraints in the optimization loop.

3.5 Thermal Approach

As it was aforementioned, a proper thermal modelling of the PMSM is critical because of the great influence of the temperature on the PMSM performance and its operation life. The losses generated in both, the ferromagnetic core and the stator winding give rise to heat, this heat is transfer to the housing and, through it, to the ambient surrounding the machine. A steady state temperature is reached when the amount of heat generated by the losses is in equilibrium with the thermal energy transferred to the ambient.

In a PMSM, the generated heat is critical since a high temperature can shorten its operation life or even cause irreversible damage in the wires insulation or in the magnets. Thus, during the design stage, it is mandatory to obtain a reliable thermal model in order to predict both, the PMSM thermal behaviour and the coupling between the thermal and the electromagnetic model. A complete small lumped thermal circuit is proposed and fully explained in the present section, including its correct coupling with the electromagnetic models.

3.5.1 Heat Transfer: Basic Principles

As it is well known, according to Fourier's law, the heat is transferred from hot to cold bodies, in opposite direction to thermal gradient. Three physical heat transfer modes are well established and studied: conduction, convection and radiation.

A complete thermal model should take into account these three processes. In this section a brief introduction to them and their major implication will be presented. For a more detailed description many undergraduate handbooks, such as [Lienhard 2003], are available.

Conduction

Conduction is a heat transfer mechanism consisting in the propagation of kinetic energy from warm molecules (which vibrate fast) to cool ones (with slower vibrations). The random collisions between fast and slow molecules cause kinetic energy transmission and tend to equalize their temperatures.

Conduction is produced in solid, liquid and gaseous materials, but it is especially important in the former since it is the state of matter where the molecules are closer to each other, so their collisions are more frequent and the heat transmission faster. In fluids this heat propagation is slower due to their more disperse molecular configurations.

The equation governing conduction heat transfer is the Fourier's law which states: "The heat flux resulting from thermal conduction is proportional to the magnitude of the temperature gradient and opposite to its sign". Thus, from the energy conservation principle it is possible to deduce the following partial differential equation:

$$\rho c \frac{\partial T}{\partial t} = \frac{\partial}{\partial x} \left(\lambda_x \frac{\partial T}{\partial x} \right) + \frac{\partial}{\partial y} \left(\lambda_y \frac{\partial T}{\partial y} \right) + \frac{\partial}{\partial z} \left(\lambda_z \frac{\partial T}{\partial z} \right) + Q, \quad (3.183)$$

where T is the absolute temperature, t is the time, (x, y, z) are the Cartesian coordinates, $(\lambda_x, \lambda_y, \lambda_z)$ are the material thermal conductivities along the three coordinate directions, Q is the volumetric rate of heat density dissipated in the medium, c is the material specific heat capacity and ρ is its density.

In many practical cases only the steady state is of interest and the heat transfer is produced just in a spatial direction, in this case (3.183) yields [Lienhard 2003]:

$$q = -\lambda_x \frac{\partial T}{\partial x}, \quad (3.184)$$

where q is the amount of heat flux density traveling along the propagation direction x , measured in W/m^2 .

Assuming that the temperature varies linearly, (3.184) is equivalent to

$$\Delta T = \frac{P \Delta x}{\lambda_x A}, \quad (3.185)$$

where P is the transmitted power across surface A , Δx the element length, ΔT the temperature difference and A the heat path cross-sectional area.

The proposed simplification is of great practical importance since an analogy between the electric and the thermal worlds could be performed. An equivalent thermal resistance (R_{th}) is defined as

$$R_{th} = \frac{\Delta x}{\lambda_x A}, \quad (3.186)$$

which yields

$$\Delta T = R_{th} P. \quad (3.187)$$

Equations (3.186) and (3.187) establish the analogy between electric and thermal circuits, where the transmitted power is seen as a current source, the temperature as the voltage and the thermal resistance is analogue to the electric one.

Another important characteristic is that the defined thermal resistance is not temperature-dependant in many materials of practical interest, since in most solids λ is constant in a wide temperature range. However, the thermal conductivity of gases exhibits remarkable temperature dependence.

Convection

Convection is the heat transfer through the motion of particles within the medium. Thus, it is only produced in fluids where the particles can change their position with relative easiness.

One of the most common cases of practical interest is produced when a fluid flows over a solid at higher temperature. The heat is transferred from the solid to the surrounding fluid (or coolant) and the heated coolant is removed from the solid surface and replaced by cold fluid which restarts the process.

The fluid replacement can be caused by a natural physical process (i.e. hot air has less density than cold air, so it tends to rise and to be replaced by colder air) or it can be forced by a pump or fan. The first case is called natural convection while the second is known as forced convection.

In both cases it is supposed that, in steady state, the heat transfer from the solid to the fluid is proportional to the temperature differences between them. This empirical law is known as the Newton law of cooling [Lienhard 2003]:

$$q = \alpha(T_w - T_\infty), \quad (3.188)$$

where T_w and T_∞ are the solid and the coolant temperatures, respectively, and α is the proportionality coefficient known as convection equivalent conduction coefficient. Parameter α depends on many variables, such as the system geometry, the fluid flow pattern near the solid surface (i.e. the boundary layer), its physical features, its speed, the nature of the convection (natural or forced), etc.

The numerical values of α are usually established by empirical methods or extrapolated from previous measured prototypes. In order to assign a proper value to α , various dimensionless parameters such as the Reynold's, Prandtl's or Nusselt's numbers are used [Lienhard 2003].

From equation (3.188) it is possible to define the convection thermal resistance as:

$$R_{th} = \frac{1}{\alpha A} \quad (3.189)$$

where A is the total surface area.

Radiation

Because of its temperature, a physical body emits energy in form of electromagnetic radiation. Even if the studied material is in the vacuum, it emits, absorbs and transmits thermal radiation. The former action is governed by Stefan-Boltzmann law:

$$q = \sigma \varepsilon T_w^4, \quad (3.190)$$

where T_w is the body absolute temperature, ε is the emissivity of the radiative surface (1 in the case of an ideal black body), q is the radiation flux density and σ is the Stefan-Boltzmann constant ($\sigma = 5.67 \cdot 10^{-8} \text{ W}/(\text{m}^2\text{K}^4)$).

It is usually considered that, if the bodies surrounding a radiative object are at fixed temperature T_∞ the radiated energy is given by

$$q = \sigma\varepsilon(T_w^4 - T_\infty^4); \quad (3.191)$$

in this case, the equivalent thermal resistance associated with the radiation process is given by

$$R_{th} = \frac{T_w - T_\infty}{\sigma\varepsilon(T_w^4 - T_\infty^4)A}. \quad (3.192)$$

As it can be seen, the defined thermal resistance has high temperature dependence so its proper application in an equivalent thermal circuit could be more complicated than in simpler cases, such as convection and conduction. It must be highlighted that, in general, the radiation plays a minor role in machine heat transfer, except when the housing achieves high temperatures.

3.5.2 Introduction to Lumped Thermal Models

The lumped thermal model is the selected approach in order to study and implement the thermal behaviour of a PMSM. This theory is based in the division of the body under study into thermal basic elements with physical and practical relevance. Each element is represented by one or more nodes linked among them by thermal resistances. These elements are part of a grid quite similar to an electric circuit, as can be seen in Figure 3.31.

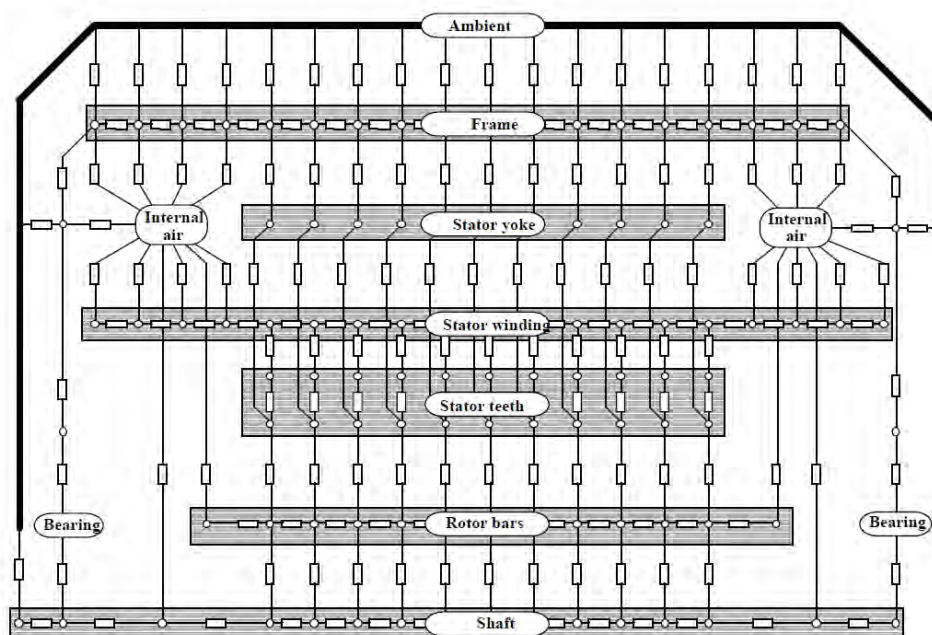


Figure 3.31. Example of an electrical machine thermal network [Kylander 1995]

The analogy between thermal and electrical circuit is shown in Table 3.4.

Electrical circuit	Thermal circuit
Electrical resistance (Ω)	Thermal resistance (K/W)
Current intensity (A)	Power (W)
Voltage (V)	Temperature (K)

Applying (3.187) and Kirchoff's current law it can be deduced that, in steady state:

$$P_i = \frac{T_i - T_{amb}}{R_{i,i}} + \sum_{j=1}^n \frac{T_i - T_j}{R_{i,j}}, \forall i = 1, \dots, n, \quad (3.193)$$

where P_i is the power dissipated at the i -th node, T_i is its temperature, $R_{i,j}$ is the thermal resistance between nodes i and j , $R_{i,i}$ is the thermal resistance between node i and the ambient, and T_{amb} is the ambient temperature selected as a reference.

It is possible to express (3.193) in matrix form:

$$\mathbf{P} = \mathbf{G}\boldsymbol{\Theta}, \quad (3.194)$$

where \mathbf{P} is the dissipated power matrix, $\boldsymbol{\Theta}$ is the relative temperature matrix and \mathbf{G} is a thermal conductance matrix, i.e. in an n nodes configuration:

$$\begin{bmatrix} P_1 \\ P_2 \\ \vdots \\ P_n \end{bmatrix} = \begin{bmatrix} \sum_{i=1}^n \frac{1}{R_{1,i}} & \frac{-1}{R_{1,2}} & \dots & \frac{-1}{R_{1,n}} \\ \frac{-1}{R_{2,1}} & \sum_{i=1}^n \frac{1}{R_{2,i}} & \dots & \frac{-1}{R_{2,n}} \\ \vdots & \vdots & \ddots & \vdots \\ \frac{-1}{R_{n,1}} & \frac{-1}{R_{n,2}} & \dots & \sum_{i=1}^n \frac{1}{R_{n,i}} \end{bmatrix} \begin{bmatrix} \theta_1 \\ \theta_2 \\ \vdots \\ \theta_n \end{bmatrix}, \quad (3.195)$$

where θ_i is the node temperature referred to the ambient, i.e.

$$\theta_i = T_i - T_{amb}, \quad \forall i = 1, \dots, n. \quad (3.196)$$

Finally, since the dissipated power is a known variable, the system is solved just inverting the conductance matrix:

$$\boldsymbol{\Theta} = \mathbf{G}^{-1}\mathbf{P}. \quad (3.197)$$

Thus, applying (3.197) it is possible to obtain the temperatures in the selected nodes from the dissipated power.

3.5.3 Simplified Thermal Network for a SPMSM

There exist two different lumped thermal modelling approaches for electric machines: the small or simplified thermal networks and the complete ones. Its main

difference is that, in small networks, many points with similar temperatures and physical behaviour are combined in the same node, e.g. all teeth are represented by just one node. On the other hand, in a complete network each physical component is usually represented by several nodes in order to characterize the temperature evolution through it. A good example of a complete network is shown in Figure 3.31.

Obviously, complete networks offer more information than simplified ones, but they are more time consuming and usually require data that are not available during the design stage. Meanwhile, simplified thermal models represent a reliable, effective and short-time consuming thermal approach [Bogglieti 2009] whose accuracy, in most cases, will be enough to estimate the temperature at some critical points of the PMSM. Many authors have proposed, with good results, a small thermal network as a suitable compromise between computation speed and accuracy [Mellor 1991, Lindström 1999].

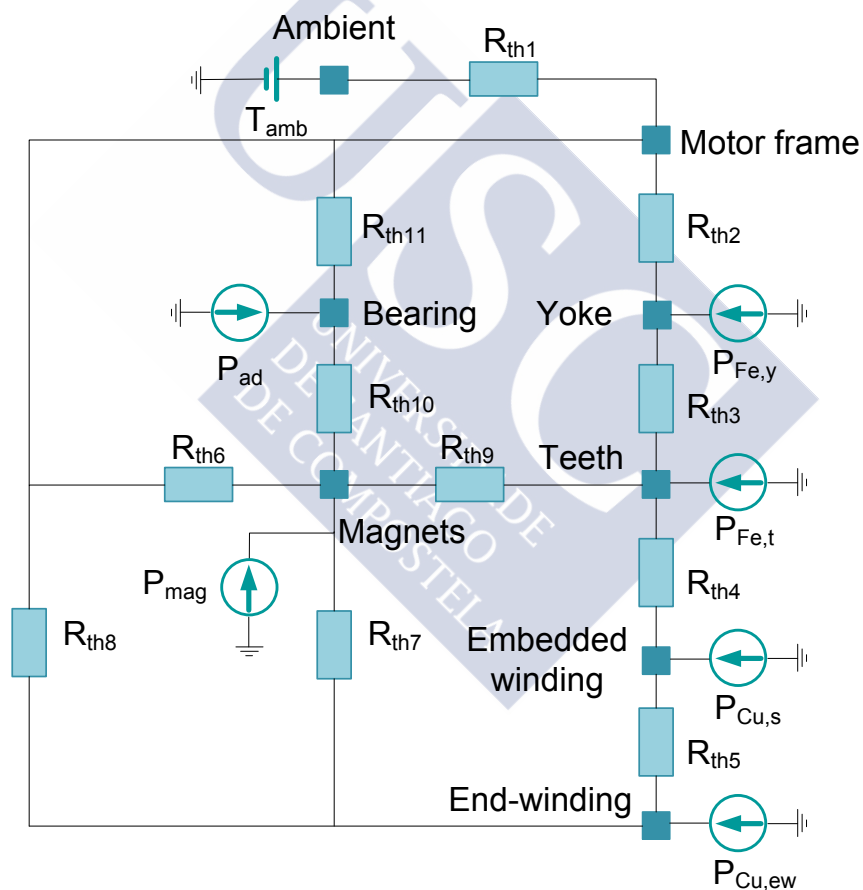


Figure 3.32. Implemented SPMSM small thermal network model.

Mellor et al. proposed the first electrical machine simplified thermal network in a foundational paper [Mellor 1991] that was used by [Kylander 1995] in order to perform two induction machine lumped thermal models: a complete and a simplified one. Lindström particularized and complemented Kylander's model for a SPMSM [Lindström 1999], proposing the eight-node thermal network shown in Figure 3.32.

The simplified thermal network used in the present thesis is a slight modification of that proposed by [Lindström 1999], so both share the same thermal circuit shown in Figure 3.32. In this section the thermal resistance calculus proposed by [Lindström 1999] will be explained, completing his work with more recent publications where needed. In order to obtain a deeper insight during the thermal resistance calculus Figure 3.32 is included, it shows a simplified SPMSM 2D-section cut in the axial direction, the main nodes and thermal resistances are represented in its physical location within the machine.

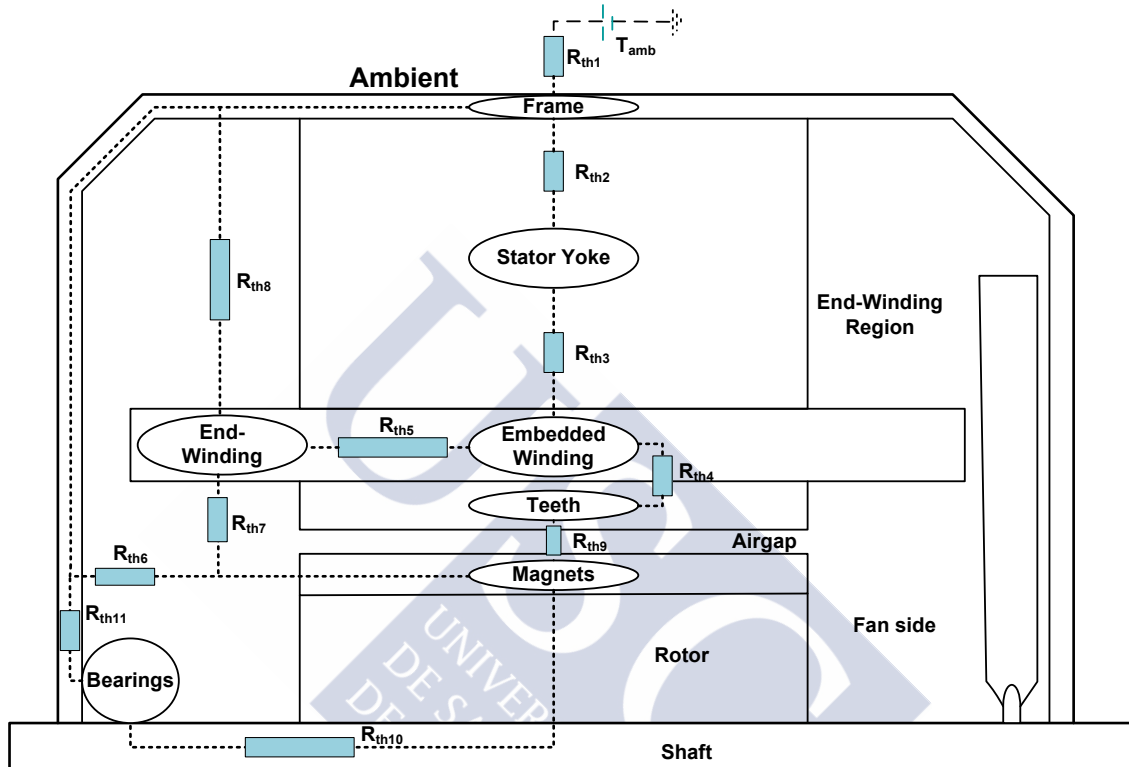


Figure 3.33. SPMSM axial 2D-section, main thermal resistances are included.

The power losses, which are the main thermal model input, are obtained according to the estimations presented in section 3.4 Efficiency and Losses Estimation. It should be highlighted that the implemented thermal model is based on the main assumption that the PMSM can be seen as a group of concentric cylinders (the shaft, the magnets and the stator) through which heating is flowing in both, their axial and radial directions. The equivalent thermal resistances of the different regions will be obtained below.

3.5.3.1 Housing and Stator Yoke

The housing and the stator yoke are two of the most important elements in thermal modelling, as far as all the evacuated heat must flow through them in order to be transmitted into the surrounding air. Therefore, it is a major concern for the designer to achieve a low thermal resistance in those elements.

It is important to remark that the resistances concerning the housing and the stator yoke (R_{th1} and R_{th2} in Figure 3.32) are very difficult to estimate and rough approximations or empirical measurements are needed in order to obtain their values.

More precisely, two thermal resistances model the housing thermal behaviour: the conduction resistance and the resistance between the housing and the ambient.

Housing-ambient thermal resistance

The resistance between ambient and housing is one of the most critical in electrical machine thermal design and it strongly depends on the cooling system (natural convection, forced air, water jacket, etc.), on the specific housing and on its fins geometry (see Figure 3.34). All these complex dependences suppose that a correct estimation is very troublesome, so experimental measurements are usually required [Kylander 1995].

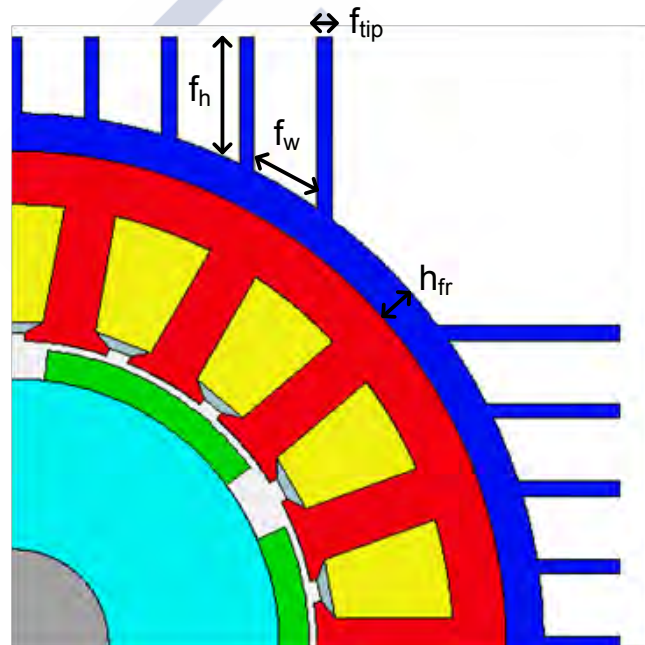


Figure 3.34. Machine 2-D section geometry. Figure from Motor-CAD®.

In the implemented model the ambient-housing thermal resistance (R_0) is estimated assuming forced convection through a fan installed in the machine shaft. In order to calculate this resistance, it will be subdivided in three parts: the first due to the natural convection process (R_{nat}), the second due to the forced convection through the fins base and sides (noted as R_{fin} , convection through surface f_h and f_w in Figure 3.34) and the last caused by the forced convection through the fins tips (noted as R_{tip} , convection through surfaces f_{tip} in Figure 3.34).

The natural convection resistance is estimated through a “root mean squared” empirical rule proposed by [Boglietti 2008].

$$R_{nat} = \frac{0.167}{A_S^{1.039}}, \quad (3.198)$$

where A_S is the total housing surface area, i.e. the sum of its lateral surfaces, the two end caps and the fins. Equation (3.198) takes into account both, natural convection and radiation processes.

The experiments leading to (3.198) are made for induction motors commercial housings in a power range from 4 to 55 kW. Therefore, it can only be used as a rough estimation over this set of machine powers and sizes.

The fins base forced convection coefficient (α_{fin}) is calculated as [Staton 2011]:

$$a = 0.1448 \cdot \frac{L^{0.946}}{D^{1.16}} \left(\frac{\lambda_{air}}{\rho_{air} c_{air} u_s} \right)^{0.214}, \quad (3.199)$$

$$\alpha_{fin} = \frac{\rho_{air} c_{air} u_s D}{4L} (1 - e^{-a}), \quad (3.200)$$

where λ_{air} , c_{air} and ρ_{air} are, respectively, the thermal conductivity, specific heat capacity and density of the air in normal conditions; L is the machine total length, D is the fin hydraulic diameter and u_s is the air velocity through the fins. D and u_s are equal to

$$D = \frac{4f_w f_h}{2(f_w + f_h)} \quad \text{and} \quad (3.201)$$

$$u_s = 0.5\omega_m R_{se}. \quad (3.202)$$

It should be noticed that u_s is estimated as 0.5 times the air speed leaving the fan, while the fan velocity is taken equal to the blades tip speed.

Applying (3.189) it is possible to obtain R_{fin} as,

$$R_{fin} = \frac{1}{\alpha_{fin} L_m n_f (f_w + 2f_h)}, \quad (3.203)$$

where n_f is the number of fins in the housing.

In order to estimate the convection heat transfer through the fin tips it is necessary to decide if the air flux is either laminar or turbulent. To model this effect, usually dimensionless numbers such as Reynolds', Nusselt's or Prandtl's are applied.

In a PMSM housing, the fin tips forced convection coefficient (α_{tip}) is usually established as

$$\alpha_{tip} = \frac{Nu \lambda_{air}}{2(R_{se} + f_h)}, \quad (3.204)$$

where Nu is the Nusselt's number, defined from the Prandtl's and Reynold's numbers as:

$$Nu = \begin{cases} 0.664 Re^{0.5} Pr^{0.33} & \text{if } Re < 5 \cdot 10^5 \\ ((0.037 Re^{0.8} - 871) Pr^{0.33}) & \text{if } Re \geq 5 \cdot 10^5 \end{cases}, \quad (3.205)$$

$$Re = \frac{\rho_{air} u_s 2(R_{se} + f_h)}{\mu_{air}} \quad \text{and} \quad (3.206)$$

$$Pr = \frac{c_{air} \mu_{air}}{\lambda_{air}}. \quad (3.207)$$

where μ_{air} is the air dynamic viscosity.

Therefore, the fin tips thermal resistance can be calculated as

$$R_{\text{tip}} = \frac{1}{\alpha_{\text{tip}} L_m n_f f_{\text{tip}}}. \quad (3.208)$$

Finally, the total housing resistance is estimated:

$$R_0 = \frac{1}{1/R_{\text{nat}} + 1/R_{\text{fin}} + 1/R_{\text{tip}}}. \quad (3.209)$$

Stator yoke conduction and contact thermal resistances

It is supposed that the heat is transmitted radially through the housing and the stator yoke. Their conduction resistances are, generally, of small value and both are well studied since the conduction process is easier to model than the convection one.

The housing is considered as a thin cylinder with a diameter much longer than its thickness, its radial thermal resistance (R_{thfr}) can be estimated as

$$R_{\text{thfr}} = \frac{h_{\text{fr}}}{2\pi R_{\text{se}} (L_{\text{Fe}} + 2L_{\text{ew}}) \lambda_{\text{Al}}}, \quad (3.210)$$

where h_{fr} is the stator thickness (see Figure 3.34), L_{ew} is the end-winding length, R_{se} is the external stator radius and λ_{Al} is the thermal conductivity of the housing material, generally aluminium.

In a similar fashion, the stator yoke is modelled as a cylindrical section of a ferromagnetic material where the heat is only flowing along its radial direction. This is a good approximation since the ferromagnetic core insulation layers (used in order to limit the iron losses) are both electric and thermal insulators. The expression of the stator yoke thermal resistance (R_{thsy}) in the radial direction is approximated by

$$R_{\text{thsy}} = \frac{\ln(R_{\text{se}}/R_{\text{ss}})}{2\pi L_e \lambda_{\text{Fe}}}, \quad (3.211)$$

where λ_{Fe} is the ferromagnetic material conductivity, and R_{ss} the radius defined by the upper part of the stator teeth, i.e.

$$R_{\text{ss}} = R_{\text{se}} - w_{\text{sy}}. \quad (3.212)$$

There exists an additional resistance defining the heat flow through the stator yoke and housing: the contact resistance between these two elements (R_{thcy}). This resistance is not null since the contact between the two surfaces is not perfect and air pockets exist. This resistance can play a major role when R_0 has a small value due to a good cooling system.

Parameter R_{thcy} is very difficult to estimate, because it depends on parameters with high manufacturing tolerances, such as the pressure between yoke and housing and the smoothness of their surfaces. A common approach consists in the definition of a fictitious equivalent airgap length between the two elements (g_e). Some studies estimate that the airgap is between 30 and 75 μm in PMSM between 1.5 and 250 kW [Lindström 1999]. [Boglietti 2008] offers a look-up table for g_e mean values.

Once a reliable approach of g_e is obtained, the equivalent R_{thcy} is given by

$$R_{thcy} = \frac{g_e}{2\pi R_{se}(L_{Fe} + 2L_{ew})\lambda_{air}} \quad (3.213)$$

where λ_{air} is the air thermal conductivity.

With the previous values calculated, the thermal resistance between the machine housing and the surroundings (R_{th1}) and between the housing and the mid-point of the stator yoke (R_{th2}) are given by (see Figure 3.32)

$$R_{th1} = \frac{R_{thfr}}{2} + R_0 \quad \text{and} \quad (3.214)$$

$$R_{th2} = \frac{R_{thys}}{2} + R_{thcy} + \frac{R_{thfr}}{2}. \quad (3.215)$$

3.5.3.2 Stator Teeth

All the stator teeth are represented with just one node, virtually located in the mid-point of any of them. The total conduction thermal resistance in the radial direction is supposed to be the parallel configuration of every teeth resistance. Axial heat flow is neglected due to the low thermal conductivity of the core insulation layers.

The thermal resistance of the stator tooth (R_{tht}) is calculated by direct integration along the stator radial dimension (see Figure 3.35):

$$R_{tht} = \frac{1}{Q} \int_0^{h_s} \frac{1}{\lambda_{Fe} L_e \hat{w}_t(y)} dy, \quad (3.216)$$

where y is the radial dimension variable, $\hat{w}_t(y)$ is the tooth width as function of y and h_s is the total tooth height. According to the dimensions shown in Figure 3.35 the previous integral can be calculated:

$$R_{tht} = \frac{1}{Q \lambda_{Fe} L_e} \left(\frac{h_0}{w_{st}} + \frac{h_2}{w_t} + \frac{h_1}{w_{st} - w_t} \ln \left(\frac{w_{st}}{w_t} \right) \right). \quad (3.217)$$

It is possible to represent the thermal resistance between the stator yoke and the teeth (R_{th3}) as

$$R_{th3} = \frac{1}{2} (R_{tht} + R_{thsy}). \quad (3.218)$$

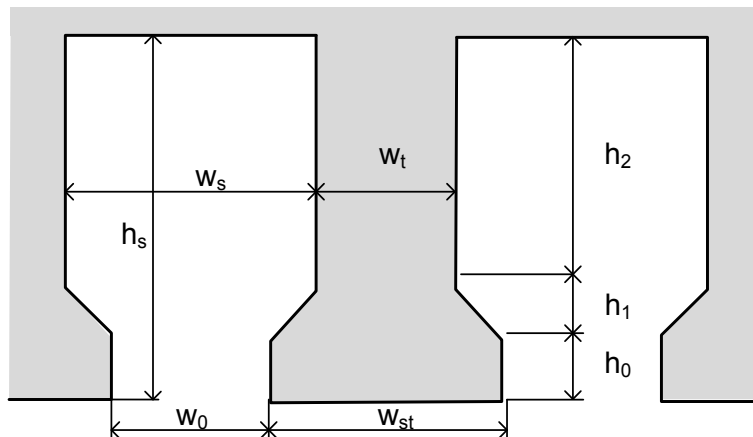


Figure 3.35. Stator teeth and slots typical geometry.

3.5.3.3 Stator Coils

The conduction resistance of the stator coils is much more difficult to model than the teeth one, because the heat flows in the three spatial directions: axial, tangential and radial. Moreover, the slot material is not isotropic, as the axial heat flux is mainly transferred through the copper to the end-winding, while the other spatial directions see an inhomogeneous material made of copper and insulation with a lower thermal conductivity.

It is quite straightforward to see that the axial heat flux is due to the heat exchange between the embedded coils and the end-windings, while the radial and tangential fluxes are related to the heat transfer to the stator yoke through the teeth. Since the wires are one of the hot spots within the machine, and due to the high dependence of their expected life with their temperature, special care is needed in order to perform a suitable thermal model.

Radial Resistance between Embedded Coils and Teeth

Most authors estimate the slot radial thermal resistance (i.e. the resistance between the slots and the teeth) through a homogenization process, i.e. supposing that the sum of the copper and the insulation behaves like an homogeneous media with a constant thermal conductivity in the radial direction (λ_s).

There exists a great controversy on the accurate estimation of λ_s . Most of authors try to achieve a correlation between its value and the physical thermal conductivity of the insulation material (λ_{imp}). As far as it was investigated in the literature, the first estimation of that relation appears in [Mellor 1991], which established that

$$\lambda_s = 2.5\lambda_{imp} \quad (3.219)$$

However, other authors investigated the strong dependence between this ratio and the manufacturing process (more precisely, the winding process that could be in-line wire rows or staggered wire rows), concluding that both, the winding technique and the slot fill factor (F_f) have a great influence in this relation. [Kylander 1995] proposed the ratio between λ_s and λ_{imp} shown in Figure 3.36, while a more recent publication [Boglietti 2008] estimates λ_s from a experimental data regression as

$$\lambda_s = 0.2425[(1 - F_f)A_s L_e]^{-0.427}, \quad (3.220)$$

where A_s is the slot cross-sectional area.

In most practical designs F_f is very close to 0.5, value where the three approaches are very close to each other. Thus, for its great simplicity, equation (3.220) will be used in this thesis.

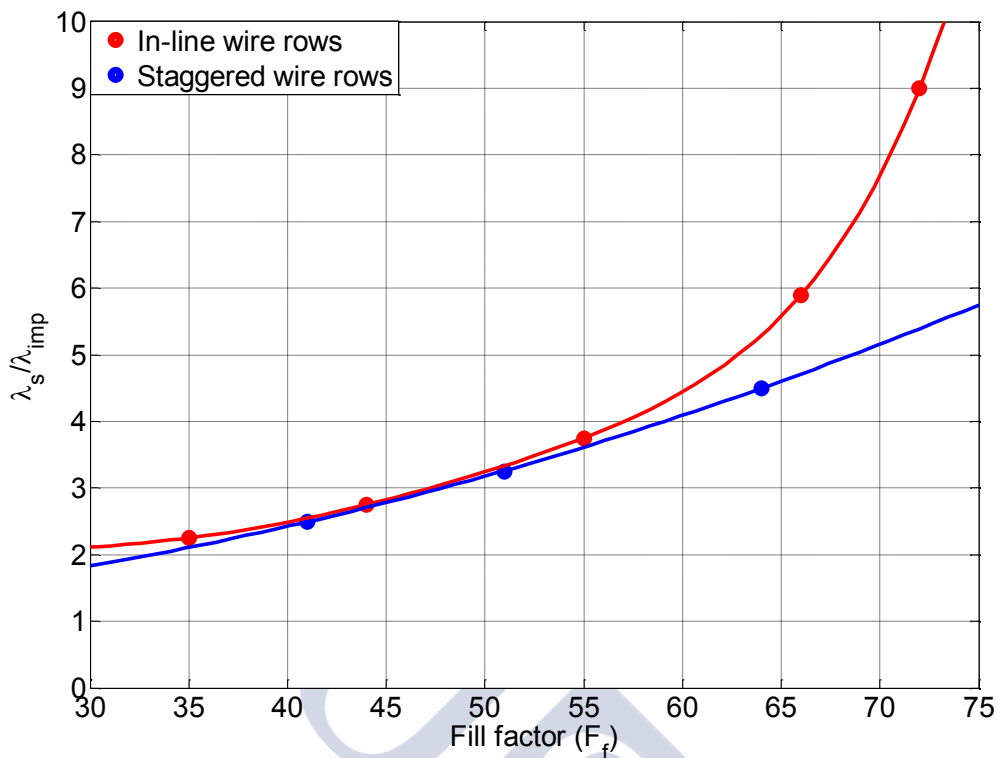


Figure 3.36. Relation between λ_{slot} and λ_{imp} as a function of the slot fill factor and the manufacture technique. Data from [Kylander 1995].

Once the equivalent slot thermal conductivity is obtained a two-dimensional heat transfer must be modelled in order to estimate the total resistance between the slot centre and the stator. The exact solution to this problem is complex and cannot be easily implemented but, if it is supposed that the heat flux in one direction is independent from the heat flux in the other, a separated thermal resistance in each dimension can be established. The equivalent slot geometry shown in Figure 3.37 is used in order to perform the calculus.

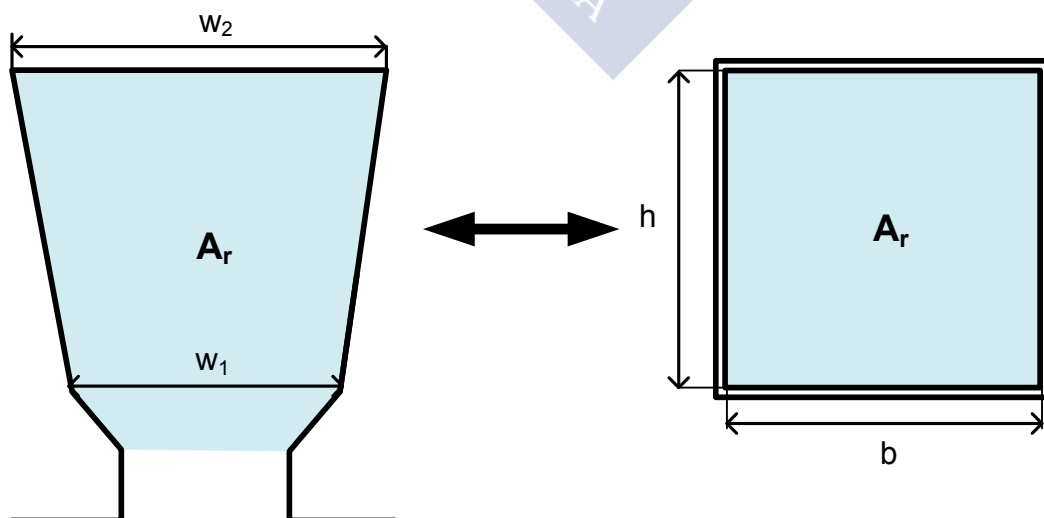


Figure 3.37. Slot geometry equivalence used in the thermal modelling by [Lindström 1999].

The slot radial thermal resistance in both coordinate directions (R_{x0} and R_{y0}) is estimated as:

$$R_{x0} = \frac{b}{h\lambda_{\text{slot}}} \quad \text{and} \quad (3.221)$$

$$R_{y0} = \frac{h}{b\lambda_{\text{slot}}}, \quad (3.222)$$

where b and h are obtained from the slot real dimensions as (see Figure 3.35):

$$b = \frac{w_1 + w_2}{2} \quad \text{and} \quad (3.223)$$

$$h = \frac{2A_r}{w_1 + w_2}. \quad (3.224)$$

Another important contribution to the thermal resistance is the insulation layer emplaced between the slot and the stator. This material is an important obstacle in the heat flux path. Moreover, within the insulation, air pockets exist, so the equivalent thermal resistance in both dimensions (R_{xi} and R_{yi}) can be estimated as

$$R_{xi} = \frac{h_3}{h\lambda_{\text{imp}}} + \frac{d_{\text{air}}}{h\lambda_{\text{air}}} \quad \text{and} \quad (3.225)$$

$$R_{yi} = \frac{h_3}{b\lambda_{\text{imp}}} + \frac{d_{\text{air}}}{b\lambda_{\text{air}}}, \quad (3.226)$$

where h_3 is the insulation width and d_{air} the equivalent air pocket length.

It is very difficult to obtain a reliable value of d_{air} , as it depends on random events during the manufacturing process. In [Kylander 1995] values of some tenths of millimetre (from 0.2 to 0.3 mm) are proposed.

Once the two contributions are obtained, the total thermal resistance in both directions (R_x and R_y) is calculated as

$$R_x = \frac{1}{2} \left(R_{xi} + \frac{R_{x0}}{6} \right) \quad \text{and} \quad (3.227)$$

$$R_y = \frac{1}{2} \left(R_{yi} + \frac{R_{y0}}{6} \right). \quad (3.228)$$

Finally, the total resistance between the slots and the stator teeth is estimated as [Lindström 1999]:

$$R_{\text{th4}} = \frac{R_x R_y}{QL_e(R_x + R_y)} \left(1 - \frac{R_{x0} R_{y0}}{720 R_x R_y} \right). \quad (3.229)$$

Axial Resistance between the Embedded Coils and the End-Winding

The heat flows in the axial direction through the copper wires, since copper is not only a good electrical conductor but also a good thermal one. The thermal connection between the mid-point of an embedded coil and the mid-point of the end-winding is represented in Figure 3.38.

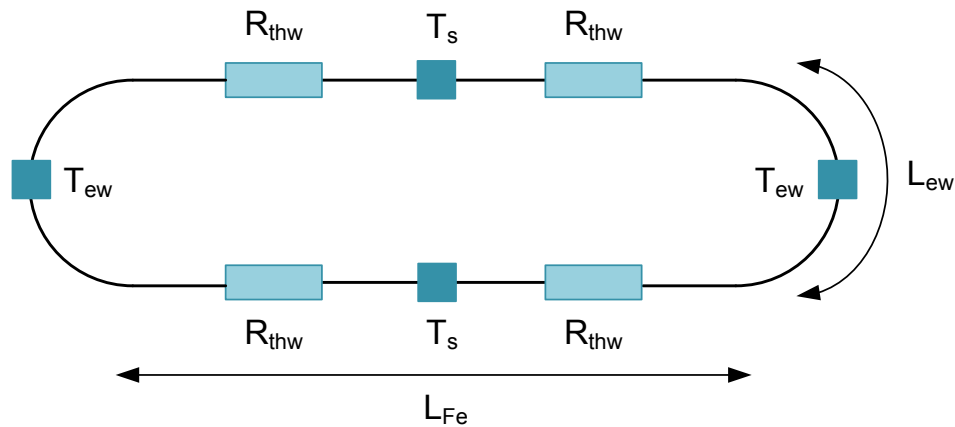


Figure 3.38. Single coil thermal model.

The wire conduction resistance (R_{thw}) will be given by

$$R_{thw} = \frac{L_{Fe} + L_{ew}}{2A_{Cu}\lambda_{Cu}} = \frac{L_{Fe} + L_{ew}}{2A_s F_f \lambda_{Cu}}. \quad (3.230)$$

Supposing that all the end-windings can be represented by a single node, it can be concluded that there exists a total of $2Q$ heat flow paths between the embedded and the end-windings points, as it is graphically shown in Figure 3.39.

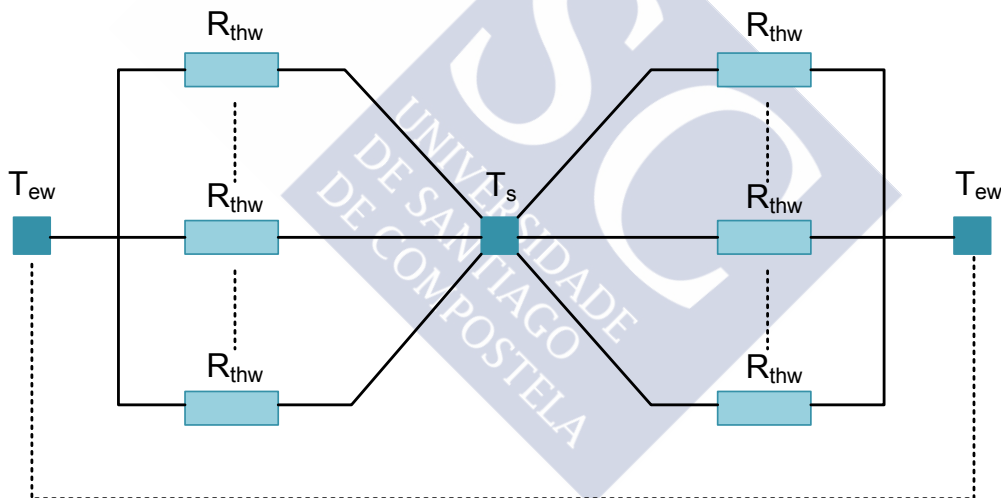


Figure 3.39. Global thermal resistance between embedded coils and end-winding.

Thus, the total thermal resistance linking the embedded coils and the end-windings is given by

$$R_{th5} = \frac{R_{thw}}{2Q}. \quad (3.231)$$

3.5.3.4 End-Winding Region

Heat transfer in the end-winding regions involves complex convection and radiation process between four main actors: the end-caps (a part of the housing), the rotor, the wires and the internal air, see Figure 3.40.

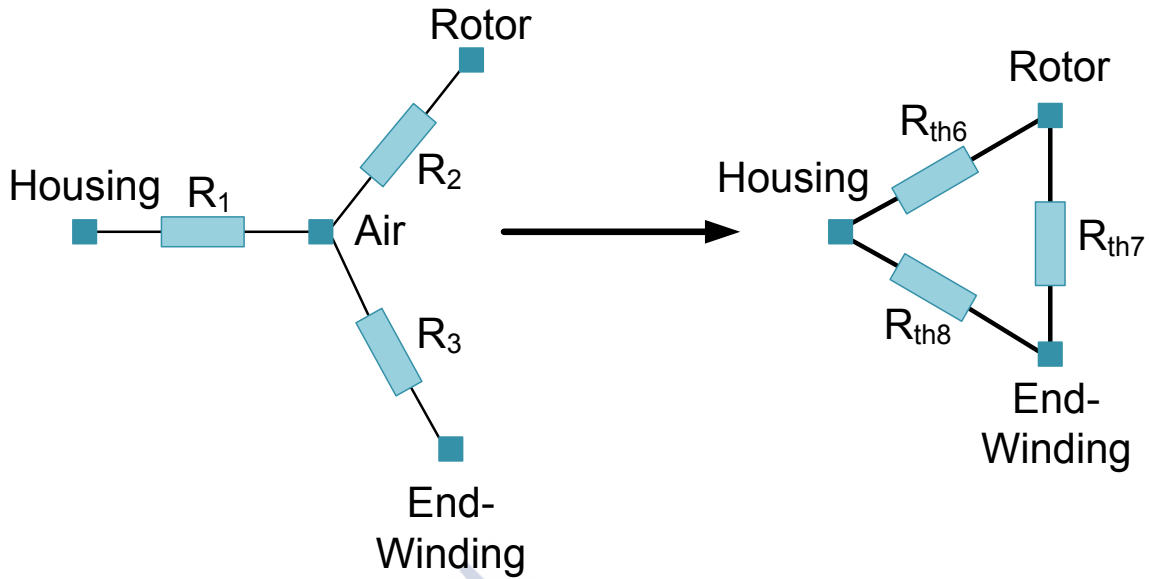


Figure 3.40. Equivalent end-wind thermal network in its Y and Δ forms [Kylander 1995].

Since the temperatures in this region are close enough, the radiation process is neglected and only the convective terms should be taken into account. In spite of this fact, their calculation is not an easy task, because the precise geometry and the heat flux paths are still unknown. In order to calculate these coefficients the Newton's heating law is applied:

$$R_x = \frac{1}{\alpha_x A_x}, \quad (3.232)$$

where x is an index equal to 1, 2 or 3 identifying the specific thermal resistance shown in Figure 3.40, A_x is the equivalent body external surface and α_x is its convection coefficient.

A lot of works have been published in order to estimate the correct values of α_x and A_x [Mellor 1991, Kylander 1995, Saari 1998, Lindström 1999, Boglietti 2008], but the complexity and uncertainties of the geometry, the rotor motion effect and the random air flux in the end-winding region cause that only rough approximations are available. In this work the approach proposed by [Lindström 1999] will be used.

The end cap convection surface (A_1) and its convection coefficient, α_1 , are approximated by

$$A_1 = 2(\pi R_{se}^2 + 2\pi R_{se} L_{ew}) \quad \text{and} \quad (3.233)$$

$$\alpha_1 = 15 + 6.75(\omega_m R_m)^{0.65}, \quad (3.234)$$

respectively, where A_1 includes all the end-winding internal housing surface, with the end-cap. It should be noticed that the $\omega_m R_m$ term is related to the rotor linear speed making the internal air flows and causing a forced convection.

The rotor and the internal end-winding air present a convection surface (A_2) and a transfer coefficient (α_2) equal to:

$$A_2 = 2\pi R_r^2 \text{ and} \quad (3.235)$$

$$\alpha_2 = 16.5(\omega_m R_m)^{0.65}. \quad (3.236)$$

The end-winding wires convection surface (A_3) is estimated as

$$A_3 = \pi L_{ew} 2(R_s + h/2), \quad (3.237)$$

where h is the total slots height. The convection heat transfer coefficient (α_3) is approximated by

$$\alpha_3 = 6.5 + 5.25(\omega_m R_m)^{0.6}. \quad (3.238)$$

Once these parameters are calculated, (3.232) is applied in order to obtain the equivalent thermal resistances.

Since the enclosed air is just a heat exchanger between other components (rotor, wires and housing), and its temperature has not real relevance, it is a common practice to eliminate its associated node through a Y- Δ conversion. This conversion is necessary in order to obtain the thermal circuit shown in Figure 3.32; the Y- Δ conversion can be found in any electric undergraduate book. The obtained resistances between the end caps, rotor and end-windings (see Figure 3.40) are equal to

$$R_{th6} = R_1 + R_2 + \frac{R_1 R_2}{R_3}, \quad (3.239)$$

$$R_{th7} = R_2 + R_3 + \frac{R_2 R_3}{R_1} \text{ and} \quad (3.240)$$

$$R_{th8} = R_1 + R_3 + \frac{R_1 R_3}{R_2}. \quad (3.241)$$

3.5.3.5 Airgap

The airgap is the natural interface between rotor and stator both in magnetic and thermal aspects. The heating is transferred through the airgap mainly by conduction and convection processes. Usually the radiation plays a minor role in heat propagation since the rotor and the stator temperatures are relatively close to each other.

The heat transfer is quite different whether the air flux through the airgap is laminar or turbulent. In the first case the air motion is distributed in radial layers, with a decreasing speed as they approach the stator so the heat is transferred through a conduction process. Notice that, in a gas, heat transfer by conduction is relatively small; on the contrary, a turbulent flow supposes a forced convection process and the heat flux is enhanced.

Assuming smooth rotor and stator surfaces the critical transition between laminar and turbulent air flow is determined by Taylor's number (Ta), defined as

$$Ta = \frac{\omega_m R_s g^3}{\nu^2}, \quad (3.242)$$

where the product $\omega_m R_s$ is the peripheral air speed and ν the air kinematic viscosity.

It is generally considered that the air flow is turbulent if Ta is above a threshold of 1740 [Kylander 1995]. Following an empirical law, the Nusselt number (Nu) is obtained as

$$Nu = \begin{cases} 2 & \text{if } Ta_m < 1740 \\ 0.409Ta_m^{0.241} - 137Ta_m^{-0.75} & \text{if } Ta_m \geq 1740 \end{cases} \quad (3.243)$$

The heat transfer coefficient is estimated from the Nusselt number:

$$\alpha_g = \frac{Nu \lambda_{air}}{2g}. \quad (3.244)$$

The airgap axial heat transfer is neglected due to its low influence in the heat propagation for most of the PMSM (except for those rotating at very high speeds). Therefore, the airgap thermal resistance is given by

$$R_{thg} = \frac{1}{\alpha_g 2\pi R_s L_{Fe}}. \quad (3.245)$$

3.5.3.6 Rotor

From a thermal point of view the rotor can be subdivided into different parts: the magnets, the ferromagnetic core, the shaft and the bearings. The most important are the magnets, since an excessive heating can lead not only to a lower machine performance but also to their permanent demagnetization.

Magnets and ferromagnetic core

The heat flux through the magnets and the core is supposed to be completely radial, since the insulation layers greatly limit the axial flux. The conduction thermal resistance is obtained just as the stator one.

The core resistance is approximated by:

$$R_{thr} = \frac{\ln(R_r/R_{shaft})}{2\pi L_e \lambda_{Fe}}, \quad (3.246)$$

where R_{shaft} is the shaft radius. If the machine under study is a SPMSM the magnets thermal resistance can be modelled as a cylindrical section:

$$R_{thm} = \frac{\ln(R_m/R_r)}{2\pi \alpha_m L_{Fe} \lambda_m}, \quad (3.247)$$

where λ_m is the magnets thermal conductivity and α_m is the fraction of the total cylindrical crown covered by the magnets.

Therefore, the thermal resistance between the stator teeth and the magnets (R_{th9}) is given by

$$R_{th9} = \frac{1}{2} (R_{thm} + R_{tht}) + R_{thg}. \quad (3.248)$$

Shaft and bearings

The shaft is supposed to transmit the heat in the axial direction with a homogeneous thermal distribution, so its thermal resistance is approximated by

$$R_{thsh} = \frac{L_b}{\pi R_{shaft}^2 \lambda_{shaft}}, \quad (3.249)$$

where L_b is the distance between the shaft mid-point and the bearings and λ_{shaft} is the shaft material thermal conductivity.

The contact resistance between the shaft and the rotor (R_{thcr}) is very difficult to estimate, so it is usually neglected.

Once the heat reaches the bearings the thermal transfer is produced through the bearing balls and their indirect contact with the frame.

The bearings thermal resistance depends on their dimensions and angular speed. [Kylander 1995] proposes an empiric approach for this resistance:

$$R_{thb} = 0.45(0.12 - d_b)(33 - \omega_m d_b), \quad (3.250)$$

where d_b is the bearings diameter. The coefficients used in (3.250) are estimated from empirical measurements carried out in two induction motors of 15 kW and 4 kW power, but significant differences may appear in other prototypes.

Two surfaces (one at each end) link the housing and the bearings, so the total thermal resistance between their mid-points is given by

$$R_{th11} = \frac{R_{thb}}{4} + \frac{R_{thfr}}{2}. \quad (3.251)$$

Finally, the last thermal resistance of the lumped circuit (Figure 3.32), which is still unknown, is the one linking magnets and bearings (R_{th10}). This resistance is the sum of the individual contributions of the magnets, the rotor core, the shaft and the bearings, so it can be calculated as

$$R_{th10} = \frac{R_{thm}}{2} + R_{thr} + \frac{R_{thsh}}{2} + \frac{R_{thb}}{4}. \quad (3.252)$$

With the previous data the proposed thermal circuit can be correctly solved and the PMSM temperatures obtained. However, as it will be explained, not only the temperatures depend on the losses through the thermal circuit introduced in this chapter; reciprocally, these losses depend on the temperatures because of the thermal dependence of material physical parameters. The linked problem is solved in the next section.

3.5.4 Thermal-Electromagnetic Coupling

Between the many physical couplings existing in an electrical machine one of the most important is the electromagnetic-thermal one. In fact, the temperature plays a

major role in two physical parameters variation: the copper resistivity and the magnet residual induction.

As it was aforementioned in 3.3.2, the copper resistivity varies with temperature according to

$$\rho_{\text{Cu}} = \rho_{\text{Cu},20^\circ} (1 + \alpha_{\text{Cu}} (T_{\text{Cu}} - 293.15\text{K})). \quad (3.253)$$

As far as the thermal dependence is considered linear in a wide temperature range, α_{Cu} is taken as a constant equal to $\alpha_{\text{Cu}} = 0.0039 \text{ K}^{-1}$, with $\rho_{\text{Cu},20^\circ} = 1.71 \cdot 10^{-8} \Omega\text{m}$.

In a similar way, the temperature dependence of the magnet residual induction is supposed to be linear, so it is approximated by

$$B_r = B_{r,20^\circ} (1 + \alpha_m (T_m - 293.15\text{K})), \quad (3.254)$$

where $B_{r,20^\circ}$ is the magnet residual inductance at 20°C , T_m is the magnet temperature and α_m is the magnet thermal coefficient. $B_{r,20^\circ}$ and α_m depend on the specific selected magnet material, e.g. the neodymium-boron N40H material has $\alpha_m = -1.54 \cdot 10^{-3} \text{ K}^{-1}$ and $B_{r,20^\circ} = 1.285\text{T}$.

It is clear that the change in these physical variables directly affects the machine losses and, therefore, the temperatures.

More precisely, the copper resistance increases linearly with temperature while the current through it, determined by an external controller, is nearly constant. Hence, at high temperatures Joule losses are incremented, enhancing the temperatures and, therefore, the electrical resistance in a vicious circle that can even damage the wires insulation.

Moreover, higher temperatures in the magnets cause a decrease of the rotor magnetic field in the stator, decreasing both, the machine performance, the iron losses and even the magnetic forces on the cores. But, the most important thermal effect in the magnets is their possible permanent demagnetization if the Curie's temperature is reached.

The aforementioned effects have two important implications: the first one is the need to perform a careful thermal design in order to avoid coils and magnet damage due to high temperatures. The second one is the coupling between the thermal and the electromagnetic models, as far as temperatures strongly depend on the losses and they are, in their turn, a function of temperature.

In order to solve this bidirectional coupling the iterative loop shown in Figure 3.41 is used:

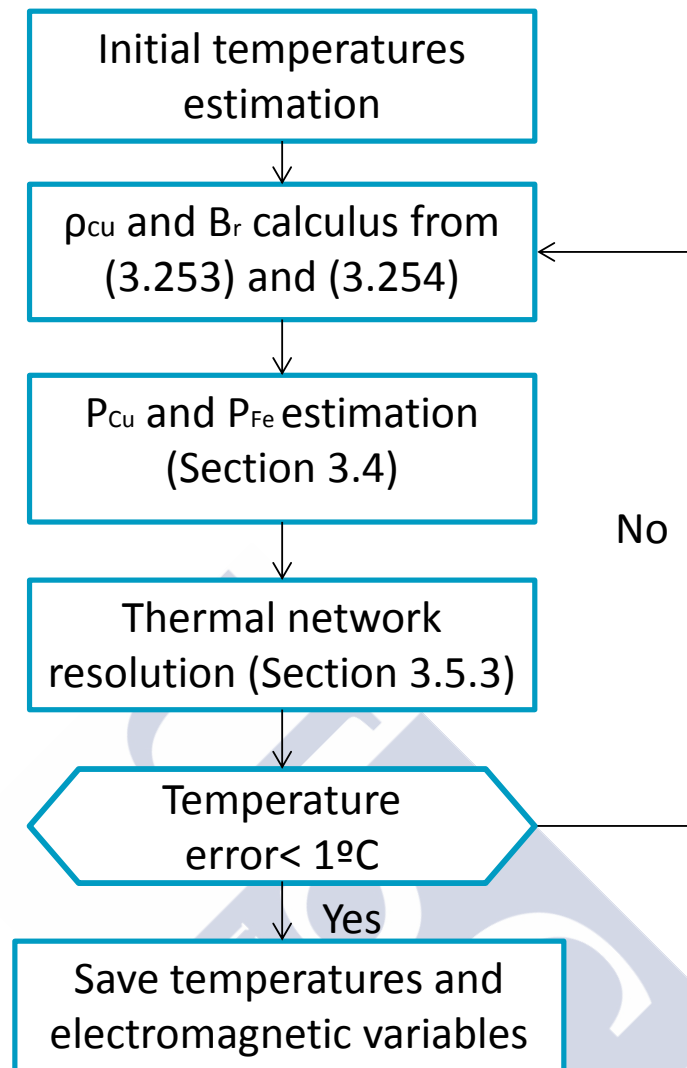


Figure 3.41. Electromagnetic-thermal coupling algorithm flowchart.

With the proposed tolerance (1°C) an accurate result and a very fast convergence are achieved, usually after less than three iterations if a good initial temperature guess is selected, e.g. $T_{\text{Cu}} = 373\text{K}$ and $T_{\text{m}} = 353\text{K}$.

3.6 Vibratory and Acoustic Behaviour

As it was previously introduced, the PMSM vibratory and acoustic study is mandatory in order to ensure compliance with regulations and a reduced noise emission. Thus, it is not surprising that complete analytical models of electrical machine vibratory behaviour have been carried out since the fifties [Jordan 1950].

In this thesis work the modal analytical approach exposed in [Yang 1981, Timar 1989, Gieras 2006] will be adopted due to its lower computing time and good features, e.g. it overcomes the difficulties, inherent to numerical methods, associated with a correct mesh of the interfaces and a proper and accurate calculus in the boundaries between a body and a flux (generally air).

As it was exposed in section 2.2.3, the complete acoustic study can be divided into different parts:

- The electromagnetic force calculus: accomplished in section 3.2.5. The magnetic excitation force was assumed to be completely radial and it is considered time and θ -dependant, so its associated magnetic pressure can be expressed by a 2D-Fourier Series as:

$$P_M(\theta, t) = \sum_{k=-\infty}^{\infty} \sum_{l=-\infty}^{\infty} P_{M,kl} e^{jk\omega_e t} e^{jl\theta}. \quad (3.255)$$

In this section, the excitation pressure is taken as an input for the developed models and equations.

- The calculus of the structural vibration modes which represent the PMSM natural vibration patterns and combine them with the excitation force in order to obtain its vibratory behaviour. The model and its main assumptions are explained in section 3.6.1
- The PMSM acoustic radiation due to the aforementioned vibrations, caused by the electromagnetic forces. The vibrating surfaces radiate sound power at different frequencies; this phenomenon is studied in section 3.6.2.

3.6.1 Structural and Vibratory Approach

Several assumptions are necessary in order to develop a suitable structural model; the most important is that the stator and frame of an electrical machine can be seen as cylindrical shells. Due to their enclosure, the rotor vibrations can be neglected, and only the external parts of the machine (i.e. the stator and the frame) will be taken into account regarding acoustic radiation.

Due to the curvature of the stator shell geometry the vibrations in the radial, axial and tangential axis are coupled to each other, so an excitation in one direction could cause vibrations in all directions. In spite of that fact, several authors consider that only the radial vibrations are of importance in noise emission, especially for axially short machines [Hubert 2001]. This approximation will be adopted.

The aforementioned assumptions imply that a radial modal basis can be used in order to express the stresses, displacements and velocities of the stator particles, so a modal approach will be used in order to characterise the stator vibrations. Figure 2.13 shows graphically some of these modal basic functions.

As far as the forces are known and previously calculated, this section will study the estimation of the stator structural and vibratory features. Firstly, vibratory basic principles will be explained and applied to a shell structure in cylindrical coordinates and then the particularities of the stator will be modelled. These results can be

obtained in a more exhaustive and rigorous way by using the principles of continuum mechanics and tensor analysis. This is briefly explained in Appendix D.

3.6.1.1 Classic Vibratory Theory: d'Alembert Principle and Hooke Law

In order to calculate the internal displacements (i.e. the vibrations) in a system it is necessary to establish a force balance and a mathematical relation between the aforementioned forces and displacements. The first requirement is satisfied through d'Alembert principle which states: *“Defining the inertial force as the minus product of the mass and acceleration, the sum of all the forces (contact, volumetric and inertial) acting on a body vanished, i.e. they are an equilibrate force system.”*

Mathematically d'Alembert principle can be expressed in its discrete form as:

$$\sum_{i=1}^n (F_i - m_i a_i) = 0, \quad (3.256)$$

where the system under study is divided in a finite number of particles (n), where the particle i is characterized by its mass (m_i), acceleration (a_i) and the force acting on it (F_i).

It should be notice that d'Alembert Principle is enunciated for a finite number of punctual particles. However, as it will be introduced, it is possible to extend the theory to a continuum through the concept of limit.

In order to study the forces acting over a section within a solid body a set of internal stresses σ_{ij} could be defined, where σ_{ij} is the stress applied in the i -axis direction on a surface which is normal to the j -axis direction. An important feature of σ_{ij} is that it is equal to σ_{ji} in order to ensure the angular momentum conservation principle.

Taking that stresses into account, it is possible to apply d'Alembert principle in 2D-cylindrical coordinates, defining an element at position (r, θ) , with a force density $\mathbf{f} = f_r \mathbf{e}_r + f_\theta \mathbf{e}_\theta$ acting on it and a total displacement $\mathbf{u} = u_r \mathbf{e}_r + u_\theta \mathbf{e}_\theta$ [Timoshenko 1951]. Figure 3.42 represents the element stresses.

In the radial direction the force equilibrium implies:

$$\begin{aligned} -r f_r dr d\theta = & [(\sigma_{rr} r)_1 - (\sigma_{rr} r)_3] d\theta - [(\sigma_{\theta\theta})_2 + (\sigma_{\theta\theta})_4] \sin\left(\frac{d\theta}{2}\right) dr \\ & + [(\sigma_{r\theta})_4 - (\sigma_{r\theta})_2] \cos\left(\frac{d\theta}{2}\right) dr - \frac{\partial^2 u_r}{\partial t^2} \rho r dr d\theta, \end{aligned} \quad (3.257)$$

where the numerical subscript represents the element face where the stress is applied, u_r is the element radial displacement and ρ is its density.

If (3.257) is divided by $dr d\theta$ and the element dimensions tend to zero (i.e. the section tends to be a differential area as $dr \rightarrow 0$ and $d\theta \rightarrow 0$) it becomes:

$$-rf_r = \frac{\partial \sigma_{rr}}{\partial r} r + \sigma_{rr} - \sigma_{\theta\theta} + \frac{\partial \sigma_{r\theta}}{\partial \theta} - \frac{\partial^2 u_r}{\partial t^2} \rho r. \quad (3.258)$$

The same procedure can be applied in the θ -axis, obtaining:

$$\begin{aligned} -rf_\theta drd\theta = & [(\sigma_{\theta\theta})_4 - (\sigma_{\theta\theta})_2] \cos\left(\frac{d\theta}{2}\right) dr + [(\sigma_{\theta r}r)_1 - (\sigma_{\theta r}r)_3] d\theta \\ & + [(\sigma_{r\theta})_2 + (\sigma_{r\theta})_4] \sin\left(\frac{d\theta}{2}\right) dr - \frac{\partial^2 u_\theta}{\partial t^2} \rho r drd\theta. \end{aligned} \quad (3.259)$$

Equation (3.259) can be reformulated in a similar way as (3.257), i.e. dividing by $drd\theta$ and making the differentials tend to zero (i.e. $dr \rightarrow 0, d\theta \rightarrow 0$):

$$-rf_\theta = \frac{\partial \sigma_{\theta\theta}}{\partial \theta} + \frac{\partial \sigma_{\theta r}}{\partial r} r + 2\sigma_{\theta r} - \frac{\partial^2 u_\theta}{\partial t^2} \rho r. \quad (3.260)$$

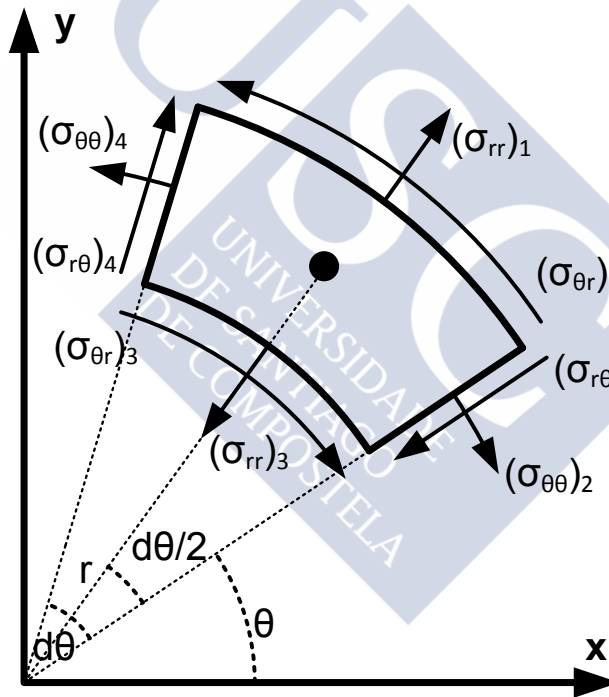


Figure 3.42. Stresses on a differential element in polar coordinates.

Once the internal stresses are estimated a relation between them and the body deformation should be established. It is supposed that the stator is an elastic, isotropic medium, characterized by its Young module (E) and its Poisson coefficient (ν),

The body elongations are measured by its strain, which establishes its deformation respect to its original configuration. The strains have several analogies with the stresses because it is possible to define a strain ϵ_{ij} which represents the differential elongation in i -axis direction respect to an infinitesimal displacement in the j -axis. It is

important to notice that ε has no units because it is a deformation with respect to a reference position. This fact also implies that ε has small values because the relative displacements are small in most of real elastic bodies. Another major feature is that $\varepsilon_{ij} = \varepsilon_{ji}$.

It is clear that ε_{ii} represents compression or traction deformations, while ε_{ij} with $i \neq j$ is a shear deformation.

An elastic, isotropic body presents a linear relation between its stresses and strains defined by the Hooke's law. The concept of strain could be clarified through its relation with the stress; an example in Cartesian coordinates will be provided. It is intuitive (and could be empirically proved) that a traction stress applied in the x direction (i.e. σ_{xx}) produces a positive elongation in the x-axis, but it also supposes a compression in the other two directions [Timoshenko 1951]. Mathematically,

$$\varepsilon_{xx} = \frac{1}{E} (\sigma_{xx} - \nu\sigma_{yy} - \nu\sigma_{zz}), \quad (3.261)$$

where $1/E$ is the relation between the stress σ_{xx} and the strain ε_{xx} and ν/E regulates the compression produced by σ_{xx} in the y and z axis (or, by analogy, by σ_{yy} in the x and z axis). It should be noticed that ε_{yy} and ε_{zz} fulfil equalities analogous to (3.261).

By the way, it could be empirically demonstrated that a shear strain ε_{ij} is only related with its shear stress σ_{ij} through the equation

$$\varepsilon_{ij} = \frac{1 + \nu}{E} \sigma_{ij}, \quad (3.262)$$

A straightforward manner to represent the relation between strains and stresses in an elastic, isotropic body is in matrix form.

In the studied case, the PMSM is modelled as a 2D-geometry close to a thin shell. Therefore, the stress in the z-direction is neglected (i.e. σ_{zz} is taken equal to 0), therefore the relation between strains and stress could be represented as:

$$\begin{bmatrix} \varepsilon_{xx} \\ \varepsilon_{yy} \\ \varepsilon_{xy} \end{bmatrix} = \frac{1}{E} \begin{bmatrix} 1 & -\nu & 0 \\ -\nu & 1 & 0 \\ 0 & 0 & 1 + \nu \end{bmatrix} \begin{bmatrix} \sigma_{xx} \\ \sigma_{yy} \\ \sigma_{xy} \end{bmatrix}. \quad (3.263)$$

In order to study a stator vibratory behaviour it is useful to express (3.263) in polar coordinates, which leads to an equivalent expression [Timoshenko 1951],

$$\begin{bmatrix} \varepsilon_{rr} \\ \varepsilon_{\theta\theta} \\ \varepsilon_{r\theta} \end{bmatrix} = \frac{1}{E} \begin{bmatrix} 1 & -\nu & 0 \\ -\nu & 1 & 0 \\ 0 & 0 & 1 + \nu \end{bmatrix} \begin{bmatrix} \sigma_{rr} \\ \sigma_{\theta\theta} \\ \sigma_{r\theta} \end{bmatrix}. \quad (3.264)$$

The relations established by Hooke's law (3.264) and d'Alembert principle (3.258) and (3.260) in the case of an elastic linear material in polar coordinates will be used in the next sections in order to estimate the vibratory behaviour of the stator of a PMSM.

3.6.1.2 Dynamics of a Thin Ring

A non-clamped stator structure can be modelled as a thin ring, so a 2D-study could be carried out. In a first step this model will be performed and then the main results will be extended to the PMSM stator case.

In order to perform this study the following assumptions are made:

- A 2D-approximation is accurate enough, stresses in the z-axis are supposed to be null (plane stress).
- A modal basis will be defined. In most practical cases the radial modes have a leading vibratory and acoustic interest; so, only these modes will be included in the basis.
- Two types of radial modes are studied: Mode 0 (the breathing mode or extension mode) and bending modes without elongation (modes 1 onwards).

Breathing Mode

The breathing mode is characterized by the expansion and contraction of the ring; changing its radius but preserving its circular geometry (see Figure 3.43).

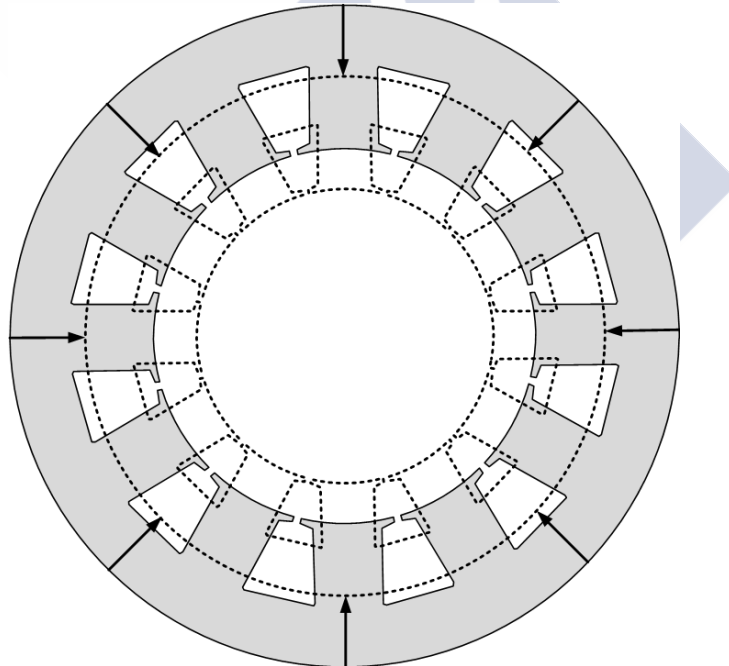


Figure 3.43. Example of a stator breathing mode.

Figure 3.44 shows a tangential differential element, with its strains and stresses. It is supposed that no external forces exist and the only significant deformation is in the tangential direction, i.e. the only non-null strain is $\varepsilon_{\theta\theta}$. By definition it is equal to:

$$\varepsilon_{\theta\theta} = \lim_{\Delta\theta \rightarrow 0} \frac{\Delta u_{\theta} + (R + u_r)\Delta\theta - R\Delta\theta}{R\Delta\theta} = \frac{1}{R} \left(\frac{\partial u_{\theta}}{\partial \theta} + u_r \right), \quad (3.265)$$

by using Hooke's law and assuming that $\sigma_{rr} = 0$:

$$\sigma_{\theta\theta} = \frac{E}{R} \left(\frac{\partial u_{\theta}}{\partial \theta} + u_r \right), \quad (3.266)$$

where E is the material Young modulus and R the ring radius. Equations (3.258) and (3.260) can be particularized:

$$\frac{E}{R} \left(\frac{\partial u_{\theta}}{\partial \theta} + u_r \right) + \frac{\partial^2 u_r}{\partial t^2} \rho R = 0, \quad (3.267)$$

$$\frac{E}{R} \left(\frac{\partial^2 u_{\theta}}{\partial \theta^2} + \frac{\partial u_r}{\partial \theta} \right) - \frac{\partial^2 u_{\theta}}{\partial t^2} \rho R = 0. \quad (3.268)$$

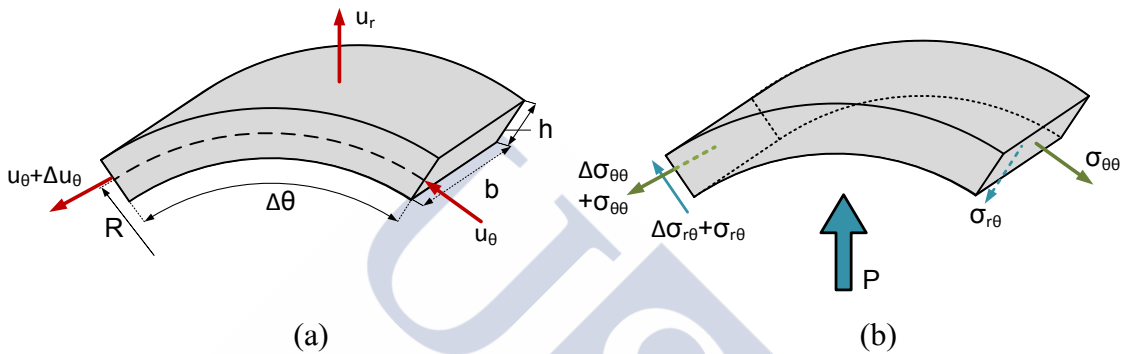


Figure 3.44. (a) Strain and dimensions in a ring element and (b) stresses in a ring.

It is supposed that the solution can be expressed in a FS basis as

$$u_{\theta} = \sum_{n=-\infty}^{\infty} U_{\theta,n} e^{j(n\theta + \omega_n t)}, \quad (3.269)$$

$$u_r = \sum_{n=-\infty}^{\infty} U_{r,n} e^{j(n\theta + \omega_n t)}. \quad (3.270)$$

where ω_n is the pulsation of the mode.

It can be deduced that an additional relation between u_{θ} and u_r must be fulfilled in order to ensure $\varepsilon_{r\theta} = 0$; $\varepsilon_{r\theta}$ is obtained similarly to $\varepsilon_{\theta\theta}$:

$$\varepsilon_{r\theta} = \frac{1}{R} \left(\frac{\partial u_r}{\partial \theta} + u_{\theta} - R \frac{\partial u_{\theta}}{\partial r} \right). \quad (3.271)$$

Since u is not r -dependent, it must be satisfied that [Hubert 2001]

$$u_{\theta} = -\frac{\partial u_r}{\partial \theta}. \quad (3.272)$$

Substituting (3.272) in (3.267):

$$\frac{E}{R} \left(\frac{\partial^2 u_r}{\partial \theta^2} - u_r \right) - \frac{\partial^2 u_r}{\partial t^2} \rho R = 0, \quad (3.273)$$

a solution in separate variables will be developed:

$$u_r(\theta, t) = V_r(\theta)\Phi_r(t). \quad (3.274)$$

From (3.273):

$$\frac{E}{R^2} \frac{V_r''(\theta) - V_r(\theta)}{V_r(\theta)} = \rho \frac{\ddot{\Phi}_r(t)}{\Phi_r(t)}, \quad (3.275)$$

where V_r' denotes the derivative of V_r and $\ddot{\Phi}_r$ the temporal second derivative of Φ_r . Since the left hand-side depends only on θ and the right hand-side only on t , both have to be constant. Thus, it leads to solve an eigenvalue problem for a second order differential equation. This problem has a countably infinite number of solutions.

For each spatial index, n , there exists a frequency that fulfils (3.275) with a non-trivial solution. This frequency is known as the resonant or natural frequency of the n^{th} mode, and in the breathing mode it is equal to

$$f_n = \frac{1}{2\pi R} \sqrt{\frac{E(n^2 + 1)}{\rho}}. \quad (3.276)$$

The so called breathing mode only presents one important spatial harmonic, when $n = 0$, with a resonant pulsation given by

$$\omega_0 = \frac{1}{R} \sqrt{\frac{E}{\rho}}. \quad (3.277)$$

If a continuous external pressure p_r with pulsation ω_f is applied, it will generate a radial displacement u_r of the same frequency, i.e.

$$p_r = P_r e^{j\omega_f t}, \quad (3.278)$$

$$u_r = U_r e^{j\omega_f t}. \quad (3.279)$$

The differential equation that must be fulfilled is

$$\frac{E}{R} \left(\frac{\partial^2 u_r}{\partial \theta^2} - u_r \right) A - \frac{\partial^2 u_r}{\partial t^2} \rho R A = p_r b R, \quad (3.280)$$

where A is the ring cross-sectional area and b is its length (see Figure 3.44). It can be deduced that

$$p_r = u_r \left[\frac{E}{\rho R^2} \rho h - \omega_f^2 \rho h \right] = u_r \rho h [\omega_0^2 - \omega_f^2], \quad (3.281)$$

where h is the ring thickness. Finally, in the cases where no resonance occurs (i.e. $\omega_f \neq \omega_0$), u_r is given by

$$u_r = \frac{P_r e^{j\omega_f t}}{\rho h [\omega_0^2 - \omega_f^2]}. \quad (3.282)$$

An important concept in vibratory study is the static displacement (Y_n), defined as the amplitude of the radial displacement per unit of static pressure (i.e. with a continuous exciting force). The static displacement could be obtained from (3.282) when $\omega_f = 0$ by

$$Y_0 = \frac{1}{\rho h \omega_0^2} = \frac{R^2}{hE}. \quad (3.283)$$

Bending Modes without Elongation

General equations (3.258) and (3.260) can be particularized for the bending modes (where no r dependence exists and σ_{rr} is assumed to be 0)[Hubert 2001].

$$\sigma_{\theta\theta} + \frac{\partial \sigma_{r\theta}}{\partial \theta} - \frac{\partial^2 u_r}{\partial t^2} \rho R = 0, \quad (3.284)$$

$$\frac{\partial \sigma_{\theta\theta}}{\partial \theta} - \sigma_{\theta r} + \frac{\partial^2 u_\theta}{\partial t^2} \rho R = 0. \quad (3.285)$$

Two additional equations are necessary in order to obtain the radial displacements as a function of the force mode and frequency. Equation (3.286) below describes the bending moment and (3.287) imposes the non-extension of the ring central line (i.e. a mode with $\sigma_{\theta\theta} = 0$, see (3.266)) [Timoshenko 1937, pp. 409].

$$\frac{\partial M}{\partial \theta} + \sigma_{\theta r} R A = 0, \quad (3.286)$$

$$u_r = -\frac{\partial u_\theta}{\partial \theta}. \quad (3.287)$$

where M is the ring bending moment and R its initial radius. Forces and torques acting on a differential section of the ring are shown in Figure 3.44.

In a deformed thin ring it is possible to establish a relation between the bending moment (M) and the radial displacements (u_r) [Timoshenko 1976-a, 1976-b]:

$$M = \frac{I_z E}{R^2} \left(\frac{\partial^2 u_r}{\partial \theta^2} + u_r \right), \quad (3.288)$$

where I_z is the moment of inertia with respect to the ring neutral axis, i.e.

$$I_z = \int_{z=-b/2}^{b/2} \int_{r=R-h/2}^{R+h/2} (r - R)^2 dr dz, \quad (3.289)$$

with h being the ring thickness and b its length.

Combining equations from (3.286) to (3.289) the shear stress on the element is given by

$$\sigma_{\theta r} = \frac{I_z E}{AR^3} \left(\frac{\partial^4 u_\theta}{\partial \theta^4} + \frac{\partial^2 u_\theta}{\partial \theta^2} \right). \quad (3.290)$$

From (3.284) the tangential stress can be deduced:

$$\sigma_{\theta\theta} = -\frac{I_z E}{AR^3} \left(\frac{\partial^5 u_\theta}{\partial \theta^5} + \frac{\partial^3 u_\theta}{\partial \theta^3} \right) - \rho R \frac{\partial^3 u_\theta}{\partial t^2 \partial \theta}. \quad (3.291)$$

Substituting (3.290) and (3.291) into (3.285):

$$-\frac{I_z E}{R^4} \left(\frac{\partial^6 u_\theta}{\partial \theta^6} + 2 \frac{\partial^4 u_\theta}{\partial \theta^4} + \frac{\partial^2 u_\theta}{\partial \theta^2} \right) + \rho A \left(\frac{\partial^2 u_\theta}{\partial t^2} - \frac{\partial^4 u_\theta}{\partial t^2 \partial \theta^2} \right) = 0. \quad (3.292)$$

As in the previous case, a solution in separate variables is developed, i.e. the displacement is expressed as:

$$u_\theta = V_\theta(\theta) \Phi_\theta(t). \quad (3.293)$$

Thus, (3.292) yields

$$\frac{I_z E V_\theta^{(6)} + 2V_\theta^{(4)} + V_\theta^{(2)}}{R^4} = \rho A \frac{\ddot{\Phi}_\theta(t)}{\Phi_\theta(t)}, \quad (3.294)$$

where $V_\theta^{(x)}$ is the x -order derivative of V_θ .

In order to solve (3.294), the next family of infinite numerable solutions is assumed:

$$V_{\theta,n}(\theta) = U_{r,n} e^{jn\theta}, \quad (3.295)$$

$$\Phi_{\theta,n}(t) = e^{j2\pi f_n t}. \quad (3.296)$$

Derivative calculus in (3.294) leads to:

$$\frac{I_z E n^2 (n^2 - 1)^2}{R^4} = \rho A \omega_n^2 (n^2 + 1). \quad (3.297)$$

Hence, each solution identifies a bending mode with its own resonant frequency. In other words, the resonance frequency of the bending mode n is given by

$$f_n = \frac{n(n^2 - 1)}{2\pi R^2} \sqrt{\frac{I_z E}{\rho A (n^2 + 1)}}. \quad (3.298)$$

A particular case of great importance is when the ring has a rectangular section, in this case (3.289) can be solved as

$$I_z = Ah^2/12, \quad (3.299)$$

and (3.298) yields

$$f_n = \frac{h}{R^2 2\sqrt{3}} \frac{n(n^2 - 1)}{2\pi} \sqrt{\frac{E}{\rho(n^2 + 1)}}. \quad (3.300)$$

If an external radial pressure P of mode n and pulsation ω_f is applied, then equation (3.284) is rewritten as

$$\sigma_{\theta\theta} + \frac{\partial\sigma_{r\theta}}{\partial\theta} - \frac{\partial^2 u_r}{\partial t^2} \rho R = -bRP \quad (3.301)$$

the angular displacement and the pressure are represented by their 2D-FS

$$p_r = \sum_{k=-\infty}^{\infty} \sum_{n=-\infty}^{\infty} P_{r,kn} e^{j(k\omega_e t + n\theta)}, \quad (3.302)$$

$$u_\theta = \sum_{k=-\infty}^{\infty} \sum_{n=-\infty}^{\infty} U_{\theta,kn} e^{j(k\omega_e t + n\theta)}. \quad (3.303)$$

Hence, in this case, the tangential stress can be calculated as

$$\sigma_{\theta\theta} = -\frac{I_z E}{AR^3} \left(\frac{\partial^5 u_\theta}{\partial \theta^5} + \frac{\partial^3 u_\theta}{\partial \theta^3} \right) - \rho R \frac{\partial^3 u_\theta}{\partial t^2 \partial \theta} - bRP \quad (3.304)$$

and (3.292) yields

$$-\frac{I_z E}{R^4} \left(\frac{\partial^6 u_\theta}{\partial \theta^6} + 2 \frac{\partial^4 u_\theta}{\partial \theta^4} + \frac{\partial^2 u_\theta}{\partial \theta^2} \right) - b \frac{\partial P}{\partial \theta} + \rho A \left(\frac{\partial^2 u_\theta}{\partial t^2} - \frac{\partial^4 u_\theta}{\partial t^2 \partial \theta^2} \right) = 0. \quad (3.305)$$

The derivatives can be computed independently for each $U_{\theta,kn}$, i.e.

$$(\omega_n^2 - k^2 \omega_e^2) U_{\theta,kn} = \frac{jn P_{r,kn}}{h\rho(n^2 + 1)}, \quad (3.306)$$

so, 2D-FS coefficients of the angular displacement field is

$$U_{\theta,kn} = \frac{jn P_{r,kn}}{h\rho(n^2 + 1)(\omega_n^2 - k^2 \omega_e^2)}. \quad (3.307)$$

The radial displacement 2D-FS coefficients can be obtained from (3.287)

$$U_{r,kn} = \frac{n^2 P_{r,kn}}{h\rho(n^2 + 1)(\omega_n^2 - k^2 \omega_e^2)}. \quad (3.308)$$

Therefore, the static displacement, Y_n , is

$$Y_n = \frac{n^2}{h\rho(1 + n^2)\omega_n^2} = \frac{12R^4}{h^3 E(n^2 - 1)^2}. \quad (3.309)$$

The previous calculations are a general, simple resolution of the vibratory behaviour of a thin ring. From them, a more accurate and complete model for an electrical machine is obtained in the next section.

3.6.1.3 Dynamic of a Stator

A complete stator is quite different from a simple 2D-thin ring. Hence, in order to use the aforementioned analytic results, it is necessary to take into account the major differences between a complete stator and the simplified thin ring model, the most important among them are listed below.

1. The stator is not just a ring, but it is loaded by additional elements such as teeth and coils that modify the mass and the stiffness of the complete body.
2. The stator is in close contact with an external housing which plays the role of a vibratory interface between it and the air.
3. There exists a viscous damping because the kinetic energy is dissipated into heat during the vibration process.
4. The internal forces are not applied on the mean radius of the external ring, but on the internal stator radius, this must be taken into account in order to estimate the static and dynamic displacements (see Figure 3.45).
5. The PMSM is clamped by its foot and its shaft, so its vibratory behaviour is not exactly the same in each axial slice, for this reason some non-negligible axial modes could appear.

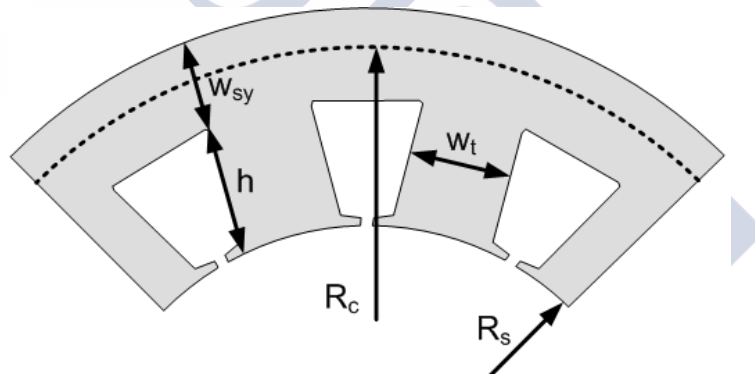


Figure 3.45. Stator seen as a ring (mean radius R_c and thickness h) with teeth.

In order to take into account the aforementioned features, the resonance pulsation and the static displacements of the breathing mode are corrected [Yang 1981, Gieras 2006]:

$$\omega_0 = \frac{1}{R_c} \sqrt{\frac{E_{Fe}}{\rho_{Fe} \Delta}}, \quad (3.310)$$

$$Y_0 = \frac{R_s R_c}{w_{sy} E_{Fe}}, \quad (3.311)$$

where R_c is the mean stator yoke radius, R_s the internal stator radius, w_{sy} the stator yoke height, E_{Fe} the Young modulus of the core material, ρ_{Fe} the core material density and Δ the mass addition factor due to the teeth and winding, i.e:

$$\Delta = \frac{M_{Fes} + M_{Fet} + M_{Cu}}{M_{Fes}}, \quad (3.312)$$

where M_{FeS} is the stator total yoke mass, M_{FeT} the total teeth mass and M_{Cu} the total coil weight.

It is important to notice that the teeth and the winding add an additional mass term in (3.310) but its stiffness is neglected as far as the teeth stiffness contribution is greatly decreased by the coils [Girgis 1979].

From the static displacement it is possible to obtain the dynamic one; in this case equation (3.282) cannot be directly applied as the core material presents a viscous damping which tends to decrease the oscillation amplitude. Therefore, (3.282) leads to [Gieras 2006]:

$$u_{r,k0} = \frac{P_{M,k0} Y_0 \omega_0^2}{\sqrt{(\omega_0^2 - k^2 \omega_e^2)^2 + 4\zeta_0^2 k^2 \omega_e^2 \omega_0^2}}, \quad (3.313)$$

where ω_e is the electrical pulsation, k the index temporal harmonic, ζ_0 the damping factor for mode 0, and $F_{r,k0}$ and $u_{r,k0}$ the FS-coefficients of the radial pressure and displacements, respectively. Thus, the total force and radial displacement can be expressed as a 2D-FS

$$P_M(\theta, t) = \sum_{k=-\infty}^{\infty} \sum_{n=-\infty}^{\infty} P_{M,kn} e^{jk\omega_e t} e^{jn\theta}, \quad (3.314)$$

$$u_r(\theta, t) = \sum_{k=-\infty}^{\infty} \sum_{n=-\infty}^{\infty} u_{r,kn} e^{jk\omega_e t} e^{jn\theta}. \quad (3.315)$$

The damping factor plays a major role in equation (3.313), because it avoids the theoretical infinite displacement when the stator is excited with a force which has just the resonant frequency of its spatial mode. However, a correct estimation of ζ_n is not an easy task and needs experimental measurements [Gieras 2006]. If measures are not available, an empirical expression proposed by [Yang 1981] can be used for model purposes during the design stage:

$$\zeta_n = \frac{1}{2\pi} (2.76 \cdot 10^{-5} f_n + 0.062), \quad (3.316)$$

where f_n is the n^{th} mode natural frequency.

In a similar way, the natural frequencies and the static and dynamic displacements can be calculated for bending modes without elongation as

$$\omega_n = \frac{w_{sy}}{R_c^2 2\sqrt{3}} n(n^2 - 1) \sqrt{\frac{E_{\text{Fe}}}{\rho_{\text{Fe}} \Delta (n^2 + 1)}} \phi_n \quad \text{and} \quad (3.317)$$

$$Y_n = \frac{12R_s R_c^3}{w_{sy}^3 E_{\text{Fe}} (n^2 - 1)^2}, \quad (3.318)$$

where ϕ_n is a correction factor which takes into account the teeth rotatoring inertia [Yang 1981]:

$$\phi_n = \left\{ 1 + \frac{w_{sy}^2}{12R_c^2} (n^2 - 1) [n^2 (4 + \Delta_{rot}/\Delta) + 3] \right\}^{-0.5} \quad \text{and} \quad (3.319)$$

$$\Delta_{rot} = 1 + \frac{Qw_t \frac{M_{Fet} + M_{Cu}}{M_{Fet}} h \{4h^2 + 6w_{sy}h + 3w_{sy}^2\}}{2\pi w_{sy}^3 R_c} \quad (3.320)$$

where Δ_{rot} is the mass addition factor for rotation. It is recalled that Q is the number of teeth, w_t their width and h their height (see Figure 3.45).

Finally, the 2D-FS coefficients of the dynamic displacement are

$$u_{r,kn} = \frac{P_{M,kn} Y_n \omega_n^2}{\sqrt{(\omega_n^2 - k^2 \omega_e^2)^2 + 4\zeta_0^2 k^2 \omega_e^2 \omega_n^2}} \quad (3.321)$$

With the aforementioned considerations a more realistic PMSM structural 2D-model can be performed. However it is convenient to explain some additional considerations about it.

First, the teeth not only add mass and rotational inertia but they can also vibrate in a circumferential direction causing additional modes called “tooth rocking modes”. Fortunately, these modes are strongly damped by the slot coils and it is assumed that the behaviour of the complete stator is quite similar to a ring (the stator yoke) loaded with an additional mass (teeth plus windings) [Girgis 1979].

Second, the presence of an external housing is usually neglected because of its small thickness compare with the stator yoke, but some authors [Gears 2006] proposed methods in order to obtain a global mode estimation taking into account both, stator and housing.

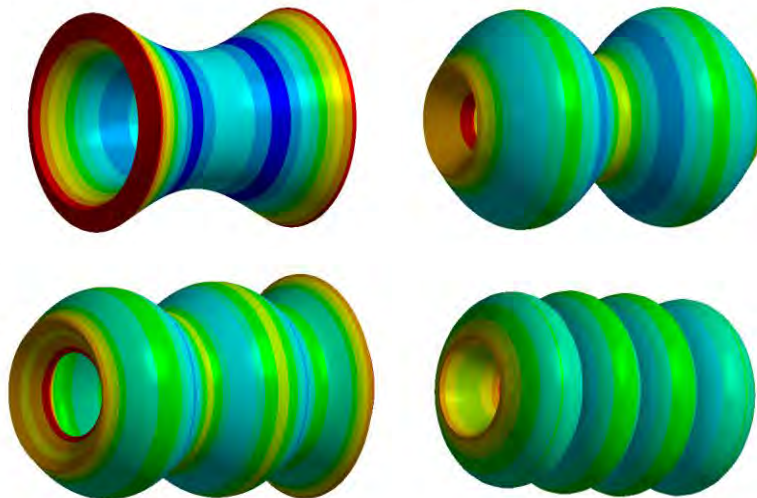


Figure 3.46. 1st to 4th stator axial modes simulated with ANSYS®. Deflections have been scaled for visual purposes.

Finally the machine surface is not free during its normal operation, but it is fixed by its feet and shaft. The feet clamping greatly affects the appearance of some radial modes, while the end-bells and the shaft often clamp the machine causing axial modes appearance (see Figure 3.46), these mode are usually neglected as far as they have small relevance, especially in short machines [Hubert 2001].

3.6.2 Acoustic Calculus

Once the forces and, through them, the PMSM surface vibrations have been obtained, the next step is to deduce the total sound power radiated by the machine. In order to do so, some basic acoustic theory should be revisited. These acoustic and sound radiation equations and principles are thoroughly explained in under-graduated books such as [Kinsler 2000]; here the main assumptions and results are included for the sake of completeness.

The most important equation in acoustics with small particle displacements is called the *linear Euler's equation*, valid for acoustic processes of small amplitudes (most of physical phenomena, excluding the great air vibrations such as explosions, which are situated far beyond the audition pain threshold). Euler's equation is enunciated as

$$\nabla p = -\rho \frac{\partial \mathbf{v}}{\partial t} \quad (3.322)$$

where ρ is the fluid density (e.g. air density), ∇p is the acoustic pressure gradient and \mathbf{v} the particles speed due to the sound propagation. In order to obtain this basic result lineal momentum conservation was applied, as shown in [Kinsler 2000].

A correct study of the radiated noise requires the definition of the energy and power carried by acoustic waves. Therefore, the concept of acoustic intensity (\mathbf{I}) is introduced. This vectorial magnitude is defined as the time averaged of the instantaneous intensity, which is the work done by one fluid element on an adjacent element per unit area, measured in W/m^2 . Mathematically,

$$\mathbf{I} = f \int_0^{1/f} p \mathbf{v} dt, \quad (3.323)$$

where f is the frequency of the radiated sound.

From (3.323) it is possible to define the mean acoustic power radiated in a time period in a space region limited by a closed surface S as:

$$W = \int_S \mathbf{I} \cdot \mathbf{n} dS = f \int_S \int_0^{1/f} p \mathbf{v} \cdot \mathbf{n} dt dS. \quad (3.324)$$

It is recalled that \mathbf{n} is the outward normal vector to S .

Gauss's theorem could be applied to (3.324) leading to

$$W = f \int_V \int_0^{1/f} \nabla \cdot (p\mathbf{v}) dt dV = f \int_V \int_0^{1/f} (p\nabla \cdot \mathbf{v} + \mathbf{v} \cdot \nabla p) dt dV. \quad (3.325)$$

where V is the total volume enclosed by S . The first term in the right-hand integral is associated to the potential energy, while the second is the kinetic one.

It is important to notice that, as far as W is the amount of energy radiated in V , it is independent of the chosen surface S since it totally encloses the studied acoustic source and no other sources are present. In other words, $\int_0^{1/f} \nabla \cdot (p\mathbf{v}) dt = 0$ if no sources are contained in V (see, for instance, [Bermúdez 2005]).

Assuming that the air particle velocities in the PMSM boundary are equal to those of the machine surface itself, it is quite straightforward to see that, in order to apply (3.324), the best enclosed surface S is precisely the PMSM boundary, as far as \mathbf{v} is a known variable.

Therefore, in order to solve the total radiated power it is necessary to associate p and \mathbf{v} through (3.322). An accurate analytical solution could be quite troublesome, because the PMSM frame geometry is complex due to its fins and lateral baffles. Moreover, the relation between p and \mathbf{v} is dependent on both, the sound frequency and its vibration spatial mode.

One of the most common definitions used in vibro-acoustic is introduced in order to simplify the aforementioned problem. The sound radiation efficiency (σ) is a magnitude related with the structure under study and it is defined as the sound radiation capability of this structure in comparison with a piston with the same surface area S and same vibration levels, assuming that the piston radius is much longer than the acoustic wavelength. For that kind of piston, equation (3.322) could be solved and the pressure is equal to

$$p = \rho c \mathbf{v}, \quad (3.326)$$

where c is the sound velocity in the medium, generally air. Therefore, σ for a pure temporal tone with rms speed value V is equal to [Gieras 2006]

$$\sigma = \frac{W}{\rho c S \langle V^2 \rangle}, \quad (3.327)$$

where W is the sound power radiated from the structure and $\langle V^2 \rangle$ the spatial averaged mean square of V over the structure radiating surface S .

Obviously, each temporal frequency and spatial mode presents its own dynamic displacement $u_{r,kn}$ defined by (3.321) and, derived from this displacement, its own particle velocity amplitude V_{kn} and sound power radiated W_{kn} . Therefore, (3.327) can be rewritten as

$$\sigma_{kn} = \frac{W_{kn}}{\rho c S \langle V_{kn}^2 \rangle}. \quad (3.328)$$

Applying (3.328) the PMSM power radiation equation (3.324) should be redefined and the total radiated power expressed as

$$W = \sum_{k=1}^{\infty} \sum_{n=-\infty}^{\infty} \rho c S \sigma_{kn} \langle V_{kn}^2 \rangle = \sum_{k=1}^{\infty} \sum_{n=-\infty}^{\infty} 2\rho c S \sigma_{kn} k^2 \omega_e^2 u_{r,kn}^2 \quad (3.329)$$

Equation (3.329) is usually found under different forms in most of the literature devoted to acoustic behaviour of electrical machines [Ait-Hammouda 2005, Besnerais 2008].

In this context, the only variable that remains unknown is the sound radiation efficiency whose deduction is usually very complicated. The solution generally adopted is to simplify the radiated PMSM to a more simple geometry where the radiation efficiency is known. Generally, the electrical machine is treated as a sphere if its length is lower than twice its external diameter (i.e. $L_{Fe} \leq 4R_{se}$) and as an infinite cylinder otherwise [Besnerais 2008]. The sound radiation efficiency of both geometries is shown in Figure 3.47.

The radiation efficiency of an infinite cylinder is equal to [Gieras 2006]:

$$\sigma_{kn} = \frac{\left(\frac{2\pi R_{se}}{\lambda_k}\right)^2 \left[Y_n\left(\frac{2\pi R_{se}}{\lambda_k}\right) J_{n+1}\left(\frac{2\pi R_{se}}{\lambda_k}\right) - J_n\left(\frac{2\pi R_{se}}{\lambda_k}\right) Y_{n+1}\left(\frac{2\pi R_{se}}{\lambda_k}\right) \right]}{\left[n J_n\left(\frac{2\pi R_{se}}{\lambda_k}\right) - \left(\frac{2\pi R_{se}}{\lambda_k}\right) J_{n+1}\left(\frac{2\pi R_{se}}{\lambda_k}\right) \right]^2 + \left[n Y_n\left(\frac{2\pi R_{se}}{\lambda_k}\right) - \left(\frac{2\pi R_{se}}{\lambda_k}\right) Y_{n+1}\left(\frac{2\pi R_{se}}{\lambda_k}\right) \right]^2} \quad (3.330)$$

and the radiation efficiency of a pulsating sphere is [Timar 1989]:

$$\sigma_{kn} = \Re \left\{ \frac{j 2\pi R_{se}}{\lambda_k} \frac{\sum_{l=0}^n \frac{(n+l)! n!}{(n-l)! l!} \left(\frac{4\pi j R_{se}}{\lambda_k}\right)^{n-l}}{\sum_{l=0}^n \frac{(n+l)! n!}{(n-l)! l!} \left(\frac{4\pi j R_{se}}{\lambda_k}\right)^{n-l} \left(1 + l + \frac{2\pi j R_{se}}{\lambda_k}\right)} \right\}, \quad (3.331)$$

where $\lambda_k = c/(kf_e)$ is the wavelength in the air for the k^{th} time harmonic, J_n is the first kind Bessel function of the n^{th} order and Y_n is the second kind Bessel function (Neumann function) of the n^{th} order.

Once σ_{kn} is known, equation (3.329) can be applied and the total sound power radiated by the PMSM obtained. However, the direct sound measure in watts is not usually applied for two main reasons: the first one is that the sound sources could vary over a wide range spreading from 10^{-9} W (a soft whisper) to 10^7 W (a rocket taking off), which is quite a wide dynamic span; the second reason is that human beings hear in a logarithmic scale rather than in a linear one, i.e. one sound with acoustic pressure p^2 is perceived only twice louder than other with sound pressure p .

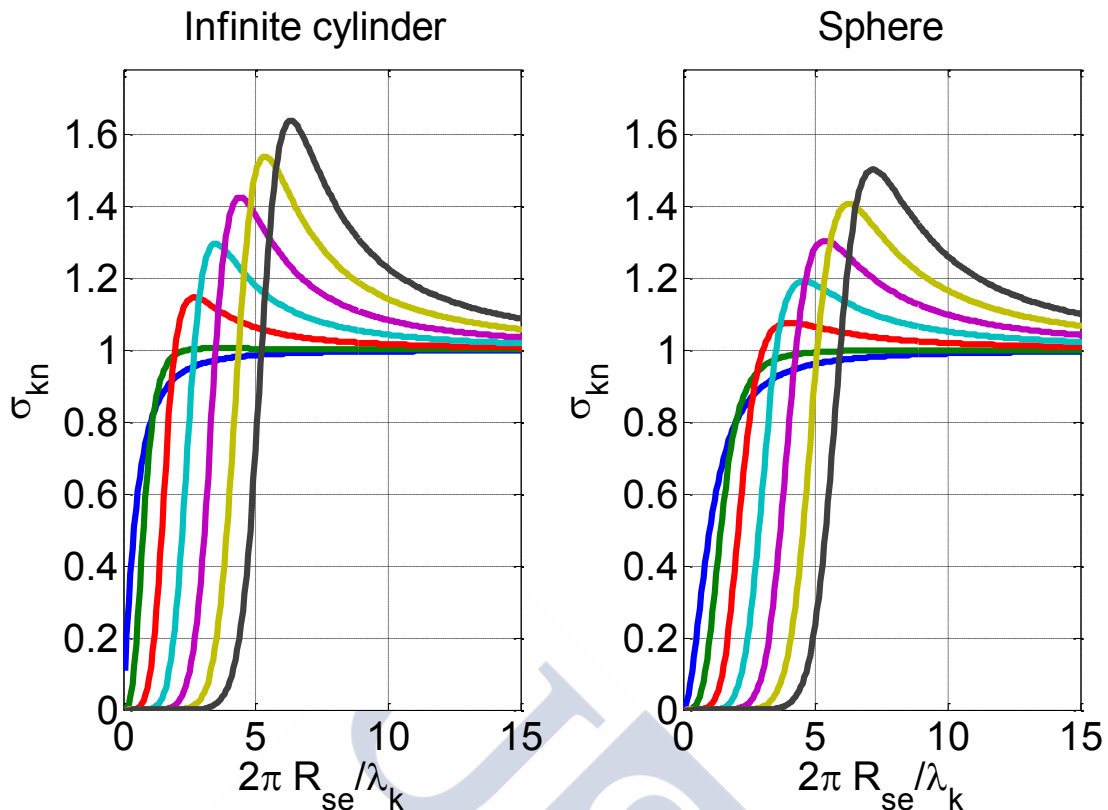


Figure 3.47. Sound radiation efficiency from mode $n=0$ (blue) to mode $n=6$ (grey).

Therefore, in order to facilitate sound classification and measurement it is usual to use a logarithmic scale with respect to a known reference; this reference is taken as $W_0 = 10^{-12} \text{W}$ because it is considered the threshold of human hearing. The used logarithmic scale is measured in decibels (dB), defined as

$$L_{\text{dB}} = 10 \log_{10} \frac{W}{W_0}. \quad (3.332)$$

It is also usual to refer the decibels scale to a pressure scale rather than a power one, because its measurement is straighter. In air, this equivalence is equal to

$$L_{\text{dB}} = 10 \log_{10} \left(\frac{p}{p_0} \right)^2 = 20 \log_{10} \frac{p}{p_0}, \quad (3.333)$$

where p_0 is the acoustic pressure reference in the medium, generally air. This reference is $p_0 = \sqrt{W_0 / (\rho_{\text{air}} c_{\text{air}})} = 2 \cdot 10^{-5} \text{N/m}^2$ for standard conditions, i.e. with $c_{\text{air}} = 340 \text{m/s}$ and $\rho_{\text{air}} = 1.19 \text{kg/m}^3$. It is worthwhile to notice that sound pressure variations under 1 dB are hardly perceived.

Moreover, the response of the human ear is not only amplitude but also frequency dependant, i.e. two sounds of the same pressure level but different amplitudes could be perceived differently. A visual comparison of the ear response to different sound frequencies is shown in Figure 3.48 where the concept of phon is used. By definition, the number of phon of a sound is the dB of a sound at a frequency of 1 kHz that is perceived just as loud.

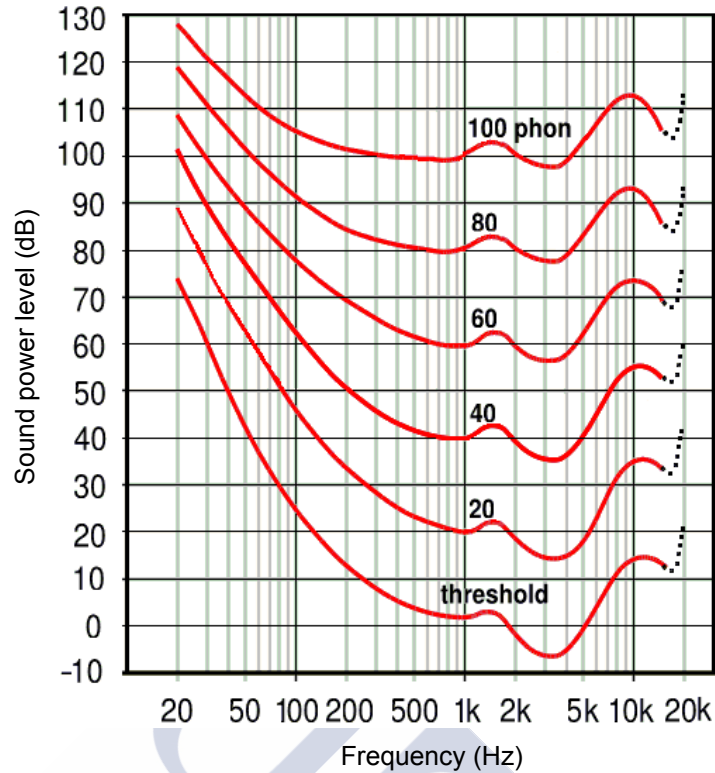


Figure 3.48. Equal-loudness curves. Standard from [ISO 2003].

As far as electrical machine noise is a problem principally for users comfort, it is very common to refer dB levels to human ear response through a pass-band filter which emulates it. These filters could be seen as a correction factor (in dB) that adapts the real sound level to that perceived by a listener. Mathematically, the sound emission in each frequency is given by

$$L_{dB}(f) = 10 \log_{10} \frac{\sum_{n=0}^{\infty} W_n(f)}{W_0}, \quad (3.334)$$

where the formalism $W_n(kf_e) = W_{kn}$ is used.

The A-weight filter is defined as:

$$R_A(f) = 2 + 20 \log_{10} \left(\frac{12200^2 f^4}{(f^2 + 20.6^2)(f^2 + 12200^2) \sqrt{(f^2 + 107.7^2) + (f^2 + 737.9^2)}} \right). \quad (3.335)$$

Finally, $L_{dB(A)}$ is the perceived sound measure which characterizes the electrical machine noisiness, its units are known as dB(A) (i.e. decibels weighted by an A-filter):

$$L_{dB(A)}(f) = L_{dB}(f) + R_A(f). \quad (3.336)$$

3.7 Multiphysical Modelling Validation

In order to carry out a first model validation and to evaluate its accuracy, a single layer, fractional slot, concentrate winding SPMSM design has been tested.

The studied PMSM is a three-phase AC machine without neutral and presents a balanced winding spatial distribution designed according to the star of slots method, see section 3.1.3 or [Bianchi 2006]. PMSM main characteristics are shown in Table 3.5 while its 2D-section is shown in Figure 3.49.

Table 3.5. PMSM main parameters.

Parameter	Value
Number of stator slots, Q	12
Number of rotor pole pairs, p	5
Number of phases, m	3
Rotational speed, n	2650 rpm
Number of conductors per slot, Z	75
Phase rms current, I_{rms}	15 A _{eff}
Rated output power, P_{out}	29.2 kW
Effective length, L_e	120 mm
Stator exterior radius, R_{se}	155.0 mm
Stator inner radius, R_s	90.0 mm
Shaft radius, R_{shaft}	35.6 mm
Airgap length, g	1.0 mm
Magnets height, l_m	6.0 mm
Tooth height, h_t	36.7 mm
Tooth width, w_t	32.0 mm
Tooth-tip height, h_0	2.5 mm
Slots opening, w_0	3.8 mm
Magnets pitch, α_p	0.15π rad

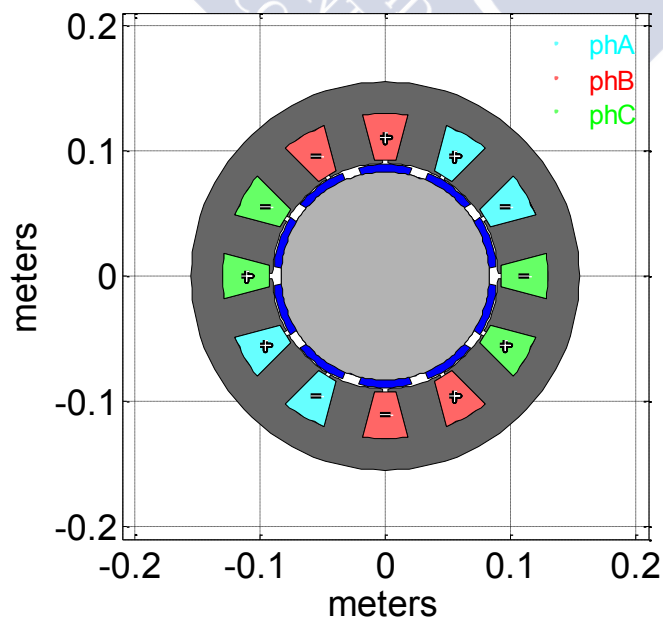


Figure 3.49. 2D section of the simulated PMSM (Q12p5).

3.7.1 Electromagnetic Validation

In order to validate the electromagnetic and the losses models the results achieved analytically are compared with those obtained by commercial FEM software of proved accuracy, FLUX®. Figure 3.25, Figure 3.50 and Figure 3.51 show both, analytical and FEM results, for the magnetic flux density in the airgap caused by the rotor magnets, the armature reaction and the sum of both contributions.

Some important conclusions can be drawn from these figures. The most important one is the high accuracy of the proposed model when the magnetic cores are unsaturated; the only distorting effect is produced at both sides of a slot opening, due to the concentration of flux in this specific regions. The chosen model does not take into account this phenomenon so it is incapable to model it properly.

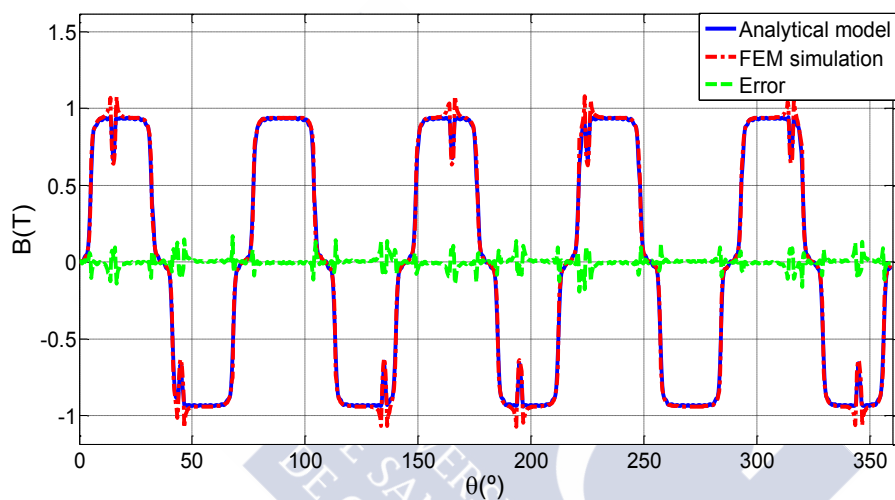


Figure 3.50. Rotor flux density in the airgap at a time instant.

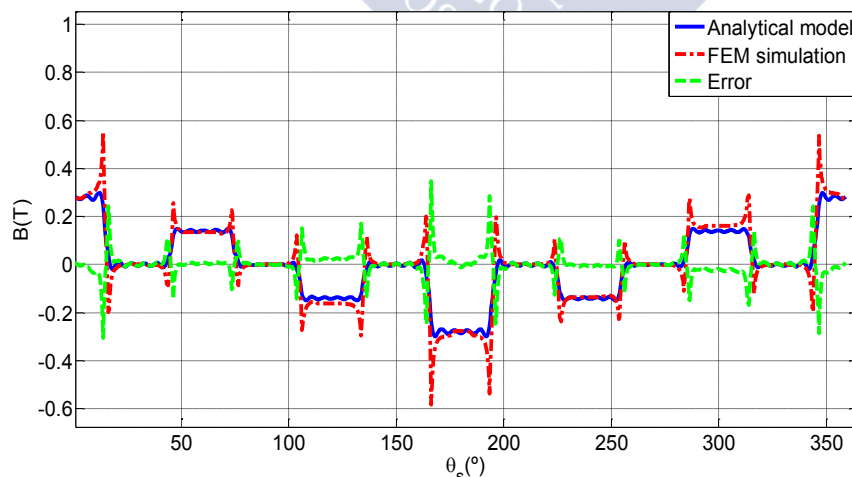


Figure 3.51. Armature reaction in the airgap at a time instant.

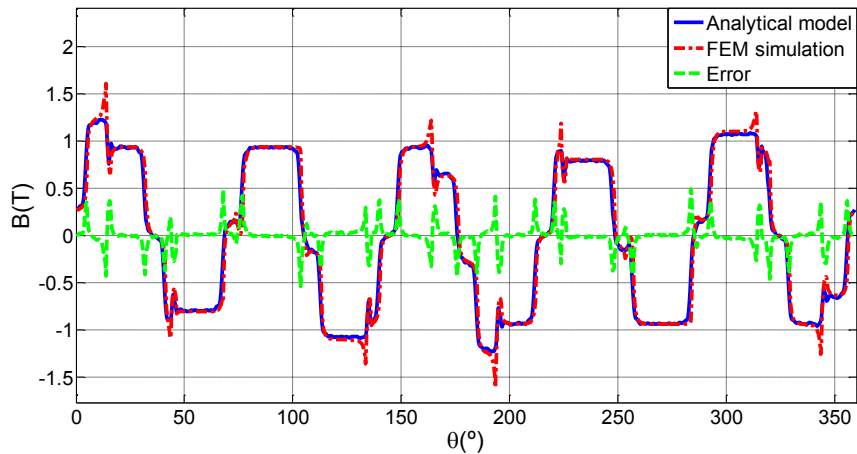


Figure 3.52. Total flux density in the airgap at a time instant.

The aforementioned slight errors are not critical since the integral calculus nature of the EMF and the electromagnetic torque greatly reduce them, as it is shown in Figure 3.53 and Figure 3.54. Moreover, the mean mutual torque (i.e. the PMSM effective torque) is equal to 108.37 Nm in both, the analytical model and the FEM simulation.

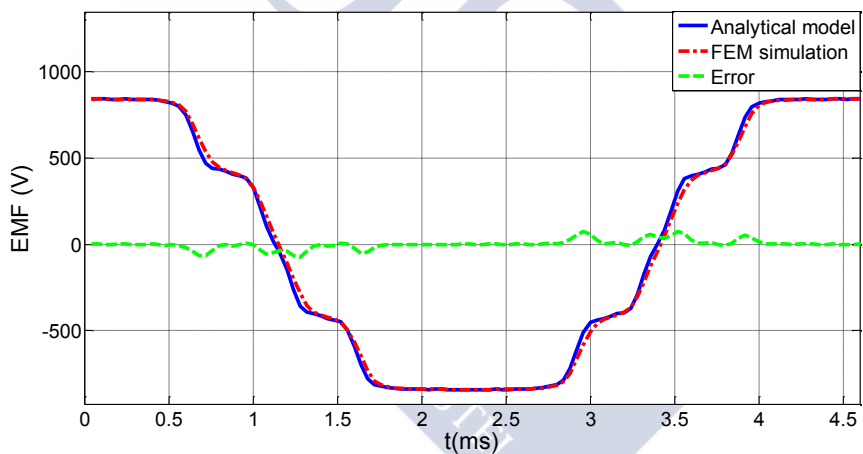


Figure 3.53. EMF induced by the magnets in phase A.

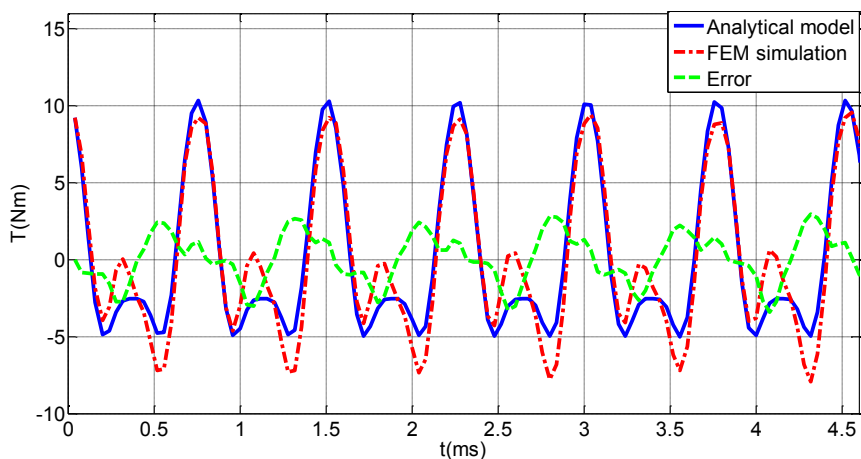


Figure 3.54. Mutual torque ripple.

The cogging torque calculated by the analytical model is also very similar to the one simulated by FEM but, since the estimation was rougher, the error is higher than in the flux and EMF calculus.

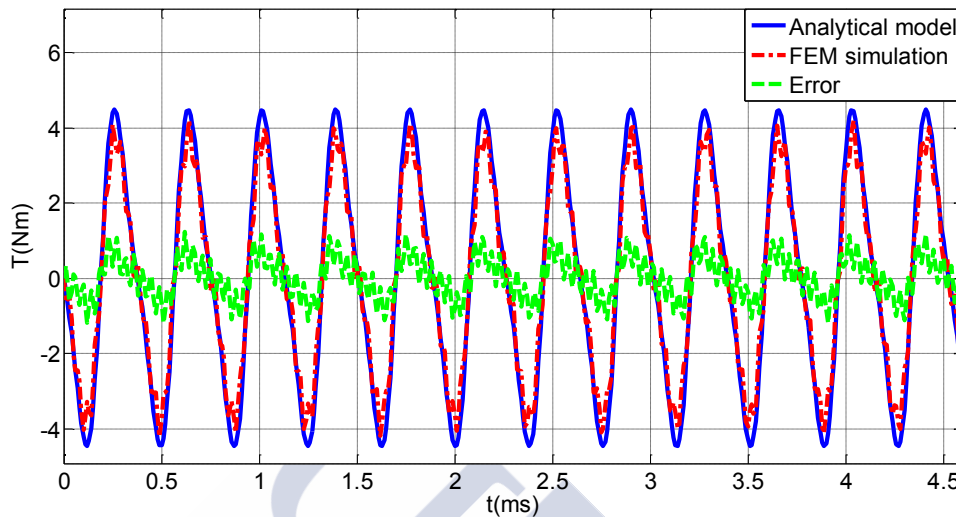


Figure 3.55. Cogging torque.

Many electrical and efficiency features of the PMSM could be validated through FEM, such as airgap and slot inductances (estimated by means of the stored energy in those regions) and the iron losses. However, the resistance and the end-winding inductance cannot be obtained from FEM simulations, since the end-winding regions geometry is still unknown and experimental measurements (or some type of analytical model similar to the implemented ones) are necessary in order to obtain these data in a specific machine prototype. This means that the PMSM equivalent circuit cannot be properly solved by a FEM simulation and, therefore, many quality parameters, such as efficiency or power factor cannot be compared with those obtained by the analytical models. The achieved results are included in Table 3.6.

Table 3.6. PMSM electrical and quality parameters

Parameter	Analytical model	FEM results
Self airgap inductance, L_g^{si}	10.9 mH	12.5 mH
Mutual airgap inductance, M_g	0.0 mH	0.0 mH
Slot inductance, $L_{\sigma s}$	5.1 mH	6.3 mH
Stator teeth losses, $P_{Fe,t}$	770 W	771 W
Stator yoke losses, $P_{Fe,y}$	558 W	549 W
Copper losses, P_{Cu}	478 W	-
Input mechanical power, P_{mec}	31.10 kW	-
Output electrical power, P_{elec}	29.21 kW	29.18 kW

The main conclusion that can be achieved is the high accuracy and short elapsed time of the magnetic and the losses models. The electric ones are able to provide a first approximation of the inductance value but with less accuracy than the magnetic ones, maybe due to the more rough geometrical approximations.

The major drawback of the introduced validation method is that the end-winding region geometry is unknown and a proper FEM analysis of this part of the machine could not be performed. This drawback will be overcome in the experimental measurement exposed in Chapter 4, where a complete and total validation will be carried out.

The presented results prove the suitability of electromagnetic models for the development of a fast, accurate, modular and optimized design methodology.

3.7.2 Thermal Validation

The results obtained with the small lumped parameter model were compared with those calculated by Motor-CAD®, a commercial software based on a complete thermal network with more nodes and an extensive library of thermal coefficients obtained during decades of experimental tests for many electrical machine technologies.

The equivalent model used by Motor-CAD® is also a lumped parameter one but, in this case, with a high number of nodes. The thermal network applied by this software can be seen in Figure 3.56, and the results obtained with both approaches are in Table 3.7. The agreement between the commercial software and the obtained results is very good, with an error less than 11°C in all measures and a mean error of 6.5°C.

It can be concluded that, at this machine design stage, the proposed lumped thermal model is a fast and accurate solution allowing to quickly compare the thermal performance of different designs and to establish safety limits to the temperature in PMSM most critical regions, such as the magnets and the end-windings. A complete comparison with measured data will be included in the next chapter.

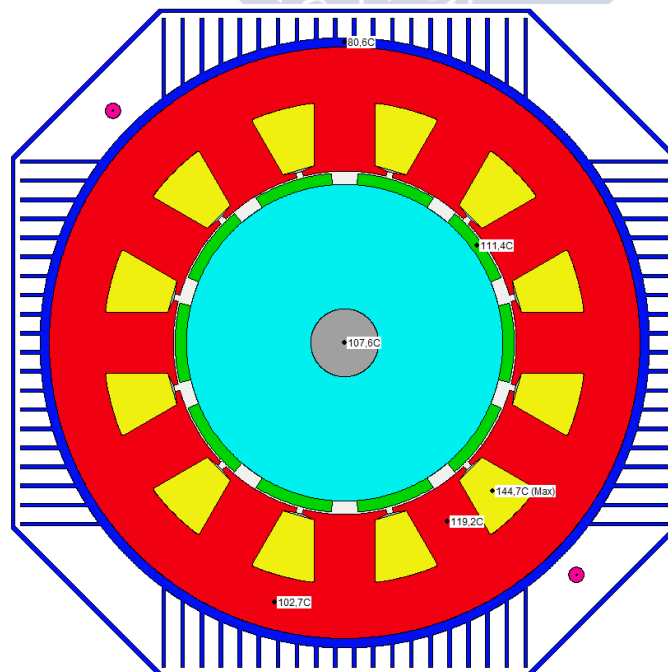


Figure 3.56. PMSM temperatures calculated by Motor-CAD®.

Table 3.7. Estimated PMSM temperatures.

Machine region	Analytical model (°C)	Motor-CAD Results (°C)
Ambient, T_{amb}	40.0	40.0
Frame, T_{fr}	86.6	80.6
Stator yoke, T_{sy}	98.6	102.7
Stator teeth, T_{st}	114.2	119.2
Embedded coils, T_s	155.4	144.7
End-winding, T_{ew}	156.1	146.2
Magnets, T_{mag}	107.4	111.4
Rotor shaft, T_{shaft}	101.3	107.6

3.7.3 Vibratory Validation

The structural results obtained with the analytical model were compared with those calculated by ANSYS®, a commercial FEM software which has a complete structural module with the possibilities of performing both a modal analysis and a random vibration response.

A complete modal analysis was carried out, and the static displacements and natural frequencies of each mode were calculated with both approaches. The obtained results can be seen in Table 3.8.

The agreement between the commercial software and the obtained results is quite good. In the five first modes the natural frequency error is less than 6% and the one in static displacement less than 8%. Higher order modes are usually neglected in acoustic calculus, because its poor sound radiation.

Although the errors may seem high, they are perfectly acceptable. Error reasons are the aforementioned neglected effects and the uncertainties inherent to material mechanical features and the precise nature of the fixed points. In spite of that fact, a fair comparison between candidate designs can be performed and it is also possible to determine the most problematic frequency bands which are the two main objectives in the design process.

Table 3.8. Simulated and estimated modal static displacements and natural frequencies

Mode	FEM Results (ANSYS®)		Analytical Model		Relative Error	
	f_n (Hz)	Y_n (m^3/N)	f_n (Hz)	Y_n (m^3/N)	f_n (%)	Y_n (%)
0	4307	$2.4 e^{-12}$	4128	$2.3 e^{-12}$	-4.16	-4.17
2	590	$91.2 e^{-12}$	554	$92.5 e^{-12}$	-6.10	1.43
3	1535	$12.9 e^{-12}$	1445	$13.0 e^{-12}$	-5.86	0.78
4	2638	$4.0 e^{-12}$	2516	$3.7 e^{-12}$	-4.63	-7.50
5	3637	$1.7 e^{-12}$	3671	$1.5 e^{-12}$	0.93	-11.76

It can be concluded that, at this stage of machine design, the proposed analytical acoustic model is a fast and suitable solution, which enables a quick comparison of the vibratory behaviour of different designs and establishes the frequencies which should be avoided in the excitation magnetic force.

As a final remark, it must be highlighted that experimental results must be performed in order to validate both, the analytical and FEM calculus, as far as external elements such as feet, shaft or housing have been neglected in both approaches. A complete comparison with measured data for a PMSM, fully design in IK4-Ikerlan, will be included in Chapter 4.





Experimental Validation



This chapter is devoted to a complete analysis of a SPMSM case of study in order to fully validate the proposed electromagnetic, thermal and vibro-acoustic models presented in Chapter 3. This is especially important because the developed modelling is the basis of an ulterior design methodology explained in Chapter 5, which is the final aim of the thesis work.

The chapter is divided in several sections. First, the SPMSM case of study is presented, it is a machine with 45 slots and 5 pole pairs (i.e. a Q45p5 machine), fully designed in IK4-Ikerlan in order to obtain a suitable experimental subject for the presented tests. Second, the laboratory facilities are described. Third, the machine parametrization is performed and, finally, the electromagnetic, thermal and vibro-acoustics test are detailed and the obtained conclusions summarized.

4.1 Case of Study: IkerMAQ Q45p5

4.1.1 Application and Initial Specifications

As it was mentioned a proper case of study in order to perform the experimental tests was desired. Therefore, a complete design was developed in IK4-IKERLAN. The final prototype, called IkerMAQ is a Q45p5 SPMSM.

IkerMAQ was designed in order to take maximum advantage of the available test-bench. Therefore, a set of specifications and constraints will be established as a function of the electric and electronic equipment and their operation limits.

The main constraints imposed by the application and the test-bench features have electrical nature. The available converter (used in some experiments in order to feed IkerMAQ) has a maximum bus DC voltage of 750 V which limits the phase voltage to $300 V_{\text{rms}}$; additionally, the phase current that the converter can handle is established at $120 A_{\text{rms}}$.

The desired nominal electrical output power (with the PMSM in generator mode) is 75 kW with a nominal speed of 1080 rpm (i.e. mechanical frequency of 18 Hz). This established a nominal torque of 700 N.m.

The machine is supposed to work with constant load in continuous nominal operation conditions, so thermal equilibrium is assumed. This kind of operation falls within class S1.

In order to ensure a proper heat removal a total enclosed air fan cooled machine is considered, i.e. a machine with a finned frame with a fan attached to the shaft in its rear part. The air is propelled by the fan and passes over the fins, ensuring an efficient convection heat transfer.

Regarding the selected materials, the chosen magnets will be N40H, because of its good magnetic properties (NdFeB magnets have the best energy product in actual market) and the coil insulation class will be H (maximum coil temperature 180°C).

4.1.2 Design, Manufacture Process and Internal Geometry

Table 4.1 shows the selected IkerMAQ design, with its main geometrical and configuration variables.

Table 4.1. IkerMAQ main geometrical and structural features.

Parameter	Symbol	IkerMAQ (Q45p5)
Power	P_{obj}	75 kW
Speed	n	1080 rpm
Torque	T	700 Nm
EMF (phase)	E_A	293 V_{rms}
Current (phase)	I_{ph}	87 A_{rms}
External stator radius	R_{se}	0.188 m
Effective length	L_e	0.31 m
Pole pairs number	p	5
Slots number	Q	45
Internal stator radius	R_s	0.139 m
Airgap	g	3.3 mm
Magnet pitch	α_m	75.0%
Magnet height	l_m	13.45 mm
Number of conductors per slot per layer	Z	3
Teeth height	h_2	29.8 mm
Teeth width	w_t	11.3 mm
Slot-opening	w_0	3 mm
Tooth-tip height	h_0	2 mm
Total slot area	A_s	140.3 cm^2

IkerMAQ was designed by the electrical machines manufacturer Lancor. Its stator and rotor were built separately and sensors (i.e. type k thermocouples and test coils) were added (see Figure 4.21), both parts can be seen, during the manufacturing process, in Figure 4.1.

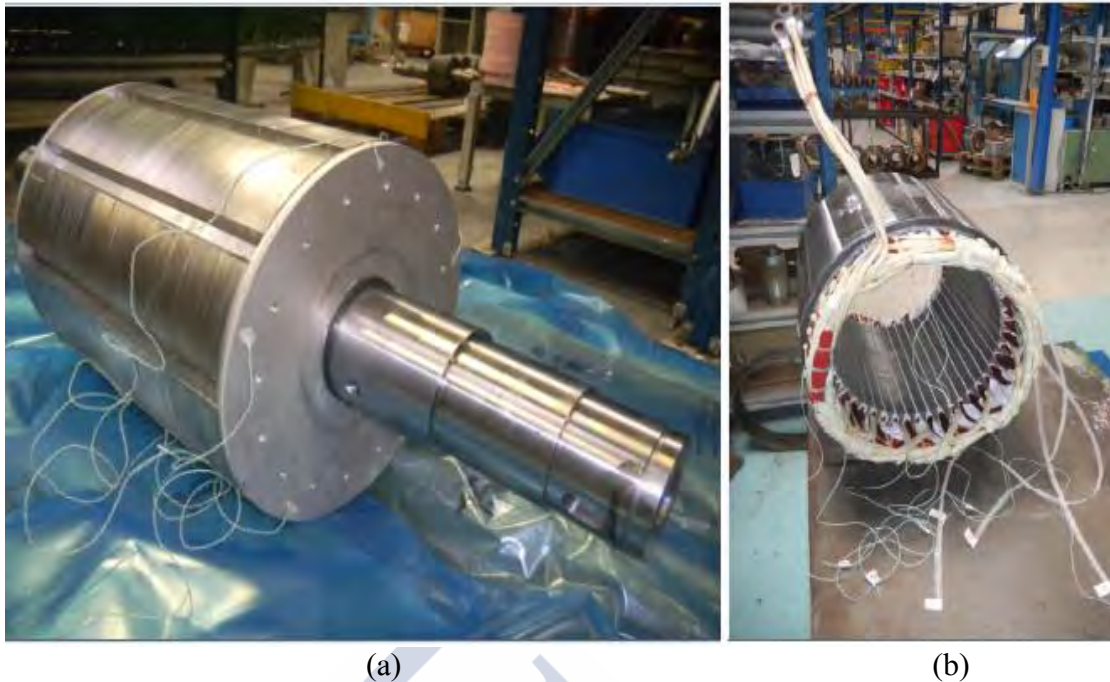


Figure 4.1. IkerMAQ (a) rotor and (b) stator. Notice the thermocouples and test coils.

The stator winding layout can be seen in Figure 4.2, where one phase coils are shown in their containers slots.

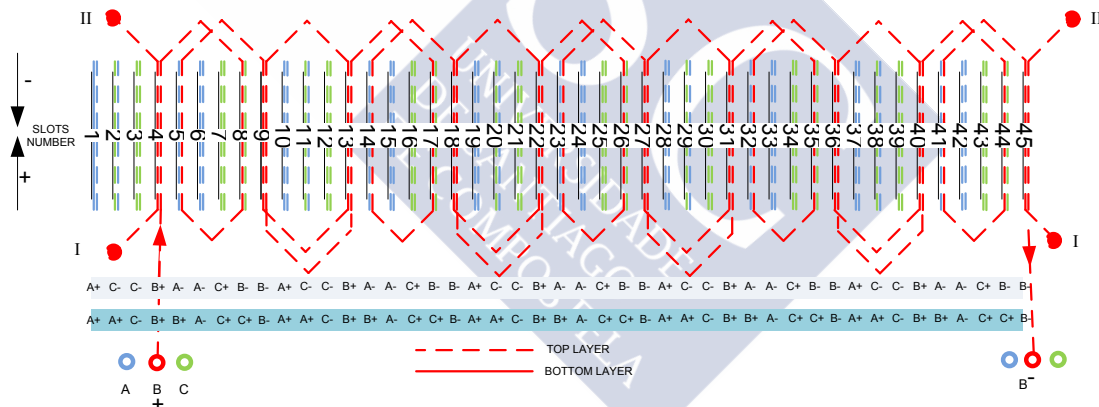


Figure 4.2. IkerMAQ phase B winding blueprint.

Regarding rotor, a critical point in any SPMSM manufacture is the magnets inset, the most popular solutions are to glue the magnets or the use of a retaining sleeve. In this case, Lancor manufactured its rotors embedding the magnets into them, through a ferromagnetic material “pole shoe”, as shown in Figure 4.3.

This “pole shoe” means that IkerMAQ is not exactly a SPMSM but an “embedded magnet” PMSM, i.e. it is in a point between internal and surface PMSM. Though the design is quite close to a surface one (i.e. the pole shoe is quite thin) its effects are evident and can be measured, as it will be explained.

The main difference between a pure SPMSM and IkerMAQ is that IkerMAQ has a little saliency and a SPMSM has not. In other words, the internal inductance of a

SPMSM is exactly the same no matter the rotor position respect to the stator, while in a salient machine is not. This is due to the influence of the pole shoe over the magnetic flux, because the flux tries to flow through the pole shoe avoiding the air between magnets where the path reluctance is higher.

Respect to the practical machine behaviour saliency means a difference both in its electric features (the inductance is not constant) and in the mechanical ones (an additional torque component, the reluctance one, due to these inductance variations, may appear). As a summary, some little differences may appear between the SPMSM models and IkerMAQ (with embedded magnets) but they are relatively small, because the pole shoes thinness.

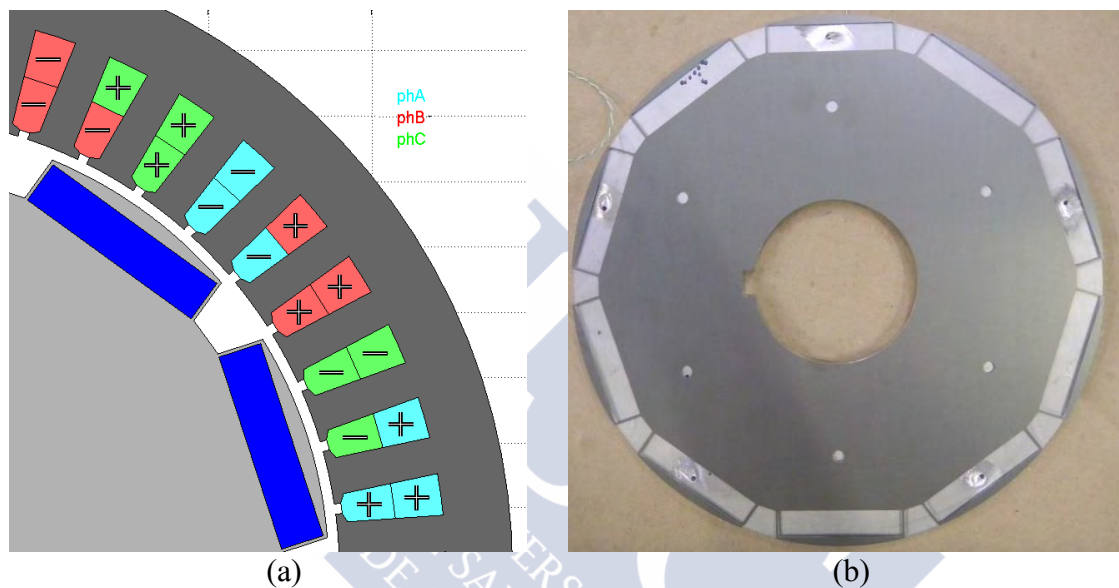


Figure 4.3. Magnets inset detail. (a) One periodicity 2D cross section, (b) rotor end-cap.

A photo of the manufactured complete prototype can be seen in Figure 4.4.



Figure 4.4. IkerMAQ (Q45p5), designed by IK4-Ikerlan during 2013 and built by Lancor in 2014

4.2 Laboratory Test-Bench

Once the test subject is presented, the next obvious step is to summarize the main features of IK4-Ikerlan laboratory facilities and the used equipment and materials.

The electromagnetic, thermal and vibro-acoustic tests can be divided into two groups: “with” and “without converter” test. During the first ones IkerMAQ is in generator operation mode and another machine is used as traction motor. This machine is controlled by a commercial converter (both, machine and converter are ABB products).

The test “with converter” uses additional equipment. More precisely, a railway traction prototype composed of a traction converter of 300 kW (developed by IK4-Ikerlan and the CAF Group) and a DC source that feed it.

The laboratory facilities in IK4-Ikerlan are shown in Figure 4.5 and Figure 4.7. They are composed of a dc source, inductors and resistive loads, an IGBT based three-phase two-level inverter, a rotor position encoder and a commercial load machine with its inverter.

4.2.1 Experimental assembly without converter

The typical assembly in the tests without converter is shown in Figure 4.5. The more important equipment is described forward.

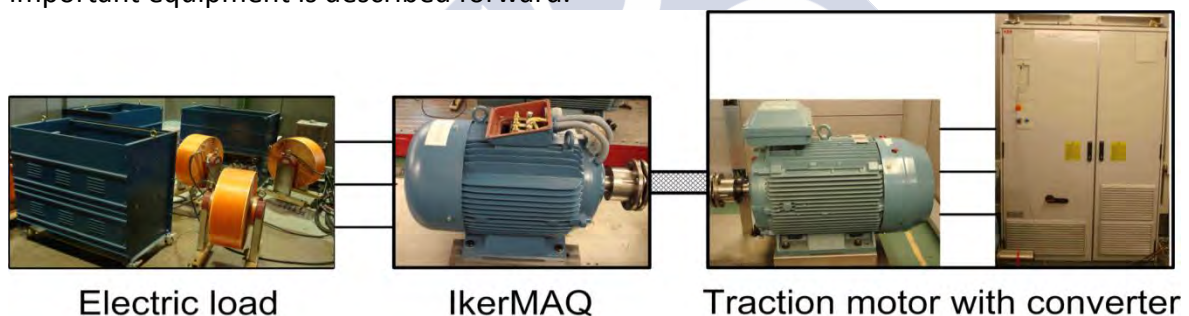


Figure 4.5. Laboratory facilities block diagram in the “without converter” configuration

Electric loads: Many passive components can be used as electric loads. In the studied cases they are inductances (3.0 mH) and resistances (boxes with four resistances each and configurable connexions. Each resistance has a value of 4.4Ω and maximum power dissipation of 10 kW).

With these two elements (inductances and resistances) many different loads can be connected, depending on the test. The selected load will be specified when the experiment be introduced. It is worthwhile to notice that some tests are carried out at no load, (i.e. IkerMAQ terminals in open circuit).

ABB induction machine and converter: During these tests IkerMAQ is in generator mode and it is driven by an ABB traction induction machine (M3BP 315SMC 6B3) since both are connected to the same shaft (see Figure 4.6). The traction motor is controlled

in speed by a commercial converter. The nominal characteristics of the traction equipment (both, machine and converter) are summarized in Table 4.2.

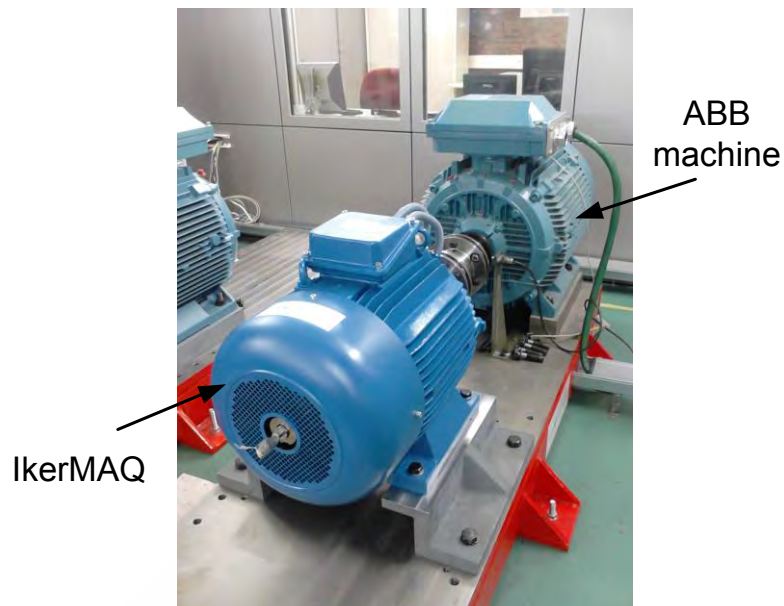


Figure 4.6. IkerMAQ and ABB machine connection within test-bench.

Table 4.2. ABB load equipment features.

Parameter	Value
Nominal power	110 kW
Nominal speed	1000 rpm
Nominal frequency	50 Hz
Nominal torque	1060 Nm
Maximum torque	3000 Nm
Pole pairs number	3

4.2.2 Experimental assembly with converter

Some tests require that IkerMAQ be controlled by a converter. As it was previously commented, this role is played by a 300 kW railway traction prototype developed by IK4-Ikerlan. The typical assembly in the configuration with converter is shown in Figure 4.5.

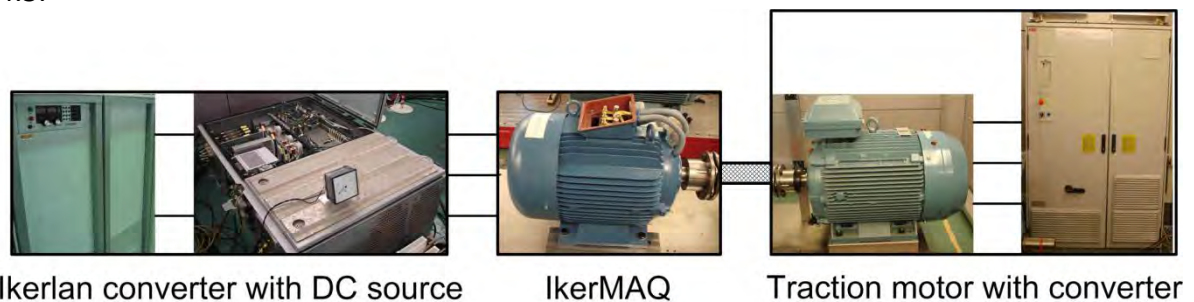


Figure 4.7. Laboratory facilities block diagram in the “with converter” configuration

In order to perform these tests some additional equipment is required (see Figure 4.8).

DC source: The DC power supply located in the laboratory is composed of two commercial DC sources commercialized by Manga Power. They are connected in parallel, in a master-slave configuration with a rated power of 100 kW and a maximum current of 100 A. Table 4.3 summarizes the principal characteristics of this DC source.

As it will be remarked later on, the DC source has been the most restrictive aspect of the carried out tests in this configuration assembly.

Table 4.3. Magna Power DC source characteristics.

Parameter	Value
Nominal power	100 kW
Nominal voltage	1000 V
Nominal current	100 A

Voltage source converter: As it can be seen in Figure 4.8 (a), a three-phase, two-level inverter has been employed for the tests. The inverter provided by CAF Power & Automation was designed for a previous project in collaboration between this company and IK4-Ikerlan so as to work with a 300 kW traction system. It can be remarked that this type of inverters are already in use in commercial trams rolling in several cities like Vitoria, Zaragoza or Sevilla.

The inverter is connected to a braking chopper which enables IkerMAQ generation mode, if desired, and an internal discharge resistor to discharge the DC-bus in case of failure or for maintenance work.

Within the inverter, the inverter control unit (ICU) can be found, it is in charge of the control and modulation of the inverter output voltages. The ICU is formed by a DSP, a FPGA, a microprocessor and an expansion card.



(a)



(b)

Figure 4.8. IkerMAQ supply and control equipment; (a) voltage converter, (b) DC source.

4.3 IkerMAQ Parametrization

A necessary prologue to more complex tests is the correct characterization of the IkerMAQ electric parameters, because they are critical in order to correctly estimate the machine equivalent circuit (see Figure 3.17). It is worthwhile to notice that this previous information is useful not only for the electromagnetic characterization but for the thermal and vibro-acoustic ones too.

Specifically, for correct equivalent circuit estimation, three parameters are required: the EMF as a function of the machine speed (E , much related with the embraced permanent magnet flux), the total phase inductance (L_{ph}) and the phase resistance (R_{ph}). During the present section this variables are measured, and the obtained values compared with those estimated by the analytical models.

4.3.1 Permanent Magnets EMF

The induced EMF is one of the most important PMSM parameters, because its variation affects both the electromagnetic torque and the machine electromagnetic features.

Two variables determine the induced EMF: the rotor speed and the total magnet flux. Applying Faraday's law to a machine rotating at constant speed it can be deduced [Almandoz 2008]:

$$|E_0|_{rms} = \sqrt{3}\omega_e\psi_m = \sqrt{3}(\pi p/30)n|\phi_{lk,1}^{m,1}|_{rms}, \quad (4.1)$$

where $|E_0|_{rms}$ is the line voltage fundamental temporal harmonic (measured in rms), n is the rotor speed measured in rpm and $|\phi_{lk,1}^{m,1}|_{rms}$ is the total magnet flux linked by phase A (measured as its fundamental temporal harmonic in rms value).

From (4.1), it is clear that the induced EMF is directly proportional to both, the rotor speed and the total magnet flux embraced by the coils. Both physical variables may change during the machine operation, the speed due to the control system requirements and the magnet flux mainly due to magnet heating, i.e. a temperature rise leads to a magnet flux reduction and, therefore, to a lower performance.

Table 4.4 shows the experimental relation between rotational speed and EMF, it is measured in cold (permanent magnets are about 20°C). The total magnet flux is deduced from the slope between the EMF (measured by a Yokogawa WT-500 wattmeter) and the rotational speed (measured by the ABB traction machine control system). As it can be clearly seen the experimental relation between the speed and the EMF is very close to the theoretical straight line, i.e. ψ_m is nearly constant in each measure.

The relation between magnet temperature and its EMF was also experimentally measured. This test is especially important because in normal operation mode

IkerMAQ magnets have a temperature of 76°C (working without converter) or 106°C (if it is controlled by the converter). Table 4.5 includes the measured results compared with those analytically inferred from the magnets datasheet [Arnold 2015]:

$$|E_0|(V_{rms}) = 559.6 - 0.667T(^{\circ}C). \quad (4.2)$$

Table 4.4. Relation between rotor speed and EMF (magnets at 20°C).

Rotor speed [rpm]	$ E_0 _{rms}$ [V _{rms}]	$ \phi_{lk,1}^{m,1} _{rms}$ [Wb]
50	25.6	0.565
100	51.5	0.568
200	101.9	0.562
300	152.8	0.561
400	203.6	0.560
500	253.7	0.560
600	304.4	0.559
700	355.0	0.559
800	404.9	0.558
900	455.5	0.558
1000	506.0	0.558
1080	546.0	0.558

Table 4.5. Relation between rotor speed and EMF (n=1080 rpm).

Magnets temperature (°C)	$ E_0 _{rms}$ [V _{rms}] (Analytical)	$ E_0 _{rms}$ [V _{rms}] (Measured)	Relative error (%)
20.0	546.3	545.6	0.12
76.3	508.7	509.2	0.10
106.0	488.9	486.9	0.41

4.3.2 Stator Resistance

The stator resistance is a key factor because it determines the copper losses and, therefore, it plays a major role in total PMSM efficiency.

Obtain an accurate stator resistance estimation is a difficult task because of many factors: its temperature dependence, the manufacture unknowns and, especially, its low value. This last inconvenient is critical because conventional measured equipment, such as a multimeter, cannot be used in order to obtain stator resistance.

Due to the end-winding length major influence on the stator resistance, it was measured in order to fit the analytical models. Table 4.6 shows the expected and the real measured values, the additional end-winding length is not surprising because of the great dispersion of this parameter during the manufacture process.

Table 4.6. End-winding length fitness.

	Analytical	Measured	Relative error (%)
L_{ew} (mm)	125	186	32.8

Three different tests were carried out: the first ones with a micro ohmmeter (Megger, BT51), the second one with a LCR (Agilent, HP 4284A) and the third one with a DC source. The two first use “four wires measured” (i.e. two wires inject a known current and the other two are connected to a voltmeter) while, during the third, a DC source (Xantrex, XDC 60-200) is used in order to feed the motor with a known DC current of 90A while a voltmeter measures the voltage on IkerMAQ terminals. The three test results and the analytically estimated stator resistance are shown in Table 4.7.

Table 4.7. Stator resistance: analytical estimation and measurements.

	Measured				Analytical	Relative error (%)
	LCR	Ohmmeter	DC source	Average		
$R_u(\text{m}\Omega)$	42.5	53.5	48.2	48.1	37.8	21.4
$R_v(\text{m}\Omega)$	57.5	59.5	56.4	57.8	37.8	34.6
$R_w(\text{m}\Omega)$	59.0	59.0	54.1	57.4	37.8	34.1
$R_{av}(\text{m}\Omega)$	53.0	57.3	52.9	54.4	37.8	30.5

From Table 4.7 some conclusions could be established. On the one hand, it is clear that the three tests present some divergences between them. On the other hand it can be noticed that one phase (noted as phase u) has lower stator resistance than the other two, likely as a consequence of manufacture tolerances. It is evident that the analytical estimation underestimates the stator resistance value with a 30% error; this fact does not match with the assumed wires length and surface. Unfortunately, this amount of error is quite common in this kind of estimation due to the nature of the manufacture process.

Finally, it is worthwhile to notice that the stator resistance is temperature and frequency dependant, as it was explained in chapter 3.

4.3.3 Stator Inductance and Saliency

The stator inductance (L_{ph}) is another major factor because it plays an important role in control strategies and it also determines machine electrical behaviour, its interaction with the converter, its transients and the values of some quality factors, such as the power factor.

As it was aforementioned the manufactured IkerMAQ is not exactly a SPMSM but an embedded magnet PMSM. Therefore, the stator inductance is not constant but it varies from a maximum (L_q) to a minimum (L_d) value as a function of the rotor position respect to the stator. The stator inductance is assumed to be the mean value of that two, i.e. $L_{ph} = (L_q + L_d)/2$.

In order to obtain these values, the LCR (Agilent HP 4284A) was used. During the test the rotor was moved 4 mechanical degrees each time. The values of each phase inductance as a function of the rotor position can be seen in Figure 4.9 while Table 4.8 establishes a comparison between the measured inductance values and the ones estimated analytically.

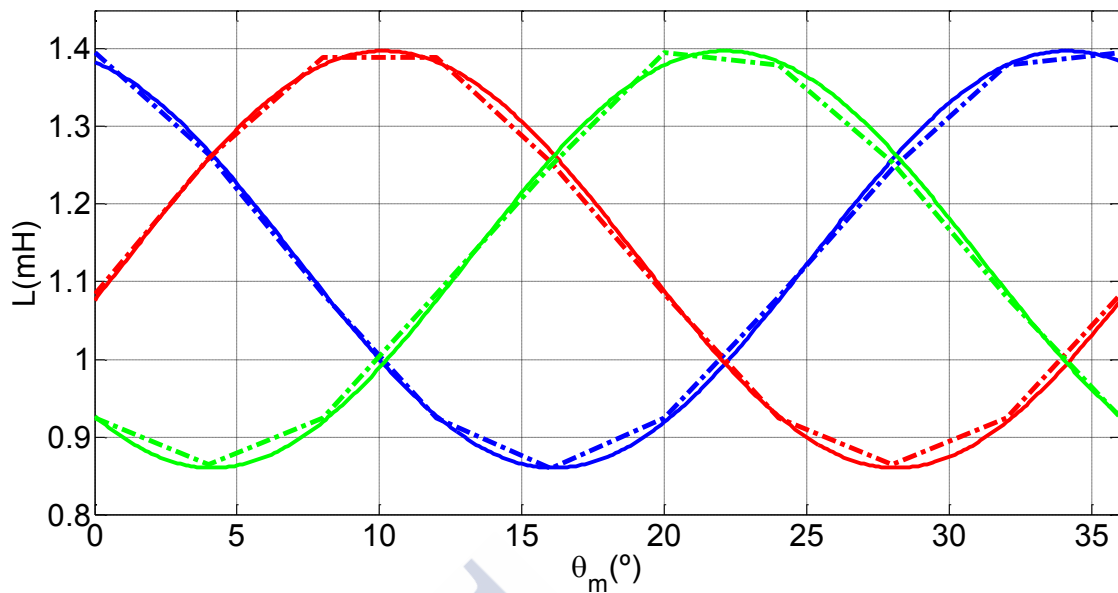


Figure 4.9. Phase stator inductance as function of the rotor position. Dotted lines represent the measured values.

Table 4.8. Stator inductance analytical estimation and measurements.

	Analytical	Measured	Relative error (%)
L_q (mH)	1.11	1.40	20.7
L_d (mH)	1.11	0.86	29.1
L_{ph} (mH)	1.11	1.13	1.8

It can be concluded that the estimation of L_{ph} is quite good; therefore, it can be used in order to accurately calculate the prototype electromagnetic behaviour. However, the presence of a non-negligible saliency (23.9% respect to L_{ph}) may have some parasitic effects that will influence IkerMAQ magnetic features, as will be exposed in section 4.4.

4.4 Electromagnetic Tests

Among the performed tests some of the most important are the electromagnetic ones. As it was previously introduced, the electromagnetic behaviour is the “machine heart” and it can be seen as the initial point where the rest of the multiphysical domains emerged.

In order to carry out these tests some important remarks should be taken into account:

- Mainly four variables are measured in order to characterize IkerMAQ behaviour: the phase current, the line voltage in the machine terminals, the torque on the shaft and the ABB asynchronous machine mechanical power. The first two parameters are measured by a Yokogawa WT-500 wattmeter, while the two last are provided by the ABB control system.
- The rotor speed is established through the ABB traction machine control.

- During the manufacture process, test coils are added in the slots in order to obtain the EMF induced in just one tooth and, through direct integration, to calculate the magnetic flux flowing through it. The coils connection can be seen in Figure 4.21.
- As far as the electromagnetic behaviour is temperature dependant most of the tests are carried out twice, the first time in “cold” (at the laboratory temperature, about 20°C) and the second one after the thermal steady state is reached (with a magnet temperature close to 76°C).

In addition to the aforementioned details, two important assumptions are made in order to fit the analytical models and compare their results with those obtained from the experimental measurements.

- The first one is a correction factor in order to take into account the ferromagnetic cores saturation level, this “saturation factor” is represented assuming that the N40H magnets residual induction is a 97.7% of its nominal value (i.e. $B_r = 1.25T$ instead of 1.28T).
- The second correction is about IkerMAQ embedded magnets configuration. Due to the pole shoes the “effective” airgap seen by the armature reaction is shorter than the airgap seen by the magnets flux density. The first one is established as $\delta_s = 1.2g = 3.96mm$, while the second is estimated as $g + l_m = 16.675mm$.

4.4.1 Open circuit

These tests are in open circuit configuration, i.e. the connexions scheme is the one shown in Figure 4.5 with the only different that no load is connected. The obtained EMF, both the line voltage and a single tooth induced voltage are shown in Figure 4.10 and Figure 4.11, respectively. The Fourier series of the measured signals are included.

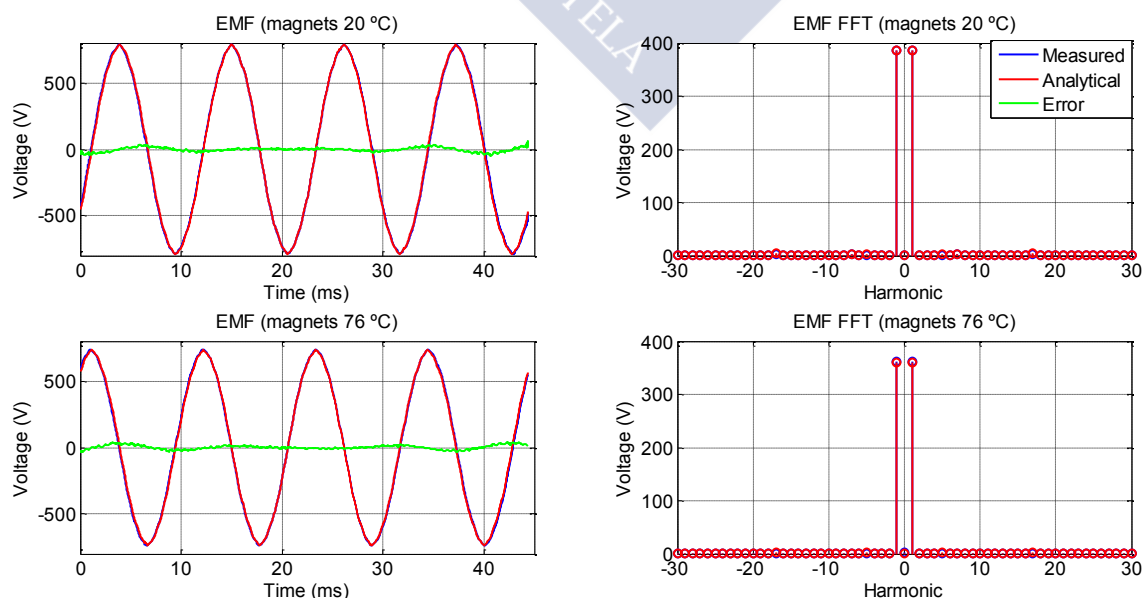


Figure 4.10. Open-circuit line EMF (measured in IkerMAQ terminals).

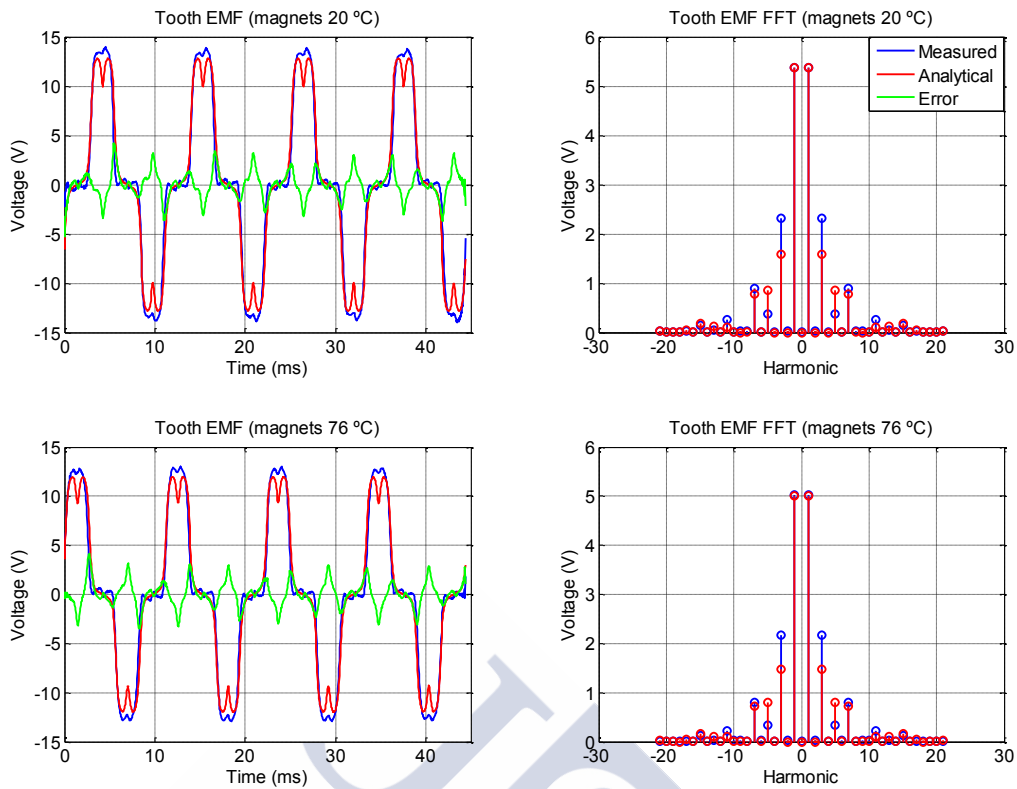


Figure 4.11. Open-circuit EMF induced in a single tooth.

Once the EMF induced in a tooth is obtained a numerical integration is performed in order to calculate the magnetic flux flowing through it. The comparison between the experimental results and the analytical calculus can be seen in Figure 4.12.

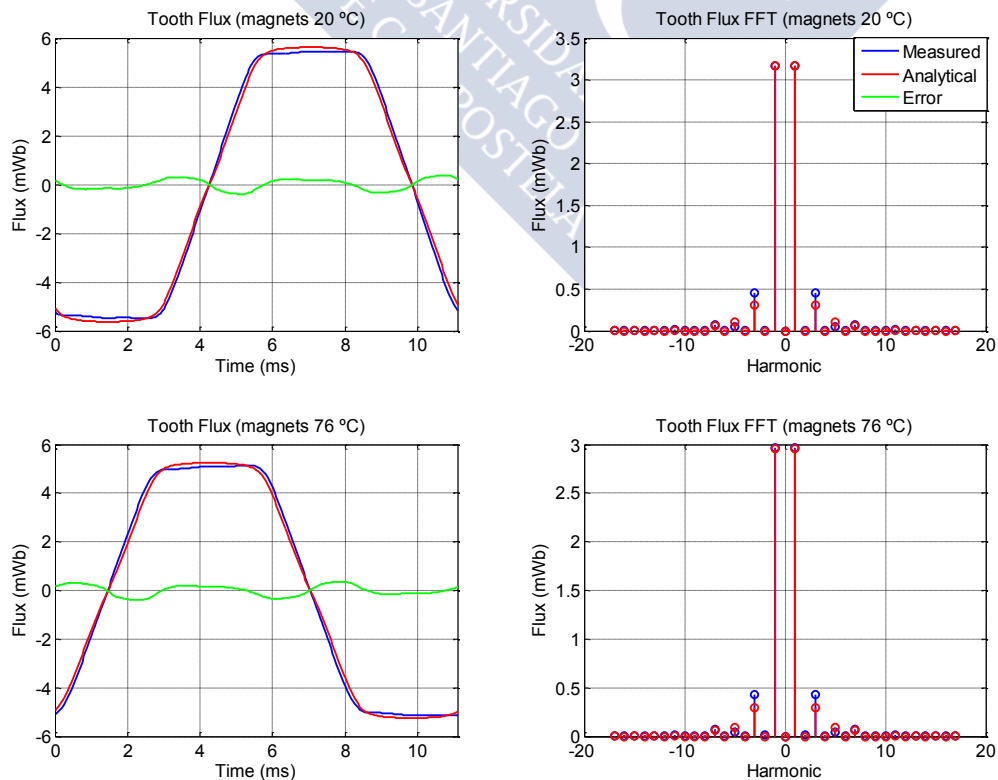


Figure 4.12. Open-circuit magnetic flux flowing through a tooth cross section.

It is remarkable the great agreement between the analytical results and the experimental ones. The reached accuracy is very high, especially in the line EMF estimation. However, a third temporal harmonic more important than the expected is measured in the teeth EMF and magnetic flux. Fortunately, this harmonic has no real relevance in IkerMAQ performance because it is filtered from the line voltage.

These noticed errors are likely caused by the embedded magnet configuration, because the magnetic flux linked by the stator coils (and, therefore, the EMF) can be slightly altered by the pole shoes.

4.4.2 On load

Several tests are performed on load, some with and some without converter. The first ones are without converter following the configuration shown in Figure 4.5.

In this case a load is fed by IkerMAQ, their R and L values are chosen in order to ensure nominal operation current at nominal speed of 1080 rpm. The test is repeated twice, the first one with magnets at 20°C at the second one at their expected temperature at nominal operation (76.3°C). The experimental conditions are included with “cold magnets” and with “hot magnets” in Table 4.9 and in Table 4.10, respectively. In addition, Figure 4.13 shows the wattmeter measurements in the “cold magnets” experiment.

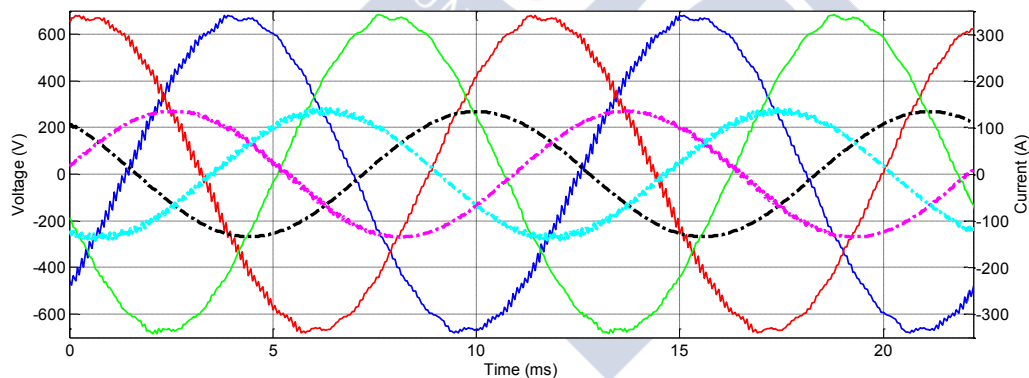


Figure 4.13. Measured electric waveforms. Current lines are dotted.

Table 4.9. Experimental electrical variables. Cold magnets test.

Parameter	Value
EMF phase voltage (V_{rms})	320.9
Load phase voltage (V_{rms})	274.2
Phase current (A_{rms})	95.1
Power factor	0.78
Load impedance (Ω)	$2.25+1.80j$
Electric frequency (Hz)	90.0
Mechanical input power (kW)	64.98
Electrical output power (kW)	61.77

Table 4.10. Experimental electrical variables. Hot magnets test.

Parameter	Value
EMF phase voltage (V_{rms})	293.9
Load phase voltage (V_{rms})	255.0
Phase current (A_{rms})	88.0
Power factor	0.79
Load impedance (Ω)	$2.28+1.79j$
Electric frequency (Hz)	90.0
Mechanical input power (kW)	56.07
Electrical output power (kW)	52.95

The obtained voltages, both the line one and the induced in a single are shown in Figure 4.14 and Figure 4.15, respectively. The Fourier series of the measured signals are also included.

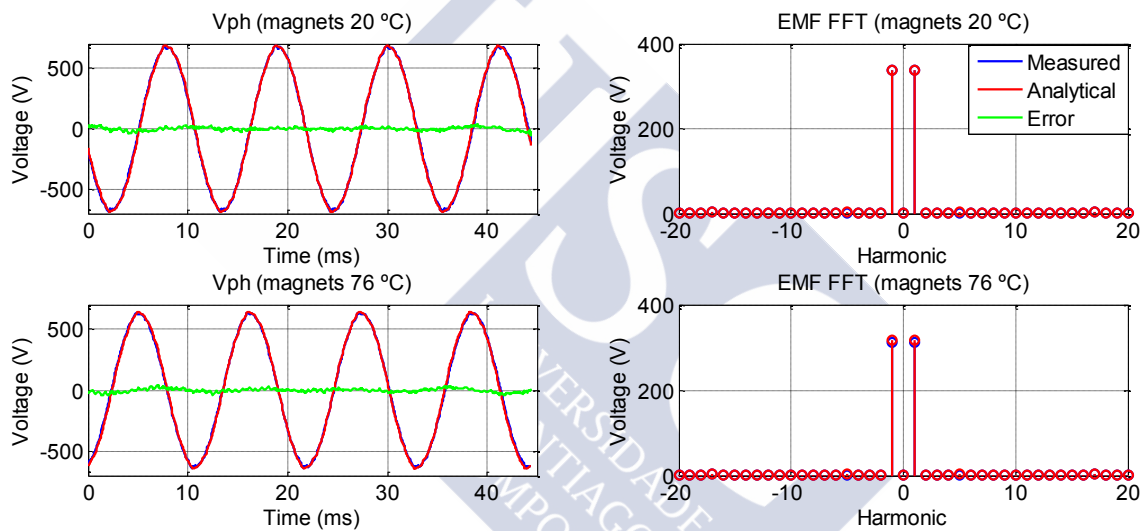


Figure 4.14. On load line voltage, measured in machine terminals.

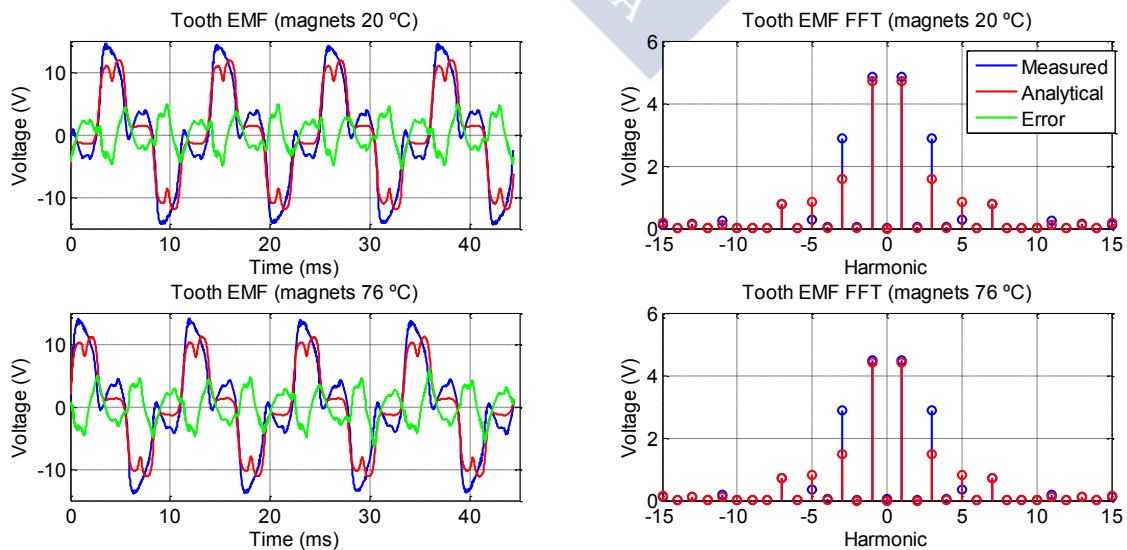


Figure 4.15. On load voltage induced in a single tooth.

As in the previous case, from the voltage induced in a tooth the magnetic flux flowing through can be obtained. The comparison between the experimental results and the analytical calculus can be seen in Figure 4.16.

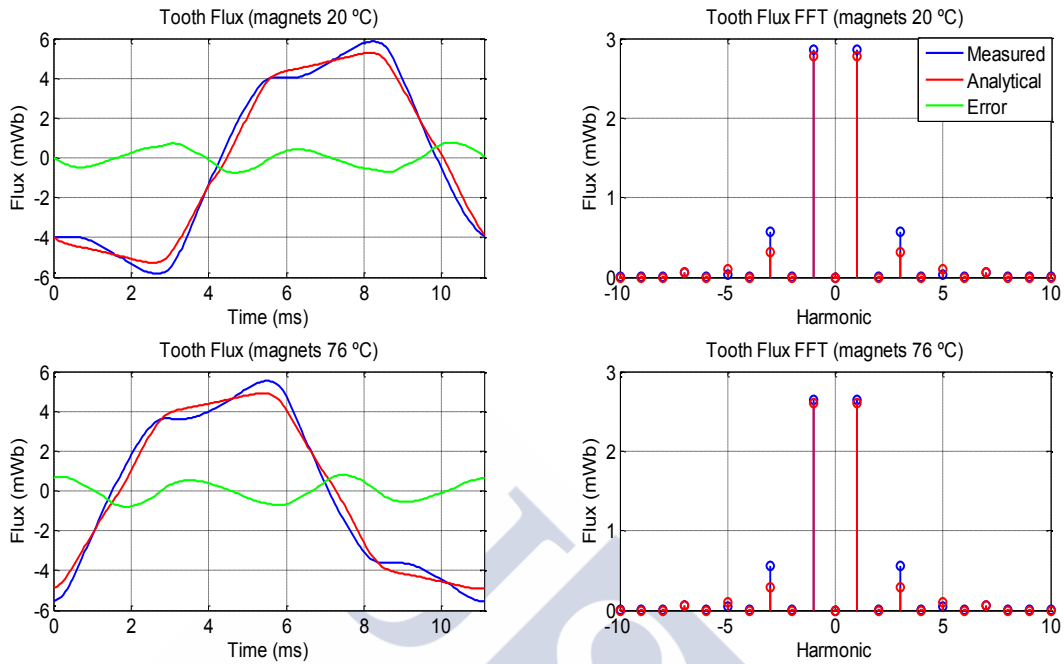


Figure 4.16. On load magnetic flux flowing through a tooth cross section.

As in the open circuit case, the good agreement between experimental measures and analytical predictions is evident, especially in the line voltage. However, it is also noticeable that the armature reaction has a higher error respect to the voltage induced by the magnets, because some of their harmonics (mainly the third one) are more important than the ones predicted by the analytical models. Therefore, the flux crossing the teeth are more distorted than expected.

The aforementioned errors are assumed to be caused by the embedded magnets geometry (i.e. the pole shoes) and the ferromagnetic cores local saturations, because both circumstances may modify the magnetic flux paths and the induced voltage frequency behaviour.

Additionally, the on load test data have been used in order to estimate the IkerMAQ electromagnetic torque (T_e). Both, in the experimental and in the analytical cases T_e is calculated as:

$$T_e(t) = \frac{\sum_{l=1}^3 V_{ph,l}(t) I_{ph,l}(t) - P_{Cu} - P_{Fe} - P_{mec}}{\omega_m}, \quad (4.3)$$

where the values of the voltages, currents, losses are the ones estimated from the analytical models or the measured during the experimental tests. The losses are supposed not to be time dependant; their estimation methods are explained in section 4.4.3.

Figure 4.17 shows the electromagnetic torque obtained both, experimentally and analytically. For visualization purposes the continuous component of the torque Fourier series has been excluded in the Fourier series representation but this mean value is included in Table 4.11.

Table 4.11. Average electromagnetic torque. Analytical estimation and measurements.

	Analytical	Measured	Relative error (%)
T_e (N.m), magnets 20°C	532.3	528.8	0.66
T_e (N.m), magnets 76°C	457.0	452.0	1.11

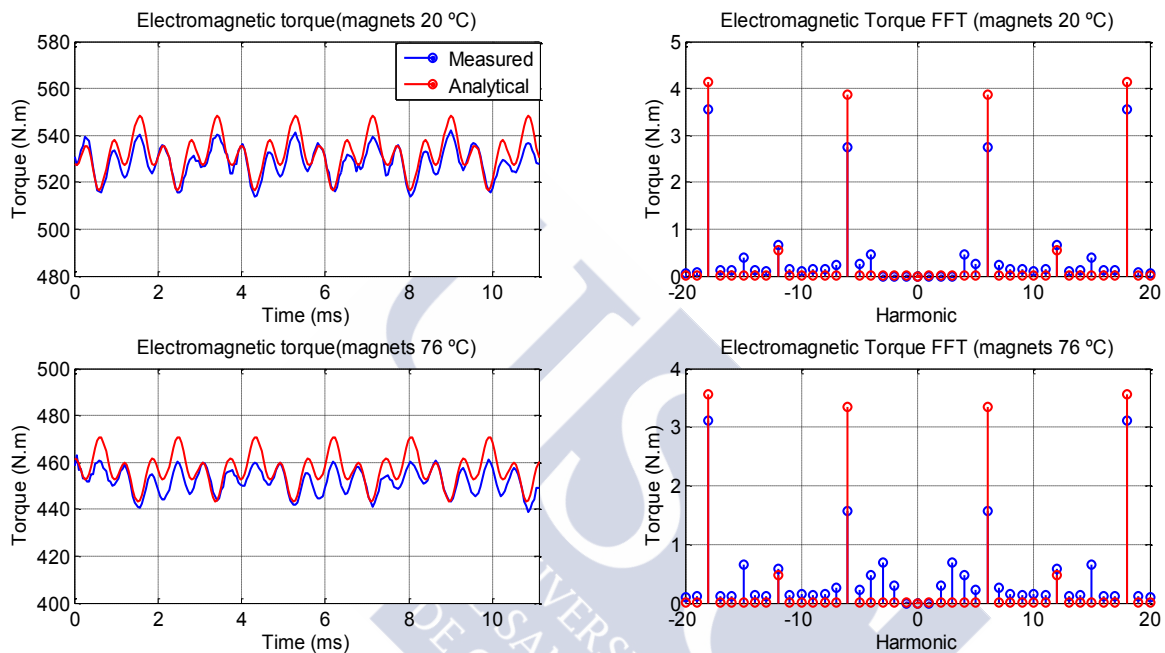


Figure 4.17. On load electromagnetic torque.

As in previous cases, an excellent correlation between experimental measures and analytical estimation can be noticed. It is remarkable that the analytical models predict accurately not only the electromagnetic torque mean value but also its ripple.

4.4.2.1 On load controlled by converter

In most of practical applications a PMSM is feed and controlled by a converter. Therefore, in order to study the machine behaviour in this scenario a specific test, with the configuration shown in Figure 4.7, is performed.

In this case IkerMAQ is directly connected to the 300 kW converter and a vector control is applied in order to ensure nominal current operation. The ABB asynchronous motor is used in its generator mode in order to establish the nominal speed of 1080 rpm. Though the optimum desired case was both at nominal speed and torque (i.e. at nominal power), the DC source feeding the converter is not capable to provide the necessary power due to its internal heating, so the phase EMF and the stator current are not in phase (as it was desirable in order to transfer the maximum power and

reach its nominal value), but they are out of phase by an amount of 47° , delay established by the converter control strategy.

The experimental conditions are included in Table 4.12; in addition, Figure 4.18 shows the wattmeter measurements. The experiment was carried out with the magnets at their steady state temperature where the PMSM is operating controlled by the converter.

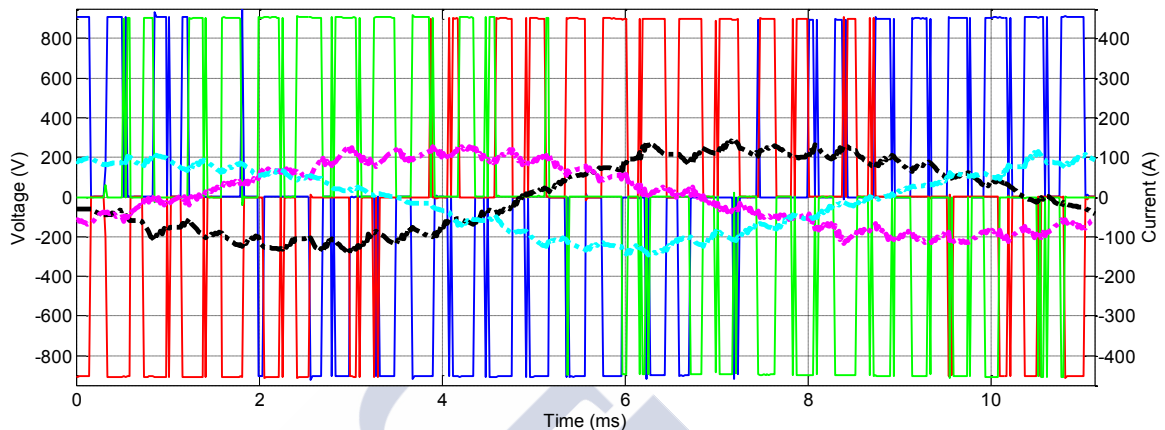


Figure 4.18. Electric waveforms in converter terminals. Current lines are dotted.

Table 4.12. Experimental electrical variables. Converter controlled test.

Parameter	Value
EMF phase voltage (V_{rms})	276.6
Converter phase voltage (V_{rms})	237.6
Phase current (A_{rms})	89.0
Power factor	0.64
Electric frequency (Hz)	90
Switching frequency (Hz)	1200
Mechanical output power (kW)	41.57
Electrical input power (kW)	45.57

The single tooth induced voltage and its Fourier series are shown in Figure 4.19. As in previous cases, from this voltage the magnetic flux flowing through this tooth is obtained (see Figure 4.20).

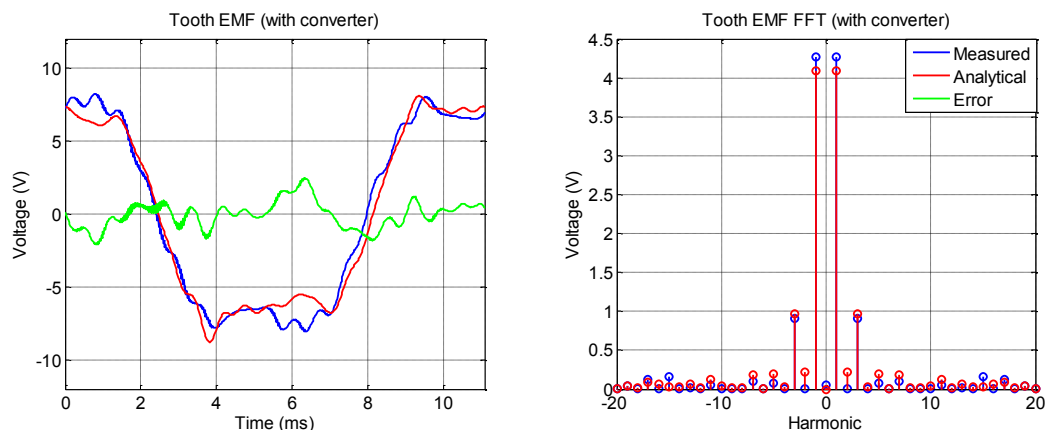


Figure 4.19. Converter test. Voltage induced in a single tooth.

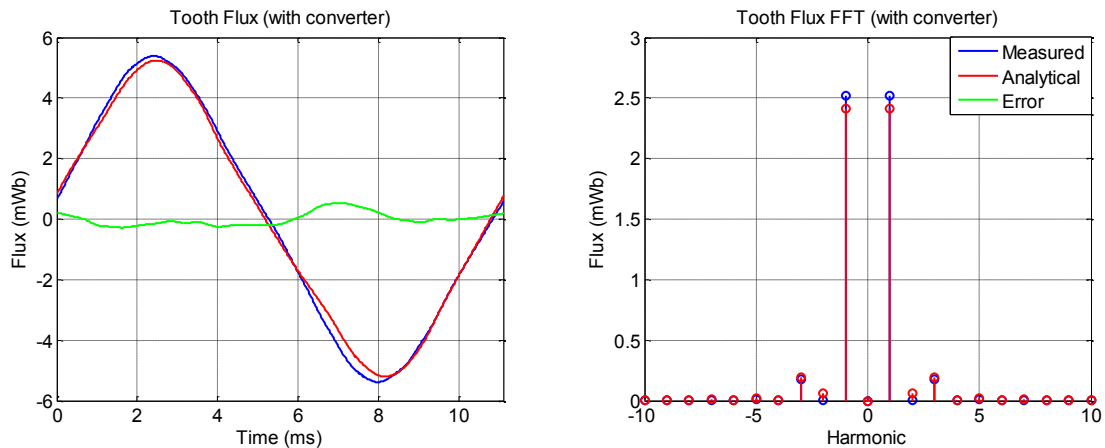


Figure 4.20. Converter test. Magnetic flux flowing through a tooth cross section.

The correlation between experimental measures and analytical estimation is still good, though the high frequency harmonics introduced by the converter current in the flux and the tooth EMF are hardly predicted by the analytical models. It is a matter of fact that at high frequency the models predicts worse the magnetic field behaviour since the saturation effects and the ferromagnetic hysteresis cycles are more problematic.

These noticed errors, caused both by the embedded magnet configuration and the injected high frequency harmonics, are of little importance; therefore, analytical estimation reveals itself as a suitable method in order to estimate PMSM performance when it is feed by a converter with noisy currents.

4.4.3 Quality Parameters

In order to perform a correlation between the real machine quality parameters and the analytical estimated ones, the two “hot” measures presented in section 4.4.2 will be used (i.e. the tests without and with converter). The electric features of both experimental configurations are included in Table 4.10 and Table 4.12, respectively. The main quality parameters studied in the present section are the copper and iron losses and the global IkerMAQ efficiency.

From the experimental tests the losses distribution within the machine cannot be directly obtained; therefore a set of assumptions are necessary in order to estimate them from the obtained measures. These simplifications are listed below.

- The electric power is obtained from the line voltage and phase current measured by the wattmeter in IkerMAQ terminals.
- The mechanical power is obtained from the torque measure provided by the ABB control software.
- Copper losses are estimated from the wattmeter current measure and the DC resistance previously obtained during the machine characterization (see 4.3.2). The copper resistance at 90 Hz and at working temperature is estimated analytically.

- Mechanical losses are assumed to be 180 W; this value is calculated from the empirical approximation (3.174).
- Iron losses are directly obtained as the difference between the input power and the sum of the output power, the copper losses and the mechanical losses, i.e. $P_{Fe} = P_{in} - P_{out} - P_{Cu} - P_{mec}$.
- IkerMAQ efficiency (η) is assumed to be $\eta = 100 \left(1 - \frac{P_{Fe} + P_{Cu} + P_{mec}}{75000} \right)$; i.e. it is considered that the losses are independent from the relative phase lag between the EMF and the stator current and it is only dependant on the rotor speed and the current amplitude. In other words, although in the performed tests P_{out} is under 75kW, it is assumed that the losses are very close to those achieved in nominal power conditions as far as the rotor speed and the current have their nominal values.
- The input current has been adjusted in the analytical models in order to obtain an exactly match with the current measured by the wattmeter during the tests. This is, the electric power is the same in both, the analytical estimations and the experimental tests.

The obtained results in the tests without and with converter are included in Table 4.13 and in Table 4.14, respectively.

Table 4.13. Test without converter. Quality parameters analytical estimation and measures.

	Analytical	Measured	Relative error (%)
P_{out} (W)	52946	52946	-
P_{in} (W)	55978	56072	0.17
P_{Fe} (W)	1579	1587	0.51
P_{Cu} (W)	1275	1360	6.25
η (%)	95.95	95.91	0.04

Table 4.14. Test with converter. Quality parameters analytical estimation and measures.

	Analytical	Measured	Relative error (%)
P_{out} (W)	41571	41400	0.41
P_{in} (W)	45567	45566	-
P_{Fe} (W)	2322	2321	0.05
P_{Cu} (W)	1489	1663	10.49
η (%)	94.67	94.45	0.24

The good correlation between experiments and analytical calculus is remarkable, with a low amount of error in every taken measure.

4.5 Thermal Validation

In order to fully characterize IkerMAQ thermal features a set of experiments were carried out: in open circuit, with the PMSM supplied by a DC current source (with blocked rotor), in nominal conditions without converter and in nominal conditions supplied by a converter. As it is explained forward, the thermal model is tested using the results of these experiments and, through them, some critical parameters are adjusted (e.g. its housing thermal resistance).

The IkerMAQ internal temperatures were measured through thermocouples introduced in the slots, in the end-windings and in the rotor magnets during the manufacture process (see Figure 4.21). Moreover, five additional thermocouples were added in the PMSM external surfaces (two in the fins, one in the foot and two more in other points of the housing, see Figure 4.22). Finally the ambient temperature was measured through a reference thermocouple.

A thermocouple is a device that is formed by the union of two different metals that produces a voltage difference in an open circuit, which is a function of the temperature difference between both ends. In particular, K type thermocouples are used within IkerMAQ while J type thermocouples are added at its surfaces, the first are composed of nickel-chromo and nickel-aluminium alloys while the last are formed of iron and copper-nickel alloy. Thermocouples typical resolution is about 1°C.

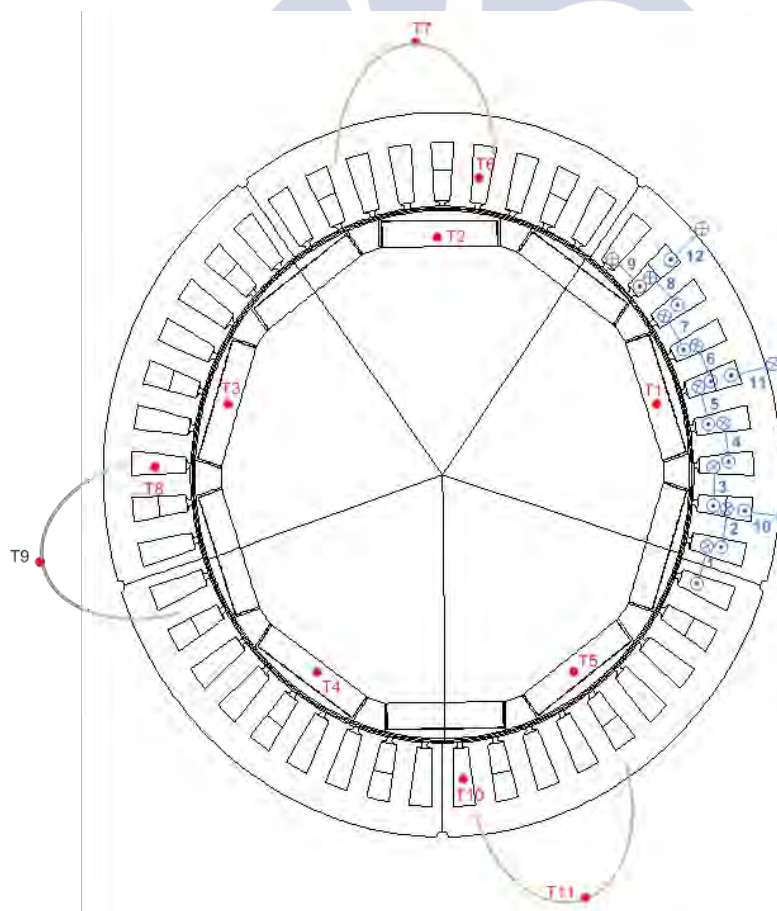


Figure 4.21. IkerMAQ internal test points. In red K thermocouples, in blue magnetic test coils.

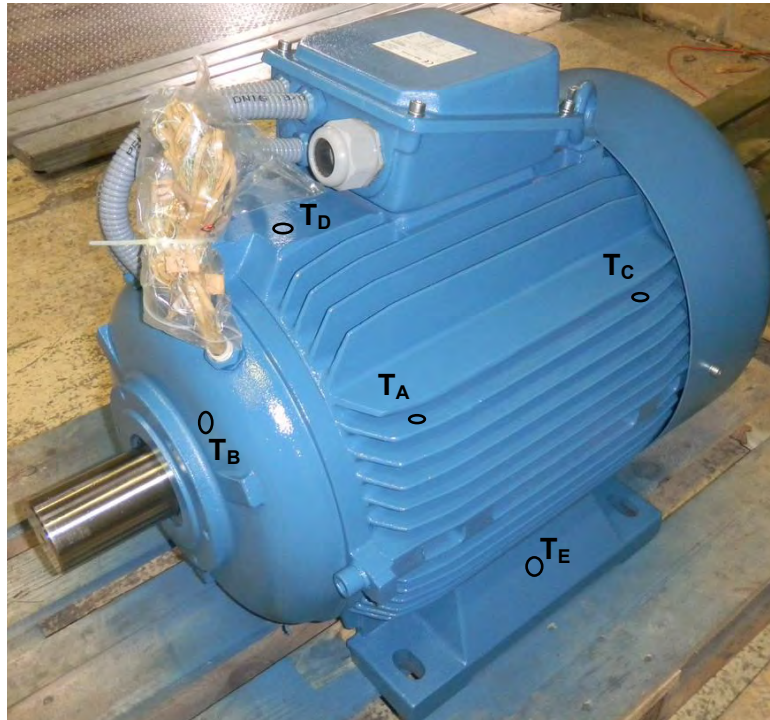


Figure 4.22. IkerMAQ external test points. Measures are carried out through J thermocouples.

Some additional considerations about measures should be addressed in order to achieve a better understanding of the performed experiments and their results.

- Losses estimation is necessary in order to fit the thermal model and compare the analytical and the experimental results. This estimation is carried out in the same way exposed in the previous sections.
- Test-bench temperature was kept nearly constant through the use of three fans cooling the room.
- A total of eleven thermocouples were used in order to obtain a complete “temperatures map” of the PMSM. Three in the slots, three in the end-winding region, five in the magnets, two in the fins and three in other housing representative points (see Figure 4.22).
- Measurements were collected by a datalogger with a sample period of 8 second.
- The final temperatures obtained from the tests in the different points of IkerMAQ (i.e. the so called “coil temperature”, “end-winding temperature”, “housing temperature” and so on) are the data average, obtained by the thermocouples in the same region in many measurements (at least two in each test configuration).

4.5.1 Thermal Measurements

As it was introduced, four different test configurations were carried out. In this section the collected data and the estimated power flow were presented, while the results and its main implications will be discussed in 4.5.2.

4.5.1.1 Open circuit at nominal speed

In this test only the mechanical and the iron losses are present. It is useful because the unknowns associated with the copper losses (e.g. the coils resistance) have no influence.

During this test the ABB machine was used as traction motor at continuous speed of 1080 rpm, the voltage was measured in IkerMAQ terminals with a wattmeter and the shaft torque was provided by the ABB control software. The test data are in Table 4.15, while the temperature rise during one of the tests can be seen in Figure 4.23.

Table 4.15. Open circuit test features

Parameter	Value
Rotor speed (rpm)	1080
Shaft torque (N.m)	32.5
Line voltage (V_{rms})	520
Final magnet temperature ($^{\circ}C$)	76.7

The coils (and, thus, the stator) and the housing temperature were recorded. It can be seen that several stops cycles were carried out in order to check the coils resistance values and the magnets temperature. One interesting fact is that, in a first moment, during a stop the housing temperature raises because the air flow propelled by the fan was removed.

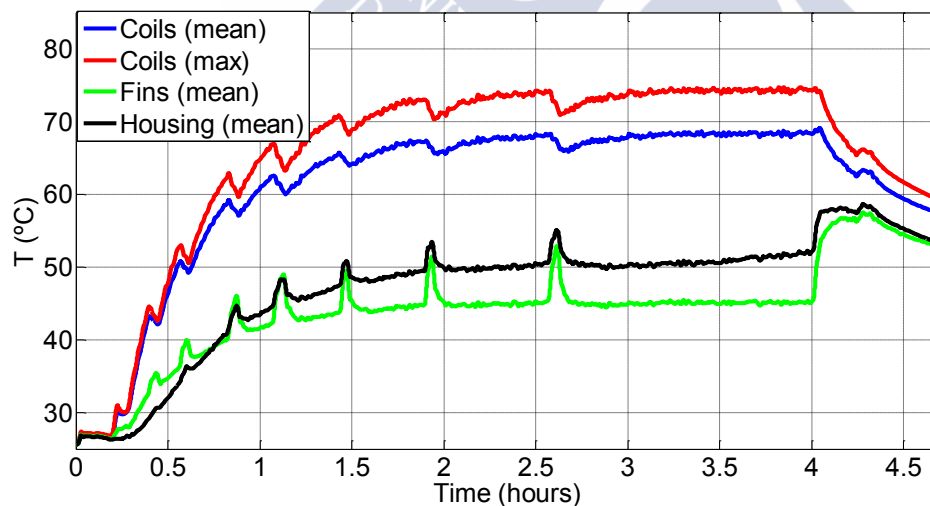


Figure 4.23. Temperatures measured during the open circuit test.

4.5.1.2 DC-current heating

This is the analogous case of the presented in the previous section. A DC source (Xantrex, XDC 60-200) feeds the machine with a continuous current of 90 A. So, only the copper losses exist, while the iron and the mechanical ones vanished. In this way it is possible to deduce the copper losses with high accuracy and, through them, the natural convection housing thermal resistance is deduced.

The voltage was also measured in IkerMAQ terminals in order to estimate the internal losses, the machine windings are connected with two of their phases in parallel between them and in series with the third phase. The test data are shown in Table 4.16, while the temperature rise during one of the tests can be seen in Figure 4.24.

Table 4.16. DC- current heating test features

Parameter	Value
Rotor speed (rpm)	0 (Blocked)
Input current (A_{DC})	90
Input voltage (V_{DC})	8.45
Phase resistance (hot, $m\Omega$)	62.6

Figure 4.24 shows mean and maximum values of the windings, both embedded (within a slot) and in the end-winding region. Measures are shown as a dotted line while the fitted exponential curves are represented as a continuous and thinner line.

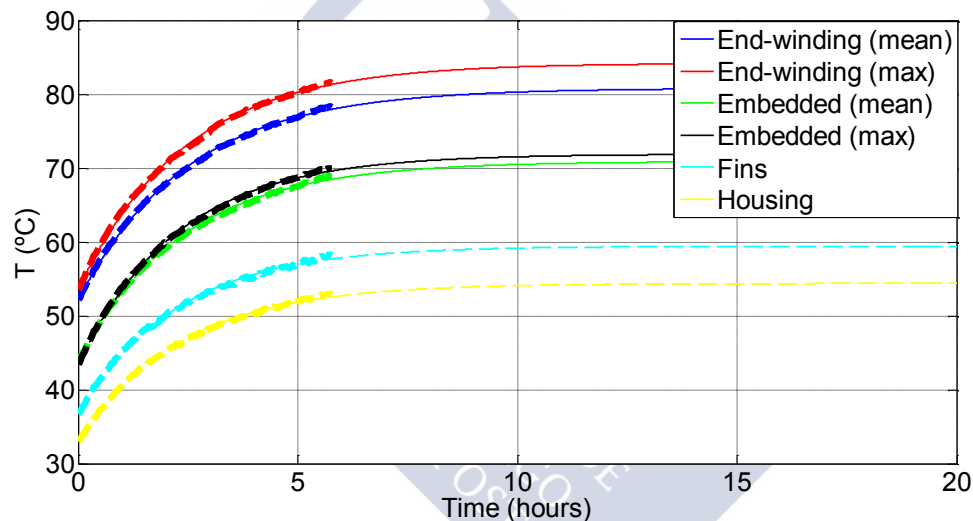


Figure 4.24. Temperatures obtained in the DC-current test. Dotted lines represent the measured values.

4.5.1.3 Nominal conditions without converter

In this thermal test IkerMAQ worked in generator mode, emulating its nominal conditions at full load, i.e. at its rated rms current and nominal speed. The used configuration is the one shown in Figure 4.5.

In order to achieve these operating conditions without a converter, the current was determined through a passive electrical load of 2.28Ω and 3.2 mH connected to IkerMAQ terminals. The 1080 rpm speed was imposed by the ABB machine used as a traction motor. In this way it is possible to establish a very sinusoidal current through the coils, very close to that assumed by most of design methodologies in technical literature.

The line voltage and phase current were measured in IkerMAQ. The test data are shown in Table 4.17, while the temperature rise during one of the tests can be seen in Figure 4.25.

Table 4.17. Nominal conditions without converter, test features

Parameter	Value
Input power (mechanical, W)	56073
Output power (electrical, W)	52946
Rotor speed (rpm)	1080
Shaft torque (N.m)	495.8
EMF voltage (V_{rms})	300.9
Phase voltage (V_{rms})	255.0
Phase current (A_{rms})	88
Load impedance (at 90 Hz, Ω)	2.28+1.79j
Final magnet temperature ($^{\circ}\text{C}$)	76.2

4.5.1.4 Nominal conditions with converter

Finally, a test very similar to the previous one is carried out. The difference, of major importance, is that the load is removed and the converter is added in order to drive IkerMAQ (see Figure 4.7). This is, in fact, the usual operation mode of a PMSM and the main variation is that the current is no longer a perfect sinusoid but, in many applications, the current is polluted with multiple harmonics, as it was shown during the electromagnetic test.

This fact that is usually neglected in design methodologies, greatly increments the losses and, through them, the heat in many PMSM critical parts (especially magnets and windings). This loss increase is mainly due to the skin effect, that increases the wires resistance at high frequencies and thereby the losses. Its effects can be clearly seen in Figure 4.25, where a comparison between temperature rising at nominal condition with and without converter is shown.

Table 4.17 shows the data relative to this last test configuration. In this case IkerMAQ is driven as a load motor, while the ABB machine acts like a generator, supplying power to the grid.

Table 4.18. Nominal conditions without converter, test features

Parameter	Value
Input power (electrical, W)	45566
Output power (mechanical, W)	41400
Rotor speed (rpm)	1080
Shaft torque (N.m)	366.1
EMF voltage (V_{rms})	276.5
Phase voltage (V_{rms})	237.6
Phase current (A_{rms})	89
Final magnet temperature ($^{\circ}\text{C}$)	105.3 $^{\circ}\text{C}$

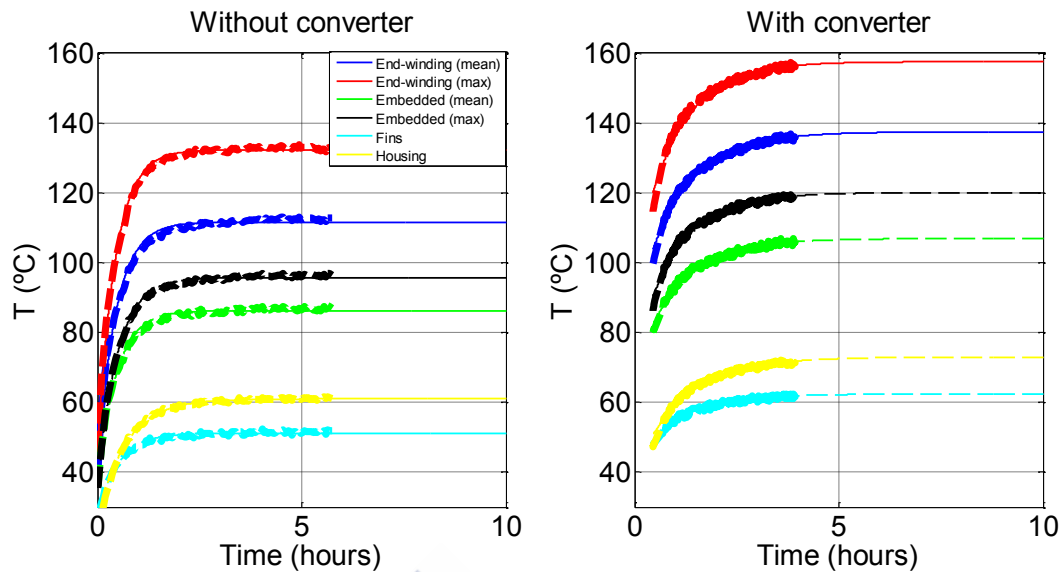


Figure 4.25. Temperatures obtained in nominal conditions with and without converted. Dotted lines represent the measured values.

4.5.2 Model fitting and experimental results

The previous results were used in order to fit the thermal circuit proposed in section 3.5.3. More specifically, the more critical unknown parameters [Boglietti 2008] were corrected.

These parameters are the housing thermal resistance (both, with natural and with forced convection), the equivalent airgap between housing and stator yoke and the thickness of the equivalent “air layer” between the slot insulator and the stator. Their typical values (the initially assumed, as were found in the literature) are compared with the corrected ones in Table 4.19.

Table 4.19. Thermal resistance experimental fit

Thermal resistance	Fit test configuration	Experimental value	Reference value
Housing-air. Forced convection	Nominal conditions (without converter)	0.0103 K/W	0.0091 K/W [Motor-CAD 2012]
Housing-air. Natural convection	DC-current	0.0570 K/W	0.0610 K/W [Boglietti 2008]
Stator-Housing. Equivalent airgap	Open circuit	48.5 μm	30 μm - 75 μm [Lindström 1999]
Slot-Stator. Air layer	DC-current	0.1 mm	0.3 mm [Kylander 1995]

Using these parameters the general equivalent circuit shown in Figure 3.32 is particularized for IkerMAQ taking into account both, its geometry and materials and the previous presented values. This particularized lumped thermal mode is shown in Figure 4.26.

Finally, the temperatures in steady state conditions are obtained from the experimental values (using an exponential fitness function if necessary) and compared with those calculated from the small thermal network shown in Figure 4.26

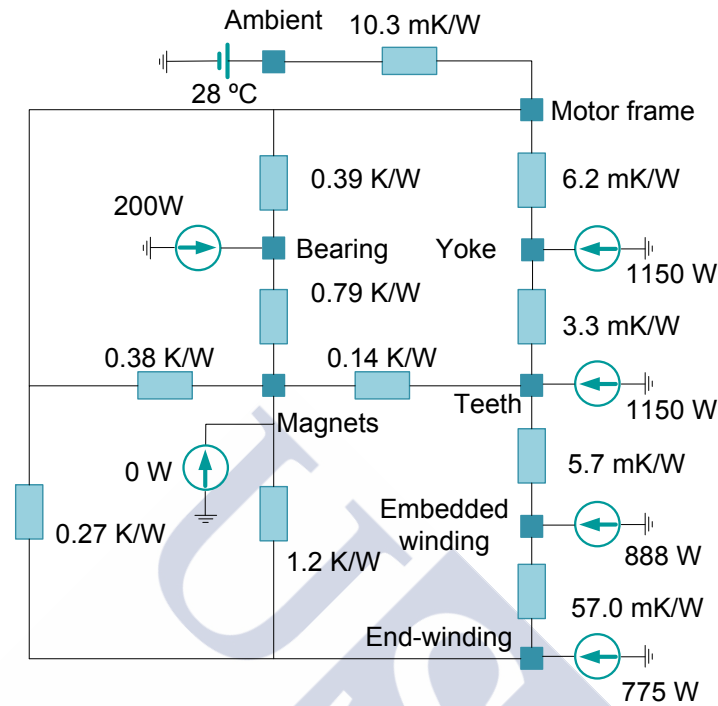


Figure 4.26. IkerMAQ particularized SPMSM small thermal network model.

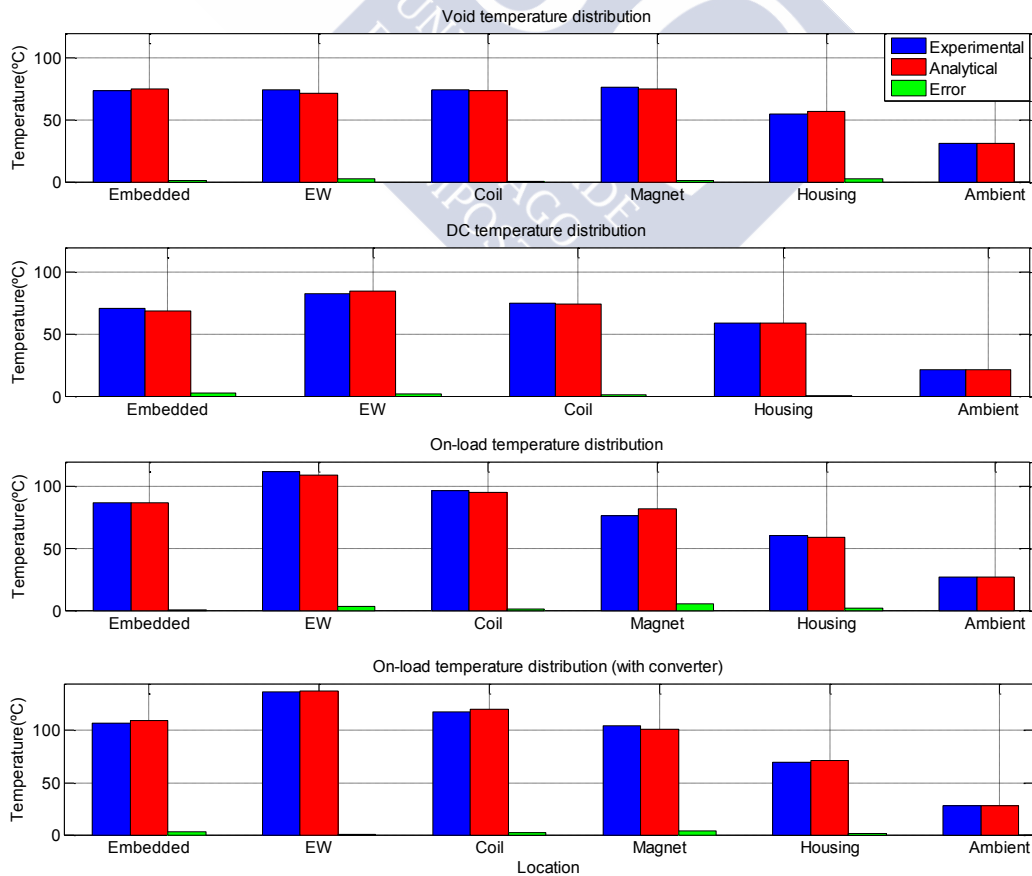


Figure 4.27. Experimental and analytical results comparison in the four test configuration.

From the obtained results many conclusions can be deduced. Three of them are especially remarkable.

The first one is that the maximum and mean temperatures in the coils (both the embedded and the end-winding ones) are very different, especially in the two test configurations at nominal conditions. Specifically, the “hot points” are the thermocouples T6 (in the embedded coils) and T7 (in the end-winding ones), see Figure 4.21. This is not surprising since many authors advice that the maximum temperature raisings in the coils may be even 50% greater than their mean values [Mellor 1991]. It is also understandable that the hotter coils are, precisely, on the top of the machine, as far as the heat rises with the hot air, and higher regions evacuate the heat generated in the lower machine zones.

This is a very important fact, as far as the insulation class should be designed in order to support not just the average temperature values, but the maximum ones in the steady state. The exposed problem does not exist in the magnet case, because the rotor has not “top” or “bottom” parts, as it is in constant motion.

The second fact is that, for that kind of power application, the use of a converter greatly enhances both the iron and the copper losses, because the current harmonics generate both skin effects in the copper and parasitic magnetic fields in the ferromagnetic cores (e.g. the maximum end-winding temperature is 25°C higher with a converter). Figure 4.25 shows the comparison in the temperature increment both with and without a converter driving the machine.

The third and most important conclusion is the excellent agreement between the measured steady state temperatures and those predicted by the lumped thermal model. After the small corrections introduced (see Table 4.19), the maximum error is lower than 6°C in the four test configurations. It should be highlighted that the used thermal network is the same in the fourth cases (the one shown in Figure 4.26). This is a new proof that a small lumped parameter model can accurately predict the thermal behaviour of a PMSM, as far as its critical parameters can be previously obtained with enough precision.

4.6 *Vibro-Acoustic Measurement*

There exist different approaches in order to characterize the vibratory behaviour of the structure. One of the most popular is the modal analysis; this technique consists in measuring and analysing the structural dynamic response during external excitation.

In order to characterize IkerMAQ, two types of modal analysis were carried out: the Experimental Modal Analysis (EMA) and the Operational Modal Analysis (OMA). An OMA is an acceleration measure in several points during IkerMAQ normal operation, i.e. the excitations forces are the electromagnetic ones, while an EMA is the

acceleration measurement at several points of the structure during the application of a shock impact, i.e. a known external force very close to an impulse.

In order to perform a modal analysis, specific hardware and software are necessary. During the performed tests the Brüel & Kjær platform PULSE was used. This platform included a shock hammer, accelerometers, an acquisition unit and specific PC software in order to analyse and process the obtained results.

The used accelerometers are a triaxial, piezoelectric model whose measurement range is from 5 Hz to 6 KHz (no valid for continuous acceleration measures).

4.6.1 IkerMAQ Experimental Modal Analysis.

An EMA main objective is the identification of the modal shapes of the structure under test; this includes the damping factors and resonance frequencies of each mode.

Usually, the EMA requires a previous FEM study in order to numerically obtain the more important modes. This initial step is critical because it determines the points where the acceleration will be measured; these points are selected in order to discriminate the main modes with a minimum number of accelerometers.

Once the FEM study is carried out and the accelerometers situated, an external excitation is applied to the structure. This excitation is close to an impulse (i.e. very short in time and, therefore, very rich in the frequency domain) and it is usually provided by a calibrated shock hammer. The process block diagram is shown in Figure 4.28.

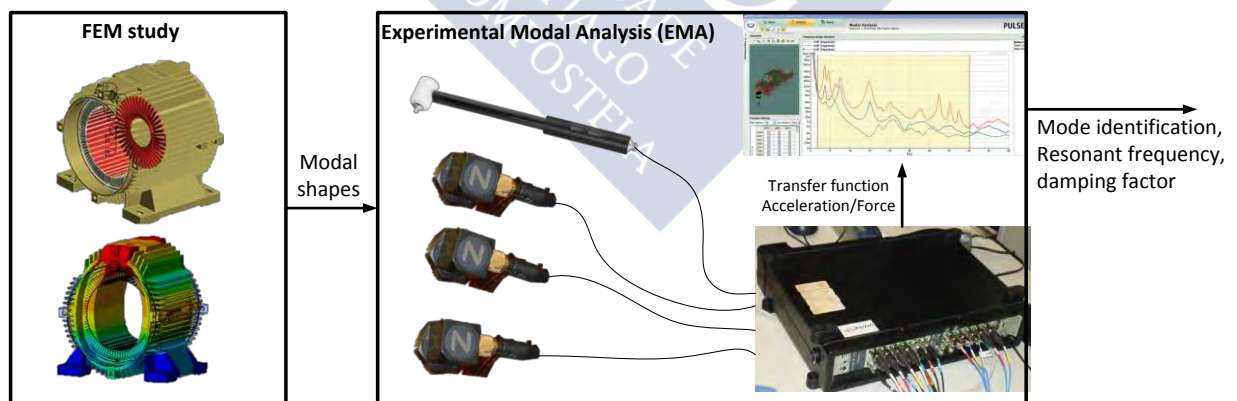


Figure 4.28. Classical EMA block diagram.

The measured accelerations are divided between the hammer excitation force and their FFT is carried out. The result is the transfer function between acceleration and force in the selected structure points.

If the points are properly chosen, the analysis of these transfer functions should lead to modal shape identifications, because the vibrations patterns could be established in the frequencies where a specific mode resonance occurs. Pulse platform

includes software in order to translate the transfer function information to mode identification. Moreover, these obtained modes are correlated with those obtained during FEM simulation.

4.6.1.1 Stator EMA

Two stator EMAs were carried out during IkerMAQ manufacture process. In the first one the stator was no wound, while in the second the coils were added. These tests were performed in order to proof the accuracy of the loaded ring approximation contained in (3.317) and (3.318) and their ability to estimate the effects of winding over the stator ring-shape.

In order to avoid additional resonances due to anchoring points or to other attached structures, EMA is carried out in free-free conditions, hanging the stator through a sling (see Figure 4.29). It is worth to noticing that the vibration caused by the sling-stator system is not important because of its slow frequency. Moreover, it is automatically filtered by the accelerometers sensivity.

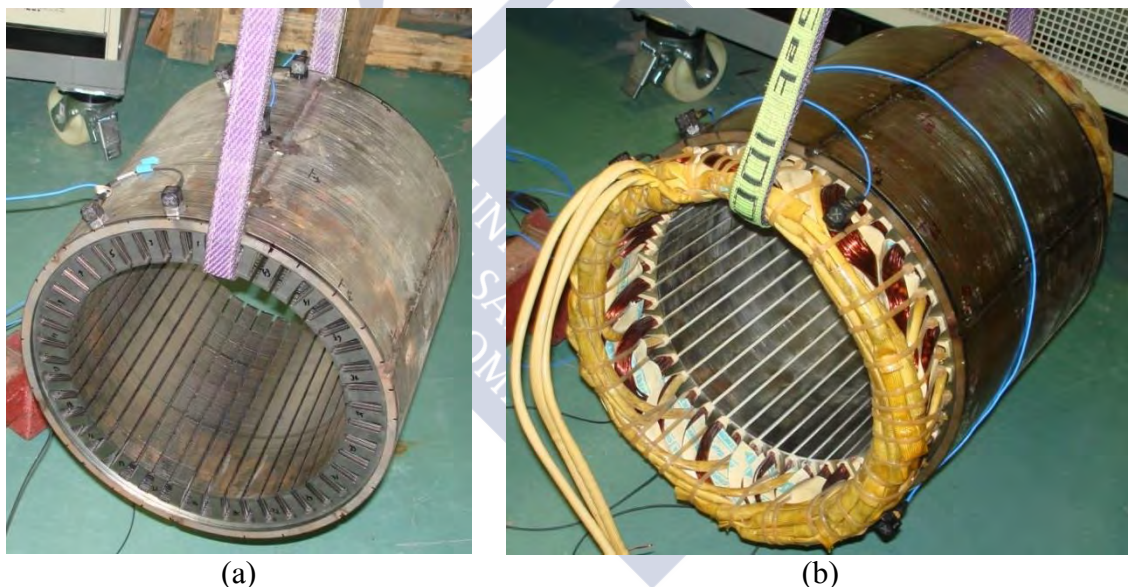


Figure 4.29. Free-free stator tests conditions (a) without coils and (b) wound.

PULSE software automatically identify and correlate the modal shape with those simulated in FEM and provide the resonant frequencies ($f_{(n,m)}$) and the damping factor ($\zeta_{(n,m)}$) for each mode. All the studied modes are vibrating only in the radial direction and they have both, tangential and axial dependency. Notations (n,m) indicate a radial mode n in the theta direction and m in the axial one (see Figure 4.30). In this case the only modes of interest are the radial ones, i.e. those identified as $(n,0)$, because they have a major contribution in electromagnetic vibration and in noise emission.

The resonant frequencies and damping factors measured during the test are included in Table 4.20.

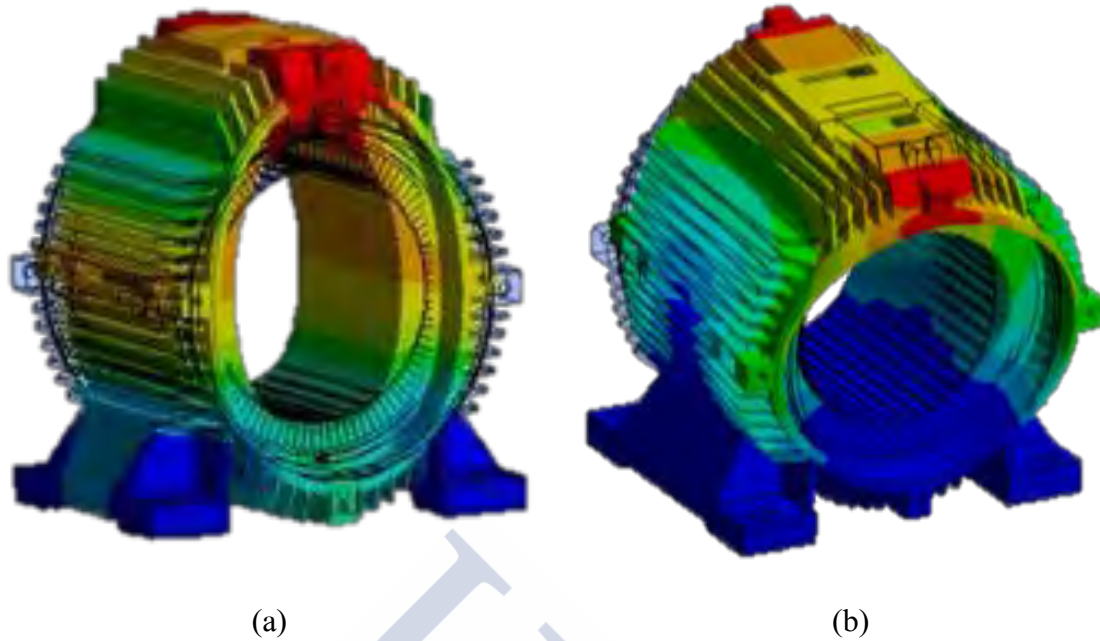


Figure 4.30. Example of FEM modal shapes (a) mode (2,0) and (b) mode (2,1). Feet anchored.

Table 4.20. EMA results. Resonant frequencies and damping factors.

Mode	Stator core		Wound stator	
	$f_{(m,n)}$ (Hz)	$\zeta_{(m,n)}$ (%)	$f_{(m,n)}$ (Hz)	$\zeta_{(m,n)}$ (%)
(2,0)	224.5	0.69	206.6	0.57
(2,0)	225.6	0.69	-	-
(2,1)	392.3	2.61	-	-
(3,0)	616.5	0.08	554.0	1.53
(3,1)	624.4	2.74	720.6	5.65
(4,0)	1127	0.11	1093.6	1.53
(4,0)	1127.5	0.11	-	-
(5,0)	1728.8	0.12	1656.0	2.29
(6,0)	2365.8	0.07	2272.8	2.59
(6,0)	2397.8	0.07	-	-

It is worthwhile to notice that most of the modes appear twice. Theoretically, in systems with perfect axial symmetry, each resonant frequency has two geometrical orthogonal modes. If the system is not perfectly symmetric one mode presents two different resonant frequencies.

The studied stator is almost symmetrical, that is why many modal shapes only have one resonant frequency, and the ones presenting two are very close one to another.

The obtained transfer functions in the radial direction are very similar in all the accelerometers. One of this transfer functions and its comparison with the analytical models are represented in Figure 4.31 (stator core) and Figure 4.32 (wound stator) in logarithmic scale. Notice that the analytical model only takes into account the $(n, 0)$ modes. That is the reason why other resonance frequencies are not visible in the analytical solution.

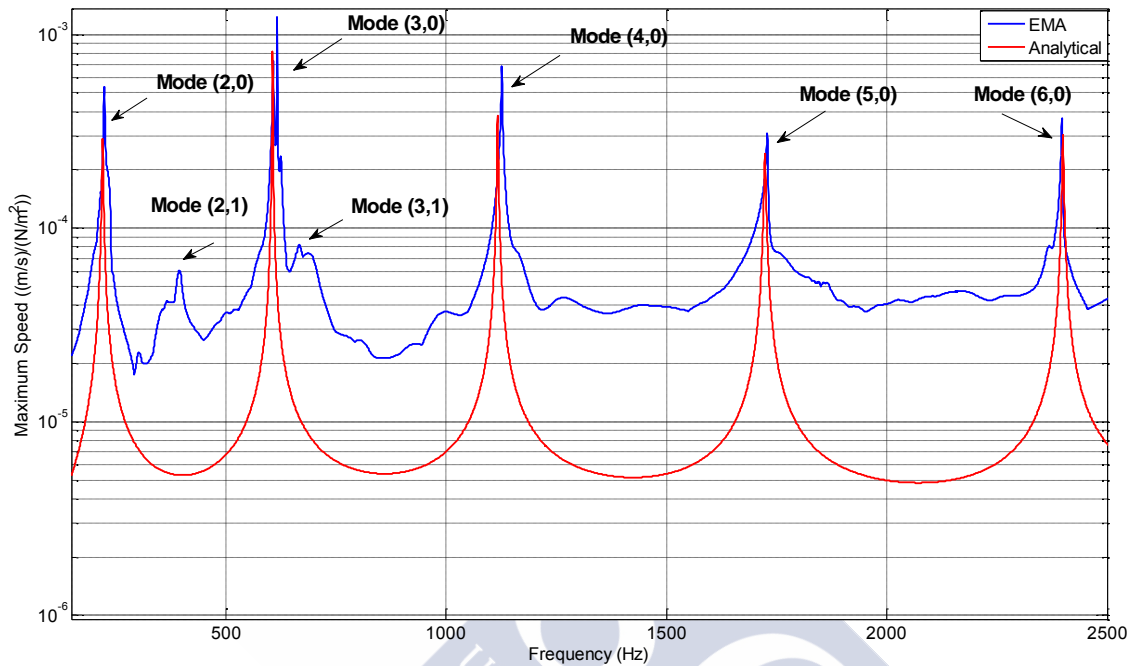


Figure 4.31. Stator core. Calculated and measured transfer function.

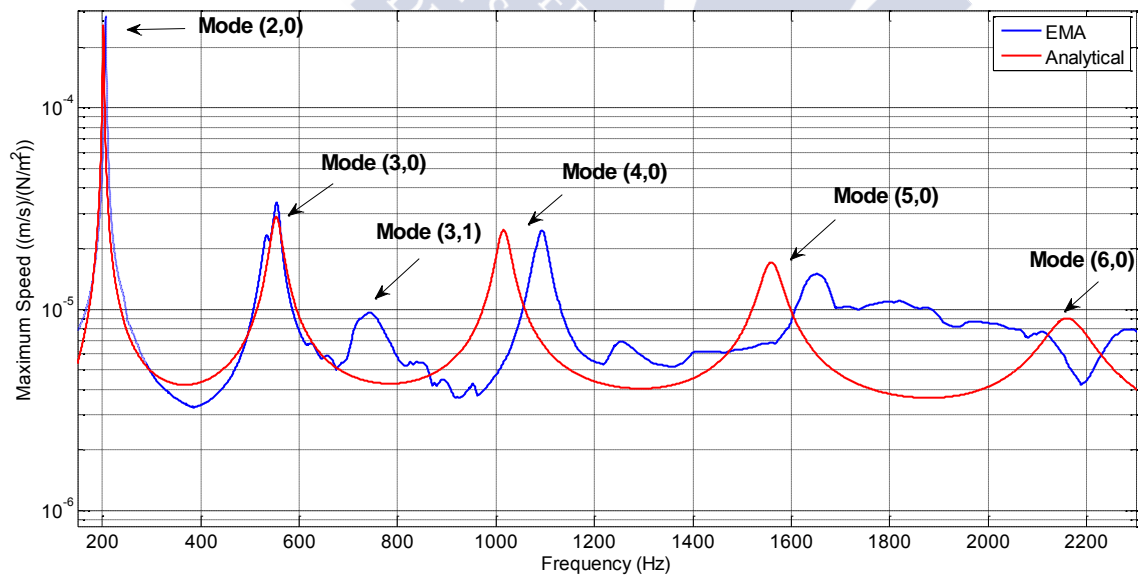


Figure 4.32. Wound stator. Calculated and measured transfer function.

From the previous transfer functions some remarkable conclusions can be deduced. The first one is that the analytically obtained function and the measured one are quite similar, identifying correctly the resonant frequency and the dynamic displacement

within a reasonable error margin. The resonant frequency estimation is especially accurate in the stator core case, while the error is higher in the wound stator, especially for high order modes.

The reason why this occur is clear: the analytical modes estimate that the winding structural behaviour can be modeled as a mass addition factor which reduces the resonant frequency; its stiffness is neglected. This is not totally true, and the tests show that the windings also increment the total structure stiffness. This is why the analytical models predict lower resonant frequencies for 4th, 5th and 6th radial modes.

Another winding major contribution is a great damping increase, i.e. the coils greatly limits stator vibrations. This fact is very important because it reduces the amount of emitted noise.

Finally, Table 4.21 and Table 4.22 contain an additional comparison of the resonant frequencies and static displacements obtained both, by analytical calculus and by EMA tests. Y_n noted the maximum displacement amplitude of mode $(n, 0)$ per unite of applied pressure.

It is important to notice that errors in resonant frequencies are very low while the errors in static displacements are higher. Although these errors may seem high they are perfectly acceptable, because the undesired effects of vibrations are perceived as noise in a logarithmic rather than in a linear scale and, therefore, the relative errors are less important.

Table 4.21. Analytical and EMA static displacements and resonant frequencies. Stator core

Mode	Analytical Model		EMA Results		Relative Error	
	f_n (Hz)	Y_n (m^3/N)	f_n (Hz)	Y_n (m^3/N)	f_n (%)	Y_n (%)
2	220.8	$26.6 \cdot 10^{-10}$	224.5	$35.34 \cdot 10^{-10}$	1.65	24.78
3	606.2	$3.97 \cdot 10^{-10}$	616.5	$3.94 \cdot 10^{-10}$	1.66	0.68
4	1117.1	$1.22 \cdot 10^{-10}$	1127.0	$1.60 \cdot 10^{-10}$	0.87	23.65
5	1723.5	$0.52 \cdot 10^{-10}$	1728.8	$0.50 \cdot 10^{-10}$	0.30	4.87
6	2399.7	$0.27 \cdot 10^{-10}$	2397.5	$0.24 \cdot 10^{-10}$	0.09	12.17

Table 4.22. Analytical and EMA static displacements and resonant frequencies. Wound stator

Mode	Analytical Model		EMA Results		Relative Error	
	f_n (Hz)	Y_n (m^3/N)	f_n (Hz)	Y_n (m^3/N)	f_n (%)	Y_n (%)
2	202.2	$23.2 \cdot 10^{-10}$	207.0	$18.34 \cdot 10^{-10}$	2.30	26.31
3	553.4	$3.48 \cdot 10^{-10}$	554.0	$3.29 \cdot 10^{-10}$	0.11	15.79
4	1015.3	$1.08 \cdot 10^{-10}$	1093.5	$0.82 \cdot 10^{-10}$	7.10	32.27
5	1559.2	$0.47 \cdot 10^{-10}$	1651.5	$0.49 \cdot 10^{-10}$	5.59	4.53
6	2160.9	$0.25 \cdot 10^{-10}$	2272.8	$0.21 \cdot 10^{-10}$	5.22	15.52

4.6.2 IkerMAQ Operational Modal Analysis and Acoustic Test

Finally, two OMAs were performed and, while these tests were carried out, the sound was measured in order to obtain not only the vibratory behaviour but also the emitted noise. Figure 4.33 shows the points where a total of 28 piezoelectric triaxial accelerometers were situated, providing a total of 84 acceleration measures.

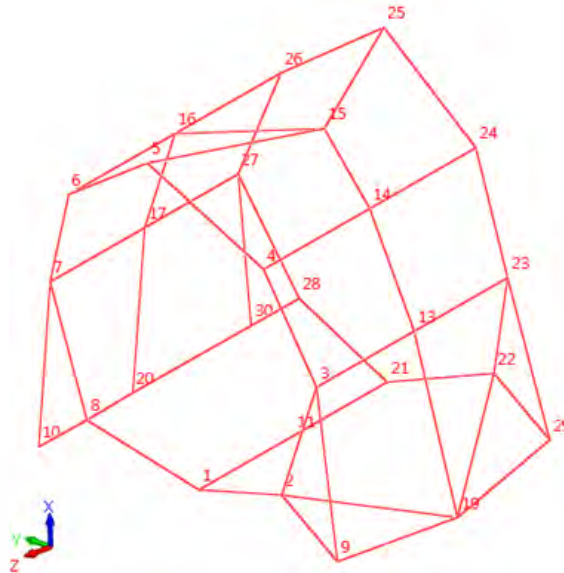


Figure 4.33. Location of accelerometers on IkerMAQ housing.

Two different configurations were tested: the first one is the no load or open circuit configuration, the same carried out in sections 4.4.1 and 4.5.1.1. The ABB machine was used as traction motor at continuous speed of 1080 rpm, the voltage was measured in IkerMAQ terminals with a wattmeter and the shaft torque was provided by the ABB control software. The test data can be consulted in Table 4.15.

In the second one, IkerMAQ was working as a generator with an electrical load of 3 mH and 2.2Ω and with a fixed angular speed of 1080 rpm, imposed by the ABB traction motor. The configuration is the same used in section 4.4.2, it is shown in Figure 4.5 and its experimental conditions are included in Table 4.9. The vibratory results obtained by the OMA tests are shown in Figure 4.34 which represents the maximum displacement of the vibratory oscillations as a function of frequency.

The obtained vibratory measures, both in no load and in loaded conditions, greatly match the analytical results. All the main peaks measured are correctly predicted by the vibratory analytical models that only takes into account the θ -dependent radial modes, i.e. the $(n, 0)$ modes.

The main difference between the measured and the predicted results are that the former present a much higher number of excited frequencies with remarkable peaks. However, it should be highlighted that the non-predicted peaks have, by far, less amplitude that the foreseen ones (notice the logarithmic scale of the y-axis in Figure 4.34). The reasons for the presence of these unpredicted peaks are multiple: on the

one hand many vibratory modes are neglected by the analytical models and, on the other hand, the test bench and the ABB machine present its own vibrations that could be easily propagated to IkerMAQ. Moreover, a certain frequency-spreading is always present; this phenomenon could produce “side bands” at both sides of an excited frequency, generating a higher number of peaks.

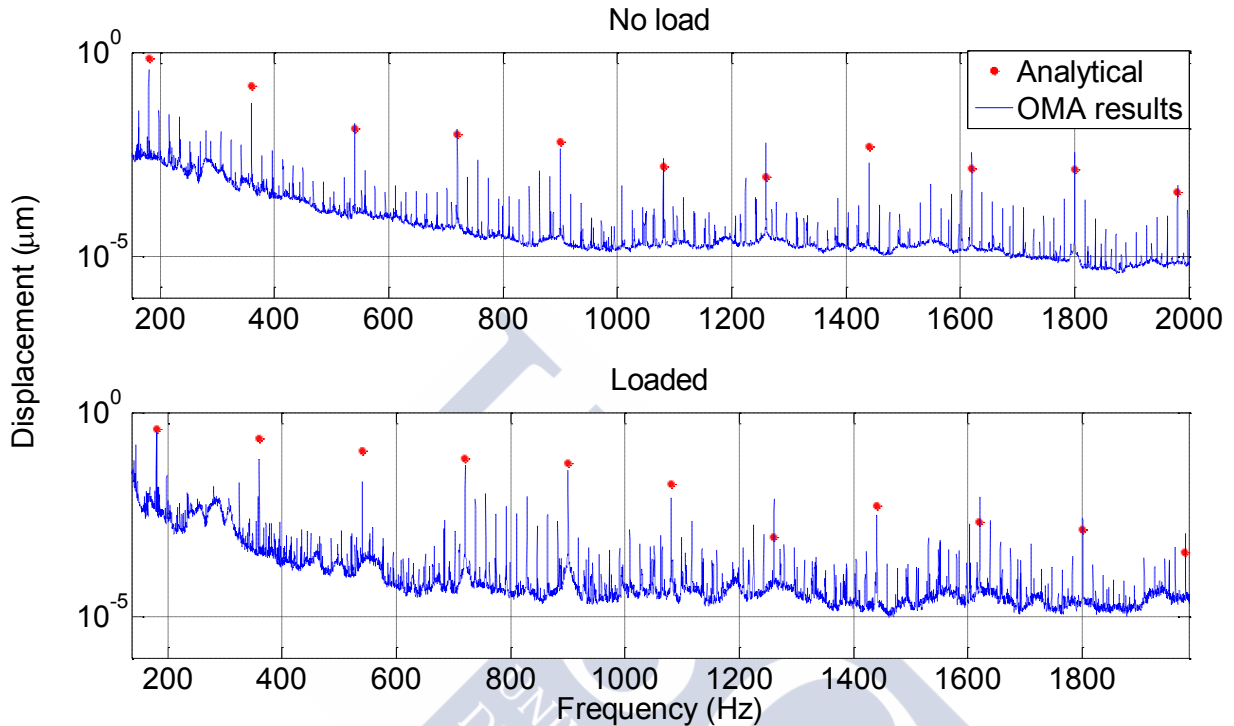


Figure 4.34. Maximum vibratory radial displacement as function of frequency. IkerMAQ OMA results and analytical calculus comparison.

The sound emitted by IkerMAQ was measured by four microphones surrounding it and located at a fixed distance of one meter. The results are shown in Figure 4.35.

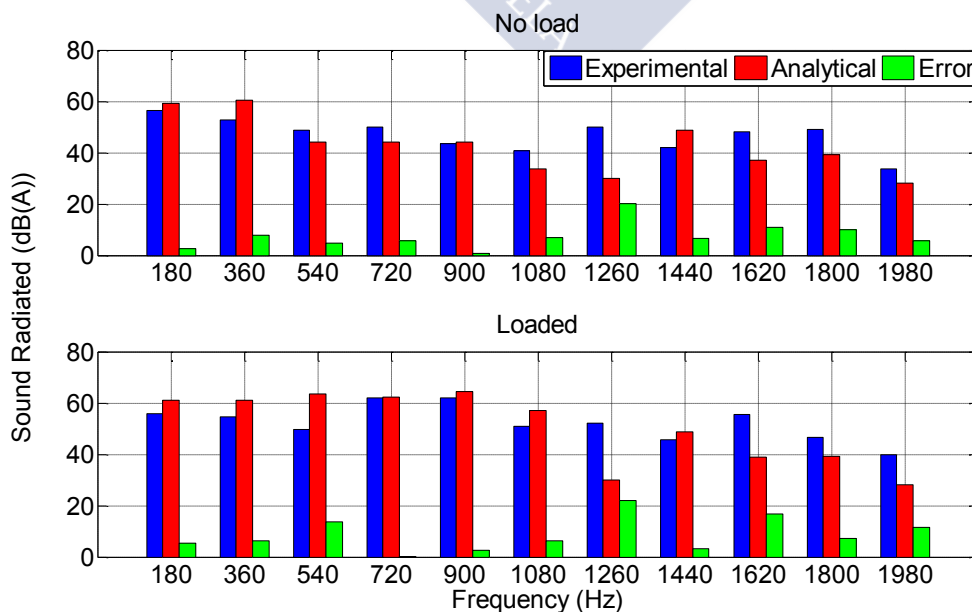


Figure 4.35. Sound emission comparison. Experimental and analytical results.

As it can be noticed, the analytical calculated sound emission presents some remarkable differences with those experimentally measured for some frequencies. There are several error sources that may be the cause for these divergences.

On the one hand, the sound measurement includes the noise emitted not only by IkerMAQ but by the ABB traction motor, the ABB converter and the test bench fans, too. Though these external elements noise has been removed through a background sound measurement it is quite difficult to completely overcome its effects in the experimental post-processed results.

On the other hand, it should be taken into account that the radiation efficiency factor (i.e. the parameter estimating the noise from the surface vibration, see equations (3.327), (3.330) and (3.331)) is quite rough and that it is analytically calculated for the case where the machine is in free-free conditions and not attached either to a test bench or to a traction motor with their own vibrations modes.

It is also remarkable that, despite the aforementioned inaccuracy, the total amount of global noise is predicted analytically with quite exactitude. However, it is evident that an important future work line is the improvement of the PMSM noise estimation, developing analytical methods more precise than those based in the radiation efficiency factor.

4.7 Conclusions

It can be concluded that the implemented models have a really high accuracy respect to the experimental results. More precisely, only with minor modifications (i.e. adding a slight correction factor to the magnets residual induction and adjusting the frame and slot thermal resistance) electromagnetic and thermal models are of great exactitude predicting both, waveform and amplitude levels.

The key features of the developed models are their fastness and their robustness, because they are capable to predict the behaviour even of PMSMs such as IkerMAQ which magnets configurations do not exactly match with a SPMSM but with a buried magnets machine.

It should be highlighted as a major thesis contribution the experimental process itself, because it supposes a complete and exhaustive characterization of a real prototype including electric, magnetic, thermal, structural, vibratory and acoustic test, some of them very resource-demanding.

Perhaps the impedance analytical models (sections 4.3.2 and 4.3.3) and the acoustic ones (section 4.6.2) are the weaker points in the overall modelling. Though the achieved results are accurate enough in order to foresee the general trends and select a proper comparison between possible designs, a more precise modelling is an interesting field of study for further research.



Optimized Methodology Proposal



5.1 *The Optimization Process: A Global View*

As it was previously introduced the development of a complete optimization methodology involves two different steps: a model definition and an optimization process selection. Previous chapters were devoted to achieve and validate the first aim; besides, a complete multidisciplinary verification was accomplished through practical experiments. Following this proposed path, the present chapter introduces the second objective: to introduce the optimization process and to demonstrate its usefulness through a complete case of study whose design will be analysed.

Among the features of the proposed methodology (analytical, fast, modular, multiphysical, complete and optimized), the last two ones are especially related to the optimization process, while the former depends mostly on the modelling.

The correct definition of an optimization methodology (i.e. an optimization problem resolution) involves the following steps:

1. Definition of a set of mathematical or physical models that accurately represent the system behaviour.
2. Selection of a set of design variables (i.e. the input variables) and the state ones.
3. Definition of one or more objective and constraint functions depending on both, the design and the state variables.
4. Selection of a suitable optimization algorithm that matches the problem features.

This chapter is devoted to the last three points, since the first one was detailed in the previous sections. The mathematical definition of an optimization problem was briefly introduced in 2.1.2.

5.1.1 **Design and State Variables**

The selected design variables are shown in Table 5.1. They are defined as the variables that the optimization algorithm directly modifies in order to minimize the objective functions. As it can be seen, they are a set of 13 geometric and configuration parameters which determine the electromagnetic, thermal and vibratory PMSM behaviour. The rest of values that are needed in order to fully describe the machine performance (i.e. the chosen ferromagnetic core material or the selected magnets) are considered as constants, since they are imposed by manufacturer constraints.

Other important variables are the state variables defined as those that are calculated from the design ones and are needed in order to obtain one or more of the objective or constraint functions.

Table 5.2 shows the defined state variables while Figure 5.1 represents the model flowchart, its interaction with the optimization algorithm and the state variables that couple the different physical domains.

Table 5.1. Design variables.

Design Variable	Units	Nature	Type
Slot number, Q	-	Configuration	Discrete
Pole pair number, p	-	Configuration	Discrete
Number of turns per coil, Z	-	Configuration	Discrete
Magnet height, I_m	m	Geometric	Continuous
Magnet pitch, α_m	-	Geometric	Continuous
Internal stator radius, R_s	m	Geometric	Continuous
External stator radius, R_{se}	m	Geometric	Continuous
Airgap length, g	m	Geometric	Continuous
Slot height, h_2	m	Geometric	Continuous
Tooth-tip height, h_0	m	Geometric	Continuous
Slot opening, w_0	m	Geometric	Continuous
Tooth width, w_t	m	Geometric	Continuous
Stator length, L_e	m	Geometric	Continuous

Table 5.2. State variables.

Status Variable	Units	Nature
Winding periodicity, t_p	-	Configuration
Output power, P_{out}	W	Electric/Mechanical
EMF, E	V	Electromagnetic
PMSM phase current, I_{ph}	A	Electric
Input voltage, V_{ph}	V	Electric
Electric load, q_e	A/m	Electric
Power factor, pf	-	Electric
Copper losses, P_{Cu}	W	Electric
Airgap armature reaction, B_g^a	T	Magnetic
Airgap rotor magnetic field, B_g^m	T	Magnetic
Stator yoke flux density, B_t	T	Magnetic
Stator teeth flux density, B_s	T	Magnetic
Iron losses, P_{Fe}	W	Magnetic
Mechanical losses, P_{ad}	W	Mechanical
Torque ripple, T_{pk-pk}	N.m	Mechanical
End-winding temperature, T_{ew}	K	Thermal
Magnets temperature, T_m	K	Thermal
Copper total mass, M_{Cu}	kg	Geometric
Iron total mass, M_{Fe}	kg	Geometric
Magnets total mass, M_m	kg	Geometric
Emitted noise level, $L_{dB(A)}$	dB(A)	Acoustic

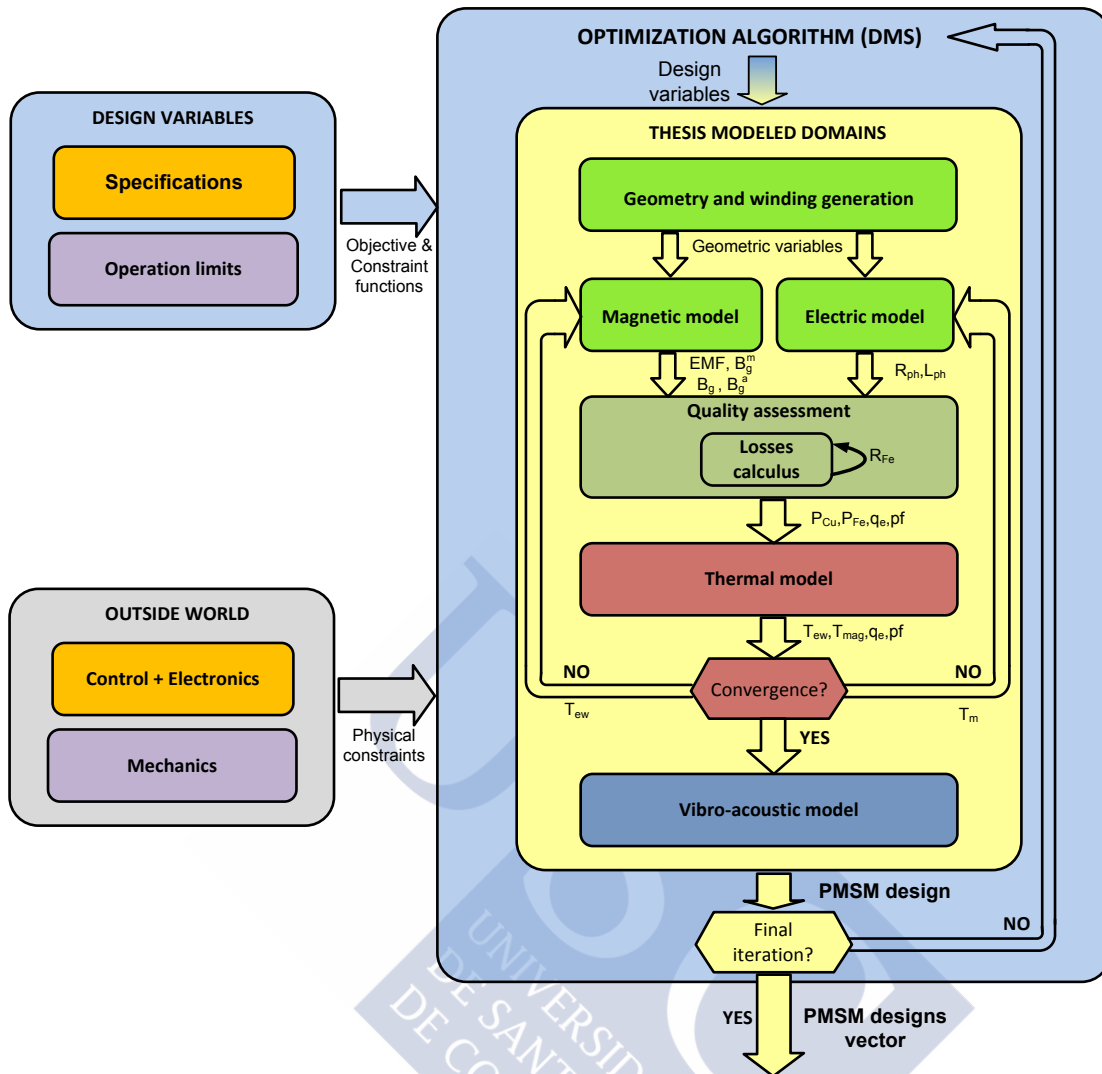


Figure 5.1. PMSM modelling flowchart.

5.1.2 Objective and Constraint Functions

As it was aforementioned, an optimization problem consists in one or more objective functions that should be minimized fulfilling a set of constraints. Both, the objective and constraint functions should be established in order to achieve a suitable and feasible solution; i.e. a correct PMSM design.

In this work a multi-objective optimization is proposed. More precisely, the efficiency will be maximized and the material costs minimized, using a Pareto frontier approach.

The efficiency was defined in Chapter 3 as

$$\eta = \frac{P_{out}}{P_{out} + P_{Fe} + P_{Cu} + P_{ad}}, \quad (5.1)$$

where P_{out} is P_{elec} if the machine is operating as a generator and P_{mec} if it is in motor operation mode.

The material cost is the sum of the prices of the copper, the iron and the magnets, i.e.

$$\text{Cost} = M_{\text{Cu}} c_{\text{Cu}} + M_{\text{Fe}} c_{\text{Fe}} + M_{\text{m}} c_{\text{m}} \quad (5.2)$$

where c_{Cu} , c_{Fe} and c_{m} are, respectively, the cost of the copper, the ferromagnetic material and the magnets per unit mass.

It is worthwhile to notice that objective functions should be jointly defined with the constraint ones, which will establish features as important as the geometrical feasibility of the design, the output power, the size and the maximum suitable temperature or noise levels. The identified constraints are included in Table 5.3 to Table 5.7 and classified according to their nature (geometric, electrical, thermal, etc.).

In order to clearly identify the design limits, italic letters are used. They are the minimum rotor radius (R_{rmin}), the minimum output power ($0.95P_{obj}$), the maximum output power ($1.05P_{obj}$), the maximum active volume (Vol_{max}), the maximum torque ripple (T_{pkmax}), the ferromagnetic core saturation threshold (B_{sat}), the maximum armature reaction (B_{gmax}^a), the maximum slot current density (J_{max}), the maximum electric load (q_{emax}), the maximum phase voltage (V_{phmax}), the maximum phase current (I_{phmax}), the minimum power factor (pf_{min}), the maximum noise emission ($L_{dB,max}$) and the maximum winding and magnets temperature (T_{Cumax} and T_{mmax}).

Table 5.3. Design constraints.

Constraint	Formulation
Minimum output power	$0.95P_{obj} - 1.5 I_{sm} E_A \cos(\phi) \leq 0$
Maximum output power	$1.5 I_{sm} E_A \cos(\phi) - 1.05P_{obj} \leq 0$
Maximum active volume	$\pi R_{se}^2 L_e - Vol_{max} \leq 0$
Maximum torque ripple	$T_{pk-pk} - T_{pkmax} \leq 0$

where the output power is defined in motor operation mode and ϕ is the angle between the fundamental components of E_A and I_{SM} (i.e. the power factor).

Table 5.4. Geometric constraints.

Constraint	Formulation
Stator yoke feasibility	$R_s + h - R_{se} \leq 0$
Minimum rotor radius	$R_{rmin} - (R_s - l_m - g) \leq 0$
Slot opening feasibility	$w_0 - \left(\frac{2\pi R_s}{Q} - w_t\right) \leq 0$
Tooth width feasibility	$w_t - \frac{2\pi R_s}{Q} \leq 0$

Table 5.5. Magnetic constraints.

Constraint	Formulation
Maximum teeth saturation level	$B_t - B_{sat} \leq 0$
Maximum yoke saturation level	$B_s - B_{sat} \leq 0$
Avoid magnets demagnetization	$B_g^a - B_{gmax}^a \leq 0$

Table 5.6. Electric constraints.

Constraint	Formulation
Maximum current density	$\frac{N_{layer} I_{sm}}{F_f h_2 \left(\frac{2\pi(R_s + h_2/2)}{Q} - w_t \right)} - J_{max} \leq 0$
Maximum electric load	$q_e - q_{emax} \leq 0$
Maximum phase input voltage	$V_{ph} - V_{phmax} \leq 0$
Maximum phase current	$I_{ph} - I_{phmax} \leq 0$
Minimum power factor	$f_{pmin} - f_p \leq 0$

Table 5.7. Thermal and acoustic constraints.

Constraint	Formulation
Maximum wire temperature	$T_{ew} - T_{Cmax} \leq 0$
Maximum magnet temperature	$T_m - T_{mmax} \leq 0$
Maximum noise emission level	$L_{dB(A)} - L_{dB,max} \leq 0$

5.1.3 The DMS Algorithm

The direct multisearch (DMS) is a novel multiobjective derivative-free heuristic algorithm that is based on the search/poll paradigm (i.e. it is closely related with the Hooke and Jeeves method) combined with the Pareto dominance concept. Due to these properties, mostly coincident with those required in the developed methodology, it is selected as the optimization algorithm used in the proposed PMSM design process.

The DMS method was first presented in 2011 and an exhaustive explanation and convergence study could be found in its foundational paper [Custódio 2011], here just the basic principles are highlighted.

Initially a set of feasible solutions (i.e. PMSM designs that fulfil the imposed constraints and defined by n coordinates, where n is the number of design variables) is selected, and a "search step vector" α_n is defined. The initial set of points is called L_0 .

From this initial population an iterative process is launched, each iteration generates its own solutions group set L_k , where k is the iteration number. The steps done in iteration k are:

- **Selection of a point:** one of the points in L_{k-1} is chosen in order to perform an exploratory step. Several algorithms can be implemented in order to select the most suitable “exploratory point” x_k .
- **Pool step:** a new set L_{add} is calculated from the exploratory point. Generally α is added and subtracted from each x_k coordinate, i.e. if $x_k = (0.5, 1.5)$ and $\alpha = (1, 1)$, $L_{add} = \{(1.5, 1.5), (0.5, 2.5), (-0.5, 1.5), (0.5, 0.5)\}$.
- **Filtering dominated points:** a new set $L_{k-1} \cup L_{add}$ is defined, and all the dominated points are filtered, i.e. if a point “a” is worse in all the objective functions than other point “b”, it is said that “a” is dominated by “b” and “a” is eliminated from $L_{k-1} \cup L_{add}$.
Thus, the new solution group will be $L_k = \text{filter}(L_{k-1} \cup L_{add})$
- **Step size parameter update:** if $L_k \neq L_{k-1}$ the iteration is considered successful and α is usually incremented for the next iteration. Otherwise α is decremented (generally halved) for the next iteration step, in order to search a better solution in a closer region.

More detailed and rigorous explanations of the DMS algorithm, with some specific examples, are included in [Custódio 2011].

5.2 Proposed “Two Round Exploratory Algorithm”

The aforementioned models, design variables, objective functions and constraint functions have been integrated in the DMS algorithm in order to obtain a complete and functional methodology which takes into account the complex requirements than real industrial applications impose on a PMSM.

The implemented algorithm can be defined as a “two round exploratory” one. It is called exploratory because from a small group of feasible PMSM (the initial population) a higher number of machine designs situated in the Pareto-optimal frontier are obtained.

The complete methodology flowchart is shown in Figure 5.2. Its different steps will be explained in detail in the following sections, including a complete design example as a case of study.

5.2.1 The Initial Population: Specifications and Pre-Design

A first requirement in order to launch an optimization process is the accurate knowledge of the specifications imposed by the PMSM application; this information should be provided by the designer, user of the developed methodology. Most of these specifications are the design constraints previously introduced (e.g. minimum

power factor, maximum torque ripple or maximum phase current), but other key features should also be established, more precisely:

- The **minimum and maximum values of the design variables**. If they are not provided as direct constraints, the methodology itself establishes a default values.
- The **desired PMSM nominal operation condition**: nominal speed (n), nominal torque (T), output power (P_{obj}), operation mode (i.e. motor or generator) and the selected materials (material costs, wire insulation class, magnets type).

If needed, additional specifications (e.g. field weakening features, closed loop dynamics, environmental considerations, fault tolerance conditions, etc.) can be added as a new set of constraints among the ones aforementioned in section 5.1.2.

One of the main drawbacks of a heuristic algorithm (as the DMS) is that not only an initial set of specifications and constraints are needed but an initial population of feasible PMSM, i.e. machines that fulfil all the imposed constraints, are required in order to run the optimization process. That could be troublesome, since the pre-design could be complex if the required specifications are very restrictive.

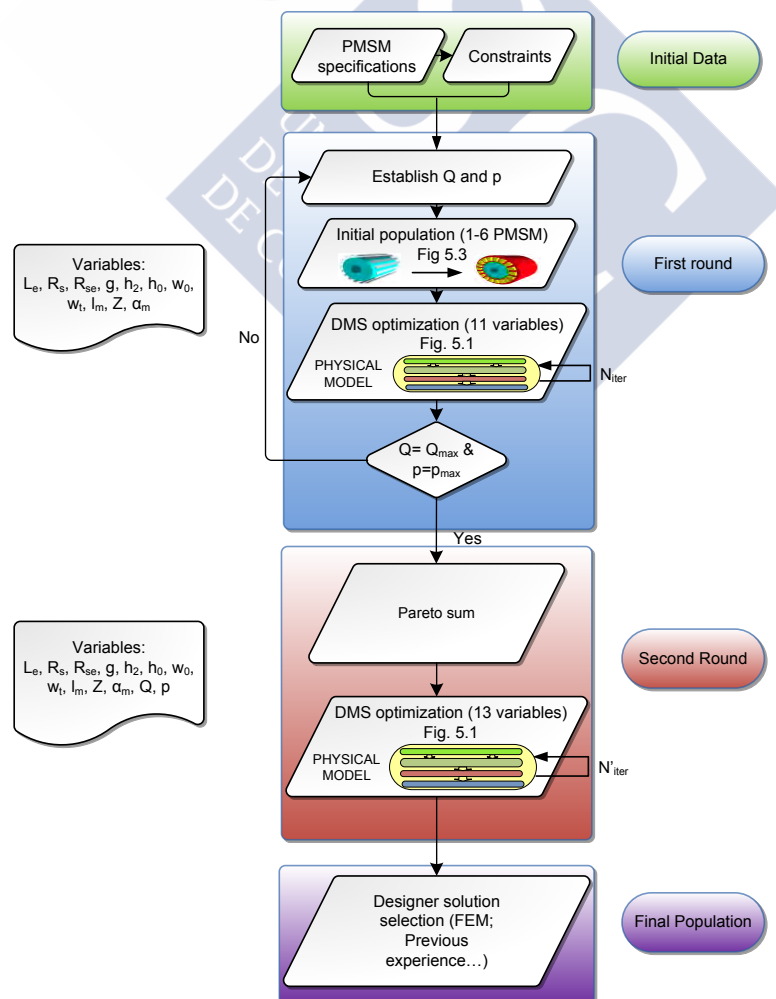


Figure 5.2. PMSM design methodology flowchart.

5.2.1.1 Analytical Pre-Design

It is quite straightforward to notice that an initial population should be defined by their design variables. The main difficulty is that the models developed in Chapter 3 could not be used as far as many of the needed variables remain unknown at this initial stage of the design process, so simplified and estimative equations are required in order to obtain a suitable initial population. This necessary step is called “the analytical pre-design”.

It is worthy of note that only the nominal operation conditions (nominal speed, nominal torque and desired output power), the available manufacture materials (magnets type, core materials and wires insulation class) and the imposed constraints (see section 5.1.2) are considered as initial inputs, so only these data are available in order to apply the analytical pre-design.

The selection of initial feasible PMSM designs is not a trivial task. Moreover, it is a very important subject because the heuristic algorithms are, in general, highly dependent of the chosen initial points (e.g. different initial points could lead to different final populations and, therefore, to non-coincident Pareto-frontiers). Therefore, a proper initial pre-design should lead to a good initial point choice and, through the DMS application, to a better Pareto-frontier.

For each tested motor configuration (i.e. for each Q-p pair) an independent pre-design will be carried out. The pre-design process is formed by four different stages; each of them establishes the values of some of the design variables that will be required in the subsequent stages.

The final output of the pre-design process (for each Q-p configuration) will be:

- An initial set of feasible PMSMs, defined by their design variables.
- A vector with the design variables maximum limits.
- A vector with the design variables minimum limits.

An important goal of the pre-design is to provide not only the initial points but also a suitable range for the design variables (i.e. their maximum and minimum values); these limits may be established by the user as constraints (e.g. limited by the maximum available space for PMSM or other key features). But, if they are not restricted by the designer, the algorithm should be able to select these limits; this is especially important since the DMS works with normalized values, so different limits choice will lead to different final results. The different pre-design stages will be fully explained hereafter. Its graphical representation is shown in Figure 5.3.

Stage 0: Assumed values

Since there are too many unknown variables in a PMSM initial design and because of the internal dependence between them, some should be established (or deduced) first, in order to estimate the others.

Fortunately, after decades of PMSM design, some well-known initial values and typical rules of the thumb could be used in order to begin a new design process. In spite of the fact that the proposed methodology tries to avoid, as far as possible, that kind of “blind designs”, some of these rules are considered useful as “assumed values” for some of the design variables whose ranges are very standardized.

Therefore, in this design stage, the initial values and ranges of the airgap (g), the tooth-tip height (h_0) and the magnet pitch (α_m) are directly chosen as assumed values as shown in Table 5.8. For the sake of a more compact notation x_m , x_M and x_{ini} denote, respectively, the minimum, the maximum and the initial chosen value of the design variable x .

Table 5.8. Stage 0: Design variables assumed values.

Design Variable	MIN	INI	MAX
Magnet pitch, α_m	$\alpha_{m,m} = 0$	$\alpha_{m,ini} = 0.8$	$\alpha_{m,M} = 1$
Airgap length, g	$g_m = 1\text{mm}$	$g_{ini} = 2\text{mm}$	$g_M = 5\text{mm}$
Tooth-tip height, h_0	$h_{0,m} = 1\text{mm}$	$h_{0,ini} = 1\text{mm}$	$h_{0,M} = 5\text{mm}$

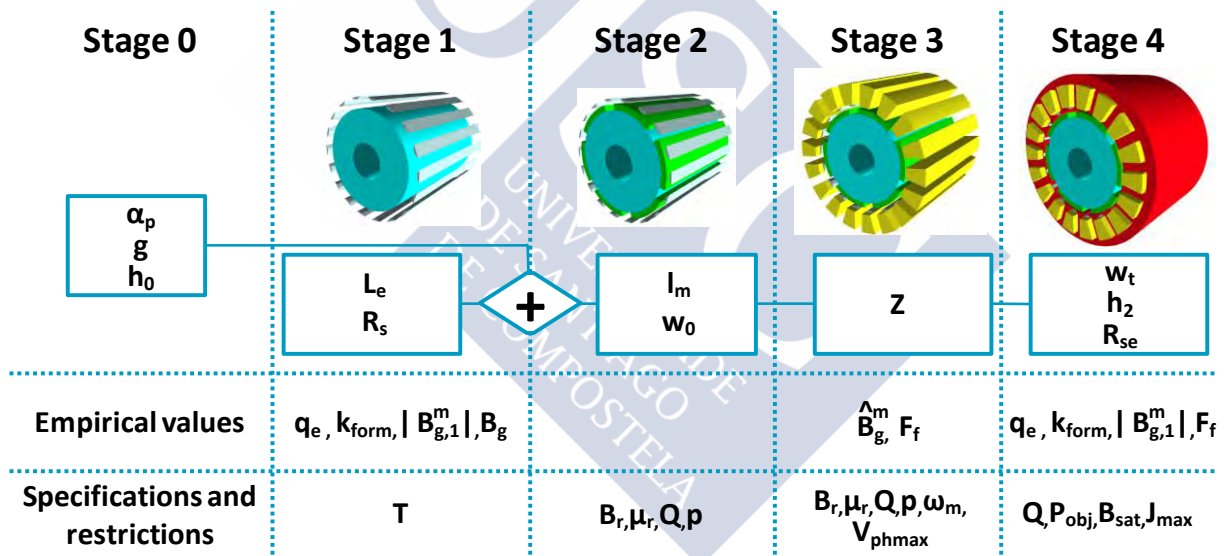


Figure 5.3. Analytical pre-design stages.

Stage 1: Rotor physical dimensions

As a general design rule, the rotor dimensions configure the PMSM magnetic properties, while the stator geometry is more related with its electrical features. Thus, it is a good approach to obtain first the rotor geometry and, through it, to deduce the rotor airgap flux density (B_g^m). Once B_g^m is obtained, it can be used in order to calculate the machine EMF (E_t). Finally, the stator dimensions are selected in order to avoid both, the magnetic saturation and an excessive current density flowing through the slots. Each of the aforementioned steps is related with one of the pre-design stages.

More specifically, stage 1 consists in the selection of a suitable rotor geometry. For this purpose an equation relating the rotor dimensions and the total torque is needed, one of the most popular is [Almandoz 2008]:

$$T = 4\pi |B_{g,1}^m| q_e R_s^2 L_e, \quad (5.3)$$

where q_e is the desired electric load and $|B_{g,1}^m|$ is the B_g^m main spatial harmonic, as it is defined in (3.11). Equation (5.3) has four unknown values: the stator internal radius (very related with the rotor external one), the PMSM effective length, the electric load and $|B_{g,1}^m|$. Therefore, some relations between them should be fixed.

The electric load is a popular figure of merit that relates the current flowing through the machine with its dimensions and its expected heating. [Gieras 2002] provides a table with typical q_e values for different cooling systems. In this work, the selected value is $q_e = 150$ A/cm, a typical electric load for a PMSM cooled by an air fan and in continuous operation mode.

In a similar way, standard values are proposed for $|B_{g,1}^m|$. For most of PMSM machines $|B_{g,1}^m|$ is between 0.425 and 0.503 T [Pyrhönen 2008], so a typical value of $|B_{g,1}^m| = 0.45$ T is chosen. It is also useful to introduce a new variable \widehat{B}_g^m defined as the maximum value of the equivalent square waveform associated with B_g^m (the black dotted line plotted in Figure 5.4).

The relations between the three values referring the rotor flux density in the airgap (B_g^m , $|B_{g,1}^m|$ and \widehat{B}_g^m) are graphically shown in Figure 5.4, where $\widehat{B}_g^m = 0.87$ T and $|B_{g,1}^m| = 0.5$ T.

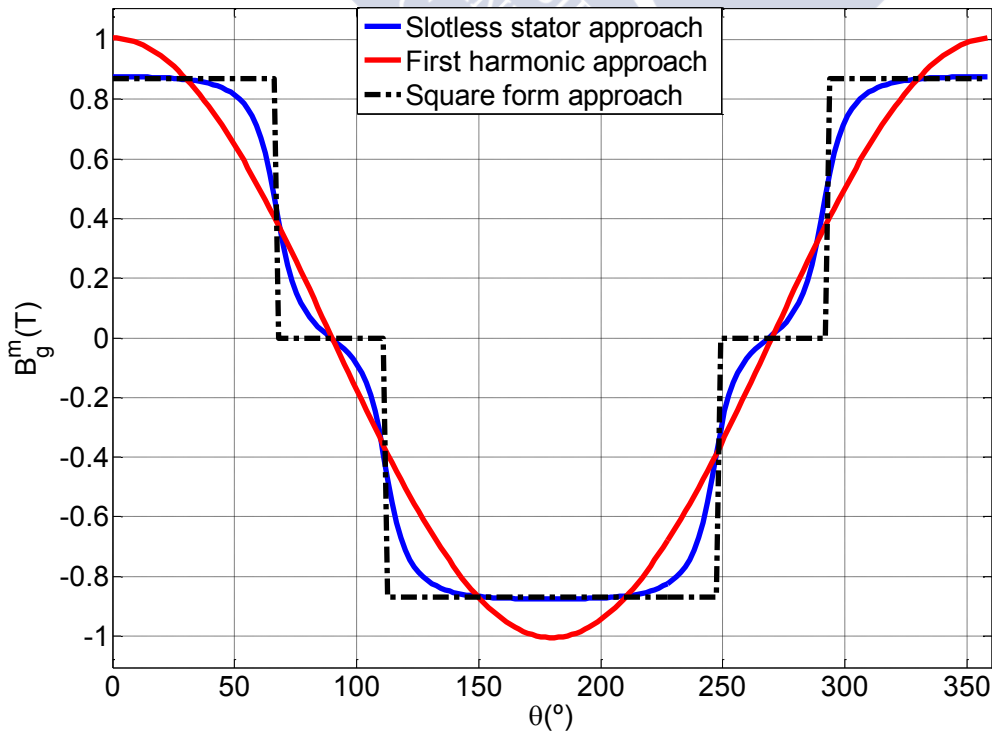


Figure 5.4. Rotor flux density in the airgap.

Mathematically an approximate relation between $|B_{g,1}^m|$ and \widehat{B}_g^m could be deduced from the FS of a square wave which expression is given by (see, for example [Almandoz 2008])

$$B_{g,squared}^m = - \sum_{k=-\infty}^{\infty} j\alpha_m \widehat{B}_g^m \sin\left(\frac{\pi}{2}k\right) \text{sinc}\left(\frac{\pi}{2}k\alpha_m\right) e^{jk\pi}, \quad (5.4)$$

and yields

$$\widehat{B}_g^m = \frac{|B_{g,1}^m|}{\alpha_m \text{sinc}(\pi\alpha_{m,ini}/2)}. \quad (5.5)$$

From the $|B_{g,1}^m|$ value and (5.5) the chosen initial value for \widehat{B}_g^m is 0.83 T. It is recalled that $\text{sinc}(x) = \sin(x)/x$ if $x \neq 0$ and $\text{sinc}(0) = 1$.

Finally, a relation between L_e and R_s is desirable in order to apply (5.3). [Soong 2008] proposes an empirical rule that establishes that R_s should be between L_e and $0.25L_e$. Therefore, a new variable k_{form} will be defined as:

$$k_{form} = R_s/L_e. \quad (5.6)$$

Many initial points could be generated just changing the “aspect relation” k_{form} . More precisely, three initial points will be selected as initial population for each Q-p configuration, those corresponding to k_{form} equal to 0.25, 0.5 and 1, respectively.

Equation (5.6) is substituted into (5.3) leading to

$$L_{e,ini} = \sqrt[3]{\frac{T}{4\pi|B_{g,1}^m|q_e k_{form}^2}} = \sqrt[3]{\frac{T}{270 \cdot 10^3 \pi k_{form}^2}}, \quad (5.7)$$

while $R_{s,ini}$ is deduced from equation (5.6): $R_{s,ini} = k_{form}L_{e,ini}$. R_s and L_e maximum and minimum values are selected as the 200% and the 50% of their initial values, if no other constraints are specified.

Stage 2: Magnetic excitation calculus

This stage is devoted to the initial magnets height (h_m) selection; additionally, the values for the slot opening (w_0) are established. From these variables the initial magnetic circuit will be fixed in order to obtain the induced EMF in the next stage.

The minimum value for w_0 is generally twice the copper wires diameter, if no constraint is provided it will be assumed that $w_{0,m} = 2\text{mm}$. The initial and the maximum slot opening will be fixed as a percentage of its maximum geometric limit as:

$$w_{0,ini} = 0.09 R_{s,ini} 2\pi/Q, \quad (5.8)$$

$$w_{0,M} = 0.9 R_{s,M} 2\pi/Q. \quad (5.9)$$

The initial value of h_m will be deduced from the relation between \widehat{B}_g^m and the magnet residual induction B_r which is given by [Hanselman 2012]

$$\widehat{B}_g^m = B_r \frac{C_\phi}{1 + \mu_r C_\phi g/h_m}, \quad (5.10)$$

where μ_r is the magnet relative permeance and C_ϕ is a geometric relation between the magnets and the airgap mean radius, i.e.

$$C_\phi = \frac{R_r + l_m/2}{R_s - g/2}. \quad (5.11)$$

In most of practical designs C_ϕ is very close to one, so from (5.10)

$$h_{m,ini} = \frac{\widehat{B}_g^m \mu_r g_{ini}}{B_r - \widehat{B}_g^m}. \quad (5.12)$$

The maximum value for the magnets height ($h_{m,M}$) is twice its initial value and its minimum value will be established in 0 mm. Table 5.9 shows the minimum, maximum and initial values deduced in this stage.

Table 5.9. Stage 2: Design variables established values.

Design Variable	MIN	INI	MAX
Slot opening, w_0	2 mm	$0.09 \cdot 2\pi R_{s,ini}/Q$	$0.9 \cdot 2\pi R_{s,M}/Q$
Magnet height, h_m	0 mm	$(\mu_r g_{ini} \widehat{B}_g^m)/(B_r - \widehat{B}_g^m)$	$2h_{m,ini}$

Stage 3: Electric excitation calculus

As it was aforementioned, from the magnetic circuit it is possible to obtain the induced phase EMF per coil turn. The initial number of conductors per slots per layer (Z_{ini}) will be fixed assuming that the total EMF should not exceed the 90% of the maximum phase input voltage (V_{phmax}), generally imposed by the converter, i.e.

$$Z_{ini} = \left\lfloor \frac{0.9 V_{phmax}}{\sqrt{2} |E_{At,1}|} \right\rfloor, \quad (5.13)$$

where $|E_{At,1}|$ is the main harmonic of the induced phase EMF per coil turn, (deduced from (3.43), taking $Z = 1$ and $k = 1$), V_{phmax} is measured in voltage rms values and $\lfloor \cdot \rfloor$ is the “round floor” function.

The minimum possible value of Z_m is 1 while its maximum value is taken as $Z_M = 1.5Z_{ini}$.

Another important electrical variable that can be determined is the phase current, I_{ph} . Although it is not a design variable, its value is important in order to calculate the stator dimensions. Assuming that the EMF is in phase with I_{ph} , from the power identity it can be deduced that

$$|I_{ph,1}| = \frac{P_{obj}}{m Z_{ini} \sqrt{2} |E_{At,1}|}, \quad (5.14)$$

where m is the number of phases (generally $m = 3$) and $|I_{ph,1}|$ is measured in rms.

Stage 3: Stator physical dimensions

Finally, the design variables related with the stator dimensions (tooth width w_t , tooth height h_2 and rotor external radius R_{se}) should be fixed.

The initial value for w_t will be chosen 50% higher than the needed one in order to avoid magnetic saturation in the teeth, i.e.

$$w_{t,ini} = 1.5 \frac{\widehat{B}_g^m 2\pi R_{s,ini}}{Q B_{sat}}. \quad (5.15)$$

The limit values for w_t will be 0 for its minimum value and a 90% of its geometric limit for its maximum value, i.e.

$$w_{t,M} = 0.9 \frac{2\pi R_{s,M}}{Q}. \quad (5.16)$$

The tooth height h_2 will be selected in order to avoid an excessive current density in the slots. It is a very common choice to limit the current density J_{max} from 5 to 10 A/mm² for air fan cooled machines [Staton 2011]. In order to avoid excessive slot current density, the minimum slot area ($A_{s,m}$) should be:

$$A_{s,m} = \frac{Z_{ini} |I_{ph,1}|}{F_f J_{max}}, \quad (5.17)$$

where F_f is the slot fill factor. A_s can be also calculated as

$$A_s = h_2 w_s = \frac{h_2^2 \pi}{Q} + \left(\frac{2\pi R_s}{Q} - w_t \right) h_2, \quad (5.18)$$

where w_s is the mean slot width.

From (5.17) and (5.18) it is possible to deduce a minimum h_2 value in order to ensure an admissible current density through the coils,

$$h_{2,m} = \frac{-w_{1,ini} + \sqrt{w_{1,ini}^2 + \frac{4\pi A_{s,m}}{Q}}}{2\pi/Q}, \quad (5.19)$$

where $w_{1,ini}$ is the slot width value when the radial coordinate is equal to $r = R_{s,ini}$, i.e.

$$w_{1,ini} = \frac{2\pi R_{s,ini}}{Q} - w_{t,ini}. \quad (5.20)$$

From $h_{2,m}$ the initial and the maximum tooth height values will be chosen as $h_{2,ini} = 2.5h_{2,m}$ and $h_{2,M} = 5h_{2,m}$.

The last design variable that should be selected is the external stator radius (R_{se}). Its initial value should ensure that the stator yoke remains magnetically unsaturated during normal machine operation. The desired minimum stator yoke is

$$w_{sy,m} = \frac{\phi_g^m}{2B_{sat} L_e} = \frac{\widehat{B}_g^m \alpha_{m,ini} R_{s,ini}}{2B_{sat}}. \quad (5.21)$$

where ϕ_g^m is the estimated rotor flux induced by a pole pair. It is assumed that the flux in a stator yoke section will be equal to $\phi_g^m/2$ [Almandoz 2008].

The initial external stator radius is selected in order to obtain a stator yoke width equal to $2w_{sy,m}$,

$$R_{se,ini} = R_{s,ini} + h_{2,ini} + 2w_{sy,m} = R_{s,ini} \left(\frac{B_{sat} + \alpha_{m,ini} \widehat{B}_g^m}{B_{sat}} \right) + h_{2,ini}. \quad (5.22)$$

The minimum limit for R_{se} is established as $R_{se,m} = R_{s,ini}$ and its maximum as a 150% of its initial value $R_{se,M} = 1.5R_{se,ini}$.

With this last variable established, the analytical pre-design is complete and a total of three PMSM designs are chosen as a valid initial population for each Q-p configuration. With those data, the DMS algorithm will be executed and the optimization process could begin. Moreover, the maximum and minimum limits for each variable are provided in order to normalize them for a proper DMS operation.

Table 5.10 shows the chosen initial, minimum and maximum values for each considered design variable.

Table 5.10. Initial variables selection in analytical pre-design.

Design Variable	MIN	INI	MAX
Magnet pitch, α_m	0	0.8	1
Airgap length, g	1 mm	2 mm	5 mm
Tooth-tip height, h_0	1 mm	1 mm	5 mm
Stator length, L_e	$0.5 L_{e,ini}$	$\left(\frac{T}{4\pi q_e k_{form}^2 B_{g,1}^m }\right)^{1/3}$	$2L_{e,ini}$
Internal stator radius, R_s	$0.5 R_{s,ini}$	$k_{form} L_{e,ini}$	$2 R_{s,ini}$
Magnet height, h_m	0 mm	$\frac{\mu_r g_{ini} \widehat{B}_g^m}{B^r - \widehat{B}_g^m}$	$2h_{m,ini}$
Number of conductors per slot per layer, Z	1	$\left\lfloor 0.9 \frac{V_{ph,max}}{\sqrt{2} E_{at,1} } \right\rfloor$	$1.5Z_{ini}$
Tooth width, w_t	0 mm	$3\pi R_{s,ini} \frac{\widehat{B}_g^m}{Q B_{sat}}$	$0.9 \frac{2\pi R_{s,M}}{Q}$
Slot opening, w_0	2 mm	$0.09 \frac{2\pi R_{s,ini}}{Q}$	$0.9 \frac{2\pi R_{s,M}}{Q}$
Slot height, h_2	$0.4 h_{2,ini}$	$\frac{-w_{1,ini} + \sqrt{w_{1,ini}^2 + \frac{4\pi A_{s,m}}{Q}}}{2.5 \frac{2\pi}{Q}}$	$2 h_{2,ini}$
External stator radius, R_{se}	$R_{s,ini}$	$R_{s,ini} \left(\frac{B_{sat} + \alpha_{m,ini} \widehat{B}_g^m}{B_{sat}}\right) + h_{2,ini}$	$1.5R_{se,ini}$

5.2.2 Exploratory Rounds:

Once the PMSM specifications and constraints are established the optimization process shall begin.

The first round, called the iterative configuration search, is divided in four steps:

- Selection of a suitable range of Q-p pairs as different feasible configurations. These configurations will be studied and their results will compete between them in an ulterior optimization step.

- Then an iterative process begins. For each Q-p configuration the next operations are carried out.
 - An analytical pre-design is fulfilled (as explained in the previous section) and a small initial population of 3 PMSM designs are selected. Moreover, maximum and minimum limits are established for each design variable.
 - The design variables of each initial PMSM design are normalized between their limits. This is a previous step for the DMS algorithm execution.
 - Finally the DMS algorithm is executed; the stop criteria will be a maximum number of evaluations of the PMSM models (N_{iter}). As a result, a Pareto-frontier of the best candidate designs is generated.

For example, if the number of slots (Q) can be 36 or 72 and the number of pole pairs (p) can be 4, 5 or 6, the DMS algorithm is run a total of six times with a maximum of N_{iter} iterations each, finally six Pareto-frontiers are obtained.

The second round is known as the global search. Although the DMS algorithm is executed again there are several important differences between the configuration search round and the global search one.

First an initial population is generated but, in this case, no analytical pre-design is needed, as far as this population is the Pareto envelope generated by the configuration search round. The envelope is calculated as follows: if a proposed design (in any of the previous Paretos) is dominated by any other (in another Pareto-frontier) the first one is eliminated and will not be part of the Pareto envelope while all the non-dominated points will be in the Pareto envelope. An example of Pareto envelope is shown in Figure 5.5.

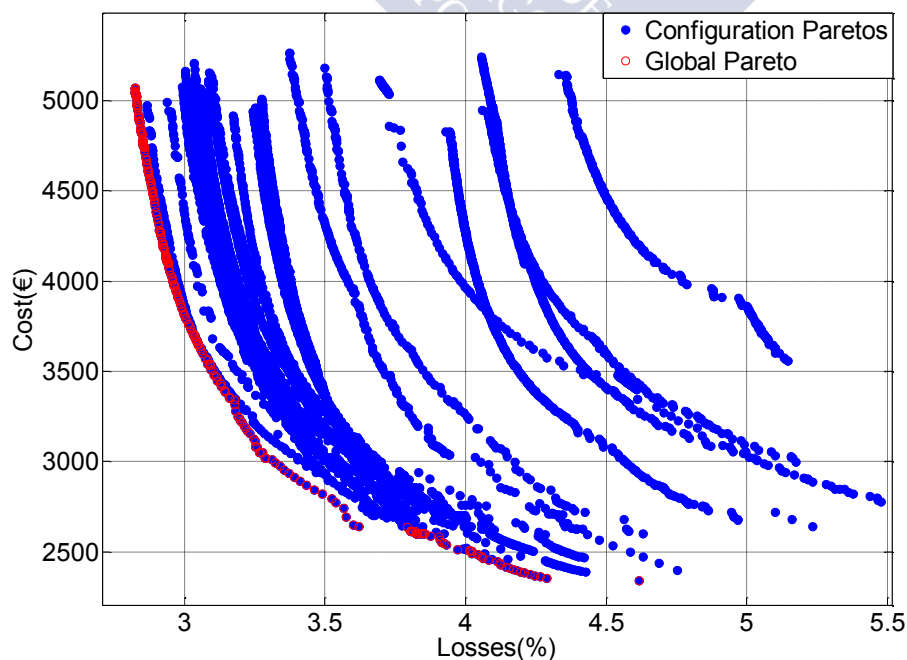


Figure 5.5. Example of Pareto envelope obtaining in the global search first step.

Once the new initial population is generated a normalization process is carried out and two new design variables are now included: the number of slots (Q) and the number of pole pairs (p). Thus, not only a competence between the different configurations is done but also there is a possibility to search in other configurations if they proved to have more promising features.

From this new initial population the DMS algorithm is run just once, in this case letting it to evaluate the objective functions (and, therefore, the PMSM physical models) N'_{iter} times, where N'_{iter} is generally much greater than N_{iter} (even 100 times greater in some cases). In this way a Pareto-frontier very close to the better feasible one is expected to be obtained.

In conclusion, the first round selects the more promising Q-p configurations while the second one analyses them very deeply in order to achieve the best possible results.

It is worth noticing that a complete developed tool programmed in Matlab® supports the proposed methodology; it executes automatically all the aforementioned steps, providing the user with a suitable set of optimal designs and intuitive visualization routines to understand them. The inputs are also established through a simple, straightforward process. The tool is shown in Figure 5.6.

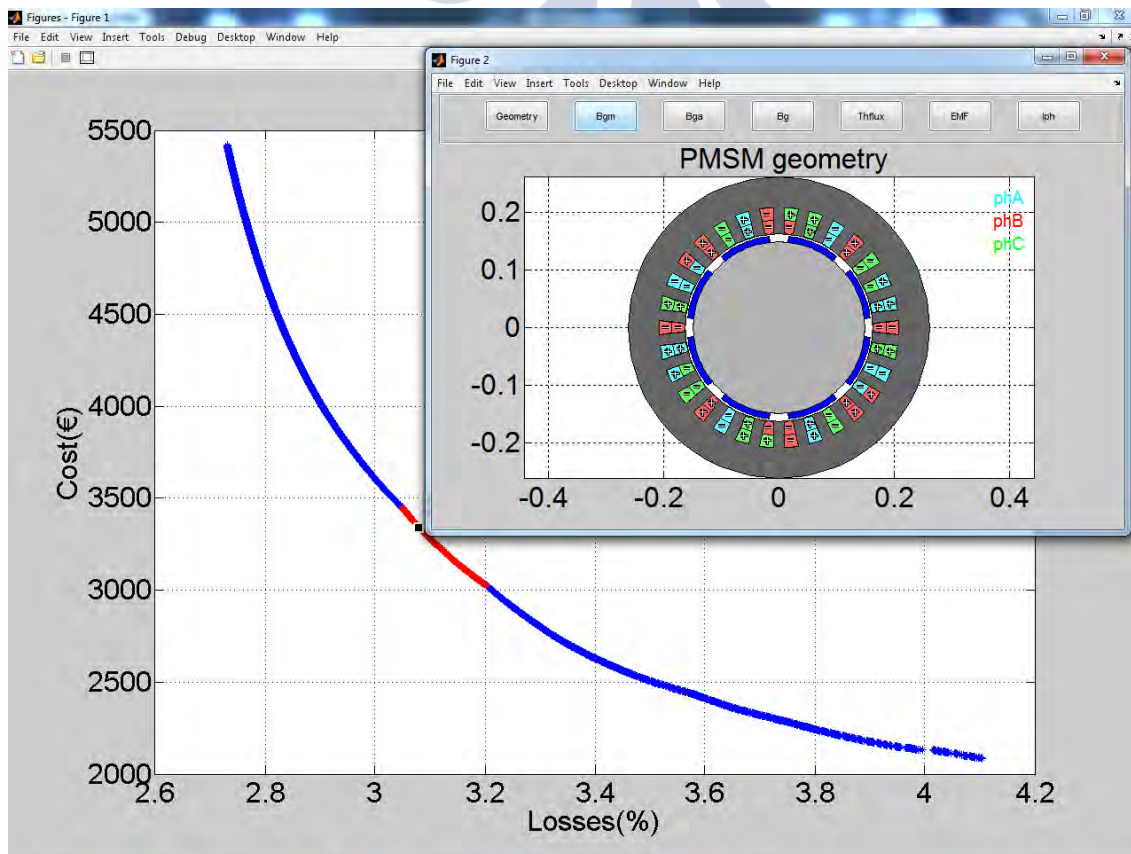


Figure 5.6. Matlab® tool which implements the proposed methodology.

Once the tool executes all the design process, it provides a Pareto of feasible optimal solutions. The designer can choose among them the most suitable one.

5.3 Practical Example: Machine Design

In order to achieve more insight in the implemented design methodology a complete case of study is developed and presented. The proposed optimization process will be fully explained step by step and its main conclusions and decisions clarified. Moreover, a fair and complete comparison of the proposed design with a real and well-known machine will be carried out.

In particular, the new design will have the same specifications and constraints than those of the real PMSM “IkerMAQ” analyzed in chapter 4.

5.3.1 Selected Application: Specifications and Constraints

The SPMSM specifications and constraints will be established in order to design a traction machine for the IK4-Ikerlan laboratory test-bench.

The main constraints imposed by the application and the test-bench features have electrical nature. The converter has a maximum bus DC voltage of 750 V which limits the phase voltage to $300 V_{rms}$. On the other hand, the phase current that the converter can handle is established at $120 A_{rms}$.

The desired nominal electrical output power (with the PMSM in generator mode) is 75 kW with a nominal speed of 1080 rpm (i.e. mechanical frequency of 18 Hz). This establishes a nominal torque of 700 N.m which is a suitable value because most of the tested machines in the test-bench have lower nominal torques.

The machine is supposed to work with constant load in continuous nominal operation conditions, so thermal equilibrium is assumed. This kind of operation falls into class S1. This is the most common duty-type class in industrial machines independently of the real use of the motor [Pyrhönen 2008].

In order to ensure a proper heat removal, a total enclosed air fan cooled machine is considered, i.e. a machine with a finned frame with a fan attached to the shaft in its rear part. The air is propelled by the fan and passes on the fins, ensuring an efficient convection heat transfer. The maximum current density for this cooling system ranges from 5 to $10 A/mm^2$ [Staton 2011], in this design process $J_{max} = 5 A/mm^2$.

Regarding the selected materials, the magnets are N40H, because of their good magnetic properties (NdFeB magnets have the best energy product in actual market) and the coil insulation class will be H (maximum coil temperature: $180^\circ C$). However, the maximum temperature in normal operation should be lower than $155^\circ C$ (the maximum value for a class F), because it is a common practice to establish this safety margin [Pyrhönen 2008]. In order to ensure that limit, the mean end-coil temperature should not exceed $130^\circ C$.

The costs that will be taken into account in the design process are just the materials costs and not the manufacturing ones. These costs have been established as $C_m = 50\$/\text{kg}$ for N40H magnets, $C_{Fe} = 5\$/\text{kg}$ for the magnetic core and $C_{Cu} = 5\$/\text{kg}$ for the coils copper [Munteanu 2012].

The PMSM specifications based on both electric and mechanical constraints and in the selected available materials are shown in Table 5.11.

Table 5.11. Drive Machine specifications.

Operation mode	Motor/ Generator
Power (nominal)	75 kW
Speed (nominal)	1080 rpm
Torque (nominal)	700 Nm
Efficiency (minimum)	95%
Phase voltage (maximum)	300 V_{rms}
Phase current (maximum)	120 A_{rms}
Magnet material	N40H (NdFeB)
Coil insulation class	H
Magnetic core material (rotor and stator)	M800-65A
Cooling system	Air fan
Duty type	Class S1

The complete constraint set derived from the specifications, the material physical properties and the machine expected features are shown in Table 5.12.

Table 5.12. Initial constraint set.

Efficiency	>95%
Torque ripple	<10% (pk-pk)
Active volume	< 0.1 m^3
Magnetic saturation level (teeth and yoke)	<1.5 T
Armature reaction (airgap)	<0.6 T
Phase voltage	<300 V_{rms}
Phase current	<120 A_{rms}
Power factor	>0.85
Current density	<5 A/mm^2
Magnet temperature	<120 °C
Windings temperature	<130 °C
Noise emission level	<80 dB(A)

Once the application is defined and its specifications established the next step is to provide this data to the implemented tool in order to begin the design methodology.

5.3.2 Methodology Practical Implementation

In order to run the optimization algorithm it is mandatory to establish a set of suitable Q-p configurations, i.e. a search range. It is also critical to determine the maximum number of iterations for the iterative configuration search (N_{iter}) and for the global search (N'_{iter}). Moreover, the total number of evaluated machines will be limited by:

$$N_{total} \leq (1 + \max(p) - \min(p)) \frac{(m + \max(Q) - \min(Q))}{m} N_{iter} + N'_{iter} \quad (5.23)$$

where N_{total} is the total number of evaluated machines, m is the number of phases (i.e. 3), $\max(p)$ and $\min(p)$ denotes, respectively, the maximum and minimum values assigned to p . It is important to notice that (5.23) inequality indicates that some of the machines will never be evaluated by the algorithm because they are not physically feasible.

From (5.23) it is clear that a compromise between elapsed time and results quality should be reached. If N_{total} is increased, the DMS algorithm will perform more PMSM evaluations (calling to the holistic models more times), therefore better results are expected. However, the achieved improvement will be less and less when N_{total} is very high. In other words, for high N_{total} values only a little improvement is expected for an important increment of N_{total} (with the inherent increase of the elapsed time). In addition, for low N_{total} values just a little more computation time leads to much better results.

In order to achieve a good final solution in a reasonable computation time the optimization parameters shown in Table 5.13 are selected. With these values a complete evaluation of the methodology algorithm lasts about six hours in an Intel® Core i7-3370 @ 3.40 GHz.

Table 5.13. Chosen optimization variables

Optimization parameter	Value
Maximum pole pair number, max(p)	16
Minimum pole pair number, min(p)	3
Maximum slots number max(Q)	90
Minimum slot number min(Q)	12
Max. Iteration per configuration (N_{iter})	20,000
Max. Iteration (second round, N'_{iter})	500,000

Figure 5.7 shows the design results with respect to the objective functions for the three stages of the proposed optimization algorithm: the initial population selection (green points), the iterative configuration round pareto-frontier (red line) and, finally, the result provided by the whole process (black line). Some remarkable general trends should be highlighted:

In first place, the initial population offers very expensive machines, mainly because of their large size, which supposes too much material cost (see Figure 5.8 (a)). In other words, equation (5.3) which relates dimensions and torque clearly underestimates the achievable torque density that could be greatly enhanced during the optimization process.

The main improvement in the objective functions is carried out during the first stage of the optimization process (the iterative configuration search). In this step many Pareto-frontiers are obtained and combined in order to reach a feasible set of good solutions for the defined application. In the iterative configuration search the DMS algorithm is executed many times, and the physical models are invoked N_{iter} times during each DMS call. The most promising Q-p configurations are selected and they are combined in the red Pareto-frontier. In the proposed example about 950,000 evaluations are carried out in this first stage.

At the end of the configuration search some machines topologies are selected as the most promising ones by the algorithm, in particular the Q18p4 (more expensive and more efficient), Q30p4 and Q69p5 (cheaper but less efficient). The most attractive configuration is the Q69p5 because it greatly decreases the cost with respect to other solutions with a relatively small loss increase.

Figure 5.8 shows a comparison between the Q69p5 initial population and one of the designs contained in the configuration search Pareto-frontiers. It is remarkable the great improvement achieved by the DMS algorithm decreasing both losses and, especially, cost (and, indirectly, total machine volume).

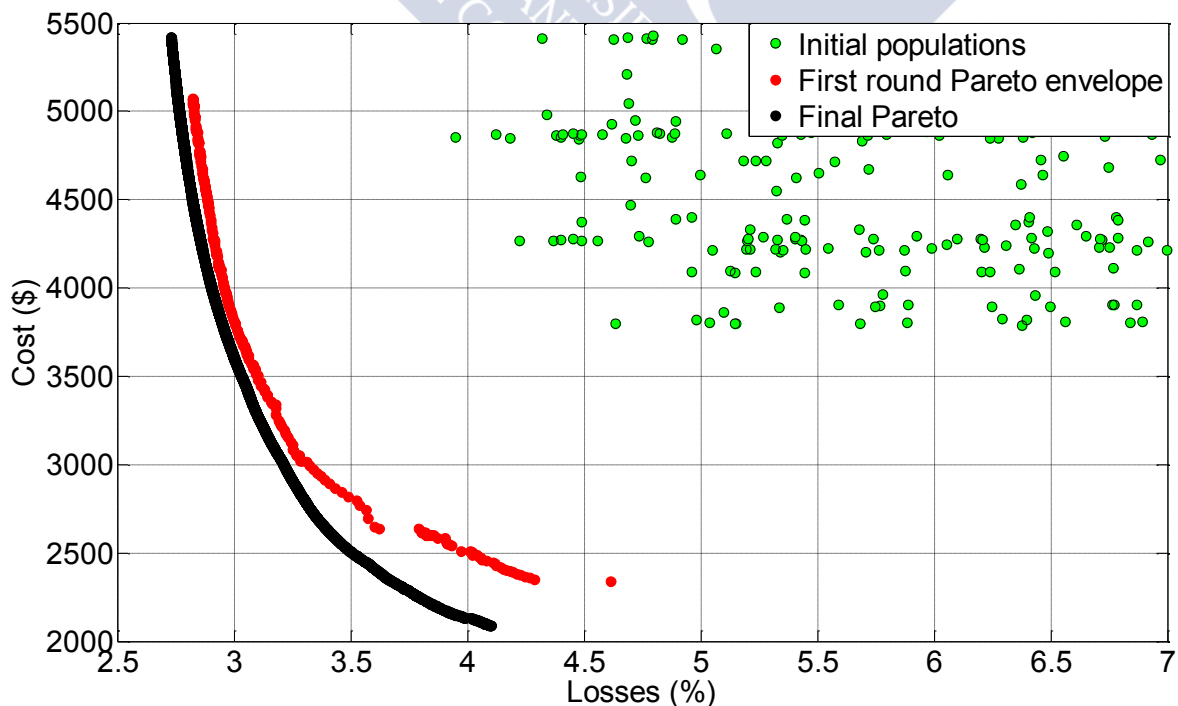


Figure 5.7. Proposed PMSM solutions generated by the algorithm during its different stages.

Finally, the global search step is run and, from the Pareto-frontier obtained in the first stage (in red in Figure 5.7) a better Pareto is obtained (the black line in Figure 5.7). In order to obtain this second Pareto-frontier a total of N'_{iter} model evaluations are performed by the DMS algorithm, i.e. 500,000 evaluations.

It is remarkable that this last stage is quite time consuming and the enhancement obtained does not seem a great one compared with that achieved in the first round. In spite of this fact, the accomplished improvement shows better results in a very interesting part of the Pareto-frontier, the zone where the machines are cheaper; e.g. for a fixed efficiency of 96% the material costs are reduced from 2500\$ in the first round to 2130\$ in the second round. This could be a remarkable difference in order to fulfil the customers' needs.

The aforementioned remarks are by no means dependent of the selected example, but they are noticed in most of the design processes that were carried out applying the methodology, so they could be considered as general rules.

It is also worthwhile to notice that, in this stage, the Q69p5 is converted into a Q69p4 one, because the DMS algorithm decided that, through this change, better performance is obtained. Therefore in the final population offered by the algorithm just the configurations Q18p4 (more expensive and more efficient), Q30p4 and Q69p4 (cheaper but less efficient) are included.

The final chosen solution is selected by the user. In this case it is the Q69p4 design, shown in Figure 5.8 (c); its section appearance is quite similar to the Q69p5 design proposed in the first stage, as can be inferred from Figure 5.7.

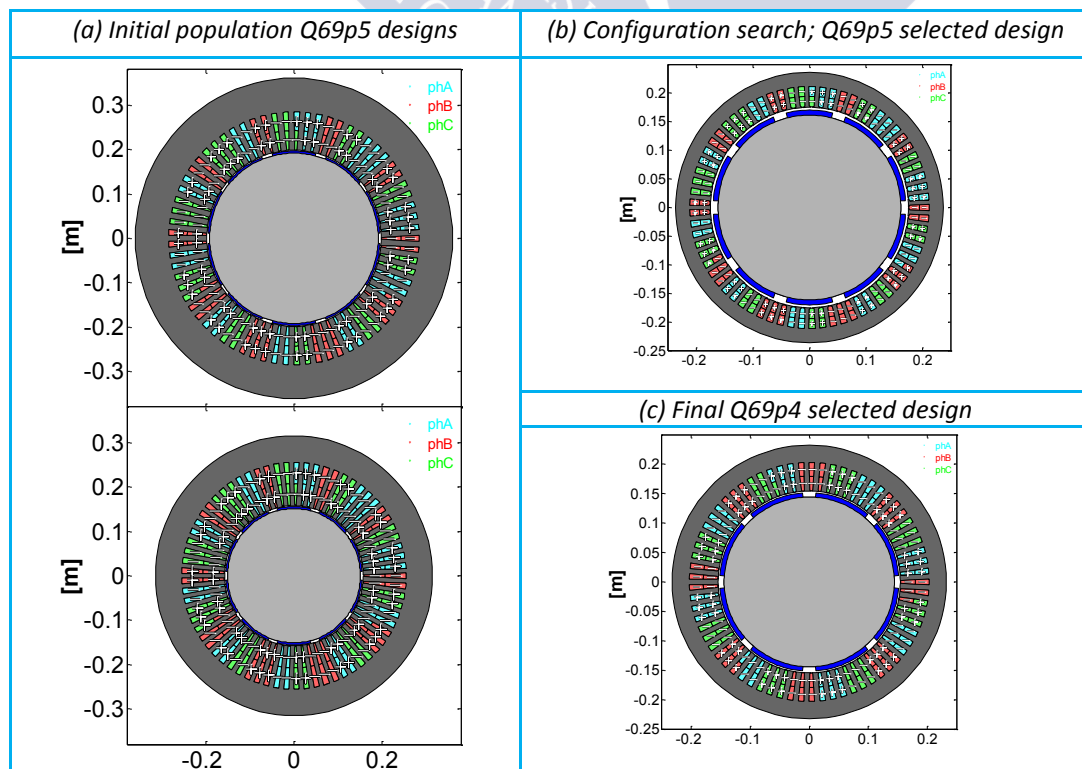


Figure 5.8. 2D sections of the PMSM solutions obtained in the different design stages.

5.3.3 Final Designs and IkerMAQ Q45p5 Comparison

In this section three different design proposals sharing the aforementioned application and specifications are compared: the IkerMAQ Q45p5 solution, the global design Q69p4 selected from the proposed optimization algorithm (see Figure 5.8 (c)) and an additional design Q60p4, called entire design, generated from the same optimization algorithm but only taking into account entire slot machines (see section 3.1.2).

Table 5.14 show the main machines features, while Figure 5.9 illustrates the three machines 2D-sections.

Table 5.14. Final designs, features comparison

Parameter	Symbol	IkerMAQ (Q45p5)	Global design (Q69p4)	Entire design (Q60p4)
Power	P_{obj}	75 kW	75 kW	75 kW
Speed	n	1080 rpm	1080 rpm	1080 rpm
Torque	T	700 Nm	700 Nm	700 Nm
EMF (phase)	E_A	293 V_{rms}	239 V_{rms}	239 V_{rms}
Current (phase)	I_{ph}	87 A_{rms}	87 A_{rms}	87 A_{rms}
Stator resistance	R_{ph}	52.1 m Ω	28.9 m Ω	29.5 m Ω
Stator inductance	L_{ph}	1.11 mH	1.97 mH	1.43 mH
External stator radius	R_{se}	0.188 m	0.232 m	0.207 m
Effective length	L_e	0.31 m	0.24 m	0.32 m
Pole pair number	p	5	4	4
Slots number	Q	45	69	60
Internal stator radius	R_s	0.139 m	0.154 m	0.145 m
Airgap	g	3.5 mm	2.7 mm	3.75 mm
Magnet pitch	α_m	75.0%	81.0%	79.6%
Magnet height	l_m	16.1 mm	7.5 mm	9.2 mm
Number of conductors per slot per layer	Z	3	2	2
Teeth height	h_2	29.8 mm	46.9 mm	37.3 mm
Teeth width	w_t	11.3 mm	9.1 mm	9.0 mm
Slot-opening	w_0	3 mm	2 mm	2 mm
Tooth-tip height	h_0	2 mm	2 mm	2 mm
Total slot area	A_s	140.3 cm ²	233.0 cm ²	184.0 cm ²

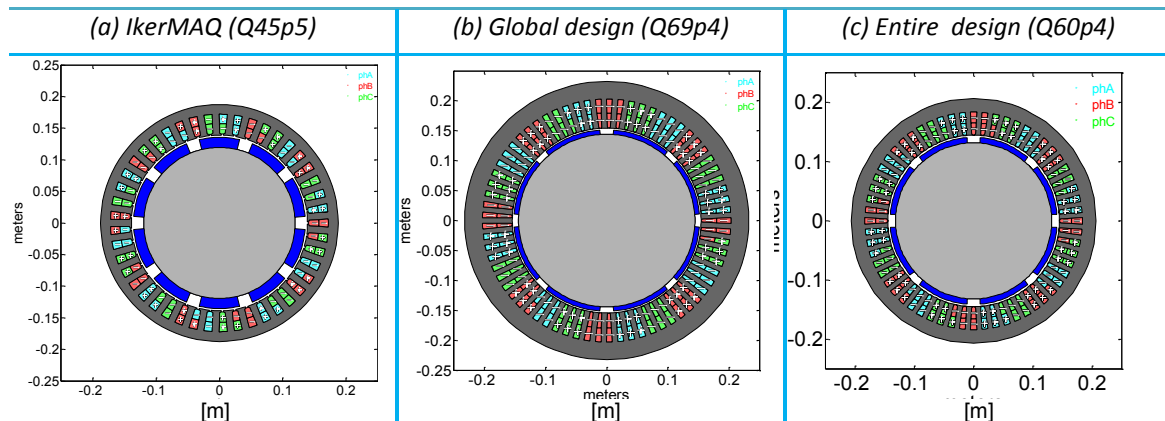


Figure 5.9. 2D sections of the considered PMSM design proposals.

The PMSM designs final values of some key constraint functions and the objective functions are shown in Table 5.15, while in Figure 5.10 the different selected solutions are graphically compared with the Pareto-frontier established by the optimization algorithm.

Table 5.15. Final designs, figures of merit comparison

Parameter	Symbol	IkerMAQ (Q45p5)	Global design (Q69p4)	Entire design (Q60p4)
Efficiency	η	95.6%	96.2 %	96.4%
Cost	C_{tot}	2510 \$	2235 \$	2520 \$
Temperature (magnets)	T_m	80.4 °C	91.1 °C	86.4 °C
Temperature (end-winding)	T_{ew}	105.5 °C	109.3 °C	104.8 °C
Power factor	pf	0.98	0.92	0.96
Torque ripple	ΔT_m	28.0 Nm _{pk-pk}	13.3 Nm _{pk-pk}	12.3 Nm _{pk-pk}
Radiated sound	$L_{dB(A)}$	69 dB(A)	76 dB(A)	60 dB(A)

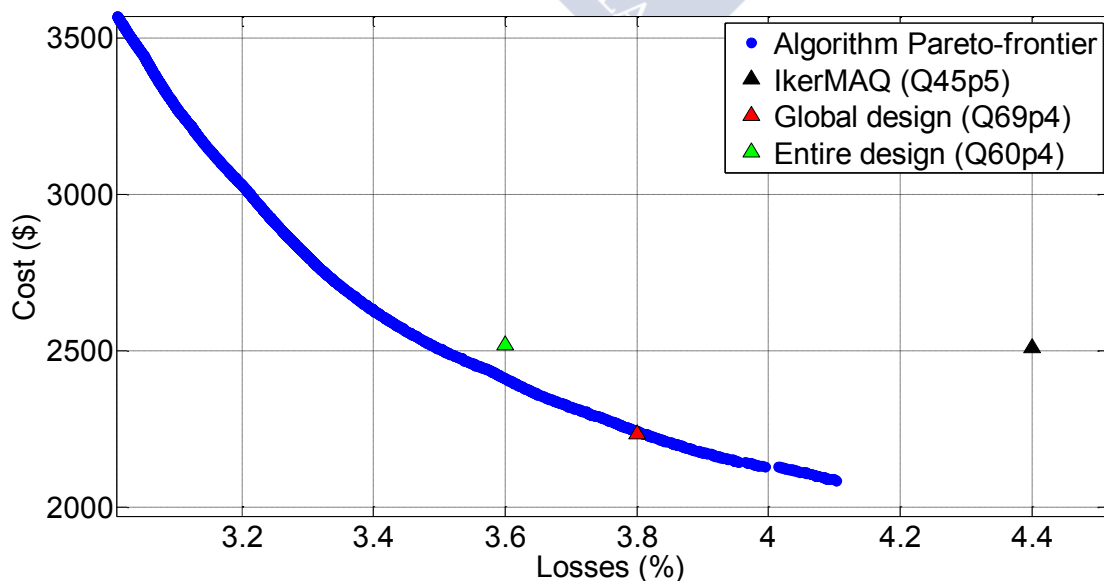


Figure 5.10. Final selected design compared with the achieved Pareto-frontier.

From the results obtained by the methodology, it can be concluded that IkerMAQ is a good design possibility that completely fulfils the application specifications and constraints at good cost and with high efficiency (95.6%). In spite of that fact, the proposed algorithm finds better solutions enhancing the efficiency, decreasing the cost and taking into account the proposed constraints.

More precisely, the global design (Q69p4) is 0.6% more efficient and 275\$ cheaper than IkerMAQ, which supposes a remarkable cost saving in mass production. This saving is achieved mainly reducing the required total magnet material.

On the other hand, the entire design (Q60p4) is also an interesting design option because entire machines are generally more robust, easier to manufacture and quieter than fractional slot machines, as is illustrated in Table 5.15. So, its main advantage with respect to IkerMAQ is not only the 0.8% better efficiency performance but its quieter operation mode (9 dB(A) less).

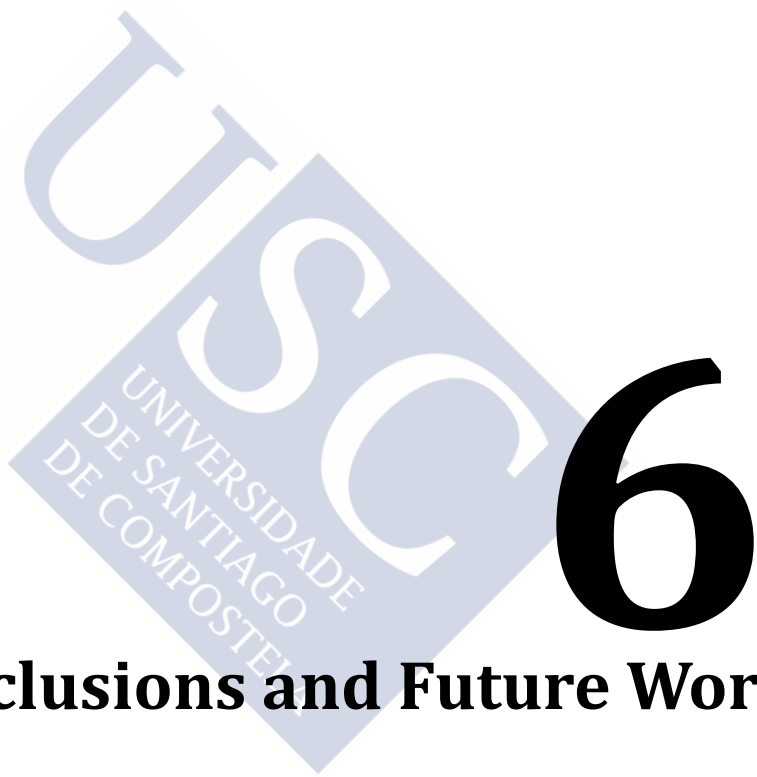
5.4 Conclusions

It can be concluded that the “two round exploratory algorithm” is an accurate, fast, robust and reliable solution for the SPMSM design optimization process. More precisely, in the developed example it was capable to improve the material cost saving 275\$ and the expected efficiency a 0.6% with respect to IkerMAQ, which was, itself, a good and very efficient design.

Two are the key features of the two round exploratory algorithm: Firstly, the design problem is evaluated from a multiphysical point of view and with fully analytical models, which are very fast. This fastness lets the algorithm to evaluate the objective functions many times which supposes a very good exploration through the problem domain in a short elapsed time.

Secondly the heuristic DMS algorithm offers a good search strategy along the selected variables, so a suitable Pareto-frontier is reached in a relatively low number of iterations.

From this two “base properties” the two round exploratory algorithm was implemented with the presented good result. It should be highlighted that another of its main advantages is its adaptability: with minor modifications the objective and/or the constraint functions could be adapted to different purposes or applications, for example including a penalization term in the objective functions if the machine is very noisy or minimizing other desired functions such as the magnet mass or the total PMSM volume.



Conclusions and Future Work



6.1 Summary

PMSMs have an important and increasing presence in many power applications, such as electric vehicle, railway traction, elevation, power generation, renewable energies and aircraft industry. It is expected that, in next years, this trend becomes even greater and an increasing number of exigent applications demand more efficient and suitable PMSMs in order to fulfil a strict set of specifications at minimum cost. Hence, it is evident that a proper design methodology is needed in order to overcome the proposed challenges.

In the present work the basic principles of a PMSM operation was introduced and a state of the art in its design methodology has been performed. However, nowadays most of the papers devoted to the subject only take into account partial aspects of the global problem, and offer unclear methodologies that are hardly replicable and rely on empirical rules and personal designer experience. Only in recent years more complex design methodologies, which include multiphysical and optimized approaches, have been developed.

In spite of this fact, to the best of the author's knowledge, a complete, analytical design methodology, covering all the key features of a PMSM design, including electrical, magnetic, thermal and vibro-acoustic domains has not been presented yet. Thus, the main aim of this thesis is to fill this gap, introducing a new PMSM design methodology offering a holistic, multiphysics, modular and fast approach.

In order to achieve the proposed goal two different objectives have been defined. The first one is the development of a complete set of PMSM physical models. Thus, a specific state of the art has been performed and, based on its results, a new improved PMSM model has been presented. Its main feature consists in a multiphysical approach which takes into account electrical, magnetic, thermal and vibratory processes coupled together through key variables. Moreover, its complete analytical nature supposes a very high computational speed and an adequate level of integration of the different physical domains.

The present work offers a complete validation process. A specific PMSM called IkerMAQ (Q45p5) and fully design in IK4-Ikerlan, was exhaustively tested and electromagnetic, thermal and vibro-acoustics experiments were carried out. The achieved results were compared with those obtained by the analytical models, obtaining very good agreements and validating them.

The high accuracy of the results, as well as the low execution time and the good level of detail achieved in the different domains under study show that the proposed model is a very suitable choice to support multiphysical and optimized design methodologies.

The development of this methodology and an associated tool was the second main objective. In that sense a "two exploratory round algorithm" was implemented, based

in the DMS global optimization algorithm presented by [Custódio 2011]. The main advantages of this exploratory algorithm are its fast, multiphysics approach, heuristic search strategy and high adaptability.

A more complete description of the contributions achieved during this thesis is detailed in the next section.

6.2 Contributions

The main contributions of the thesis are listed below.

- **Development of a multiphysical SPMSM modelling.**
 - **Electromagnetic, thermal and vibro-acoustic models are included.** Models and improvements of different authors are combined and completed, in a unique, integrated model.
 - **Syncretic, analytical and modular.** The links between modules are established in such way that a complete and holistic PMSM analysis could be performed.
 - **Specific analytical contributions were developed.** Concrete modelling challenges leading to new solutions and additional developments were carried out when needed. These improvements suppose “derived contributions” that are listed below in this section.
- **Proposal of a new design methodology adapted for SPMSM working in continuous operation mode.**
 - **Complete and holistic.** It covers all the design process, beginning with the application constraints and specifications and ending with a complete, suitable and optimized PMSM design.
 - **Analytical and fast.** The use of the analytical models aforementioned allows a very fast simulation. Moreover, time saving in a singular machine evaluation also means that more PMSM can be studied leading to a better final solution.
 - **Multiphysical:** Since the used models include electromagnetic, thermal and vibro-acoustic domains, concrete requirements and constraints could be added in any of them. This is critical because the optimum of a global problem is usually different from the “sum” of the optima of its parts.
 - **Optimized:** DMS (a heuristic, deterministic and multiobjective global optimization algorithm) was applied, obtaining very promising results.

- **Implementation of a SPMSM design tool programmed in Matlab®.**

Finally, the methodology and the physical models running behind were implemented and tested in a design tool programmed in Matlab®. It includes both, the optimization algorithm and a graphical interface that shows the achieved Pareto results and their geometries and features.

Moreover, through this tool the need of great design experience and the dependence of “rules of thumb” are overcome because the most suitable dimensions or Q-p configurations are automatically evaluated by the tool, and cumbersome and conflicting rules are no longer necessary.

These main contributions could be considered the natural answer to the proposed goals. However, from them, additional needs arise and new specific studies were launched. These new investigation lines were developed until new unexpected contributions that, in many cases, have the same importance as the main ones.

These *derived contributions* are summarized below.

- **Definition of a new airgap inductance calculus method.** Its main novelty is that the slotting effect is taken into account in order to obtain the magnetic energy stored in the airgap. [Rodríguez 2013].
- **Development of a novel analytical method for PMSM magnet loss estimation,** based on Fourier series. The proposed model is quite straightforward and offers very good results, validated through FEM simulation. [Rodríguez 2014-b].
- **Study of the validity of the Maxwell stress tensors in the case of magnets and other non-linear media.** Previous Maxwell stress tensor definitions are revisited and corrected and new more general equations are derived, analysed and applied. Moreover, practical experiments were carried out in order to demonstrate the validity of the reformulated Maxwell stress tensor.
- **Vibratory study of PMSM components.** In order to obtain a deeper insight in a machine vibratory behaviour, many experiments were carried out using the IkerMAQ (Q45p5) elements. Vibratory measurement on its stator without coils, its wound stator, its frame and the complete machine were carried out. Many conclusions about the influence of singular components in the overall vibratory process were obtained.

6.3 Future Work

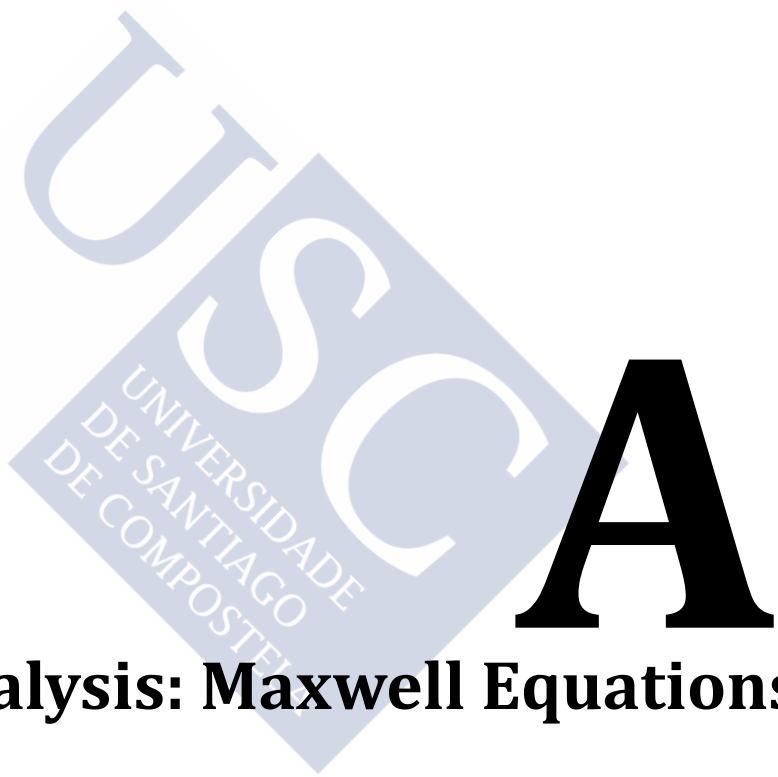
There is an old saying: “Rome was not built in a day”. It is an accurate statement in any exhaustive investigation project, such as the one explained in the present thesis. Therefore, there are many possible improvements and contributions that can be

added to the methodology and its associated tool, as a natural continuation of the developed work. Amongst them, the most representative ones are listed below.

- **Inclusion of other machine topologies:** such as induction, reluctance or DC ones. The methodology is itself quite general and can be slightly modified in order to test and provide solutions taking into account different machines technologies. Moreover, many programmed scripts could be used with minor modifications for many kinds of electrical machine, such as the thermal and the vibro-acoustic ones.
- **Possibility to define applications with many operation points:** an amount of applications require a machine with many operation points, each of them with particular speed and torque, e.g. the electric vehicle. The proposed methodology could be adapted in order to fulfil these specifications.
- **Extension of the analytical models,** especially in the electromagnetic domain, related with a more accurate representation of the magnetic saturation effect, the use of the conformal transformation in order to model the stator slotting fringe effect and the representation of the skew. Moreover, with minor modifications other stator geometries, frame types, magnet shapes or operation conditions could be taken into account in the analytical models.
- **Implementation of supplementary numerical methods:** in order to achieve a deeper insight in the designs provided by the optimization process and to obtain a completely independent tool. For instance, the user could use provided FEM software in order to select one of the Pareto-frontier design options.
- **Improvement of the graphical interface,** including more intuitive input and output flows.

As a final thought, it is obvious that PMSMs have been a “young hope” from decades. As an example, in 1953 it was asserted that the emerging PMSMs will be the standard technology among electrical machines when magnets become more powerful and cheaper [Ginsberg 1953].

Since those years much has been done, new topologies and analysis tools have emerged, NdFeB magnets have become a reality and, due to its better performance, more power could be obtained at lower price. In spite of that fact, Ginsberg’s words remain true. If magnets cost is not reduced PMSM machines will not be able to reach its great potential and they will not become the “standard solution”, while induction machines will continue to play such role. Thus, that price reduction is the most important “future work” that should be accomplished in PMSM technologies.



PMSM Analysis: Maxwell Equations



The backbone of the analytical models is the deduction of the airgap flux density in a simplified concentric cylinders geometry (see section 3.2.1 and Figure 2.6), firstly carried out by [Zhu 1993-a] and readapted for many authors (see, for example [Hanselman 2012]).

The flux density calculus from first principles (i.e. Maxwell's equations) in that canonical problem is of capital importance because it is the base where all the posterior analysis relies on. In this appendix the complete mathematical development of (3.11) and (3.14) from Maxwell's equations will be carried out.

A.1 Definition of the Electromagnetic Problem

The electromagnetic field is governed by the following system of partial differential equations (the Maxwell's equations).

$$\nabla \cdot \mathbf{D} = \rho \quad (\text{A.1})$$

$$\nabla \cdot \mathbf{B} = 0 \quad (\text{A.2})$$

$$\frac{\partial \mathbf{B}}{\partial t} + \nabla \times \mathbf{E} = 0 \quad (\text{A.3})$$

$$\frac{\partial \mathbf{D}}{\partial t} - \nabla \times \mathbf{H} = -\mathbf{J} \quad (\text{A.4})$$

and the constitutive laws

$$\mathbf{B} = \mu(\mathbf{H})\mathbf{H} + \mathbf{B}_r \quad (\text{A.5})$$

$$\mathbf{D} = \varepsilon\mathbf{E} \quad (\text{A.6})$$

$$\mathbf{J} = \sigma\mathbf{E}, \quad (\text{A.7})$$

where \mathbf{E} is the electric field, \mathbf{D} the electric displacement, \mathbf{H} the magnetic field intensity, \mathbf{B} the magnetic induction, \mathbf{J} the current density, μ the magnetic permeability, \mathbf{B}_r the residual magnetic induction, ε the electric permittivity and σ the electrical conductivity. It should be noted that the four last variables are properties depending on the medium.

If the characteristic electromagnetic wavelength is much longer than the size of the device under study (e.g. a PMSM) then the term $\partial \mathbf{D} / \partial t$ can be neglected. Moreover, if no significant eddy current exist the previous equation system can be simplified to the so called transient magnetics problem, i.e.

$$\nabla \cdot \mathbf{B} = 0 \quad (\text{A.8})$$

$$\nabla \times \mathbf{H} = \mathbf{J} \quad (\text{A.9})$$

$$\mathbf{B} = \mu(\mathbf{H})\mathbf{H} + \mathbf{B}_r. \quad (\text{A.10})$$

The above assumptions are fulfilled in the case of an electric machine. Moreover, unless at its ends, the field exhibit longitudinal symmetry so it is possible to solve the problem on a cross-section. That 2D-cross section where the simplified problem is defined is shown in Figure 2.6.

Some additional assumptions could be addressed: on the one hand the current density vector is only non-null in the slots occupied by the coils. On the other hand, the magnetic constitutive law will be considered linear, i.e. it is supposed that $\mathbf{B} = \mu\mathbf{H}$ where $\mu = \mu_0$ on the domains occupied by the coil and the airgap, and $\mu \rightarrow \infty$ in the ferromagnetic cores; additionally in the magnets the constitutive law is not exactly linear and $\mathbf{B} = \mu_r\mu_0\mathbf{H} + \mathbf{B}_r$ where μ_r (the magnets relative permeability) is very close to unity.

In order to obtain the solutions of this simplified problem, it can be decomposed into two ones corresponding to the magnets and the coils contributions. The first one will be solved in the subsequent sections.

A.2 Flux Density Generated by the Magnets

If only the magnets contribution is studied it is possible to ignore the coils, so $\mathbf{J} = 0$ in all the PMSM and $\nabla \times \mathbf{H} = 0$. This implies the existence of a magnetic scalar potential ϕ such that:

$$\mathbf{H} = \nabla\phi. \quad (\text{A.11})$$

Then (A.2) and the magnetic constitutive laws yields

$$-\nabla \cdot (\mu \nabla \phi) = \begin{cases} \nabla \cdot \mathbf{B}_r, & \text{in the magnets} \\ 0, & \text{in air and cores} \end{cases} \quad (\text{A.12})$$

$$\mathbf{B}_r = \mu_0 \mathbf{M}, \quad (\text{A.13})$$

where \mathbf{M} the magnetization vector; (A.12) is an elliptic partial differential equation that can be solved as far as suitable boundary conditions are prescribed.

Because of the special geometry of the problem it is interesting to write (A.12) in polar coordinates (r, θ) . This yields

$$\begin{aligned} & -\frac{1}{r} \frac{\partial}{\partial r} \left(\mu r \frac{\partial \phi}{\partial r} \right) - \frac{1}{r^2} \frac{\partial}{\partial \theta} \left(\mu \frac{\partial \phi}{\partial \theta} \right) = \\ & = \begin{cases} \frac{1}{r} \frac{\partial}{\partial r} (\mu_0 r M_r) + \frac{1}{r} \frac{\partial}{\partial \theta} (\mu_0 M_\theta), & \text{in the magnets} \\ 0, & \text{in air and cores,} \end{cases} \end{aligned} \quad (\text{A.14})$$

where M_r and M_θ are, respectively, the magnetization vector components in r and θ directions. In the magnets, the above equation becomes, after dividing both sides by μ

$$-\frac{1}{r} \frac{\partial}{\partial r} \left(r \frac{\partial \phi_m}{\partial r} \right) - \frac{1}{r^2} \frac{\partial^2 \phi_m}{\partial \theta^2} = \frac{1}{r\mu_r} \left(\frac{\partial}{\partial r} (r M_r) + \frac{\partial M_\theta}{\partial \theta} \right), \quad (\text{A.15})$$

and in the airgap

$$\frac{1}{r} \frac{\partial}{\partial r} \left(r \frac{\partial \varphi_g}{\partial r} \right) + \frac{1}{r^2} \frac{\partial^2 \varphi_g}{\partial \theta^2} = 0. \quad (\text{A.16})$$

The transmission conditions at the magnets-air interface $r = R_m$ impose:

$$[\mathbf{H} \times \mathbf{n}] = [\mathbf{H} \times \mathbf{e}_r] = \mathbf{0} \Leftrightarrow H_{m,\theta}(R_m, \theta) = H_{g,\theta}(R_m, \theta) \quad (\text{A.17})$$

$$[\mathbf{B} \cdot \mathbf{e}_r] = 0 \Leftrightarrow \mu_r \mu_0 r \frac{\partial \varphi_m}{\partial r} + \mu_0 M_r = \mu_0 \frac{\partial \varphi_g}{\partial r} \quad (\text{A.18})$$

where subindex m represents the variable (i.e. the magnetic intensity or the magnetic potential) in the magnet region and the subindex g this variable in the airgap.

Additionally, neglecting the slotting effect, it is assumed that, on the surfaces $r = R_s$ and $r = R_r$, $\mathbf{H} \times \mathbf{e}_r = \mathbf{0}$, that is, the flux density is perpendicular to these surfaces because the magnetic permeability of the core is very large. Indeed, since $\mathbf{B} = \mu \mathbf{H} + \mathbf{B}_r$ and \mathbf{B}_r and \mathbf{B} have to be finite, then $\mathbf{H} \rightarrow \mathbf{0}$ as $\mu \rightarrow \infty$. Hence, \mathbf{H} has to be null in the magnetic core. Moreover, the jump of $\mathbf{H} \times \mathbf{e}_r$ across the interfaces with the cores has to be null because there is no surface current on these interfaces. The conclusion is that $\mathbf{H} \times \mathbf{e}_r = \mathbf{0}$ on the surfaces defined by $r = R_s$ and $r = R_r$, just as claimed. This means

$$H_{m,\theta}(R_r, \theta) = 0, \quad H_{g,\theta}(R_s, \theta) = 0. \quad (\text{A.19})$$

Since $H_{g,\theta} = \frac{1}{r} \frac{\partial \varphi_g}{\partial r}$ and $H_{m,\theta} = \frac{1}{r} \frac{\partial \varphi_m}{\partial r}$ these boundary conditions imply that φ_g and φ_m are constant on $r = R_s$ and $r = R_r$, respectively. One of these constants, let us say φ_g at R_s , can be taken as zero because φ is unique up to a constant.

A.2.1 Resolution in the airgap

In order to solve the boundary-value problem (A.16) separation of variables is used (see, for instance [Pinsky 2003]). In principle (A.16) is valid for $r > 0$ and $\theta \in [0, 2\pi]$ with $\varphi_g(r, 0) = \varphi_g(r, 2\pi)$ and $\frac{\partial \varphi_g(r, 0)}{\partial \theta} = \frac{\partial \varphi_g(r, 2\pi)}{\partial \theta}$ (φ_g smooth). It can be written in the form:

$$\frac{\partial^2 \varphi_g}{\partial r^2} + \frac{1}{r} \frac{\partial \varphi_g}{\partial r} + \frac{1}{r^2} \frac{\partial^2 \varphi_g}{\partial \theta^2} = 0, \quad (\text{A.20})$$

the desired solution has the form

$$\varphi_g(r, \theta) = f(r)g(\theta), \quad (\text{A.21})$$

the next step is replacing (A.21) in (A.20)

$$f''g + \frac{1}{r} f'g + \frac{1}{r^2} f g'' = 0. \quad (\text{A.22})$$

Divide by $f g$ and multiply by r^2 yields to

$$r^2 \frac{f'' + \frac{1}{r}f'}{f} + \frac{g''}{g} = 0. \quad (\text{A.23})$$

Since the first term on (A.23) only depends on r and the second only on θ , both must be constant. Hence

$$g'' + \beta^2 g = 0, \quad g(0) = g(2\pi), \quad g'(0) = g'(2\pi) \quad (\text{A.24})$$

$$f'' + \frac{1}{r} f' - \frac{\beta^2}{r^2} f = 0, \quad (\text{A.25})$$

Problem (A.24) is an eigenvalue Sturm-Liouville problem whose solution is:

$$g(\theta) = A_\beta e^{j\beta\theta}, \quad A_\beta \in \mathbb{C}, \quad \beta = 0, \pm 1, \pm 2, \dots \quad (\text{A.26})$$

Regarding (A.25), it has two linear independent solutions r^β and $r^{-\beta}$ for $\beta \neq 0$. If $\beta = 0$, the two solutions for f are 1 and $\log(r)$.

Combining the computations previously obtained the following family of solutions for (A.20) can be deduced:

$$\varphi_g(r, \theta) = \begin{cases} A_\beta r^\beta e^{j\beta\theta} + B_\beta r^{-\beta} e^{j\beta\theta} & \beta = \pm 1, \pm 2, \dots \\ A_0 + B_0 \ln(r) & \end{cases} \quad (\text{A.27})$$

A.2.2 Resolution in the magnets

The next step is to find a particular solution of Poisson's equation (A.15). It is supposed that \mathbf{M} is independent of r . The Fourier series of M_r and M_θ with respect to θ can be written as

$$M_r = \frac{B_r}{\mu_0} \sum_{k=-\infty}^{\infty} K_{r,k} e^{jkp\theta}, \quad (\text{A.28})$$

$$M_\theta = \frac{B_r}{\mu_0} \sum_{k=-\infty}^{\infty} K_{\theta,k} e^{jkp\theta}, \quad (\text{A.29})$$

notice that functions M_r and M_θ are periodic with respect to θ of period $2\pi/p$ and then in the Fourier series only the frequencies which are multiple of p are present.

Then, $\nabla \cdot \mathbf{M}$ is equal to

$$\begin{aligned}\nabla \cdot \mathbf{M} &= \frac{1}{r} \left(M_r + \frac{\partial M_\theta}{\partial \theta} \right) = \frac{B_r}{\mu_0 r} \left(\sum_{k=-\infty}^{\infty} K_{r,k} e^{jkp\theta} + jp \sum_{k=-\infty}^{\infty} k K_{\theta,k} e^{jkp\theta} \right) \\ &= \frac{B_r}{\mu_0 r} \sum_{k=-\infty}^{\infty} (K_{r,k} + j\beta_k K_{\theta,k}) e^{j\beta_k \theta},\end{aligned}\quad (\text{A.30})$$

where $\beta_k = kp$.

The solution of the Poisson equation (A.15) is a series, each of its terms corresponding to one of those in the sum (A.30). The one corresponding to $e^{j\beta_k \theta}$ is

$$\varphi_m(r, \theta) = C_k r e^{j\beta_k \theta}, \quad C_k \in \mathbb{C}, \quad \beta_k = \pm pk, \quad (\text{A.31})$$

where, for $\beta_k \neq \pm 1$,

$$C_k = -\frac{B_r (K_{r,k} + j\beta_k K_{\theta,k})}{(1 - \beta_k^2) \mu_r \mu_0}, \quad k = \beta_k / p. \quad (\text{A.32})$$

In the case of machines with one pole pairs $p = 1$ and the case $\beta_1 = \pm 1$ may occur. If $p = 1$ the solution for $\beta_1 = 1$ is

$$\varphi_m(r, \theta) = C_1 r \ln(r) e^{j\theta}, \quad (\text{A.33})$$

with

$$C_1 = -\frac{B_r (K_{r,1} + j\beta_1 K_{\theta,1})}{2\mu_r \mu_0}, \quad (\text{A.34})$$

and for $\beta_1 = -1$

$$\varphi_m(r, \theta) = C_{-1} r \ln(r) e^{-j\theta}, \quad (\text{A.35})$$

with

$$C_{-1} = C_1^* \quad (\text{A.36})$$

Finally, the general solution of the Poisson's equation is

$$\varphi_m(r, \theta) = \sum_{k=-\infty}^{\infty} (C_k r + D_k r^{\beta_k} + E_k r^{-\beta_k}) e^{j\beta_k \theta}, \quad \beta_k = \pm pk, \quad pk \neq 1 \quad (\text{A.37})$$

If $p = 1$:

$$\begin{aligned}\varphi_m(r, \theta) &= (C_1 r \ln(r) + D_1 r + E_1 r^{-1}) e^{j\theta} + (C_{-1} r \ln(r) + D_{-1} r + E_{-1} r^{-1}) e^{-j\theta} \\ &\quad + \sum_{\substack{k=-\infty \\ k \neq \pm 1}}^{\infty} (C_k r + D_k r^k + E_k r^{-k}) e^{jk\theta} +\end{aligned}\quad (\text{A.38})$$

From (A.27) and (A.37), and taking into account boundary conditions (A.17), (A.18) and (A.19) it is possible, but quite tedious, deduce the next expression for the magnetic potential in the airgap:

$$\varphi_g(r, \theta) = \sum_{k=-\infty}^{\infty} \frac{R_m^{-\beta_k+1} \left((\beta_k - 1)R_m^{2\beta_k} + 2R_r^{\beta_k+1}R_m^{\beta_k-1} - (\beta_k - 1)R_r^{2\beta_k} \right)}{(\mu_r + 1)(R_s^{2\beta_k} - R_r^{2\beta_k}) - (\mu_r - 1) \left(R_m^{2\beta_k} - \left(\frac{R_s R_r}{R_m} \right)^{2\beta_k} \right)} C_k \left(r^{\beta_k} - R_s^{2\beta_k} r^{-\beta_k} \right) e^{j\beta_k \theta}, \quad (\text{A.39})$$

$\beta_k = \pm pk, \quad pk \neq 1$

From (A.39) it is possible to deduce the expression of the flux density in the airgap [Zhu 1993-a]:

$$B_r(r, \theta) = \mu_0 \sum_{k=-\infty}^{\infty} \frac{R_m^{-\beta_k+1} \left((\beta_k - 1)R_m^{2\beta_k} + 2R_r^{\beta_k+1}R_m^{\beta_k-1} - (\beta_k - 1)R_r^{2\beta_k} \right)}{(\mu_r + 1)(R_s^{2\beta_k} - R_r^{2\beta_k}) - (\mu_r - 1) \left(R_m^{2\beta_k} - \left(\frac{R_s R_r}{R_m} \right)^{2\beta_k} \right)} C_k \beta_k \left(r^{\beta_k-1} + R_s^{2\beta_k} r^{-\beta_k-1} \right) e^{j\beta_k \theta} \quad (\text{A.40})$$

$$B_\theta(r, \theta) = j\mu_0 \sum_{k=-\infty}^{\infty} \frac{R_m^{-\beta_k+1} \left((\beta_k - 1)R_m^{2\beta_k} + 2R_r^{\beta_k+1}R_m^{\beta_k-1} - (\beta_k - 1)R_r^{2\beta_k} \right)}{(\mu_r + 1)(R_s^{2\beta_k} - R_r^{2\beta_k}) - (\mu_r - 1) \left(R_m^{2\beta_k} - \left(\frac{R_s R_r}{R_m} \right)^{2\beta_k} \right)} C_k \beta_k \left(r^{\beta_k-1} - R_s^{2\beta_k} r^{-\beta_k-1} \right) e^{j\beta_k \theta}. \quad (\text{A.41})$$

If (A.40) is particularized for the case $r = R_s$ and the magnetization vector \mathbf{M} has only radial component it yields

$$B_r(R_s, \theta) = \sum_{k=-\infty}^{\infty} \frac{B_r K_{r,k}}{(\beta_k^2 - 1)\mu_r} \beta_k R_s^{\beta_k-1} \frac{R_m^{-\beta_k+1} \left((\beta_k - 1)R_m^{2\beta_k} + 2R_r^{\beta_k+1}R_m^{\beta_k-1} - (\beta_k - 1)R_r^{2\beta_k} \right)}{(\mu_r + 1)(R_s^{2\beta_k} - R_r^{2\beta_k}) - (\mu_r - 1) \left(R_m^{2\beta_k} - \left(\frac{R_s R_r}{R_m} \right)^{2\beta_k} \right)} e^{j\beta_k \theta}, \quad (\text{A.42})$$

where $\beta_k \neq \pm 1$. Equation (A.42) can be understood as a spatial FS, it should be noticed that the coefficient of this FS exactly match with those of the expression (3.11), just as expected.



Fourier Series



Due to its relevance during this thesis development it is considered interesting to include an appendix regarding Fourier Series (FS), its general properties, and the specific significance of the 2D-FS in PMSM analysis. Many studies about FS can be found, see, for example, [Gago 2002].

B.1 Definition

A FS is an expansion of a periodic function in terms of an infinite sum of complex exponentials. The computation and study of FS is known as harmonic analysis and it is extremely useful as a way to break up an arbitrary periodic function into a set of simple terms that, through the superposition principle, can be plugged in, solved individually and then recombined to obtain the solution to the original problem or an approximation to it to whatever accuracy is desired or practical.

A “smooth enough” function $A(t)$ with period T can be expressed as a series of complex exponentials converging to $A(t)$ in some sense. More precisely,

$$A(t) = \sum_{k=-\infty}^{\infty} A_k e^{jk2\pi t/T}, \quad (\text{B.1})$$

where A_k are the FS coefficients, $A_k \in \mathbb{C}$. These coefficients can be obtained from $A(t)$ as

$$A_k = \frac{1}{T} \int_0^T A(t) e^{-jk2\pi t/T} dt. \quad (\text{B.2})$$

The analytical properties of Fourier series such as convergence, derivability, etc. will not be addressed either in this appendix or in the rest of the document because it is not the subject of this work. Thus, the thesis will focus in FS formal computations, enough regularity in functions for their validity is assumed.

B.2 Main properties

FS present many important properties that, in many cases, make simpler operate on the FS-coefficients rather than on the periodic function itself.

Many of these features are applied during this thesis work. They are listed in Table B.1, where $A(t)$ and $B(t)$ denote arbitrary periodic functions with the same period T and A_k and B_k denote, respectively, their FS coefficients, and α and β are known scalars.

Table B.1. Fourier Series main properties.

Property	Periodic Function	FS-coefficients
Linearity	$\alpha A(t) + \beta B(t)$	$\alpha A_k + \beta B_k$
Displacement	$A(t - t_0)$	$A_k e^{-jk2\pi t_0/T}$
First derivative	$dA(t)/dt$	$(jk2\pi/T)A_k$
nth derivative	$d^n A(t)/dt^n$	$(jk2\pi/T)^n A_k$
Integration (when $B_k=0$)	$\int_0^t A(\tau) d\tau$	$\frac{TA_k}{jk2\pi}, \forall k \neq 0$

Another critical property can be expressed as:

$$A(t) \in \mathbb{R} \quad \forall t \Leftrightarrow A_k = A_{-k}^* \quad \forall k. \quad (\text{B.3})$$

where A_{-k}^* is A_{-k} conjugate. In other words, if a periodic function is real, its FS-coefficients are hermitian with respect to k . This feature has high relevance since all the physical magnitudes (and, therefore, its associated fields) are real. Moreover, it is sufficient to know A_k only for $k \geq 0$ in order to restore $A(t)$. More precisely

$$A(t) = A_0 + 2 \sum_{k=1}^{\infty} |A_k| \cos\left(\frac{2\pi kt}{T} + \psi_k\right), \quad A(t) \in \mathbb{R} \quad \forall t, \quad (\text{B.4})$$

where ψ_k is A_k argument. Notice that, as a (B.3) direct implication, $B_0 \in \mathbb{R}$.

Previous exposed properties are easy to prove from (B.1) and (B.2) direct application.

Additionally, FS fulfil the Parseval's identity which establishes:

$$\frac{1}{T} \int_0^T |B(t)|^2 dt = \sum_{k=-\infty}^{\infty} |B_k|^2. \quad (\text{B.5})$$

This equality is especially useful in order to compute the averaged power dissipated by a magnetic or an electric waveform because it allows obtaining the medium power dissipated by the harmonics one by one (i.e. the calculus of the power associated with each FS coefficient) and then sum all the contributions.

Parseval's identity is extensively used in electrical engineering and it is applied several times during this thesis, especially during the power and losses calculus in section 3.4.

B.3 2D-Fourier Series

Most of the studied physical properties (especially the magnetic ones) have both, time and spatial dependence and they are periodic with respect to time t with period $1/f_e$, and to the rotor position, θ with period $2\pi/t_p$. Therefore, it is not unusual that FS with respect to both, time and angle, be performed. If FS is applied twice (i.e. with respect to time and angle simultaneously) a 2D-Fourier Series (2D-FS) arises.

Mathematically a 2D-FS is defined as:

$$A(\theta, t) = \sum_{k=-\infty}^{\infty} \sum_{n=-\infty}^{\infty} A_{k,n} e^{jk\theta} e^{jn2\pi f_e t}, \quad (\text{B.6})$$

2D-FS has major implications in airgap flux density and in stator surface forces definition and analysis, because many calculations are based on 2D-FS coefficients. Moreover, some key features of these magnitudes are more easily deduced from the 2D-FS coefficients than from the functions themselves.

Coefficients index absolute value, i.e. $|n|$ and $|k|$, have an important physical meaning. The first one identifies the frequency of the temporal harmonic, while the second is related with the spatial mode (see sections 2.2.3 and 3.6.2).

For example, a coefficient $A_{2,-1}$ identifies a second order mode rotating at known angular speed πf_e . Some additional remarks should be given in order to achieve a deeper insight in the index meaning, because there also exists additional coefficient that share $|n|$ and $|k|$ values, e.g. $A_{2,1}$, $A_{-2,1}$ and $A_{-2,-1}$.

It is worthwhile to notice that property (B.3), associated with FS is still valid for 2D-FS. Therefore, taking into account that $A(\theta, t) \in \mathbb{R}$, (B.3) can be reformulated for the 2D case as

$$A(\theta, t) \in \mathbb{R} \quad \forall(\theta, t) \Leftrightarrow A_{k,n} = A_{-k,-n}^* \quad \forall(k, n). \quad (\text{B.7})$$

In conclusion, $A_{2,1}$ and $A_{-2,-1}$ are a pair referring to the same second radial mode at the same rotation speed. A typical associated question is “what is the different between the pair $A_{2,1}$ $A_{-2,-1}$ and the $A_{-2,1}$ $A_{2,-1}$ one, since both represent the same mode rotating at the same speed?”

The answer is that they rotate in opposite directions. This will be evident if (B.6) is rewritten in a “cosine series” form, taking into account that $A(\theta, t) \in \mathbb{R}$, i.e.

$$A(\theta, t) = A_{0,0} + 2 \sum_{k=1}^{\infty} \sum_{n=-\infty}^{\infty} |A_{k,n}| \cos(k\theta + n2\pi f_e t + \psi_{k,n}). \quad (\text{B.8})$$

It is evident that the sinusoid defined by a specific pair k and n rotates at constant speed $-(2\pi n f_e)/k$. Three cases are possible: first, if n and k have the same sign the speed is negative and the waveform is rotating clockwise; second, if n and k have opposite signs the speed is positive and the waveform is rotating counter-clockwise; third, if $n = 0$ the associated frequency is 0, i.e. the mode k is static and do not rotate at all. Figure B.1 schematically represents the waveforms associated to pairs $(k, n) = (2, 1)$ and $(k, n) = (2, -1)$.

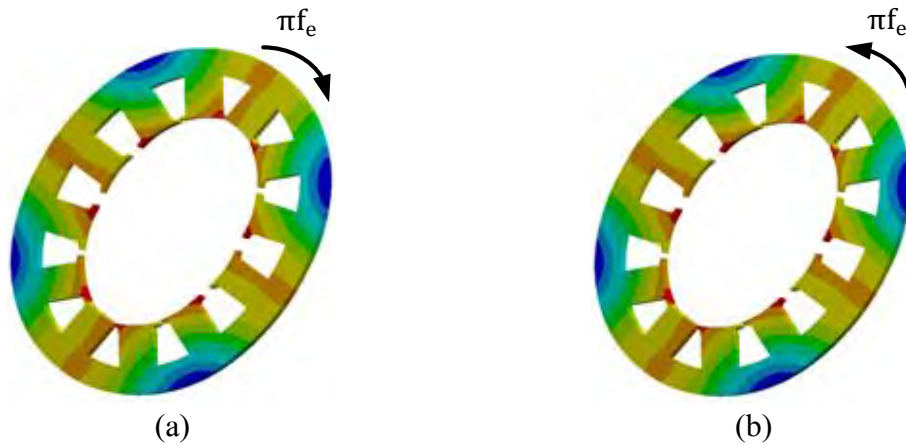


Figure B.1. Spatial mode 2 rotating at angular speed (πf_e) rad/s , (a) clockwise and (b) counter-clockwise.

It is worthwhile to notice that, in literature, it is common to find many texts that divide the “machines spatial harmonics” (i.e. the $A(\theta, t)$ single spatial FS coefficients) as a function of their rotating direction (i.e. clockwise or counter-clockwise) in an opaque and unclear manner. This is a direct consequence of the use of a simple FS where a 2D one is needed, so the resulting data are difficult to interpret in the best case. That is why in this work the 2D-FS approach, which integrates both, time, angular dependence and rotating direction, is preferred.

In order to illustrate these properties and provide some 2D-FS examples from both, airgap flux density and forces over the stator, the IkerMAQ analytical values for these magnitudes and their FS are represented and explained below.

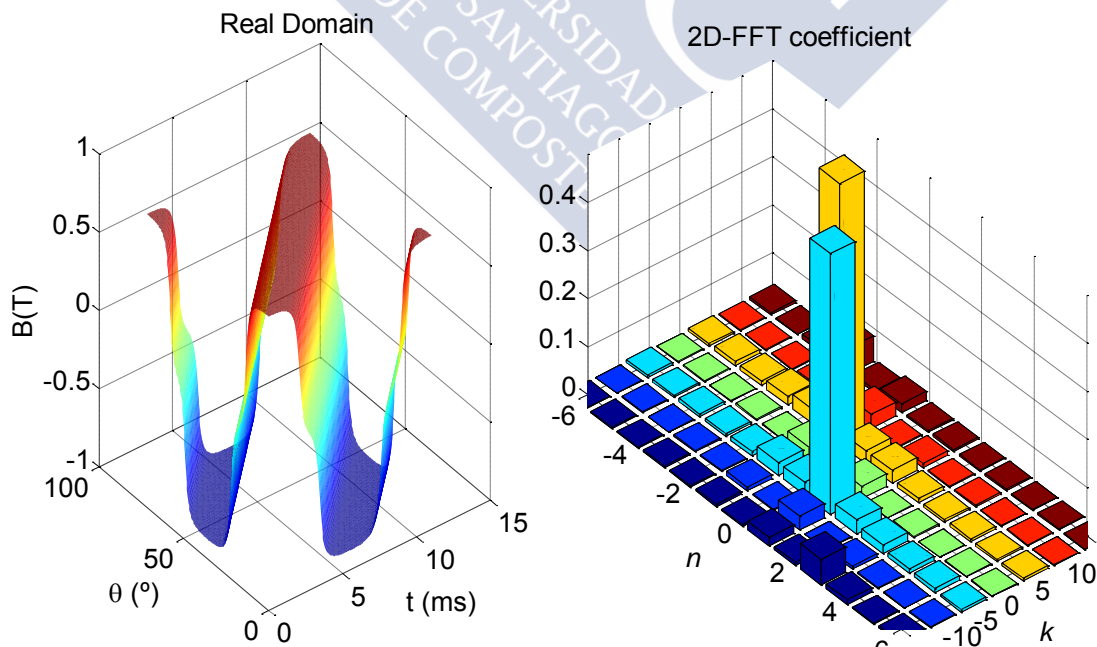


Figure B.2. IkerMAQ airgap magnets flux density, B_g^m , and its 2D-FS coefficients.

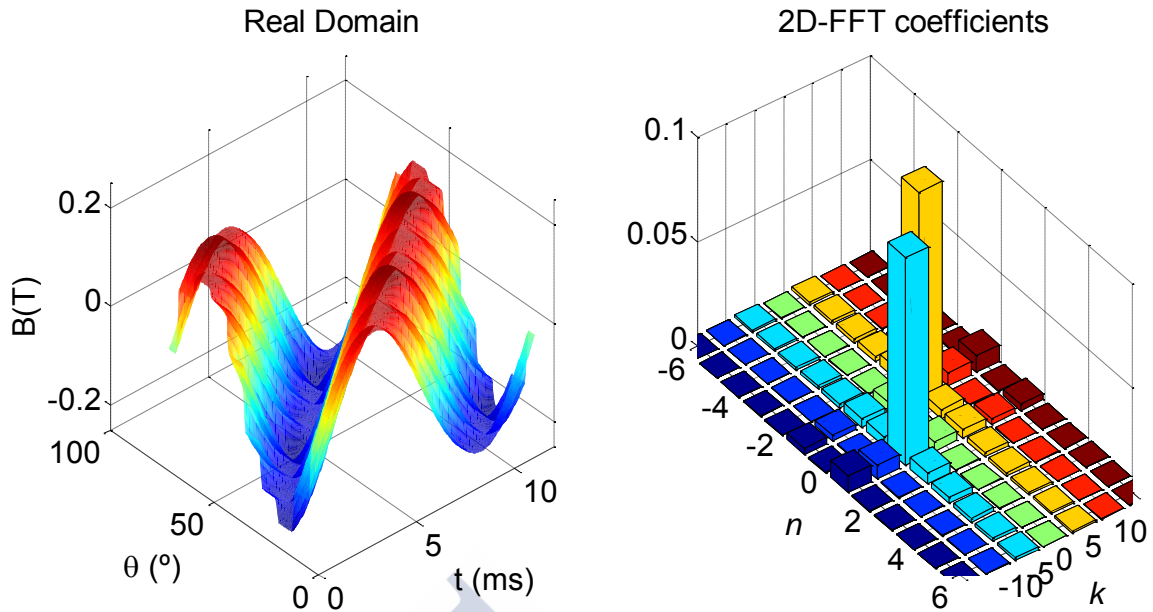


Figure B.3. IkerMAQ armature reaction, B_g^a , and its 2D-FS coefficients.

From Figure B.2 and Figure B.3 some important features of the airgap magnetic flux can be inferred. The first one is that, due to the fact that the inherent spatial periodicity is $2\pi/p$ (in this case $2\pi/5$) $B_{k,n}$ is null if k is not multiple of p . It is also clear that the magnets are rotating at a constant speed in the counter-clockwise direction and thus B_g^m time dependence is equal to the spatial one except for a variable scale factor (actually, this factor is equal to the pole pair number p).

Additionally, B_g^a “rotates” following B_g^m at the same speed. It is obvious that its temporal dependence is sinusoidal, because the current generating the magnetic fields has this property. However, its spatial dependence shows the typical stair form due to the abrupt field change when a slot opening is crossed.

Another characteristic that can be deduced from figures direct observation is that IkerMAQ is working in generator operation mode. This can be inferred because the magnets flux density leads and “guides” the armature reaction, i.e. the magnets induce a current in the wires whose magnetic field follows the inductor one. This can also be clearly seen in Figure B.4 which represents the total airgap magnetic induction. On the contrary, with IkerMAQ working in motor operation mode, the armature reaction leads the magnets magnetic field and, therefore, their movement.

Another important conclusion is that the main B_g^m (and, thus, B_g^a) harmonic is the $B_{p,-1}$ one. This is true even in fractional slot machines where $t_p \neq p$. This is always the main spatial-temporal harmonic storing most of the energy and enabling the electric-mechanical energy conversion. Other harmonics turning in the same direction (e.g. $B_{2p,-2}$, $B_{p,-2}$ and so on) play a minor role, while harmonics turning in the opposite direction (in the studied case, clockwise) usually have no relevance.

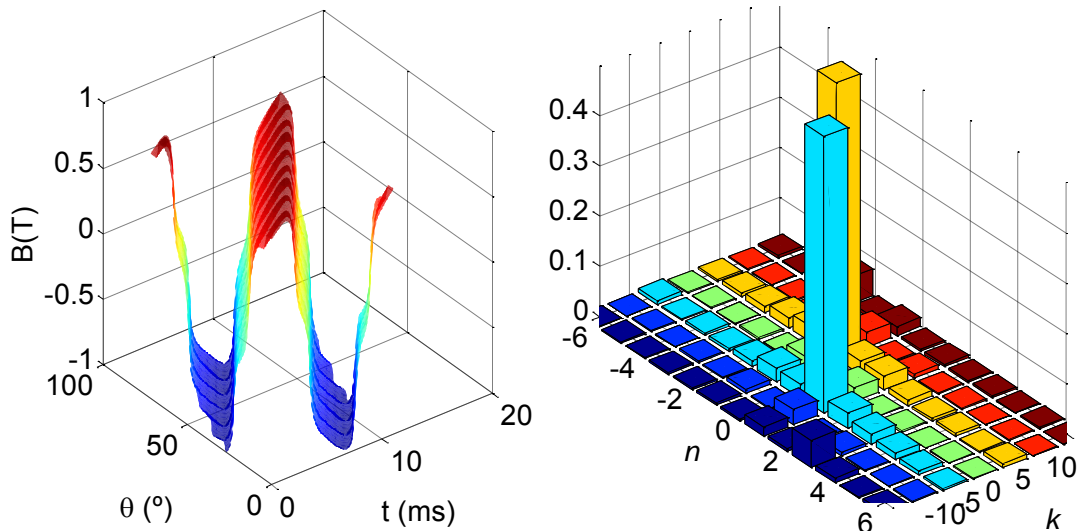


Figure B.4. IkerMAQ airgap total flux density, B_g , and its 2D-FS coefficients.

Figure B.5 shows the magnetic pressure over the stator teeth. It is interesting to notice that, due to its dependence with the square of the airgap flux density, the non-rotating breathing mode $F_{0,0}$ appears (associated with the static attraction that the magnets continuously exert over the stator ferromagnetic core). $F_{2p,-2}$ becomes the most important harmonic, while the $F_{2sp,-2s}$ harmonics (with $s \in \mathbb{N}$) acquire special relevance.

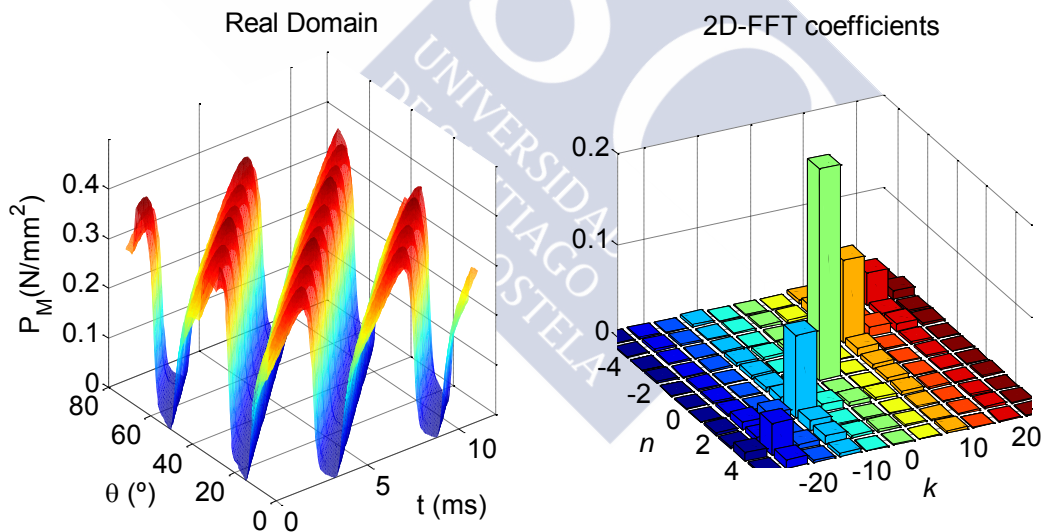
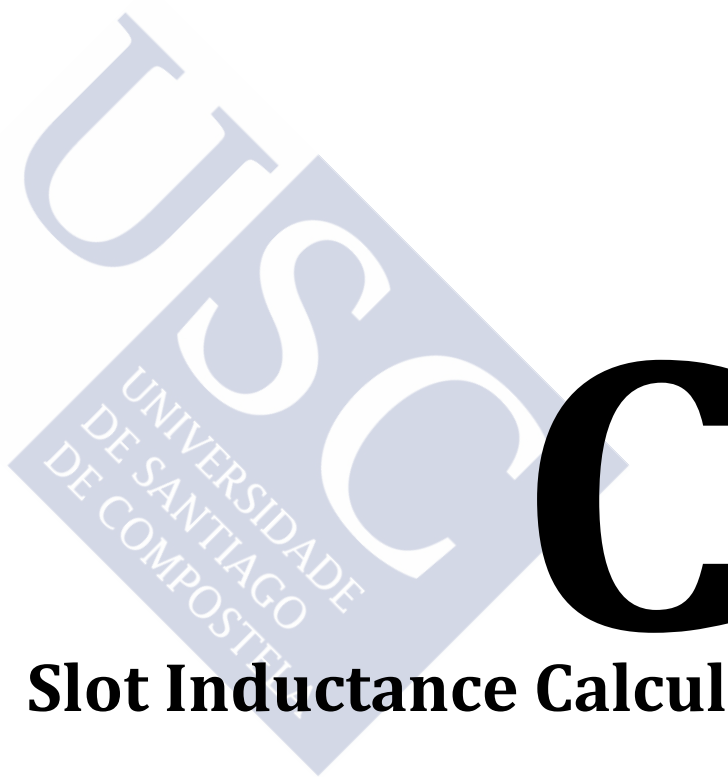


Figure B.5. IkerMAQ magnetic pressure over stator teeth, P_M , and its 2D-FS coefficients.



Slot Inductance Calculus



C.1 Slot Types

As it was exposed in section 3.3.1.2, the coils generate a magnetic field not only in the airgap and in the ferromagnetic cores but also in the same slots where they are wound. Since a magnetic field exists in the slots air and copper, a non-negligible inductance will appear, especially in the slots openings, as far as they are a low reluctance flux path.

This inductance presents a high dependence of the winding configuration (single or double layer) and of the slot geometry, whose multiple types are listed in [Pyrhönen 2008]; among them the most popular are the uniform and the non-uniform geometries. Figure C.1 shows the four types of basic slots as a function of their winding and geometry.

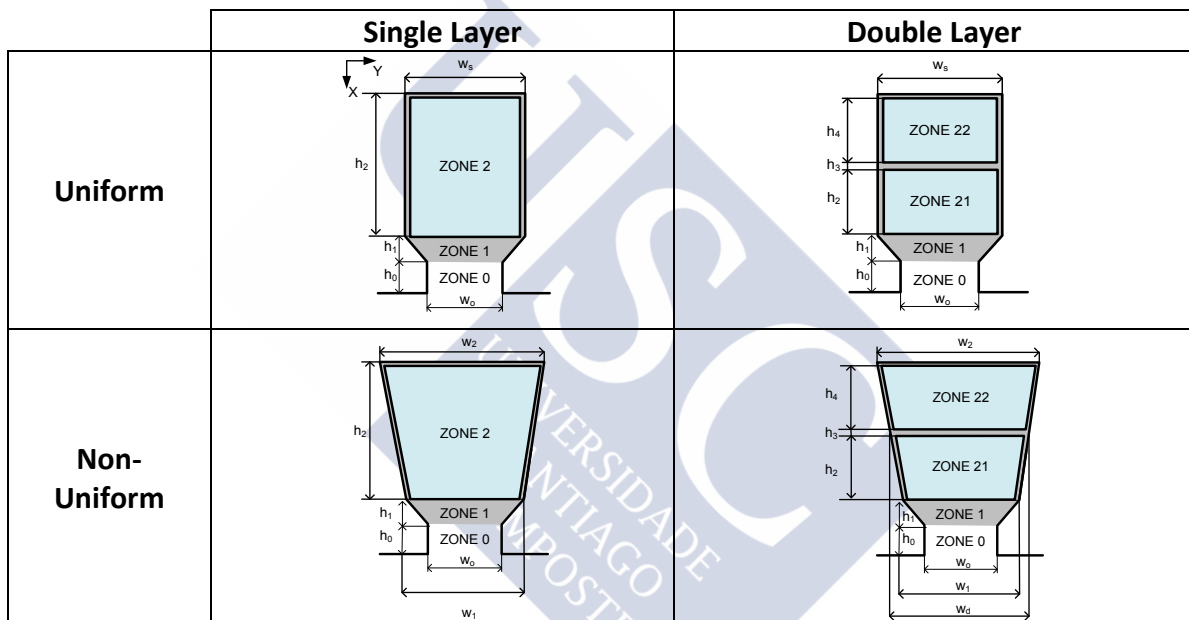


Figure C.1. Most popular slot types.

C.2 Analytical Method

The inductance of the four presented slot configurations can be calculated in a similar way. However, though the uniform geometry calculus can be easily found in many undergraduate books, at the best of the author’s knowledge, the non-uniform case has not been developed in detail and only rough, non-demonstrated approximations can be found (e.g. [Pyrhönen 2008]). That is why, in this appendix, a complete, detailed and proper inductance calculus of the four proposed configuration will be developed. An analytic model could be performed assuming the following approximations:

- It is supposed straight slot geometry, so the radial coordinate will be assimilated to the x-axis, and the tangential one will be projected on the y-axis (see Figure 3.20).

- It is supposed that the magnetic intensity field, \mathbf{H} , only has y-directed component and it only has x-dependence. The latter is a consequence of the former because $\nabla \cdot \mathbf{H} = 0$.
- As far as the ferromagnetic material is infinitely permeable H is considered to be null inside the ferromagnetic core.

Taking these approximations into account the magnetic field intensity will be obtained in the four exposed cases. Ampere's law is applied leading to:

$$\oint_C \mathbf{H} \cdot d\mathbf{l} = \int_y H_y dy = I_C \quad (\text{C.1})$$

where H_y is the y component of the vector \mathbf{H} , C is a curve that totally encloses an slot current I_C and $d\mathbf{l}$ its length differential (see Figure C.2). Since H is only no null in the inferior line of C (i.e. the line crossing the slot) only this path should be taken into account in order to compute the integral. Moreover, H_y has no y dependence, so (C.1) can be reduced to the product $H_y(x')l(x') = I_C(x')$.

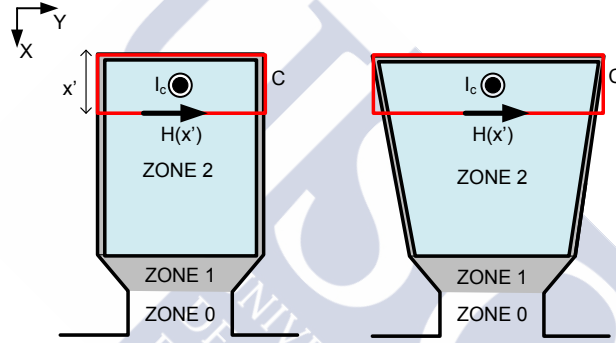


Figure C.2. Circular paths chosen in order to apply Ampere's law

Once $H_y(x)$ is known, the inductance could be calculated using its relation with the magnetic energy stored in the slot.

C.2.1 Uniform single-layer configuration

In this case the identity of stored magnetic energy leads to:

$$\frac{1}{2} L_s I^2 = \frac{1}{2} \mu_0 \int_V H_y^2 dV, \quad (\text{C.2})$$

where L_s is the inductance due to a single slot and V is the space region occupied by the slot. Applying Ampere's Law H_y in a single layer slot is equal to:

$$H_y(x) = \begin{cases} \frac{ZI}{w_s} \frac{x}{h_2} & x \leq h_2 \\ \frac{ZI}{w_s + (w_0 - w_s)(x - h_2)/h_1} & h_2 \leq x \leq h_1 + h_2 \\ \frac{ZI}{w_0} & h_1 + h_2 \leq x \leq h_0 + h_1 + h_2 \end{cases} \quad (\text{C.3})$$

where w_s is the slot width, w_0 is the slot opening (in meters), h_2 the effective slot height, h_1 and h_0 the slots opening heights and I the current flowing through it (see Figure C.1).

The inductance in each zone (see Figure 3.20) can be calculated from (C.2) and (C.3):

$$\begin{cases} L_2 = \mu_0 L_{Fe} Z^2 \frac{h_2}{3w_s} & \text{Zone 2} \\ L_1 = \mu_0 L_{Fe} Z^2 \frac{h_1 \ln(w_s/w_0)}{w_s - w_0} & \text{Zone 1} \\ L_0 = \mu_0 L_{Fe} Z^2 \frac{h_0}{w_0} & \text{Zone 0} \end{cases} \quad (C.4)$$

where L_{Fe} is the effective machine length and Z the number of turns within a coil. The total slot inductance will be given by

$$L_s = \mu_0 Z^2 L_{Fe} \left[\frac{h_2}{3w_s} + \frac{h_1}{w_s - w_0} \ln \left(\frac{w_s}{w_0} \right) + \frac{h_0}{w_0} \right]. \quad (C.5)$$

It should be noticed that the main component of L_s is generally provided by the slot opening, due to the low value of w_0 .

C.2.2 Uniform double-layer configuration

It is clear that, as far as two different coils are wound in the same slot, three different inductances will appear: the self-inductance of the “up” coil (L_{su}), the self-inductance of the “down” coil (L_{sd}) and the mutual inductance (L_{sm}). The three inductances can be deduced from the magnetic energy balance:

$$\frac{1}{2} L_{su} I_u^2 + \frac{1}{2} L_{sd} I_d^2 + L_{sm} I_u I_d = \frac{1}{2} \mu_0 \int_V H(x)^2 dV. \quad (C.6)$$

In this case, H_y calculated through Ampere’s law (C.1) leads to

$$H_y(x) = \begin{cases} \frac{Z I_u x}{w_s h_4} & x \leq h_4 \\ \frac{Z I_u}{w_s} & h_4 \leq x \leq \sum_{i=3}^4 h_i \\ \frac{Z I_u}{w_s} + \frac{Z I_d (x - \sum_{i=3}^4 h_i)}{h_2} & \sum_{i=3}^4 h_i \leq x \leq \sum_{i=2}^4 h_i \\ \frac{Z(I_u + I_d)}{w_s + (w_0 - w_s)(x - \sum_{i=2}^4 h_i)/h_1} & \sum_{i=2}^4 h_i \leq x \leq \sum_{i=1}^4 h_i \\ \frac{Z(I_u + I_d)}{w_0} & \sum_{i=1}^4 h_i \leq x \leq \sum_{i=0}^4 h_i. \end{cases} \quad (C.7)$$

where I_u and I_d are the current flowing through the coils in the “up” and in the “down” positions. A typical $H_y(x)$ waveform when $I_u = I_d$ is shown in Figure C.3.

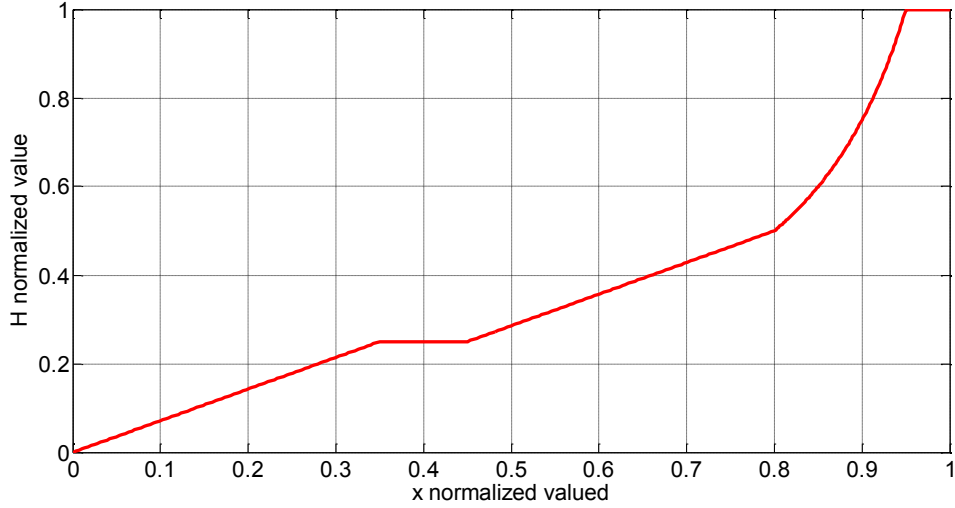


Figure C.3. Example of magnetic field intensity due to armature reaction.

Replacing equation (C.7) in (C.6) the following expressions are obtained:

$$L_{su} = \mu_0 L_{Fe} Z^2 \left(\frac{h_4}{3w_s} + \frac{h_2+h_3}{w_s} + \frac{h_1}{w_s - w_0} \ln \left(\frac{w_s}{w_0} \right) + \frac{h_0}{w_0} \right), \quad (C.8)$$

$$L_{sd} = \mu_0 L_{Fe} Z^2 \left(\frac{h_2}{3w_s} + \frac{h_1}{w_s - w_0} \ln \left(\frac{w_s}{w_0} \right) + \frac{h_0}{w_0} \right), \quad (C.9)$$

$$L_{sm} = \mu_0 L_{Fe} Z^2 \left(\frac{h_2}{2w_s} + \frac{h_1}{w_s - w_0} \ln \left(\frac{w_s}{w_0} \right) + \frac{h_0}{w_0} \right). \quad (C.10)$$

C.2.3 Non-uniform single-layer configuration

This case is very similar to the uniform single-layer configuration. Its main difference is that $H_y(x)$ expression is not so simple because the current enclosed by the circular curves (chosen in order to apply Ampere's Law, see Figure C.2) are no longer directly proportional to x , because the slot wide directly depends on the radius (i.e. on x).

This fact means that, although calculations are very similar to those explained in previous sections, they are not so simple and the final closed-form formulas are more cumbersome:

$$H_y(x) = \begin{cases} ZI \frac{(w_1 - w_2)x^2 + 2h_2w_2x}{h_2(w_1 + w_2)(x(w_1 - w_2) + w_2h_2)} & x \leq h_2 \\ \frac{ZI}{w_s + (w_0 - w_s)(x - h_2)/h_1} & h_2 \leq x \leq h_1 + h_2 \\ \frac{ZI}{w_0} & h_1 + h_2 \leq x \leq h_0 + h_1 + h_2. \end{cases} \quad (C.11)$$

Slot zones 0 and 1 have the same inductance expression as in the uniform case but zone 2 inductance is quite different. By tedious but straightforward computations the following expressions for zone 2 inductance can be obtained from (C.2):

$$L_2 = \frac{\mu_0 L_{Fe} Z^2 h_2}{(w_1 + w_2)^2} \left(\frac{w_1 + 3w_2}{4} - \frac{w_2^2}{2(w_2 - w_1)} - \frac{w_2^3}{(w_2 - w_1)^2} + \frac{w_2^4}{(w_2 - w_1)^3} \ln \left(\frac{w_2}{w_1} \right) \right) \quad (C.12)$$

Therefore, the total slot inductance will be given by

$$L_s = \mu_0 Z^2 L_{Fe} \left[\frac{h_2}{(w_1 + w_2)^2} \left(\frac{w_1 + 3w_2}{4} - \frac{w_2^2}{2(w_2 - w_1)} - \frac{w_2^3}{(w_2 - w_1)^2} + \frac{w_2^4}{(w_2 - w_1)^3} \ln \left(\frac{w_2}{w_1} \right) \right) + \frac{h_1}{w_1 - w_0} \ln \left(\frac{w_1}{w_0} \right) + \frac{h_0}{w_0} \right]. \quad (C.13)$$

C.2.4 Non-uniform double-layer configuration

As in the previous case, the non-uniform double layer configuration is very close to the uniform one. In fact, the calculation procedure is almost the same; the only difference is the complexity of the necessary integral calculus.

In this case $H_y(x)$, obtained applying (C.1), is given by

$$\left\{ \begin{array}{ll} ZI_u \frac{(w_d - w_2)x^2 + 2h_4 w_2 x}{h_4 (w_d + w_2)(x(w_d - w_2) + w_2 h_4)} & x \leq h_4 \\ \frac{ZI_u}{w_d + (w_d - w_2)(x - h_4)/h_4} & h_4 \leq x \leq \sum_{i=3}^4 h_i \\ \frac{ZI_u}{w_d + (w_1 - w_d)x/h_2} + ZI_d \frac{(w_1 - w_d)(x - \sum_{i=3}^4 h_i)^2 + 2h_2 w_d (x - \sum_{i=3}^4 h_i)}{h_2 (w_1 + w_d)((x - \sum_{i=3}^4 h_i)(w_1 - w_d) + w_d h_2)} & \sum_{i=3}^4 h_i \leq x \leq \sum_{i=2}^4 h_i \\ \frac{Z(I_u + I_d)}{w_1 + (w_0 - w_1)(x - \sum_{i=2}^4 h_i)/h_1} & \sum_{i=2}^4 h_i \leq x \leq \sum_{i=1}^4 h_i \\ \frac{Z(I_u + I_d)}{w_0} & \sum_{i=1}^4 h_i \leq x \leq \sum_{i=0}^4 h_i. \end{array} \right. \quad (C.14)$$

where I_u and I_d are the current flowing through the coil in the “up” and in the “down” position, respectively.

Replacing equation (C.14) in (C.6) the following expressions are obtained:

$$L_{su} = \mu_0 L_{Fe} Z^2 \left(\frac{h_4}{(w_d + w_2)^2} \left(\frac{w_d + 3w_2}{4} - \frac{w_2^2}{2(w_2 - w_d)} - \frac{w_2^3}{(w_2 - w_d)^2} + \frac{w_2^4}{(w_2 - w_d)^3} \ln \left(\frac{w_2}{w_d} \right) \right) + \frac{h_2 + h_3}{(w_d - w_1)} \ln \left(\frac{w_d}{w_1} \right) + \frac{h_1}{w_1 - w_0} \ln \left(\frac{w_1}{w_0} \right) + \frac{h_0}{w_0} \right), \quad (C.15)$$

$$L_{sd} = \mu_0 L_{Fe} Z^2 \left(\frac{h_2}{(w_1 + w_d)^2} \left(\frac{w_1 + 3w_d}{4} - \frac{w_d^2}{2(w_d - w_1)} - \frac{w_d^3}{(w_d - w_1)^2} + \frac{w_d^4}{(w_d - w_1)^3} \ln \left(\frac{w_d}{w_1} \right) \right) + \frac{h_1}{w_1 - w_0} \ln \left(\frac{w_1}{w_0} \right) + \frac{h_0}{w_0} \right), \quad (C.16)$$

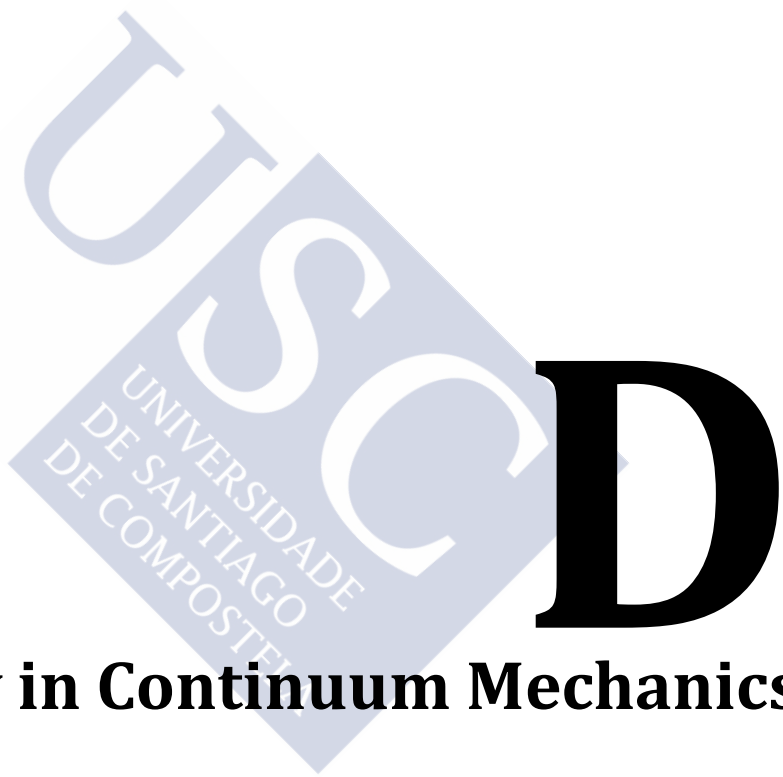
$$L_{sm} = \mu_0 L_{Fe} Z^2 \left(\frac{h_2}{(w_1 + w_d)} \left(0.5 - \frac{w_d}{(w_d - w_1)} + \frac{w_d^2}{(w_d - w_1)^2} \ln \left(\frac{w_d}{w_1} \right) \right) + \frac{h_1}{w_1 - w_0} \ln \left(\frac{w_1}{w_0} \right) + \frac{h_0}{w_0} \right). \quad (C.17)$$

C.3 Slot inductances

Finally, Table 3.3 contains the achieved results. These slots inductance estimations will be used as valid analytical approximation in order to model the PMSM electromagnetic behaviour.

Table C.1. Slot inductance analytical approach for different slot geometries.

Type	Geometry	Inductance
Single layer, uniform		$L_s = \mu_0 Z^2 L_e \left[\frac{h_2}{3w_s} + \frac{h_1}{w_s - w_0} \ln \left(\frac{w_s}{w_0} \right) + \frac{h_0}{w_0} \right] \quad (C.18)$
Single layer, non-uniform		$L_s = \mu_0 Z^2 L_e \left[\frac{h_0}{w_0} + \frac{h_1}{w_1 - w_0} \ln \left(\frac{w_1}{w_0} \right) + \frac{h_2}{(w_1 + w_2)^2} K_w \right] \quad (C.19)$ $K_w = \left(\frac{w_1 + 3w_2}{4} - \frac{w_2^2}{2(w_2 - w_1)} - \frac{w_2^3}{(w_2 - w_1)^2} + \frac{w_2^4}{(w_2 - w_1)^3} \ln \left(\frac{w_2}{w_1} \right) \right) \quad (C.20)$
Double layer, uniform		$L_{su} = \mu_0 L_e Z^2 \left(\frac{h_4}{3w_s} + \frac{h_2 + h_3}{w_s} + \frac{h_1}{w_s - w_0} \ln \left(\frac{w_s}{w_0} \right) + \frac{h_0}{w_0} \right) \quad (C.21)$ $L_{sd} = \mu_0 L_e Z^2 \left(\frac{h_2}{3w_s} + \frac{h_1}{w_s - w_0} \ln \left(\frac{w_s}{w_0} \right) + \frac{h_0}{w_0} \right) \quad (C.22)$ $L_{sm} = \left(\frac{h_2}{2w_s} + \frac{h_1}{w_s - w_0} \ln \left(\frac{w_s}{w_0} \right) + \frac{h_0}{w_0} \right) \quad (C.23)$
Double layer, non-uniform		$L_{su} = \mu_0 Z^2 L_e \left[\frac{h_0}{w_0} + \frac{h_1}{w_1 - w_0} \ln \left(\frac{w_1}{w_0} \right) + \frac{h_2 + h_3}{w_d - w_1} \ln \left(\frac{w_d}{w_1} \right) + \frac{h_4}{(w_d + w_2)^2} K_{wu} \right] \quad (C.24)$ $L_{sd} = \mu_0 Z^2 L_e \left[\frac{h_0}{w_0} + \frac{h_1}{w_1 - w_0} \ln \left(\frac{w_1}{w_0} \right) + \frac{h_2}{(w_1 + w_2)^2} K_{wd} \right] \quad (C.25)$ $L_{sm} = \mu_0 Z^2 L_e \left[\frac{h_0}{w_0} + \frac{h_1}{w_1 - w_0} \ln \left(\frac{w_1}{w_0} \right) + \frac{h_4}{(w_d + w_1)} K_{wm} \right] \quad (C.26)$ $K_{wu} = \left(\frac{w_d + 3w_2}{4} - \frac{w_2^2}{2(w_2 - w_d)} - \frac{w_2^3}{(w_2 - w_d)^2} + \frac{w_2^4}{(w_2 - w_d)^3} \ln \left(\frac{w_2}{w_d} \right) \right) \quad (C.27)$ $K_{wd} = \left(\frac{w_1 + 3w_d}{4} - \frac{w_d^2}{2(w_d - w_1)} - \frac{w_d^3}{(w_d - w_1)^2} + \frac{w_d^4}{(w_d - w_1)^3} \ln \left(\frac{w_d}{w_1} \right) \right) \quad (C.28)$ $K_{wm} = \left(0.5 - \frac{w_d}{w_d - w_1} + \frac{w_d^2}{(w_d - w_1)^2} \ln \left(\frac{w_d}{w_1} \right) \right) \quad (C.29)$



Elasticity in Continuum Mechanics



In order to expose a more exhaustive and general analysis of an elastic body structural behaviour this appendix is included. The general principles of continuum mechanics will be briefly introduced in order to reach in a more rigorous way the results used in section 3.6.1. For more detailed insight into continuum mechanics see, for instance, [Gurtin 1981, Chandrasekharaiah 1994].

As it was explained in 3.6.1, two main relations are necessary in order to describe a body vibratory behaviour, the first one is a force balance and the second the link between the aforementioned forces and the displacements. The first requirement is fulfilled through the Cauchy stress tensor and the momentum equation, while the second is established through material constitutive laws (e.g. in case of elastic bodies through Hooke's law).

D.1 Cauchy Stress Tensor

The key factor in order to characterize the forces acting over a continuum medium is the Cauchy stress tensor. Hence, in this section it will be briefly introduced.

It is considered a set of forces, volumetric and superficial, acting over a continuum medium. In an arbitrary instant t a particle is located at point x . Let S be an oriented surface passing through x , and let \mathbf{n} be one of its two unit normal vectors at x . Surface S divides the medium in two regions that are noted as $+$ and $-$ with vector \mathbf{n} pointing to $+$ (see Figure D.1).

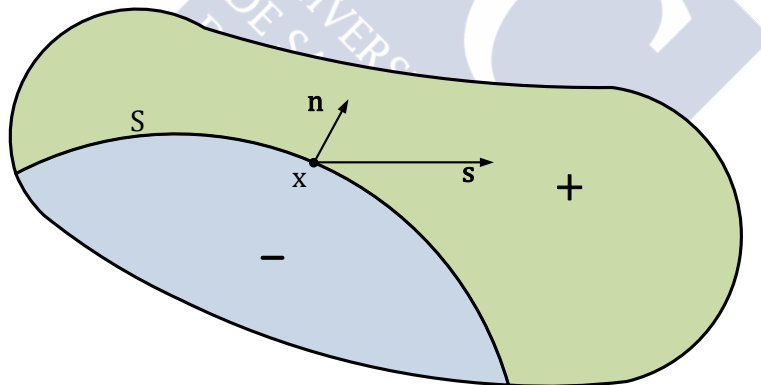


Figure D.1. Example of forces density on a body internal surface.

The Cauchy hypothesis establishes that the force surface density exerted by the $+$ region on the $-$ one at point x and time t , only depends on \mathbf{n} and not on S . It will be denoted by $\mathbf{s}(x, t, \mathbf{n})$ in order to highlight this dependence.

The Cauchy theorem establishes that it is possible to define a symmetric tensor field, $\boldsymbol{\sigma}(x, t)$ such that

$$\mathbf{s}(x, t, \mathbf{n}) = \boldsymbol{\sigma}(x, t) \mathbf{n}, \quad (\text{D.1})$$

moreover,

$$\rho(\mathbf{x}, t) \left(\frac{\partial \mathbf{v}(\mathbf{x}, t)}{\partial t} + (\nabla \mathbf{v}(\mathbf{x}, t)) \mathbf{v}(\mathbf{x}, t) \right) = \nabla \cdot \boldsymbol{\sigma}(\mathbf{x}, t) + \mathbf{f}(\mathbf{x}, t), \quad (\text{D.2})$$

where $\rho(\mathbf{x}, t)$ is the material density, $\mathbf{f}(\mathbf{x}, t)$ is the volumetric force density (e.g. the gravity force among others) and $\mathbf{v}(\mathbf{x}, t)$ the velocity of the particle located at point \mathbf{x} at instant t .

General motion equation (D.2) can be approximated for the particular case where only “small” deformations are present (e.g. a vibrating PMSM stator). In this case (D.2) leads to

$$\rho \frac{\partial^2 \mathbf{u}}{\partial t^2} = \nabla \cdot \boldsymbol{\sigma} + \mathbf{f}, \quad (\text{D.3})$$

where \mathbf{u} is the particle displacement field.

In 2D-cylindrical coordinates (D.3) yields

$$-r f_r = \frac{\partial \sigma_{rr}}{\partial r} r + \sigma_{rr} - \sigma_{\theta\theta} + \frac{\partial \sigma_{r\theta}}{\partial \theta} - \frac{\partial^2 u_r}{\partial t^2} \rho r, \quad (\text{D.4})$$

$$-r f_\theta = \frac{\partial \sigma_{\theta\theta}}{\partial \theta} + \frac{\partial \sigma_{r\theta}}{\partial r} r + 2\sigma_{r\theta} - \frac{\partial^2 u_\theta}{\partial t^2} \rho r. \quad (\text{D.5})$$

where subscripts r and θ denotes the component of the tensor or vector. In other words, $\sigma_{r\theta}$ could be interpreted as the element (1,2) in its matrix form.

It should be noticed that equations (D.4) and (D.5) exactly match equations (3.258) and (3.260) obtained by other means in section 3.6.1.

D.2 Lineal Elastic Bodies: Hooke's Law

Solid elastic bodies have a constitutive law which imposes that Cauchy stress tensor is function of the particle movement gradient. This relation is usually non-linear but, under certain hypothesis that will be exposed below, it could be linearized.

Assuming that the body deformation is “small” and that its material is isotropic (i.e. its mechanical behaviour is the same in all spatial directions) it can be proved that two parameters are enough in order to establish its elastic constitutive law. More precisely,

$$\boldsymbol{\sigma}(\mathbf{x}, t) = 2\mu \boldsymbol{\varepsilon}(\mathbf{x}, t) + \lambda \text{tr}[\boldsymbol{\varepsilon}(\mathbf{x}, t)] \mathbf{I}, \quad (\text{D.6})$$

where μ and λ are the Lamé's coefficients of the material, \mathbf{I} is the identity tensor, tr is the function trace (i.e. $\text{tr}[\boldsymbol{\varepsilon}] = \boldsymbol{\varepsilon} \cdot \mathbf{I}$) and $\boldsymbol{\varepsilon}$ is the infinitesimal strain tensor which is defined from the displacement field \mathbf{u} as

$$\boldsymbol{\varepsilon} = \nabla \mathbf{u} + (\nabla \mathbf{u})^T, \quad (\text{D.7})$$

where the superscript T denotes the transposed tensor.

It should be noticed that, choosing a system of coordinates, ε_{ij} represents the differential elongation in the i -axis direction respect to an infinitesimal displacement in the j -axis. In other words, ε_{ii} represents compression or traction deformations, while ε_{ij} with $i \neq j$ implies a shear deformation.

Equation (D.6) is the Hooke's law for isotropic, linear, elastic media. It can be reversed in order to obtain $\boldsymbol{\varepsilon}$ as a function of $\boldsymbol{\sigma}$:

$$\boldsymbol{\varepsilon} = \frac{1}{2\mu} \boldsymbol{\sigma} - \frac{\lambda}{2\mu(2\mu + 3\lambda)} \text{tr}[\boldsymbol{\sigma}] \mathbf{I}. \quad (\text{D.8})$$

For the purposes of this thesis, it is useful to particularize (D.8) to a PMSM stator geometry. More precisely, it is assumed that the stator structural behaviour is very close to that presented by a thin cylindrical shell.

Hence, cylindrical coordinates will be used and a 2D approximation will be performed, neglecting the stresses in the z -direction (i.e. $\sigma_{zz} = \sigma_{z\theta} = \sigma_{zr} = 0$, plane stress assumption). In this case (D.8) becomes,

$$\begin{bmatrix} \varepsilon_{rr} \\ \varepsilon_{\theta\theta} \\ \varepsilon_{r\theta} \\ \varepsilon_{zz} \end{bmatrix} = \begin{bmatrix} \frac{1}{2\mu} - \frac{\lambda}{2\mu(2\mu+3\lambda)} & -\frac{\lambda}{2\mu(2\mu+3\lambda)} & 0 \\ -\frac{\lambda}{2\mu(2\mu+3\lambda)} & \frac{1}{2\mu} - \frac{\lambda}{2\mu(2\mu+3\lambda)} & 0 \\ 0 & 0 & \frac{1}{2\mu} \\ -\frac{\lambda}{2\mu(2\mu+3\lambda)} & -\frac{\lambda}{2\mu(2\mu+3\lambda)} & 0 \end{bmatrix} \begin{bmatrix} \sigma_{rr} \\ \sigma_{\theta\theta} \\ \sigma_{r\theta} \end{bmatrix}. \quad (\text{D.9})$$

It is quite common to express the material elastic properties with other pair of parameters instead of Lamé's coefficients. They are the Young modulus (E) and the Poisson's coefficient (ν). They are usually preferred in mechanical engineering because of their clearer physical meaning. Their equivalence with Lamé's coefficients is

$$E = \frac{\mu(2\mu + 3\lambda)}{\mu + \lambda}, \quad (\text{D.10})$$

$$\nu = \frac{\lambda}{2(\mu + \lambda)}. \quad (\text{D.11})$$

In mechanical engineering literature it is common to find (D.9) written as function of the Young modulus and Poisson's coefficient, i.e.

$$\begin{bmatrix} \varepsilon_{rr} \\ \varepsilon_{\theta\theta} \\ \varepsilon_{r\theta} \end{bmatrix} = \frac{1}{E} \begin{bmatrix} 1 & -\nu & 0 \\ -\nu & 1 & 0 \\ 0 & 0 & 1 + \nu \end{bmatrix} \begin{bmatrix} \sigma_{rr} \\ \sigma_{\theta\theta} \\ \sigma_{r\theta} \end{bmatrix}, \quad (\text{D.12})$$

which exactly match equation (3.264), previously presented in Chapter 3.

The previous equations are applied in section 3.6.1 in order to characterize the radial modes that will cause most of the PMSM radiated sound.





E

Resumen



E.1 Objetivos de la tesis

Actualmente la mayoría de metodologías de diseño de máquinas eléctricas utilizadas a nivel industrial se basan en conocimiento empírico previamente adquirido y en reglas heurísticas que requieren una elevada experiencia personal por parte del diseñador y cuya exactitud depende, principalmente, de datos de otros diseños realizados con anterioridad [Amrhein 2013]. La mayoría de los modelos empleados para sustentar estas metodologías son de naturaleza mayoritariamente electromagnética y otros estudios, tales como el térmico o el vibro-acústico se tienen en cuenta en forma de imprecisas figuras de mérito en el mejor de los casos.

Por otro lado, la bibliografía académica ofrece una cantidad limitada de trabajos relacionados con el diseño de máquinas de eléctricas y la mayoría de ellos consisten en propuestas que sólo contemplan aspectos parciales del problema global, más centradas en mejorar un diseño preexistente que en abordar un nuevo problema desde sus inicios, diseñando una máquina completamente adaptada a unas nuevas especificaciones [Goss 2013].

Ambos enfoques, tanto el industrial como el más académico, ofrecen sólo una primera aproximación que suele requerir de ulteriores algoritmos de ensayo y error, usualmente usando métodos numéricos con un alto coste computacional. Esto conlleva que estas metodologías sólo sean aplicables a aplicaciones muy conocidas o a diseños de bajas prestaciones debido a que su naturaleza poco sistemática hace muy difícil la extrapolación de resultados a nuevos diseños o a aplicaciones muy exigentes con requerimientos referentes a su miniaturización o limitaciones de la radiación acústica emitida.

Es evidente que las máquinas eléctricas son sistemas complejos donde una gran cantidad de fenómenos físicos se producen simultáneamente interactuando entre ellos. Por tanto, se hace necesario un estudio interdisciplinar que tenga en cuenta este acoplamiento entre diferentes dominios físicos de forma que pueda dar soporte a una metodología de diseño rápida, precisa, robusta y optimizada.

En concordancia con lo anteriormente expuesto el principal objetivo de esta tesis es el desarrollo de una metodología de diseño optimizada y multidisciplinar para máquinas eléctricas de imanes permanentes (PMSM por sus siglas en inglés).

Para alcanzar este ambicioso objetivo global, se han definido las siguientes metas parciales:

- 1) Revisión de la bibliografía y redacción de un estado del arte en metodologías de diseño y modelado de máquinas eléctricas (especialmente PMSM), centrándose en aquellas que incorporasen algoritmos de optimización y/o modelados multidisciplinarios.
- 2) Modelado multifísico de PMSM incluyendo su dominio eléctrico, magnético, térmico, estructural y vibro-acústico. Su característica más importante es

que utiliza exclusivamente aproximaciones analíticas, la mayoría basadas en series de Fourier. Este modelo no sólo es multidisciplinar sino que además es modular y rápido, lo que le convierte en un candidato ideal para ser utilizado en conjunción con un algoritmo de optimización. Un resumen de este modelo ha sido presentado en la conferencia ICEM 2014 [Rodríguez 2014].

- 3) Desarrollo de una nueva metodología de diseño multidisciplinar para PMSM, para ello se acoplan las diferentes partes del modelo anteriormente mencionado, incluyendo un algoritmo de optimización por encima de ellas.
- 4) Por último se diseñará un prototipo de máquina eléctrica de tal manera que el modelado quede validado en un caso real, medido en laboratorio.

E.2 Máquina Síncrona de Imanes Permanentes

La energía eléctrica es uno de los soportes de la civilización moderna. En el contexto actual, las máquinas eléctricas son de capital importancia dado que la mayoría de las centrales generadoras de energía, desde las plantas nucleares a los molinos eléctricos, necesitan una máquina eléctrica trabajando como generador. Por otro lado, se estima que el 65% de la energía eléctrica producida es consumida por motores eléctricos en un entorno industrial [Rahman 2013].

El uso generalizado de máquinas eléctricas en la industria a lo largo de todo el siglo XX ha supuesto un activo campo de investigación que, a su vez, ha llevado a una importante mejora y a la madurez de esta tecnología. Hasta los años 50 los motores de continua eran la única opción disponible a coste razonable debido a que posibilitaban un control exacto y preciso; sin embargo, su uso tenía muchos inconvenientes, como los altos requisitos de mantenimiento, su gran tamaño y su escasa robustez.

Durante los años 80 los avances en electrónica permitieron un control preciso de las máquinas de inducción. En tan solo una década remplazaron a las máquinas de continua en la mayoría de las aplicaciones industriales debido a su tamaño más reducido, su mayor robustez, y, sobre todo, su menor coste de mantenimiento, debido sobre todo a la ausencia de conmutador y de escobillas [Novotny 1996]. La Figura E.1 muestra un una máquina de inducción y otra de continua.

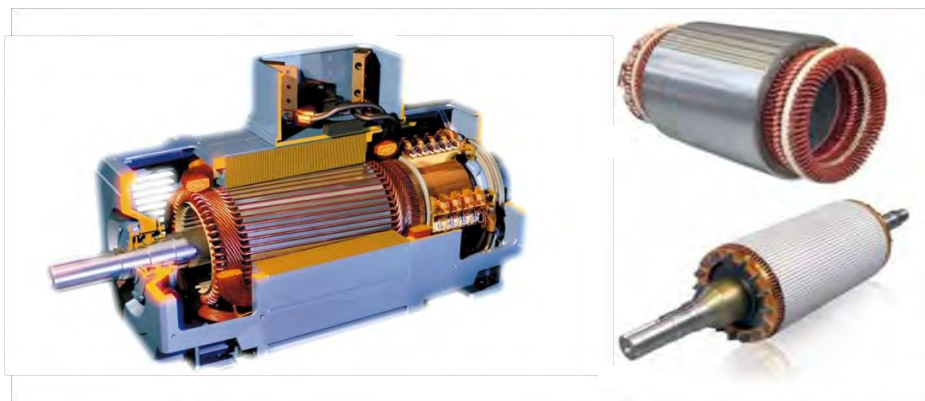


Figura E.1. Motores de ABB. A la izquierda un motor de continua, a la derecha el rotor y el estátor de una máquina de inducción. [Fotos propiedad de la corporación ABB]

La existencia de PMSMs operativas ha sido documentada en fechas tan tempranas como los años 30 y se ha localizado la presencia de diseños prácticos en la literatura científica en 1953 [Ginsberg 1953]. No obstante, no es hasta los años 90 cuando las PMSMs se convirtieron en una opción factible para su utilización industrial a gran escala, gracias a la comercialización de los potentes imanes de neodimio-hierro-boro (NdFeB).

Comparados con las máquinas de inducción, las PMSMs presentan remarcables ventajas tales como la ausencia de pérdidas en el rotor, un mayor factor de potencia, mayor densidad de potencia y mejor eficiencia [Islam 2009]. Además, al igual que las máquinas de inducción, las PMSMs no necesitan escobillas lo que permite eliminar el mantenimiento asociado a ellas. Estas buenas características hacen que las PMSMs se empleen en una gran diversidad de aplicaciones tales como industria aeronáutica, elevación, vehículo eléctrico o generación eléctrica, dónde suponen una alternativa económica y técnicamente viable frente a las máquinas de inducción.

No obstante, dos desventajas clave de las PMSMs son la principal razón de que las máquinas de inducción continúen siendo la opción preferida en la mayoría de aplicaciones industriales: el alto coste de los imanes y el riesgo de que se desmagneticen de forma permanente ante agresiones externas durante su funcionamiento; en la práctica esto significa que estas máquinas son más caras y menos robustas que sus homólogas de inducción. Además, existen ciertos inconvenientes asociados a que los imanes sean “permanentes” y que mantengan su flujo tanto si la máquina está siendo alimentada por una fuente externa como si no; esto significa que durante condiciones de fallo puede resultar difícil detener el movimiento de la máquina, incluso tras haberle retirado la alimentación.

Pese a los inconvenientes expuestos hay una clara tendencia hacia una mayor presencia de las PMSMs tanto en aplicaciones domésticas como industriales lo que supone que éstas máquinas se han convertido en una tecnología emergente y en un activo campo de estudio científico, como demuestran la gran cantidad de publicaciones que se han dedicado a este tema durante los últimos años.

Por las razones anteriormente expuestas serán las máquinas síncronas de imanes permanentes las elegidas para llevar a cabo la metodología de diseño que dará soporte a esta tesis. Durante este resumen se introducirán de forma sucinta los principios de funcionamiento y la clasificación de las PMSM así como los principales retos a los que se enfrentan sus diseñadores.

E.2.1 Principio de Funcionamiento

Tanto los motores como los generadores eléctricos operan bajo el mismo principio de funcionamiento: la interacción entre campos magnéticos. En la mayoría de los casos (excepto en algunas topologías, basadas en disposiciones geométricas de reluctancia variable) existen dos campos electromagnéticos que interactúan entre sí, siendo el

resultado principal de dicha interacción la conversión de energía eléctrica en mecánica o viceversa, almacenando dicha energía en forma de campo magnético como paso intermedio en la transformación.

La topología más simple de motor consiste en dos imanes permanentes externos que se mantienen en posiciones fijas (constituyendo el estátor) y otro imán interno con libertad de rotar sobre su propio eje (formando el rotor), tal y como muestra la Figura E.2 (a). Por supuesto, el imán interno tratará de alinearse con los otros dos, generando par en el proceso, debido al bien conocido principio físico de que polos de diferente signo se atraen mientras que polos de igual signo se repelen. El movimiento acabará en el momento en que el imán interior se alinee con los dos externos en una posición de equilibrio.

El siguiente paso es sustituir el imán interior por un electroimán cuya polaridad pueda invertirse a conveniencia, sólo con cambiar la dirección de la corriente continua que fluye a través de él. De esta forma es posible cambiar la polaridad del imán cuando éste haya alcanzado una posición de equilibrio, prolongando el movimiento indefinidamente. La Figura E.2 (b) muestra un electroimán sometido a las condiciones previamente explicadas. Cabe destacar la presencia de escobillas y un conmutador que permiten, respectivamente, la propagación de corriente en el rotor durante su movimiento e invertir la dirección de las corrientes.

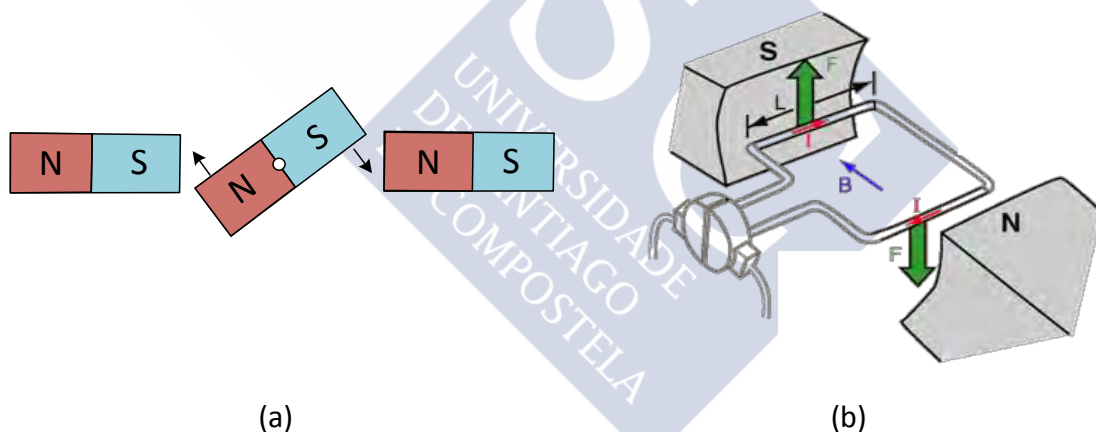


Figura E.2. Principios básicos del funcionamiento de un motor; (a) sólo con imanes permanentes y (b) con un electroimán en el rotor.

En el caso de las PMSMs los principios de funcionamiento son los mismos que en el de los ejemplos explicados pero con algunas relevantes modificaciones: generalmente hay un número mayor de imanes (llamados polos) y, comúnmente, se sitúan en el rotor y no en el estátor, de forma que se pueda evitar la necesidad de escobillas. Por otro lado, la corriente inyectada suele ser alterna polifásica, con una o más bobinas correspondientes a cada fase (ver Figura E.3) y no una sola bobina alimentada con corriente continua.

Como principio general, durante un funcionamiento normal del motor, el campo magnético provocado por las bobinas del estátor (que, de hecho, constituyen un electroimán) dirige el movimiento del rotor, haciendo que los imanes roten. Este

movimiento se produce porque el campo magnético generado por los imanes se encuentra especialmente retrasado respecto al del estátor un ángulo constante ϕ que, normalmente, se encuentra cerca de los 90° de forma que se maximice la transferencia de energía entre estátor y rotor, esto es, que se genere el máximo par posible.

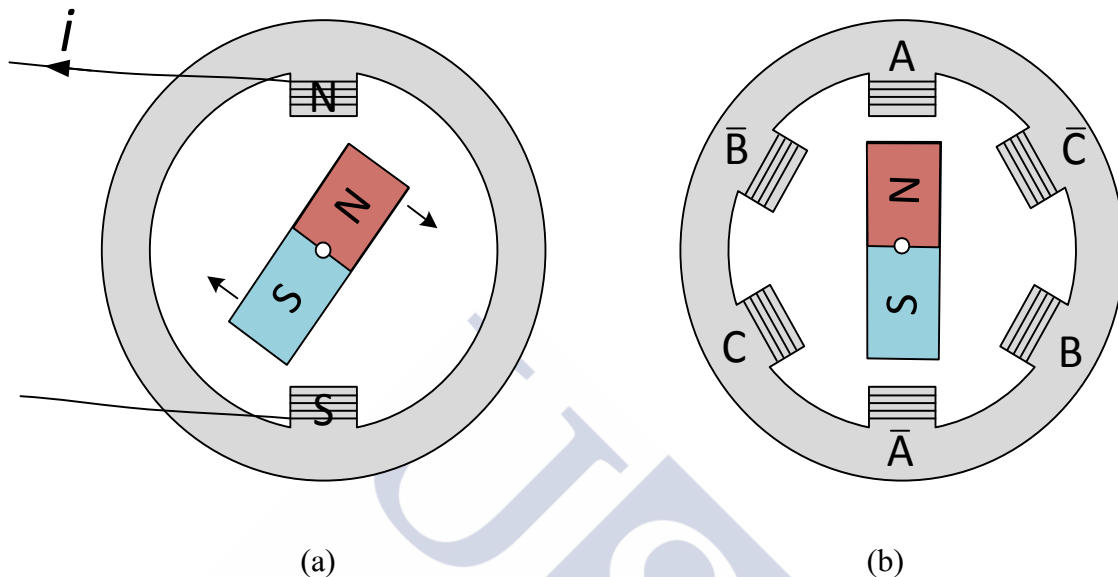


Figura E.3. Configuraciones PMSMs; (a) ejemplo con una sola bobina y (b) ejemplo con una configuración trifásica.

E.2.2 Clasificación y Estructura Interna de los PMSMs

La estructura clásica de una PMSM consiste en una parte móvil (rotor) donde se insertan los imanes permanentes y una parte fija o estátor donde se sitúan las bobinas, generalmente en ranuras practicadas en el cuerpo del estátor. Ambos, estátor y rotor, están contruidos con materiales ferromagnéticos de forma que el flujo magnético se dirija en la dirección deseada. Entre el estátor y el rotor se sitúa una fina capa de aire llamada entrehierro donde se almacena la mayor parte de la energía magnética.

Estátor, rotor y entrehierro configuran el circuito magnético de la máquina. La Figura E.4 (a) muestra una representación 2D de una PMSM radial y con imanes de montaje superficial cuyo flujo magnético fluye radialmente a través del entrehierro, presentado sólo dependencia de la coordenada tangencial (esto es, de θ); este hecho permite realizar el estudio magnético únicamente en una sección transversal de la PMSM. El esquema simplificado de Figura E.4 (a) representa a una PMSM genérica, como la mostrada en Figura E.4 (b), en la que pueden apreciarse sus partes más importantes, tales como las cabezas de ranura, la carcasa o el eje del rotor.

Existen una gran cantidad de topologías PMSM cuya clasificación se realiza atendiendo a la situación de los imanes en el rotor, la posición relativa del rotor o su forma de bobinado. La clasificación que se adjunta en este resumen es la más común y general pero no es exhaustiva, fundamentalmente porque algunas topologías han sido

inventadas recientemente, desafiando las viejas clasificaciones y generando otras nuevas.

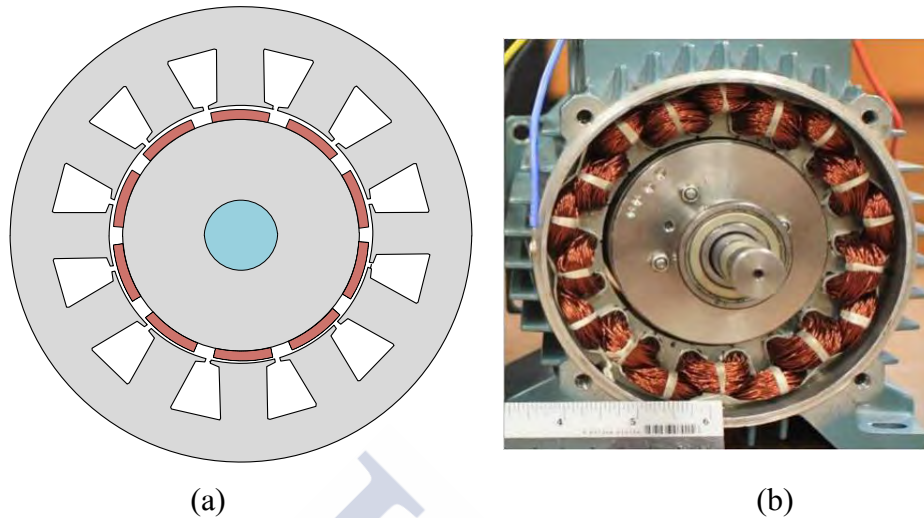


Figura E.4. (a) Esquema de una sección 2D de una PMSM radial, (b) PMSM radial.

E.2.2.1 Posición Relativa del Rotor

El rotor puede tener dos posiciones diferentes respecto del estátor: interior o exterior. La Figura E.5 muestra ambas alternativas.

La principal ventaja del rotor exterior es que permite un diseño de máquina con un diámetro de entrehierro mayor para un mismo volumen total. Esto es debido a que, generalmente, la altura de los imanes es bastante menor que la altura total del estátor (que viene impuesta por el tamaño de las ranuras). Teniendo en cuenta que la potencia total de la PMSM es, en términos generales, proporcional al cuadrado de su diámetro de entrehierro los diseños de rotor exterior suelen gozar de una mayor densidad de potencia [Kazmin 2008]. Otra ventaja es que los imanes están más próximos a la superficie exterior de la máquina lo que les permite evacuar el calor más fácilmente y evitar el riesgo de desmagnetización causada por las altas temperaturas.

La principal desventaja asociada a esta configuración es el confinamiento del estátor. Es en el estátor dónde la mayor parte de las pérdidas se concentran; si a esta elevada disipación de potencia se le suma la dificultad de evacuación debido a la separación entre el estátor y la superficie exterior de la máquina el resultado es un elevado calentamiento, lo que supone un grave problema de diseño. Es esta dificultad el principal motivo de que la inmensa mayoría de PMSMs presenten una configuración de rotor interior.

Otro problema de menor importancia asociado a una configuración de rotor exterior es que el rotor está más expuesto lo que puede redundar en fallos o rupturas durante el funcionamiento de la máquina.

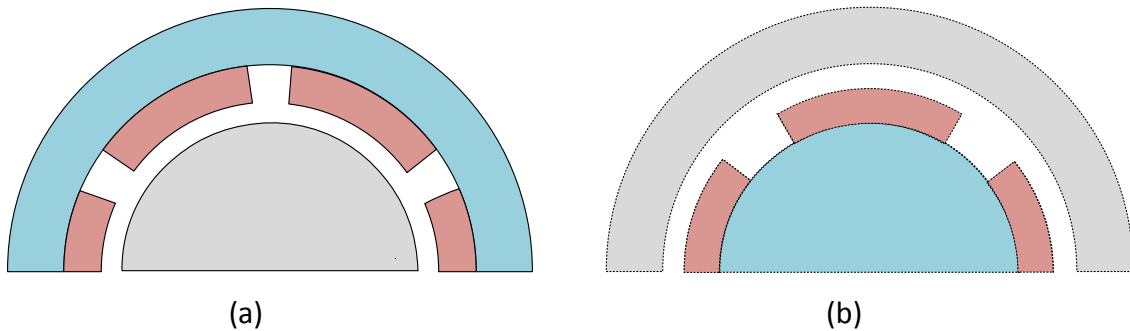


Figura E.5. (a) Configuración de rotor exterior. (b) Configuración de rotor interior.

E.2.2.2 Situación de los Imanes en el Rotor

En términos generales, existen tres configuraciones principales bien conocidas en la literatura: la PMSM de imanes superficiales (SPMSM), la PMSM de imanes interiores (IPMSM) y la PMSM de imanes insertados. En esta última topología los imanes están embebidos en el rotor, pero muy cercanos al entrehierro. En términos prácticos, las máquinas de imanes insertados son más similares a las de imanes interiores y sus características son relativamente similares. La Figura E.6 muestra dos ejemplos de rotor, uno de una SPMSM y otro de una IPMSM.



Figura E.6. (a) Rotor de una SPMSM [Wu 2015], (b) rotor de una IPMSM [Rahman 2013].

La característica más definitoria de una IPMSM es que presenta una fuente adicional de par llamada par reluctante, que no está directamente provocada por la interacción de los campos magnéticos del rotor y del estator sino por la tendencia de los electroimanes del estator de alinearse con aquellas regiones del rotor con una menor reluctancia. La consecuencia obvia de este efecto es las configuraciones IPMSM presentan una mayor densidad de par y, por tanto, una mayor densidad de potencia que una SPMSM.

Otra consecuencia importante de que los imanes se encuentren situados dentro del rotor es que el entrehierro puede ser de mucha menor longitud dado que los imanes

ya no serían parte de él [Kazmin 2008]. Esto suele suponer que la inducción magnética es mayor que en las SPMSM causando una mayor saturación magnética en el rotor y un mayor riesgo de desmagnetización permanente de los imanes.

Por lo tanto, comparados con las SPMSM, la topología IPMSM presenta una mayor densidad de potencia y, debido a su confinamiento en el rotor, los imanes están más protegidos de esfuerzos mecánicos locales y posibles rupturas. Sin embargo, también presenta los inconvenientes de un proceso de manufactura del rotor bastante más complicado, mayor rizado de par, más saturaciones locales, mayores pérdidas en el núcleo del rotor así como mayor calentamiento de los imanes.

La conclusión final es a la hora de escoger entre ambas topologías la mejor opción dependerá de las exigencias concretas de la aplicación para la que será diseñada.

E.2.2.3 Tipo de Bobinado

A la hora de cablear el estátor existen dos opciones principales (ver Figura E.7): bobinados concentrados o distribuidos. En bobinados concentrados las bobinas se cablean en ranuras consecutivas, mientras que en los distribuidos se cablean de forma que se maximice el flujo magnético abrazado por el rotor, sin importar la distancia existente entre las ranuras conectadas.

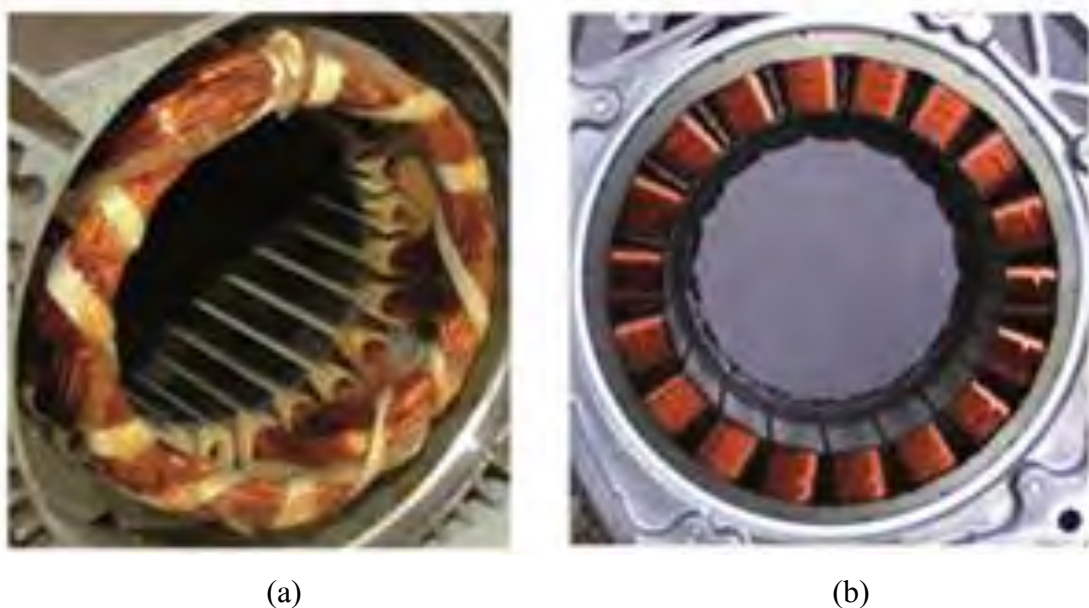


Figura E.7. Comparación entre máquinas de bobinado (a) distribuido y (b) concentrado.

Las principales ventajas de los bobinados concentrados sobre los distribuidos están relacionadas con sus cabezas de bobinas de menor longitud. Cabezas más cortas conllevan menos pérdidas en el cobre, menos volumen total de máquina y procesos de fabricación más sencillos y baratos.

Sin embargo, la fuerza electromotriz inducida por los imanes en las bobinas tendrá mayor cantidad de armónicos lo que conlleva mayores rizados de par y de corriente

que los causados por el bobinado distribuido [Patel 2013]. Por otro lado, la cantidad de ruido emitido y las fuerzas magnéticas sobre el estátor suelen ser mayores en máquinas de bobinado concentrado [Chen 2014].

E.3 Diseño de una SPMSM Radial: el Punto de Partida

La topología seleccionada para implementar el modelo analítico y multifísico así como una posterior metodología a la que dará soporte es una PMSM de rotor interior e imanes de montaje superficial debido a que es la topología de motores más frecuente y, por tanto, la más común en aplicaciones industriales, con buenas características de funcionamiento y un proceso de manufactura maduro.

Las principales características y ventajas de esta topología en particular y de las PMSM en general respecto a otras opciones competidoras se listan a continuación.

- Alta densidad de par y densidad de potencia.
- Pérdidas de rotor muy bajas. Alta eficiencia.
- Se evita el uso de conmutadores o escobillas.
- Factor de potencia más alto que el de las máquinas de inducción.
- Rotor más sencillo y robusto ya que se hace innecesaria la presencia de oquedades internas o una corona de barras en su estructura.
- Niveles de radiación sonora y vibraciones más bajas que las de las máquinas de inducción o las de reluctancia variable.

Debido a las ventajas que reportan estas características, las SPMSM radiales son la opción escogida para la realización de la metodología de diseño.

A continuación una se bosquejará el modelo multifísico utilizado en la metodología, de forma que se obtenga una visión general del proceso de diseño que será pormenorizadamente explicado en la tesis. La Figura E.8 muestra un diagrama simplificado que constituye la base de dicho modelo.

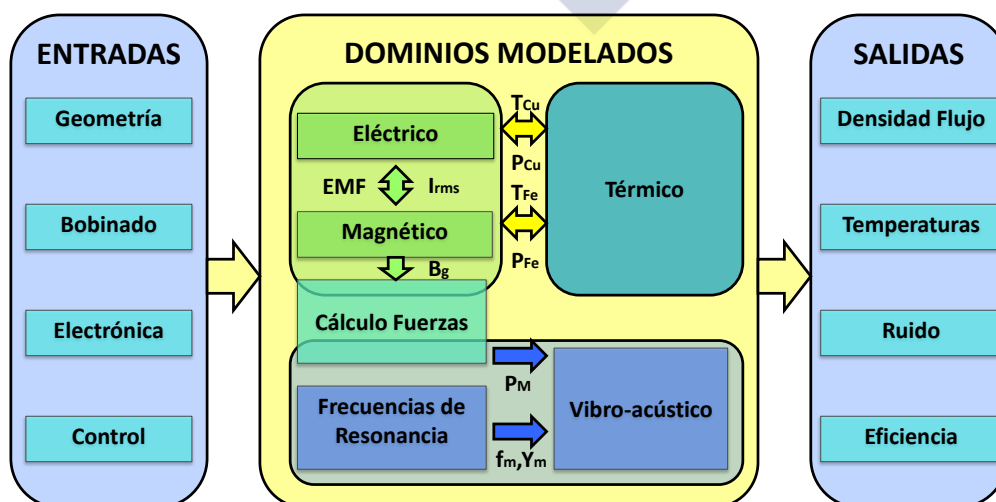


Figura E.8. Diagrama de bloques y relación entre los diferentes dominios modelados.

Tal y como ya se ha explicado con objeto de ahorrar el mayor tiempo de cálculo posible, los modelos serán analíticos. Dichos modelos requieren de las simplificaciones que se listan a continuación.

- 1) Se considera que el material ferromagnético del rotor y el estátor es infinitamente permeable.
- 2) El perfil de magnetización de los imanes será bien radial bien paralelo.
- 3) La máquina tendrá m fases sin neutro y se considerará una distribución especial equilibrada del bobinado.
- 4) Sin pérdida de generalidad, la máquina se considera girando en sentido anti horario, por tanto los dientes y las ranuras se numerarán de 1 a Q siguiendo dicho sentido de avance (ver Figura E.9.).

La primera simplificación es la más importante de todas porque es la que puede significar una mayor pérdida de exactitud si los núcleos ferromagnéticos presentan un elevado nivel de saturación. De hecho ésta es la principal limitación de los métodos analíticos, pero el error puede minimizarse asegurando que el material ferromagnético no se encuentra en la zona de saturación durante el normal funcionamiento de la máquina.

Es importante notar que las variables de entrada son de diferente naturaleza según el tratamiento que la metodología hace de ellas.

Especificaciones de diseño: Establecidas por el usuario para dar respuesta a las necesidades de una aplicación concreta. Una vez se ha iniciado el proceso de diseño no pueden ser modificadas, ni siquiera entre diferentes iteraciones del algoritmo de optimización. Ejemplos de especificaciones de diseño son la velocidad del rotor, la potencia mecánica nominal o el número de fases de la máquina.

Constantes físicas: Son constantes físicas conocidas y, por tanto, están inicialmente establecidas y no pueden ser modificadas, ni por el usuario ni por el algoritmo de optimización. Dos ejemplos serían la permeabilidad magnética del vacío o las propiedades físicas de los materiales usados en la construcción de la máquina.

Variables de diseño: Son las variables fundamentales que definen un diseño completo. Serán modificadas entre las diferentes iteraciones del algoritmo de optimización de forma que se alcancen los mejores resultados posibles en términos de una o varias funciones objetivo que suelen estar relacionada con la eficiencia y/o el coste de la máquina.

Se adjunta la Figura E.9 para facilitar una mejor comprensión de las variables geométricas utilizadas durante la tesis. Dicha figura muestra una sección de la PMSM así como la vista detallada de una de sus ranuras.

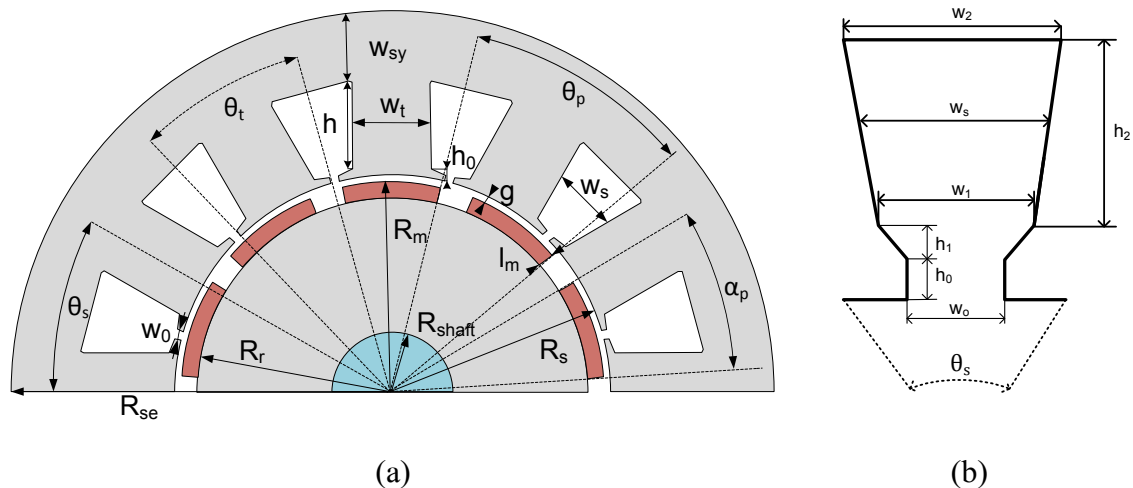


Figura E.9. (a) Principales dimensiones de una PMSM; (b) detalle de una ranura.

Con objeto de validar la metodología de diseño, así como para obtener una herramienta para realizar diseños PMSM de utilidad práctica se ha elaborado una herramienta software programada en Matlab®. Los resultados facilitados por esta novedosa herramienta se han comparado con los obtenidos utilizando programas comerciales que calculan campos magnéticos mediante el uso de métodos numéricos.

E.4 Estructura de la Tesis

La tesis se dividirá de la forma siguiente:

En el primer capítulo se expandirán muchos de los conceptos contenidos en este resumen detallándose los objetivos del trabajo, el contexto del problema y el punto de partida de la tesis. También se incluirá una breve introducción al modo de funcionamiento de las máquinas de imanes permanentes, las diferentes topologías que puede presentar y su evolución histórica.

El capítulo 2 muestra el estado del arte y las principales contribuciones técnicas y científicas hechas durante los últimos años en el modelado y diseño de PMSM, prestando especial atención a las metodologías interdisciplinarias y usuarias de algoritmos de optimización.

El capítulo 3 explica los modelos físicos implementados, mostrando los resultados obtenidos y demostrando su utilidad, exactitud y precisión a través de comparaciones con los datos arrojados por software comercial que utiliza métodos numéricos (FLUX2D®, ANSYS® y Motor-CAD®).

Más concretamente, la primera parte está dedicada al modelado electromagnético y su influencia en la generación de par y potencia mecánica, así como una estimación de la eficiencia general y la definición de figuras de mérito. Posteriormente se introducirá el dominio térmico, modelado como una red de parámetros concentrados. Finalmente, se detalla una aproximación analítica que representa el comportamiento estructural y vibro-acústico de la máquina.

En el capítulo 4 se incluye una validación experimental a través de un prototipo diseñado ad hoc en IK4-Ikerlan: IkerMAQ (Q45p5), una PMSM de 75 kW. Se detallarán las condiciones experimentales y los resultados obtenidos serán comparados con aquellos calculados por los modelos explicados durante el capítulo 3.

Una vez que los modelos se han validado durante el capítulo 4, el capítulo 5 explica su aplicación en la implementación de una metodología de diseño totalmente analítica, holística, original y optimizada. Para dar soporte a dicha metodología se ha programado una herramienta en Matlab®, válida para la realización de diseños PMSM reales.

Finalmente, el capítulo 6 recoge las conclusiones y las contribuciones de esta tesis, así como las propuestas para futuras líneas de investigación.



Bibliography

[Agamloh 2013] Agamloh, E.B.; Cavagnino, A., "High efficiency design of induction machines for industrial applications," Electrical Machines Design Control and Diagnosis (WEMDCD), 2013 IEEE Workshop on , vol., no., pp.33,46, 11-12 March 2013

[Ait-Hammouda 2005] Ait-Hammouda,A., "Pré-dimensionnement et étude de sensibilité vibro-acoustique de machines à courant alternatif et à vitesse variable" Ph.D. dissertation, Laboratoire d'Electricité et d'Electronique de Puissance de Lille, École Centrale de Lille, 2005

[Almandoz 2008] Almandoz, G., "Metodología avanzada de diseño para máquinas multipolares de imanes permanentes, orientada a la aplicación" Ph.D. dissertation, Mondragón Goi Eskola Polik teknikoa, Mondragón Unibertsitatea 2008

[Amdouni 2012] Amdouni, I.; Amraoui, L.E.; Gillon, F.; Benrejeb, M.; Brochet, P., "Optimal design approach developed for permanent magnet motors," Electrical Machines (ICEM), 2012 XXth International Conference on , vol., no., pp.1374,1379, 2-5 Sept. 2012

[Amrhein 2013] Amrhein, M.; O'Connell, T.C.; Wells, J.R., "An integrated design process for optimized high-performance electrical machines," Electric Machines & Drives Conference (IEMDC), 2013 IEEE International , vol., no., pp.847,854, 12-15 May 2013

[Anwar 2000] Anwar, M. N.; Husain, I., "Radial force calculation and acoustic noise prediction in switched reluctance machines," Industry Applications, IEEE Transactions on , vol.36, no.6, pp.1589,1597, Nov/Dec 2000

[Anyuan 2010] Anyuan Chen; Nilssen, R.; Nysveen, A., "Performance Comparisons Among Radial-Flux, Multistage Axial-Flux, and Three-Phase Transverse-Flux PM Machines for Downhole Applications," Industry Applications, IEEE Transactions on , vol.46, no.2, pp.779,789, March-april 2010

[Arnold 2015] On line document. Arnold Magnetic Technologies. "N40H datasheet", <http://www.arnoldmagnetics.com/WorkArea/DownloadAsset.aspx?id=5034>. Consulted 19/05/2015

[Atallah 2000] Atallah, K.; Howe, D.; Mellor, P.H.; Stone, D.A., "Rotor loss in permanent-magnet brushless AC machines," *Industry Applications, IEEE Transactions on*, vol.36, no.6, pp.1612,1618, Nov/Dec 2000

[Aydin 2015] Aydin, E.; Yingjie Li; Aydin, I.; Timur Aydemir, M.; Sarlioglu, B., "Minimization of torque ripples of interior permanent magnet synchronous motors by particle swarm optimization technique," in *Transportation Electrification Conference and Expo (ITEC), 2015 IEEE*, vol., no., pp.1-6, 14-17 June 2015

[Bermúdez 2005] Bermúdez, A.; "Continuum Thermomechanics". Birkhäuser Verlag, *Progress in Mathematical Physics*, Vol. 43, 2005

[Bermúdez 2011] Bermúdez, A.; Pena, F., "Galerkin lumped parameter methods for transient problems", *Numerical methods in Engineering, International Journal for*, vol. 87, Issue 10, pp. 943,961, September 2011

[Bermúdez 2014] Bermúdez, A.; Salgado, P.; Gómez, D., "Mathematical Models and Numerical Simulation in Electromagnetism". Springer, series: UNITEXT, Vol. 74, 2014

[Bertotti 1988] Bertotti, Giorgio, "General properties of power losses in soft ferromagnetic materials," *Magnetics, IEEE Transactions on*, vol.24, no.1, pp.621,630, Jan 1988

[Besnerais 2008] Le Besnerais, J., "Réduction du bruit audible d'origine magnétique dans les machines asynchrones alimentées par MLI – règles de conception silencieuse et optimisation multi-objectif–" Ph.D. dissertation, Laboratoire d'Electricité et d'Electronique de Puissance de Lille, École Centrale de Lille, 2008

[Besnerais 2009] Le Besnerais, J.; Lanfranchi, V.; Hecquet, M.; Brochet, P., "Optimal Slot Numbers for Magnetic Noise Reduction in Variable-Speed Induction Motors," *Magnetics, IEEE Transactions on*, vol.45, no.8, pp.3131,3136, Aug. 2009

[Besnerais 2010] Le Besnerais, J.; Lanfranchi, V.; Hecquet, M.; Brochet, P., "Characterization and Reduction of Audible Magnetic Noise Due to PWM Supply in Induction Machines," *Industrial Electronics, IEEE Transactions on*, vol.57, no.4, pp.1288,1295, April 2010

[Besnerais 2015] Le Besnerais, J., "Vibroacoustic Analysis of Radial and Tangential Air-Gap Magnetic Forces in Permanent Magnet Synchronous Machines," in *Magnetics, IEEE Transactions on*, vol.51, no.6, pp.1-9, June 2015

[Bettayeb 2010] Bettayeb, A.; Jannot, X.; Vannier, J. -C, "Analytical calculation of rotor magnet eddy-current losses for high speed IPMSM," Electrical Machines (ICEM), 2010 XIX International Conference on , vol., no., pp.1,6, 6-8 Sept. 2010

[Bianchi 2006] Bianchi, N.; Dai Pre, M., "Use of the star of slots in designing fractional-slot single-layer synchronous motors," Electric Power Applications, IEE Proceedings - , vol.153, no.3, pp.459,466, 1 May 2006

[Boglietti 2003] Boglietti, A.; Cavagnino, A.; Lazzari, M.; Pastorelli, M., "Predicting iron losses in soft magnetic materials with arbitrary voltage supply: an engineering approach," Magnetics, IEEE Transactions on , vol.39, no.2, pp.981,989, Mar 2003

[Boglietti 2008] Boglietti, A.; Cavagnino, A.; Staton, D., "Determination of Critical Parameters in Electrical Machine Thermal Models," Industry Applications, IEEE Transactions on , vol.44, no.4, pp.1150,1159, July-aug. 2008

[Boglietti 2009] Boglietti, A.; Cavagnino, A.; Staton, D.; Shanel, Martin; Mueller, M.; Mejuto, C., "Evolution and Modern Approaches for Thermal Analysis of Electrical Machines," Industrial Electronics, IEEE Transactions on , vol.56, no.3, pp.871,882, March 2009

[Bossavit 2011] Bossavit, A., "Virtual power principle and Maxwell's tensor: which comes first?" The International Journal for Computation and Mathematics in Electrical and Electronic Engineering, Vol. 30 Iss: 6, pp.1804 – 1814, 2011.

[Bossavit 2014] Bossavit, A., "On Forces in Magnetized Matter," Magnetics, IEEE Transactions on , vol.50, no.2, pp.229,232, Feb. 2014

[Bracikowski 2012] Bracikowski, N.; Hecquet, M.; Brochet, P.; Shirinskii, S.V., "Multiphysics Modeling of a Permanent Magnet Synchronous Machine by Using Lumped Models," Industrial Electronics, IEEE Transactions on , vol.59, no.6, pp.2426,2437, June 2012

[Carlson 2012] Carlson, R.; Wurtz, F.; Voltolini, H., "Sizing and optimization models: Design of a set of two permanent magnet generators," Electrical Machines (ICEM), 2012 XXth International Conference on , vol., no., pp.1358,1363, 2-5 Sept. 2012

[Cassimere 2009] Cassimere, B.N.; Sudhoff, S.D., "Population-Based Design of Surface-Mounted Permanent-Magnet Synchronous Machines," Energy Conversion, IEEE Transactions on , vol.24, no.2, pp.338,346, June 2009

[Chandrasekharaiah 1994] Chandrasekharaiah D.S., Debnath, L.; "Continuum Mechanics". Academic Press Inc., 1994

[Chen 2002] Yicheng Chen; Pillay, P., "An improved formula for lamination core loss calculations in machines operating with high frequency and high flux density excitation," Industry Applications Conference, 2002. 37th IAS Annual Meeting. Conference Record of the , vol.2, no., pp.759,766 vol.2, 13-18 Oct. 2002

[Chen 2014] Xiao Chen; Jiabin Wang; Patel, V.I., "A Generic Approach to Reduction of Magnetomotive Force Harmonics in Permanent-Magnet Machines With Concentrated Multiple Three-Phase Windings," in Magnetics, IEEE Transactions on , vol.50, no.11, pp.1-4, Nov. 2014

[Cho 2000] Dong-Hyeok Cho; Hyun-Kyo Jung; Tae-Kyung Chung; Cheol-Gyun Lee, "Design of a short-time rating interior permanent magnet synchronous motor using a niching genetic algorithm," Magnetics, IEEE Transactions on , vol.36, no.4, pp.1936,1940, Jul 2000

[Comanescu 2003] Comanescu, Mihai; Keyhani, A.; Min Dai, "Design and analysis of 42-V permanent-magnet generator for automotive applications," Energy Conversion, IEEE Transactions on , vol.18, no.1, pp.107,112, Mar 2003

[Custódio 2011] Custódio, A.L.; Madeira, J.F.A.; Vaz A. I. F.; and Vicente, L.N., "Direct multisearch for multiobjective optimization", SIAM Journal on Optimization, vol. 21, pp. 1109,1140, 2011

[Dong 2014] Jianning Dong; Yunkai Huang; Long Jin; Baocheng Guo; Heyun Lin; Jiyong Dong; Ming Cheng; Hui Yang, "Electromagnetic and Thermal Analysis of Open-Circuit Air Cooled High-Speed Permanent Magnet Machines With Gramme Ring Windings," in Magnetics, IEEE Transactions on , vol.50, no.11, pp.1-4, Nov. 2014

[Dorrell 2006] Dorrell, D.G.; Staton, D.A.; McGilp, M.I., "Design of Brushless Permanent Magnet Motors - A Combined Electromagnetic and Thermal Approach to High Performance Specification," IEEE Industrial Electronics, IECON 2006 - 32nd Annual Conference on , vol., no., pp.4853,4858, 6-10 Nov. 2006

[Duan 2013-a] Yao Duan; Ionel, D.M., "A Review of Recent Developments in Electrical Machine Design Optimization Methods With a Permanent-Magnet Synchronous Motor Benchmark Study," Industry Applications, IEEE Transactions on , vol.49, no.3, pp.1268,1275, May-June 2013

[Duan 2013-b] Yao Duan; Qin Sun; Ionel, D.M., "Methods for studying the pareto-fronts in multi-objective design optimization problems of electrical machines," Energy Conversion Congress and Exposition (ECCE), 2013 IEEE , vol., no., pp.5013,5018, 15-19 Sept. 2013

[Ede 2007] Ede, J.D.; Atallah, K.; Jewell, G.W.; Wang, J.B.; Howe, D., "Effect of Axial Segmentation of Permanent Magnets on Rotor Loss in Modular Permanent-Magnet Brushless Machines," Industry Applications, IEEE Transactions on , vol.43, no.5, pp.1207,1213, Sept.-oct. 2007

[Elosegui 2008] Elosegui, I.; Egana, I.; Fontan, L.; Garcia Rico, A.; Martinez-Iturralde, M., "Fast sizing and simulation of multipole radial flux permanent magnet synchronous machines," Power Electronics, Electrical Drives, Automation and Motion, 2008. SPEEDAM 2008. International Symposium on , vol., no., pp.1445,1450, 11-13 June 2008

[El-Refaie 2004] EL-Refaie, A.M.; Harris, N.C.; Jahns, T.M.; Rahman, K.M., "Thermal analysis of multibarrier interior PM synchronous Machine using lumped parameter model," Energy Conversion, IEEE Transactions on , vol.19, no.2, pp.303,309, June 2004

[Fadriansyah 2012] Fadriansyah, T.; Strous, T. D.; Polinder, H., "Axial segmentation and magnets losses of SMPM machines using 2D FE method," Electrical Machines (ICEM), 2012 XXth International Conference on , vol., no., pp.577,581, 2-5 Sept. 2012

[Favi 2011] Favi, C.; Germani, M.; Marconi, M.; Mengoni, M.; Tirabassi, A., "EROD: New collaborative design platform for developing energy efficient electric motors," Electric Machines & Drives Conference (IEMDC), 2011 IEEE International , vol., no., pp.59,64, 15-18 May 2011

[Fiedler 2010] Fiedler, J.O.; Kasper, K.A.; De Doncker, R.W., "Calculation of the Acoustic Noise Spectrum of SRM Using Modal Superposition," Industrial Electronics, IEEE Transactions on , vol.57, no.9, pp.2939,2945, Sept. 2010

[Gago 2002] Gago-Ribas, Emilio, "Señales y Sistemas Escalares Unidimensionales de Variable Real". GR Editores S.L., Serie Introducción y Análisis General Señales y Sistemas de Variable Continua, Vol. ST-I, León 2002

[García 2014] García, A., "Optimal Design of Medium-Frequency High-Power Converters". Ph.D. dissertation, Université de Lausanne, 2014

[Gieras 2002] Gieras, J., Wing, M.; "Permanent Magnet Motor Technology". ,Marcel Dekker, Inc., 2002

[Gieras 2006] Gieras, J., Wang C., Lai J.; "Noise of polyphase electric motors". ,US: CRC Press, 2006

[Ginsberg 1953] Ginsberg, David; Misenheimer, Leo J., "Design Calculations for Permanent-Magnet Generators [includes discussion]," Power Apparatus and Systems, Part III. Transactions of the American Institute of Electrical Engineers , vol.72, no.2, pp., Jan. 1953

[Girgis 1979] Girgis, R. S.; Verma, S. P., "Resonant Frequencies and Vibration Behaviour of Stators of Electrical Machines as Affected by Teeth, Windings, Frame and Laminations," Power Apparatus and Systems, IEEE Transactions on , vol.PAS-98, no.4, pp.1446,1455, July 1979

[Giurgea 2008] Giurgea, S.; Fodorean, D.; Cirrincione, G.; Miraoui, A.; Cirrincione, M., "Multimodel Optimization Based on the Response Surface of the Reduced FEM Simulation Model With Application to a PMSM," Magnetics, IEEE Transactions on , vol.44, no.9, pp.2153,2157, Sept. 2008

[Gómez 2014] Gomez, D.J.; Rodriguez, A.L.; Villar, I.; Lopez-de-Heredia, A.; Etxeberria-Otadui, I., "New Improved Lumped Circuit Model for Embedded Magnet Synchronous Machines" Electrical Machines (ICEM), 2014 International Conference on., 2-5 September 2014.

[Goss 2013-a] Goss, J.; Wrobel, R.; Mellor, P.; Staton, D., "The design of AC permanent magnet motors for electric vehicles: A design methodology," Electric Machines & Drives Conference (IEMDC), 2013 IEEE International , vol., no., pp.871,878, 12-15 May 2013

[Goss 2013-b] Goss, J.; Staton, D.; Wrobel, R.; Mellor, P., "Brushless AC interior-permanent magnet motor design: Comparison of slot/pole combinations and distributed vs. concentrated windings," Energy Conversion Congress and Exposition (ECCE), 2013 IEEE , vol., no., pp.1213,1219, 15-19 Sept. 2013

[Grobler 2015] Grobler, A.J.; Holm, S.R.; van Schoor, G., "A Two-Dimensional Analytic Thermal Model for a High-Speed PMSM Magnet," in Industrial Electronics, IEEE Transactions on , vol.62, no.11, pp.6756-6764, Nov. 2015

[Gurtin 1981] Gurtin M.E.; "An Introduction to Continuum Mechanics". Academic Press Inc., Mathematics in Science and Engineering, Vol.158, 1981

[Hafner 2011] Hafner, Martin; Finken, T.; Felden, M.; Hameyer, K., "Automated Virtual Prototyping of Permanent Magnet Synchronous Machines for HEVs," *Magnetics, IEEE Transactions on*, vol.47, no.5, pp.1018,1021, May 2011

[Hanselman 2012] Hanselman, D.; "Brushless Motors. Magnetic Design, Performance, and Control". US: E-Man Press LLC, 2012

[Hecker 2013] Hecker, Q.; Ccoa, J.A.B.; Meyer, W.; Herzog, H.-G., "Automated design of squirrel-cage induction machines by predefined torque-speed-characteristic," *Electric Machines & Drives Conference (IEMDC), 2013 IEEE International*, vol., no., pp.1160,1165, 12-15 May 2013

[Hofmann 2014] Hofmann, A.; Qi, F.; Lange, T.; De Doncker, R.W., "The breathing mode-shape 0: Is it the main acoustic issue in the PMSMs of today's electric vehicles?," in *Electrical Machines and Systems (ICEMS), 2014 17th International Conference on*, vol., no., pp.3067-3073, 22-25 Oct. 2014

[Hubert 2001] Hubert, A., "Contribution à l' étude des bruits acoustiques générés lors de l'association machines électriques -convertisseurs statiques de puissance. Application à la machine asynchrone" Ph.D. dissertation, Université de Technologie de Compiègne, 2001

[Hwang 2013] Chang-Chou Hwang; Chia-Ming Chang; Cheng-Tsung Liu, "A Fuzzy-Based Taguchi Method for Multiobjective Design of PM Motors," *Magnetics, IEEE Transactions on*, vol.49, no.5, pp.2153,2156, May 2013

[Iles-Klumpner 2004] Iles-Klumpner, D.; Boldea, I., "Comparative optimization design of an interior permanent magnet synchronous motor for an automotive active steering system," *Power Electronics Specialists Conference, 2004. PESC 04. 2004 IEEE 35th Annual*, vol.1, no., pp.369,375 Vol.1, 20-25 June 2004

[Ishak 2005] Ishak, D.; Zhu, Z.Q.; Howe, D., "Eddy-current loss in the rotor magnets of permanent-magnet brushless machines having a fractional number of slots per pole," *Magnetics, IEEE Transactions on*, vol.41, no.9, pp.2462,2469, Sept. 2005

[Ishibashi 2003] Ishibashi, F.; Kamimoto, K.; Noda, S.; Itomi, K., "Natural frequency of stator core of small induction motor," *Electric Power Applications, IEE Proceedings -*, vol.150, no.2, pp.210,214, Mar 2003

[Islam 2009] Islam, M.R., "Cogging torque, torque ripple and radial force analysis of permanent magnet synchronous machines" Ph.D. dissertation, Akron University, 2009

[Islam 2010] Islam, R.; Husain, I., "Analytical Model for Predicting Noise and Vibration in Permanent-Magnet Synchronous Motors," *Industry Applications, IEEE Transactions on* , vol.46, no.6, pp.2346,2354, Nov.-Dec. 2010

[Islam 2014] Islam, M.S.; Islam, R.; Sebastian, T., "Noise and Vibration Characteristics of Permanent-Magnet Synchronous Motors Using Electromagnetic and Structural Analyses," in *Industry Applications, IEEE Transactions on* , vol.50, no.5, pp.3214-3222, Sept.-Oct. 2014

[ISO 2003] International Organization for Standardization. "Acoustics- Normal equal loudness-level contours", ISO 226:2003 -BS 3383. 2003

[Jannot 2011] Jannot, X.; Vannier, J. -C; Marchand, C.; Gabsi, M.; Saint-Michel, J.; Sadarnac, D., "Multiphysic Modeling of a High-Speed Interior Permanent-Magnet Synchronous Machine for a Multiobjective Optimal Design," *Energy Conversion, IEEE Transactions on* , vol.26, no.2, pp.457,467, June 2011

[Lienhard 2003] John H. Lienhard IV, John H. Lienhard V. *A Heat Transfer Textbook*, third edition, Phlogiston Press, 2003

[Jordan 1950] Jordan, H.; "Electric motor silencer- formation and elimination of the noises in the electrical motors". W. Giradet-Essen editor, 1950

[Kazmin 2008-a] Kazmin, E.V.; Lomonova, E.A.; Paulides, J. J H, "Brushless traction PM machines using commercial drive technology, Part I: Design methodology and motor design," *Electrical Machines and Systems*, 2008. ICEMS 2008. International Conference on , vol., no., pp.3801,3809, 17-20 Oct. 2008

[Kazmin 2008-b] Kazmin, E.V.; Lomonova, E.A.; Paulides, J. J H, "Brushless traction PM machines using commercial drive technology, Part II: Comparative study of the motor configurations," *Electrical Machines and Systems*, 2008. ICEMS 2008. International Conference on , vol., no., pp.3772,3780, 17-20 Oct. 2008

[Kinsler 2000] Kinsler, L.E, Frey, A.R., Coppens A.B. and Sanders J.V, "Fundamentals of Acoustics" John Wiley & Sons, Inc., fourth edition 2000

[Kolehmainen 2010] Kolehmainen, J., "Optimal Dovetail Permanent Magnet Rotor Solutions for Various Pole Numbers," *Industrial Electronics, IEEE Transactions on* , vol.57, no.1, pp.70,77, Jan. 2010

[Kral 2014] Kral, C.; Haumer, A.; Sang Bin Lee, "A Practical Thermal Model for the Estimation of Permanent Magnet and Stator Winding Temperatures," in Power Electronics, IEEE Transactions on , vol.29, no.1, pp.455-464, Jan. 2014

[Kreuawan 2007] Kreuawan, S.; Gillon, F.; Moussouni, F.; Brisset, S.; Brochet, P., "Optimal design of traction motor in railway propulsion system," Electrical Machines and Power Electronics, 2007. ACEMP '07. International Aegean Conference on , vol., no., pp.343,348, 10-12 Sept. 2007

[Kylander 1995] Kylander, G.; "Thermal modelling of small cage induction motors" Department of Electrical Machines and Power Electronics, Chalmers University of Technology, Göteborg, Sweden, Tech. Rep., February 1995

[Lee 2009] Sang-Ho Lee; Jung-Pyo Hong; Sang-Moon Hwang; Woo-Taik Lee; Ji-Young Lee; Young-Kyoun Kim, "Optimal Design for Noise Reduction in Interior Permanent-Magnet Motor," Industry Applications, IEEE Transactions on , vol.45, no.6, pp.1954,1960, Nov.-dec. 2009

[Lee 2015] Ki-Doek Lee; Won-Ho Kim; Chang-Sung Jin; Ju Lee, "Local demagnetisation analysis of a permanent magnet motor," in Electric Power Applications, IET , vol.9, no.3, pp.280-286, 3 2015

[Legranger 2008] Legranger, J.; Friedrich, G.; Vivier, S.; Mipo, J.C., "Combination of Finite Element and Analytical Models in the Optimal Multi-Domain Design of Machines: Application to an Interior Permanent Magnet Starter Generator," Industry Applications Society Annual Meeting, 2008. IAS '08. IEEE , vol., no., pp.1,6, 5-9 Oct. 2008

[Lindström 1999] Lindström, J.; "Thermal model of a permanent-magnet motor for a hybrid electric vehicle," Department of Electric power Engineering, Chalmers University of Technology, Göteborg, Sweden, Tech. Rep., Apr. 1999

[Liu 2008] Liu, Z.J.; Li, J.T., "Accurate Prediction of Magnetic Field and Magnetic Forces in Permanent Magnet Motors Using an Analytical Solution," Energy Conversion, IEEE Transactions on , vol.23, no.3, pp.717,726, Sept. 2008

[Lu 2006] Lu, K.; Rasmussen, P.O.; Ritchie, E., ""An Analytical Equation for Cogging Torque Calculation in Permanent Magnet Motors"". Electrical Machines, 2006 International Conference on , Chania, Kreta, Greece, 2006.

[Lu 2013] Xiaomin Lu; Iyer, K.L.V.; Mukherjee, K.; Kar, N.C., "Development of a Novel Magnetic Circuit Model for Design of Premium Efficiency Three-Phase Line Start

Permanent Magnet Machines With Improved Starting Performance," *Magnetics, IEEE Transactions on* , vol.49, no.7, pp.3965,3968, July 2013

[Madina 2011] Madina, P.; Poza, J.; Ugalde, G.; Almandoz, G., "Magnet eddy current loss calculation method for segmentation analysis on permanent magnet machines," *Power Electronics and Applications (EPE 2011), Proceedings of the 2011-14th European Conference on* , vol., no., pp.1,9, Aug. 30 2011-Sept. 1 2011

[Makni 2007] Makni, Z.; Besbes, M.; Marchand, C., "Multiphysics Design Methodology of Permanent-Magnet Synchronous Motors," *Vehicular Technology, IEEE Transactions on* , vol.56, no.4, pp.1524,1530, July 2007

[Malloy 2015] Malloy, A.C.; Martinez-Botas, R.F.; Lamperth, M., "Measurement of Magnet Losses in a Surface Mounted Permanent Magnet Synchronous Machine," in *Energy Conversion, IEEE Transactions on* , vol.30, no.1, pp.323-330, March 2015

[Marignetti 2006] Marignetti, F.; Tomassi, Giovanni; Cancelliere, P.; Delli Colli, V.; Di Stefano, R.; Scarano, Maurizio, "Electromagnetic and Mechanical design of a Fractional-slot-windings Axial-flux PM synchronous machine with Soft Magnetic Compound Stator," *Industry Applications Conference, 2006. 41st IAS Annual Meeting. Conference Record of the 2006 IEEE* , vol.1, no., pp.62,69, 8-12 Oct. 2006

[Markovic 2007] Markovic, M.; Perriard, Y., "An Analytical Determination of Eddy-Current Losses in a Configuration With a Rotating Permanent Magnet," *Magnetics, IEEE Transactions on* , vol.43, no.8, pp.3380,3386, Aug. 2007

[Mellor 1991] Mellor, P.H.; Roberts, D.; Turner, D.R., "Lumped parameter thermal model for electrical machines of TEFC design," *Electric Power Applications, IEE Proceedings B* , vol.138, no.5, pp.205,218, Sep 1991

[Mi 2006] Mi, C.C., "Analytical design of permanent-magnet traction-drive motors," *Magnetics, IEEE Transactions on* , vol.42, no.7, pp.1861,1866, July 2006

[Mirahki 2014] Mirahki, H.; Moallem, M.; Rahimi, S.A., "Design Optimization of IPMSM for 42 V Integrated Starter Alternator Using Lumped Parameter Model and Genetic Algorithms," in *Magnetics, IEEE Transactions on*, vol.50, no.3, pp.114-119, March 2014

[Motor-CAD 2012] "Motor-CAD Help." In: Ltd., M.D. (ed.), 2012

[Muetze 2008] Muetze, A., "A neglected stepchild?," Industry Applications Magazine, IEEE , vol.14, no.2, pp.14,22, March-April 2008

[Munteanu 2012] Munteanu, A.; Boldea, I.; Tutelea, L., "Novel hybrid design methodology for a surface permanent magnet synchronous motor," Power Electronics, Electrical Drives, Automation and Motion (SPEEDAM), 2012 International Symposium on , vol., no., pp.603,608, 20-22 June 2012

[Nerg 2008] Nerg, J.; Rilla, M.; Pyrhonen, J., "Thermal Analysis of Radial-Flux Electrical Machines With a High Power Density," Industrial Electronics, IEEE Transactions on , vol.55, no.10, pp.3543,3554, Oct. 2008

[Nipp 1999] Nipp, E., "Permanent Magnet Motor Drives with Switched Stator Windings" Ph.D. dissertation, Royal Institute of Technology Department of Electric Power Engineering Electrical Machines and Drives, Stockholm 1999

[Novotny 1996] Novotny, D.W.; Lipo, T.A.; "Vector Control and Dynamics of AC Drives". Us: Oxford University Press, 1996

[Ombach 2007] Ombach, G.; Junak, J., "Design of PM Brushless Motor Taking into Account Tolerances of Mass Production - Six Sigma Design Method," Industry Applications Conference, 2007. 42nd IAS Annual Meeting. Conference Record of the 2007 IEEE , vol., no., pp.2139,2146, 23-27 Sept. 2007

[Patel 2013] Patel, V.I.; Jiabin Wang; Weiya Wang; Xiao Chen, "Analysis and design of 6-phase fractional slot per pole per phase permanent magnet machines with low space harmonics," Electric Machines & Drives Conference (IEMDC), 2013 IEEE International , vol., no., pp.386,393, 12-15 May 2013

[Pérez 1979] Perez, I.J.; Kassakian J.G., "A stationary thermal model for smooth airgap rotating electrical machines". Electric Machines and Electromechanics 3, p. 285-303. 1979

[Pinsky 2003] Pinsky, M.A.; "Partial Differential Equations and Boundary-Value Problems with Applications", 3rd edition. Waveland Press, 2003

[Proca 2003] Proca, A.B.; Keyhani, A.; El-Antably, A.; Wenzhe Lu; Min Dai, "Analytical model for permanent magnet motors with surface mounted magnets," Energy Conversion, IEEE Transactions on , vol.18, no.3, pp.386,391, Sept. 2003

[Pyrhönen 2008] Pyrhönen, J., Jokinen T., Hrabovcová V.; "Design of Rotating Electrical Machines". UK. John Wiley & Sons Ltd., 2008

[Pyrhönen 2012] Pyrhonen, J.; Jussila, H.; Alexandrova, Y.; Rafajdus, P.; Nerg, J., "Harmonic Loss Calculation in Rotor Surface Permanent Magnets—New Analytic Approach," Magnetics, IEEE Transactions on , vol.48, no.8, pp.2358,2366, Aug. 2012

[Rahman 2013] Rahman, M.A., "History of interior permanent magnet motors (History)," Industry Applications Magazine, IEEE , vol.19, no.1, pp.10,15, Jan.-Feb. 2013

[Rodríguez 2013] Rodriguez, A.L.; Gomez, D.J.; Villar, I.; Lopez-de-Heredia, A.; Etxeberria-Otadui, I., "New improved estimation method for airgap self and mutual inductance in electric machines," Power Electronics and Applications (EPE), 2013 15th European Conference on , vol., no., pp.1,9, 2-6 Sept. 2013

[Rodríguez 2014-a] Rodriguez, A.L.; Gomez, D.J.; Villar, I.; Lopez-de-Heredia, A.; Etxeberria-Otadui, I., "Improved Analytical Multiphysical Modeling of a Surface PMSM" Electrical Machines (ICEM), 2014 International Conference on., 2-5 September 2014

[Rodríguez 2014-b] Rodriguez, A.L.; Gomez, D.J.; Villar, I.; Lopez-de-Heredia, A.; Etxeberria-Otadui, I., "New Analytical Method for PMSM Magnet Losses Estimation based on Fourier Series" Electrical Machines (ICEM), 2014 International Conference on., 2-5 September 2014

[Ruoho 2009] Ruoho, S.; Santa-Nokki, T.; Kolehmainen, J.; Arkkio, A., "Modeling Magnet Length In 2-D Finite-Element Analysis of Electric Machines," Magnetics, IEEE Transactions on , vol.45, no.8, pp.3114,3120, Aug. 2009

[Saari 1998] Saari,J.,"Thermal analysis of high-spped induction machines" Ph.D. dissertation, Helsinki University of Technology, Laboratory of Electromechanics, 1998

[Saito 2010] Saito, N.; Kijima, R.; Shimomura, S., "The design method to minimize torque ripple in interior permanent magnet synchronous motor with concentrated winding," Power Electronics Conference (IPEC), 2010 International , vol., no., pp.1293,1298, 21-24 June 2010

[Sanchez 2006] Sanchez-Grandia, R.; Vives-Fos, R and Aucejo-Galindo, V., "Magnetostatic Maxwell's tensors in magnetic media applying virtual works method from either energy or co-energy." The European Physical Journal Applied Physics, 35, pp 61-68. 2006

[Sarikhani 2012] Sarikhani, A.; Mohammed, O.A., "HIL-Based Finite-Element Design Optimization Process for the Computational Prototyping of Electric Motor Drives," Energy Conversion, IEEE Transactions on , vol.27, no.3, pp.737,746, Sept. 2012

[Schlensok 2007] Schlensok, C.; Van der Giet, M.; Gracia, M.H.; Van Riesen, D.; Hameyer, K., "Structure-Dynamic Analysis of an Induction Machine depending on Stator-Housing Coupling," Electric Machines & Drives Conference, 2007. IEMDC '07. IEEE International , vol.2, no., pp.1540,1545, 3-5 May 2007

[Semidey 2011] Semidey, S.A.; Yao Duan; Mayor, J.R.; Harley, R.G.; Habetler, T.G., "Optimal Electromagnetic-Thermo-Mechanical Integrated Design Candidate Search and Selection for Surface-Mount Permanent-Magnet Machines Considering Load Profiles," Industry Applications, IEEE Transactions on , vol.47, no.6, pp.2460,2468, Nov.-Dec. 2011

[Sirvent 2012] G. Sirvent. "El mercado de tierras raras: Un mercado estratégico". Instituto Español de asuntos estratégicos. Ministerio de defensa. September 2012. [Available at: <http://www.ieee.es/documentos/areas-tematicas/retos-y-amenazas/2012/detalle/DIEEO72-2012.html>]

[Soong 2008] Soong, W. L., "Sizing of Electrical Machines". 2008. [Available at: <http://www.eleceng.adelaide.edu.au/research/power/pebn/pebn009%20sizing%20of%20electrical%20machines.pdf>]

[Staton 2008] Staton, D.A.; Cavagnino, A., "Convection Heat Transfer and Flow Calculations Suitable for Electric Machines Thermal Models," Industrial Electronics, IEEE Transactions on , vol.55, no.10, pp.3509,3516, Oct. 2008

[Staton 2011] Staton, D. A.; Dan, M.; Dorrell; David, G.; Pellegrino, G., "Practical Aspect in Modern Design Process of Electric Motors", IEEE Energy Conversion Congress & Exposition , 2011.

[Tessarolo 2012] Tessarolo, A.; Bortolozzi, M.; Mezzarobba, M., "On the validity of the harmonic superposition principle for computing rotor eddy current losses in permanent magnet machines," Electrical Machines (ICEM), 2012 XXth International Conference on , vol., no., pp.1369,1373, 2-5 Sept. 2012

[Timar 1989] Timar, P.; "Noise and Vibration of Electrical Machines". Amsterdam, The Netherlands: Elsevier, 1989

[Timoshenko 1951] Timoshenko, S. and Goodier J.N., "Theory of Elasticity" McGraw-Hill, second edition 1951

[Timoshenko 1976-a] Timoshenko, S., "Strength of materials. Part I" Robert E. Krieger Publishing Company, third edition 1976

[Timoshenko 1976-b] Timoshenko, S., "Strength of materials. Part II" Robert E. Krieger Publishing Company, third edition 1976

[Torregrossa 2012] Torregrossa, D.; Fahimi, B.; Peyraut, F.; Miraoui, A., "Fast Computation of Electromagnetic Vibrations in Electrical Machines via Field Reconstruction Method and Knowledge of Mechanical Impulse Response," Industrial Electronics, IEEE Transactions on , vol.59, no.2, pp.839,847, Feb. 2012

[Tsampouris 2013] Tsampouris, E.M.; Kakosimos, P.E.; Kladas, A.G., "Coupled Computation of Electric Motor Design and Control Parameters Based on Ant Colonies Speed Trajectory Optimization," Magnetics, IEEE Transactions on , vol.49, no.5, pp.2177,2180, May 2013

[Tutelea 2010] Tutelea, L.; Boldea, I., "Surface permanent magnet synchronous motor optimization design: Hooke Jeeves method versus genetic algorithms," Industrial Electronics (ISIE), 2010 IEEE International Symposium on , vol., no., pp.1504,1509, 4-7 July 2010

[Van der Giet 2010] Van der Giet, M.; Franck, D.; Rothe, R.; Hameyer, K., "Fast-and-easy acoustic optimization of PMSM by means of hybrid modeling and FEM-to-measurement transfer functions," Electrical Machines (ICEM), 2010 XIX International Conference on , vol., no., pp.1,6, 6-8 Sept. 2010

[Verez 2015] Verez, G.; Barakat, G.; Amara, Y.; Hoblos, G., "Impact of Pole and Slot Combination on Vibrations and Noise of Electromagnetic Origins in Permanent Magnet Synchronous Motors," in Magnetics, IEEE Transactions on , vol.51, no.3, pp.1-4, March 2015

[Vese 2010] Vese, I.; Marignetti, F.; Radulescu, M.M., "Multiphysics Approach to Numerical Modeling of a Permanent-Magnet Tubular Linear Motor," Industrial Electronics, IEEE Transactions on , vol.57, no.1, pp.320,326, Jan. 2010

[Vijayraghavan 1999] Vijayraghavan, P.; Krishnan, R., "Noise in electric machines: a review," Industry Applications, IEEE Transactions on , vol.35, no.5, pp.1007,1013, Sep/Oct 1999

[Villar 2010] Villar, I., "Multiphysical Characterization of Medium-Frequency Power Electronic Transformers" Ph.D. dissertation, Laboratoire d'Électronique Industrielle, École Polytechnique Fédérale de Lausanne, 2010

[Wang 2012] Daohan Wang; Xiuhe Wang; Mun-Kyeom Kim; Sang-Yong Jung, "Integrated Optimization of Two Design Techniques for Cogging Torque Reduction Combined With Analytical Method by a Simple Gradient Descent Method," *Magnetics, IEEE Transactions on* , vol.48, no.8, pp.2265,2276, Aug. 2012

[Wang 2013] Jiabin Wang; Xibo Yuan; Atallah, K., "Design Optimization of a Surface-Mounted Permanent-Magnet Motor With Concentrated Windings for Electric Vehicle Applications," *Vehicular Technology, IEEE Transactions on* , vol.62, no.3, pp.1053,1064, March 2013

[Weidong 2007] Weidong Zhu; Pekarek, S.; Fahimi, B.; Deken, B.J., "Investigation of Force Generation in a Permanent Magnet Synchronous Machine," *Energy Conversion, IEEE Transactions on* , vol.22, no.3, pp.557,565, Sept. 2007

[Weilharter 2012] Weilharter, B.; Biro, O.; Lang, H.; Ofner, G.; Rainer, S., "Validation of a Comprehensive Analytic Noise Computation Method for Induction Machines," *Industrial Electronics, IEEE Transactions on* , vol.59, no.5, pp.2248,2257, May 2012

[Wrobel 2006] Wrobel, R.; Mellor, P.H., "Particle Swarm Optimisation for the Design of Brushless Permanent Magnet Machines," *Industry Applications Conference, 2006. 41st IAS Annual Meeting. Conference Record of the 2006 IEEE* , vol.4, no., pp.1891,1897, 8-12 Oct. 2006

[Wu 2012] Wu, L. J.; Zhu, Z.Q.; Staton, D.; Popescu, M.; Hawkins, D., "Analytical Model for Predicting Magnet Loss of Surface-Mounted Permanent Magnet Machines Accounting for Slotting Effect and Load," *Magnetics, IEEE Transactions on* , vol.48, no.1, pp.107,117, Jan. 2012

[Wu 2014] Wu, L.J.; Zhu, Z.Q., "Analytical Modeling of Surface-Mounted PM Machines Accounting for Magnet Shaping and Varied Magnet Property Distribution," *Magnetics, IEEE Transactions on* . To be published. 2014

[Wu 2015] Wu, D.; Zhu, Z., "Design Trade-off between Cogging Torque and Torque Ripple in Fractional Slot Surface-Mounted Permanent Magnet Machines," *Magnetics, IEEE Transactions on* . Accepted for publication, 2015

[Wurtz 1996] Wurtz, F.; Bignon, J.; Poirson, C., "A methodology and a tool for the computer aided design with constraints of electrical devices," *Magnetics, IEEE Transactions on* , vol.32, no.3, pp.1429,1432, May 1996

[Yang 1981] Yang, S.J.; "Low-Noise Electrical Motors". Oxford: Clarendon Press, 1981

[Zarko 2006] Zarko, D.; Ban, D.; Lipo, T.A., "Analytical calculation of magnetic field distribution in the slotted airgap of a surface permanent-magnet motor using complex relative air-gap permeance," *Magnetics, IEEE Transactions on*, vol.42, no.7, pp.1828,1837, July 2006

[Zarko 2008] Zarko, D.; Ban, D.; Lipo, T.A., "Analytical Solution for Cogging Torque in Surface Permanent-Magnet Motors Using Conformal Mapping," *Magnetics, IEEE Transactions on*, vol.44, no.1, pp.52,65, Jan. 2008

[Zhang 2014] Peng Zhang; Sizov, G.Y.; Muyang Li; Ionel, D.M.; Demerdash, N.A.O.; Stretz, S.J.; Yeadon, A.W., "Multi-Objective Tradeoffs in the Design Optimization of a Brushless Permanent-Magnet Machine With Fractional-Slot Concentrated Windings," in *Industry Applications, IEEE Transactions on*, vol.50, no.5, pp.3285-3294, Sept.-Oct. 2014

[Zhang 2015] Bin Zhang; Ronghai Qu; Jin Wang; Wei Xu; Xinggong Fan; Yu Chen, "Thermal Model of Totally Enclosed Water-Cooled Permanent-Magnet Synchronous Machines for Electric Vehicle Application," in *Industry Applications, IEEE Transactions on*, vol.51, no.4, pp.3020-3029, July-Aug. 2015

[Zhu 1992] Zhu, Z.Q.; Howe, D., "Analytical prediction of the cogging torque in radial-field permanent magnet brushless motors," *Magnetics, IEEE Transactions on*, vol.28, no.2, pp.1371,1374, Mar 1992

[Zhu 1993-a] Zhu, Z.Q.; Howe, D.; Bolte, E.; Ackermann, B., "Instantaneous magnetic field distribution in brushless permanent magnet DC motors. I. Open-circuit field," *Magnetics, IEEE Transactions on*, vol.29, no.1, pp.124,135, Jan 1993

[Zhu 1993-b] Zhu, Z.Q.; Howe, D., "Instantaneous magnetic field distribution in brushless permanent magnet DC motors. II. Armature-reaction field," *Magnetics, IEEE Transactions on*, vol.29, no.1, pp.136,142, Jan 1993

[Zhu 2004] Zhu, Z.Q.; Ng, K.; Schofield, N.; Howe, D., "Improved analytical modelling of rotor eddy current loss in brushless machines equipped with surface-mounted permanent magnets," *Electric Power Applications, IEE Proceedings -*, vol.151, no.6, pp.641,650, 7 Nov. 2004

[Zhu 2010] Zhu, Z.Q.; Xia, Z.P.; Wu, L. J.; Jewell, G.W., "Analytical Modeling and Finite-Element Computation of Radial Vibration Force in Fractional-Slot Permanent-Magnet Brushless Machines," *Industry Applications, IEEE Transactions on*, vol.46, no.5, pp.1908,1918, Sept.-Oct. 2010

[Zuo 2015] Shuguang Zuo; Fu Lin; Xudong Wu, "Noise Analysis, Calculation, and Reduction of External Rotor Permanent-Magnet Synchronous Motor," in Industrial Electronics, IEEE Transactions on , vol.62, no.10, pp.6204-6212, Oct. 2015

